

# **Thermal and Radiation Processing of Porous Extraterrestrial Water Ice**

---

A Dissertation

Presented to  
the faculty of the School of Engineering and Applied Science  
University of Virginia

---

in partial fulfillment  
of the requirements for the degree

Doctor of Philosophy

by

Emily H. Mitchell

August  
2016

## APPROVAL SHEET

The dissertation  
is submitted in partial fulfillment of the requirements  
for the degree of  
Doctor of Philosophy

Emily H. Mitchell

AUTHOR

The dissertation has been read and approved by the examining committee:

Petra Reinke

*Advisor*

Materials Science Engineering

Robert E. Johnson

*Advisor*

Engineering Physics

Gary J. Shiflet

Materials Science Engineering

Ian Harrison

Chemistry

Charles A. Sackett

Physics

Ujjwal Raut

Southwest Research Institute

Accepted for the School of Engineering and Applied Science:



Craig H. Benson, Dean of the School of Engineering and Applied Science

August  
2016

## Table of Contents

Abstract	6
Acknowledgements	9
Symbols and Abbreviations	11
List of Figures	19
 Chapter 1: Introduction	 22
 Chapter 2: Instrumentation and Methods	 
2.1. Ultrahigh Vacuum Chamber	37
2.2. Microcapillary Array Doser	43
2.3. Quartz Crystal Microbalance	44
2.4. Ion Accelerator	45
2.5. Infrared Spectrometer	47
2.6. Ultraviolet-Visible Spectrometer	51
2.7. Quadrupole Mass Spectrometer	53
2.8. Excimer Laser	54
2.9. Data Acquisition	54
2.10. Sources of Experimental Error	55
 Chapter 3: Crystallization of Porous Ices in the Outer Solar System	 
3.1. Isothermal Crystallization Kinetics of Amorphous Solid Water	
3.1.1 Introduction	58
3.1.2 Experimental Methods	61
3.1.3 Results and Discussion	62
3.1.4 Summary and Conclusions	72
3.2. Effects of Growth Porosity on Ice Crystallization	
3.2.1 Introduction	76
3.2.2 Experimental Methods	79
3.2.3 Results	
I. Porosity in ASW films	81
II. Thermal Compaction	83
III. Crystallization Kinetics	87

3.2.4	Discussion	95
3.2.5	Astrophysical Implications	104
3.2.6	Conclusions	107
Chapter 4: Ultraviolet Photodesorption as a Driver of Water Migration on the Lunar Surface		
4.1.	Introduction	114
4.2	Experimental Methods	
I.	Photodesorption Experiments	117
II.	Sputtering Experiments	118
4.3	Results	119
4.4	Discussion	
I.	Photodesorption	122
II.	Estimation of Lifetime of Adsorbed Water	124
Chapter 5: Irradiation Effects of Methane-Laden Porous Amorphous Solid Water Films in the Outer Solar System		
5.1	Introduction	130
5.2	Experimental Methods	133
5.3	Results and Discussion	
I.	Temperature Dependence of Methane Adsorption in Ice Pores	135
II.	Ion-Enhanced Gas Adsorption	137
III.	Radiolytic Conversion of Methane and Water into New Species	140
IV.	Thermal Desorption of Irradiated Films	147
5.4	Summary and Conclusions	151
Chapter 6: Irradiation Effects of H <sub>2</sub> -Laden Porous Water Ice Films: Implications for Interstellar Ices		
6.1.	Ion Irradiation of H <sub>2</sub> -Laden Porous Water Ice Films	
6.1.1	Introduction	156
6.1.2	Experimental Methods	158
6.1.3	Results and Discussion	
I.	Kinetics: H <sub>2</sub> Sputtering and Adsorption	160

II.	Effects of Film Thickness	164
III.	Effects of H <sub>2</sub> Pressure	167
IV.	Rate Equations	169
V.	Infrared Results	171
VI.	Effects of Irradiation Flux	175
VII.	$\zeta$ -Dependent H <sub>2</sub> Trapping	177
6.1.4	Astrophysical Implications	177
6.1.5	Conclusions	180
6.2.	Suppression of H <sub>2</sub> O <sub>2</sub> in Radiolyzed H <sub>2</sub> -Laden Ice Films	
6.2.1	Introduction	184
6.2.2	Experimental Methods	187
6.2.3	Results and Discussion	189
6.2.4	Discussion and Astrophysical Implications	198
Chapter 7:	Conclusion	202

## Abstract

This dissertation is an experimental study of the factors responsible for the state of water ice in extraterrestrial environments, and the changes induced in these ices due to pervasive space phenomena such as thermal processing and UV and energetic particle irradiation. The properties of frozen water are strongly dependent on the astronomical environment that harbors the ice. Ice morphology, phase, and chemical composition continually evolve due to processes such as thermal cycling, exposure to exospheric gases, and interaction with cosmic rays and stellar UV and particle fluxes. In this project, analytical techniques such as quartz crystal microgravimetry, infrared spectroscopy, ultraviolet-visible spectroscopy, and mass spectrometry were used in tandem to probe physical and chemical changes induced in laboratory-scale analogs of astronomical ices

First, we characterized the transformation of amorphous ice to the cubic crystalline phase, extrapolating our results to estimate the crystallization time of ices on Outer Solar System satellites, where a puzzling distribution of amorphous and crystalline ice has been detected. We vapor-deposited amorphous ice at 10 K and examined the effects of ice porosity on crystallization kinetics at 130 to 141 K, finding that ices of high porosity crystallize significantly faster than less porous ices. The experiments reveal a surface-driven crystallization process that can explain observations of crystalline ice on Jovian moons.

We have also simulated monolayer coverage of water on the lunar surface and performed 193-nm photon and 4-keV  $\text{He}^+$  irradiations to investigate processes responsible for the observed diurnal and latitudinal variation in water abundance. We found that photodesorption by solar photons is four orders of magnitude more efficient than the solar wind in removing water

molecules from the lunar regolith, with a lifetime of  $\sim 12$  hours for average solar activity at the sub-solar point.

We then studied synergistic effects induced in ices exposed to ambient methane and ion irradiation, to mimic surficial gas trapping observed on trans-Neptunian objects by space missions such as NASA's *New Horizons*. We found that adsorption of methane by the ice increased during 100-keV proton irradiation at 40 to 50 K, due to competition between enhanced uptake in radiation-modified ice pores and pore collapse. Additionally, we observed complex radiation chemistry between the ice and adsorbed methane, detecting more than a dozen new molecular species synthesized from dissociated radicals in the radiolyzed film.

Finally, we simulated irradiation effects of ice-covered dust grains immersed in gaseous hydrogen in the interstellar medium. In contrast to the irradiation of ices exposed to ambient methane, we determined that 100-keV proton irradiation led to net loss of adsorbed  $H_2$  from porous ice films at 7 K, with a desorption cross-section independent of film thickness,  $H_2$  flux, and ion flux. We found residual amounts of hydrogen trapped within the radiolyzed ice at high ion doses, and estimate as high as 8% concentration of trapped gas at interstellar  $H_2$  accretion rates due to the cosmic ray flux. We also found that the ambient  $H_2$  caused suppression in radiolytic peroxide production due to H-enrichment and the decrease in OH concentration in the film, compared to the irradiation of  $H_2O$  ices without deliberate exposure to  $H_2$ .

These experiments show that the ice pores strongly affect the changes induced in extraterrestrial ices by thermal and radiation processing. The pores facilitate crystallization, trap atmospheric gases, harbor radiolytic molecules, and govern physical and chemical transformations of icy surfaces. The results obtained in this dissertation can be compared with

results from astronomical observations and used to interpret the history and predict the evolution of icy surfaces in space.



## Acknowledgements

This dissertation is the result of work that has spanned six years. It would not have been possible without the support of a group of people that I have been privileged to call my advisors and colleagues.

First, this research project was envisioned and supported by my advisor, Raúl A. Baragiola, who passed away on June 21, 2015. Raúl is remembered for his limitless scientific curiosity, insightful questions, astute critiques, and optimism even in the midst of the most daunting undertakings. I am grateful that Raúl accepted me into the research group, and am hopeful that he would be pleased with the work presented here.

I thank Bob Johnson and Petra Reinke for generously stepping up to serve as my Ph.D. advisors after Raúl's passing. They each contributed to steering me toward the completion of this work over the last year of my project, and I am grateful to them both.

The person most singly helpful to me over all six years of my graduate studies was Ujjwal Raut. At first a post-doctoral researcher, Ujjwal took me under his wing when I first arrived in the lab and taught me nearly everything I know about how to operate the equipment, plan and execute an experiment, analyze and contextualize data, and respond to the inevitable laboratory catastrophes. Ujjwal has, for all intents and purposes, acted as my research advisor during my time as a graduate student, overseeing the scope of my entire project and providing invaluable guidance. I could not have completed this work without his support.

The members of the Laboratory for Astrophysics and Surface Physics have been a constant source of support over the years. Cathy Dukes, in particular, has been immeasurably helpful, and I could not have asked for better colleagues over the years than Caixia Bu, Micah

Schaible, Daniele Fulvio, Adam Woodson, and Gerard Rodríguez López. Having these people around me has made my experimental challenges more solvable and my days more fulfilling.

My family has been my backbone throughout my entire life, and this work is dedicated to them. My parents made my education a topmost priority throughout my childhood. My mother, Cynthia Thornton, has been a constant, unwavering source of support for me. There has not been a single time in my life when she was not there for me, and there has not been a single decision I have made that she has not lovingly and often selflessly supported.

I have always tried to emulate my dad, Dan Mitchell, who is utterly enthusiastic about being a math and science nerd. So many girls go through their childhood believing that they lack ability in math and science, or are not encouraged to challenge themselves in problem-solving. In the eighth grade, I was homeschooled for a year and my dad taught me algebra, telling me that he knew I would be good at it. Over the course of that year, I realized that I was good at problem-solving, just like my dad. I would not have pursued physics if I didn't have him as a role model.

Finally, I would to thank my four siblings – Reed, Annie, Aaron, and Drew Mitchell – for their uplifting and loving support, not to mention comic relief, over our entire lives. They are all incredibly talented, stunningly intelligent, well-rounded, and thoughtful people. I am so proud of everything they have accomplished, and I am lucky to have all four of them as siblings.

### List of Symbols and Abbreviations

$a$	H <sub>2</sub> uptake constant
$A$	active area of the QCM
AC	alternating current
ASW	amorphous solid water
AU	astronomical unit
$B$	magnetic field
$B_0$	pre-irradiation band area
$B_\infty$	saturation band area
BDI	background-deposited ice
BE	binding energy
$C$	crystallization term in Avrami exponent
CCD	charge-coupled device
cm	centimeter
CMA	cylindrical-mirror electron energy analyzer
conc.	concentration
CR	cosmic ray
C-type ice	co-deposited H <sub>2</sub> -H <sub>2</sub> O ice film
$D$	decrease in $\eta(\text{H}_2)$
d	day
$d$	ice thickness
DB	dangling bond absorption bands
DB1	dangling bond absorption band at $\sim 3270 \text{ cm}^{-1}$

DB2	dangling bond absorption band at $\sim 3696\text{ cm}^{-1}$
DC	direct current
$dE/dx$	ion stopping power
DI	Deep Impact
DSC	differential scanning calorimetry
$E$	energy
EFL	effective focal length
eq.	equivalent
eV	electron Volt
$F$	irradiation fluence
$f$	irradiation flux
$F_H$	H <sub>2</sub> flux
FTIR	Fourier transform infrared spectrometry
FWHM	full-width half-maximum
g	gram
GeV	giga-electron Volt
h	hour
HPLC	high-performance liquid chromatography
HRI	High-Resolution Instrument
HST	Hubble Space Telescope
Hz	Hertz ( $\text{s}^{-1}$ )
$I$	solar irradiance
$IB$	irradiation pulse

IR	infrared
IS	interstellar
ISO	Infrared Space Observatory
ISM	interstellar medium
J	Joule
$K$	Avrami rate constant
$K_0^{1/n}$	Avrami pre-exponential factor
$K_1^{1/n1}$	Avrami rate constant for first crystallization stage
$K_2^{1/n2}$	Avrami rate constant for second crystallization stage
$K_{2_0}^{1/n_2}$	Avrami pre-exponential factor derived using $n_2$ and $K_2^{1/n2}$
KBO	Kuiper Belt Object
keV	kilo-electron Volts
kg	kilogram
kJ	kilo-Joule
km	kilometer
kV	kilovolt
L	Langmuir = $10^{-6}$ Torr-sec.
LN <sub>2</sub>	liquid nitrogen
m	minute
$m$	mass
M <sup>3</sup>	Moon Mineralogy Mapper
MCA	microcapillary array
MCP	microchannel plate

MCT	mercury cadmium telluride
MHz	mega-Hz
ML	monolayer
mol	mole
mm	millimeter
mTorr	milli-Torr
Myr	million years
$N$	nucleation term in Avrami exponent
$N$	net decrease in $\eta(\text{H}_2)$
$n$	Avrami exponent
$n_1$	Avrami exponent for first crystallization stage
$n_2$	Avrami exponent for second crystallization stage
NIMS	Near Infrared Mapping Spectrometer
NIR	near infrared
nm	nanometer
ns	nanosecond
OFHC	oxygen-free high thermal conductivity
$P$	pressure
$p$	ratio between $P$ and $P_{\max}$
$P_{\max}$	maximum pressure
PSD	photon-stimulated desorption
P-type ice	$\text{H}_2\text{O}$ ice film that is exposed to ambient $\text{H}_2$ after deposition
$q$	charge

QCM	quartz crystal microbalance
QMS	quadrupole mass spectrometer
$R$	gas constant
$R$	reflectance of bare gold substrate
$\dot{R}$	H <sub>2</sub> uptake rate
$r$	radius of curvature
$R_0$	reflectance of film-substrate system
$R_{\text{CsI}}$	deposition rate, measured by QCM, when doser faces CsI substrate
$R_{\text{QCM}}$	deposition rate, measured by QCM, when doser faces QCM substrate
RF	radio frequency
$S$	synthetic infrared spectrum generated using factor analysis
s	second
$s$	sticking coefficient
sl.	slope
SIMS	Secondary Ion Mass Spectroscopy
$T$	temperature
$T$	transmittance of bare CsI substrate
$t$	time
$T_0$	transmittance of film-substrate system
$T_A$	infrared spectrum of pure amorphous ice
$T_C$	infrared spectrum of pure crystalline ice
TEM	transmission electron microscopy
Torr	unit of pressure (1 atm = 760 Torr)

TNI	transient negative ion
TNO	trans-Neptunian object
TPD	temperature-programmed desorption
UHV	ultrahigh vacuum
UV	ultraviolet
V	Volt
$V$	potential
VIMS	Visual and Infrared Mapping Spectrometer
W	Watt
$W$	XPS work function
XPS	X-ray Photoelectron Spectroscopy
Y	sputtering yield
y	year
$\alpha$	ratio between $R_{QCM}$ and $R_{CsI}$
$\beta$	QCM proportionality constant
$\Delta f$	frequency shift
$\Delta H$	crystallization activation energy
$\zeta$	ratio between $f$ and $F_H$
$\eta$	column density
$\eta_0$	equilibrium column density
$\eta_1$	column density of ice in <i>Type I</i> pores
$\eta_2$	column density of ice in <i>Type II</i> pores
$\eta_m$	saturation column density



$\eta_{\infty}$	column density of residual H <sub>2</sub>
$\mu\text{g}$	microgram
$\mu\text{m}$	micron
$\xi$	desorption rate
$\rho$	ice density
$\rho_c$	compact ice density
$\sigma_1$	initial destruction cross-section
$\sigma_2$	final destruction cross-section
$\sigma_d$	destruction cross-section
$\sigma_G$	mass gain cross-section
$\sigma_{L1}$	sputtering cross-section for ice in <i>Type I</i> pores
$\sigma_{L12}$	cross-section to transfer gas from <i>Type I</i> to <i>Type II</i> pores
$\sigma_{L2}$	sputtering cross-section for ice in <i>Type II</i> pores
$\sigma_{L23}$	cross-section to transfer gas from <i>Type II</i> to <i>Type III</i> pores
$\sigma^*$	effective H <sub>2</sub> net loss cross-section
$\sigma'_L$	effective H <sub>2</sub> loss cross-section
$\tau$	lifetime
$\tau_{\text{ad}}$	time constant for H <sub>2</sub> adsorption
$\tau_C$	time elapsed in ice reaching $\phi_C = 0.63$
$\Phi$	ice porosity
$\phi$	solar wind flux
$\Phi_0$	initial ice porosity
$\phi_A$	amorphous fraction

$\phi_c$  crystalline fraction

$\Omega$  Ohm

## List of Figures and Tables

Figure 2.1 – Schematic illustration of the UHV chamber	38
Figure 2.2 – Photograph of the copper assembly block (front side)	39
Figure 2.3 – Photograph of the copper assembly block (back side)	40
Figure 2.4 – Photograph of the aluminum heat shield	42
Figure 2.5 – Schematic illustration of the beamline Faraday cup	46
Figure 2.6 – Example infrared spectrum of a CH <sub>4</sub> -laden H <sub>2</sub> O film	50
Figure 2.7 – Example UV-visible spectrum of H <sub>2</sub> O film	52
Figure 3.1.1 – Changes in optical depth of ~3- $\mu$ m absorption band for 0° amorphous ice due to heating from 10 - 140 K	63
Figure 3.1.2 – Changes in optical depth of ~3- $\mu$ m absorption band for 0° film due to crystallization at 140 K	64
Figure 3.1.3 – Decrease in amorphous fraction for 0° ice during isothermal crystallization at 136 – 140 K	66
Figure 3.1.4 – Double natural logarithm representation of Figure 3.1.3	68
Figure 3.1.5 – Arrhenius temperature dependence of second-stage crystallization rate for 0° ice	70
Figure 3.1.6 – Experimental measurements of temperature-dependent crystallization times for 0° ice, with extrapolation to low temperatures and comparison to previous studies	71
Figure 3.2.1 – Dangling bond absorptions and UV-visible transmittance spectra for ices deposited at varying incidences at 10 K	82
Figure 3.2.2 – Changes in optical depth of ~3- $\mu$ m absorption band for 45° amorphous ice during heating from 10 – 136 K, and measured decrease in dangling bond absorption bands and porosity	84
Figure 3.2.3 – Decrease in porosity for amorphous ice deposited at varying incidences during heating from 10 – 140 K.	86
Figure 3.2.4 – Changes in optical depth of ~3- $\mu$ m absorption band for 45° ice due to crystallization at 136 K, with example calculation of crystalline fraction $\phi_C$ using factor analysis	88
Figure 3.2.5 – Decrease in amorphous fraction for ices of varying porosity during isothermal crystallization at 136 K, and dependence of crystallization time on porosity	91
Figure 3.2.6 – Double natural logarithm representation of Figure 3.2.5.	94
Figure 3.2.7 – Arrhenius temperature dependence of second-stage crystallization rate for ices of varying porosity	96
Figure 3.2.8 – Experimental measurements of temperature-dependent crystallization times for ices of varying porosity, with extrapolation to low temperatures and comparison to previous studies	101
Figure 3.2.9 – Latitudinal variation of crystallization time on Europa for	106

## amorphous ice with different porosities

Figure 4.1 – Decrease in column density of water during irradiation with 193 nm photons	121
Figure 4.2 – Decrease in O-Si XPS signal due to sputtering by 4 keV ions	123
Figure 4.3 – Water desorption rate/nm at sub-solar point	126
Figure 5.1 – Temperature dependence on methane uptake kinetics in ice	136
Figure 5.2 – Dependence of 100 keV H <sup>+</sup> fluence and flux on ion-induced methane uptake in ice film	138
Figure 5.3 – Changes in infrared absorption bands of ice film due to 100 keV H <sup>+</sup> irradiation	141
Figure 5.4 – Fluence dependence of decrease in <sup>13</sup> CH <sub>4</sub> band area and simultaneous increase in band areas of radiolytic species	145
Figure 5.5 – Thermal desorption of radiolyzed <sup>13</sup> CH <sub>4</sub> -H <sub>2</sub> O film, analyzed using QCM, QMS, and FTIR	149
Figure 5.6 – Infrared spectra of trace amounts of radiolytic product, residual from irradiated <sup>13</sup> CH <sub>4</sub> -H <sub>2</sub> O ice, between 184 – 250 K	152
Figure 6.1.1 – Kinetics of H <sub>2</sub> adsorption following sputtering due to 100 keV H <sup>+</sup> irradiation of H <sub>2</sub> -laden porous ice film with constant H <sub>2</sub> pressure	161
Figure 6.1.2 – Decrease in H <sub>2</sub> column density with ion fluence in ice films of varying thickness, with residual H <sub>2</sub> at high fluence	165
Figure 6.1.3 – Decrease in H <sub>2</sub> column density with ion fluence in ice films loaded with H <sub>2</sub> at varying pressures	168
Figure 6.1.4 – Decrease in intensities of H <sub>2</sub> and dangling O-H absorptions during 100 keV H <sup>+</sup> irradiation of H <sub>2</sub> -laden porous ice film	172
Figure 6.1.5 – Adsorbed H <sub>2</sub> vs. fluence in porous ice films irradiated with 100 keV H <sup>+</sup> using different fluxes	176
Figure 6.1.6 – Increase in residual H <sub>2</sub> concentration as a function of $\zeta$ , the ratio of ion to H <sub>2</sub> fluxes	178
Figure 6.2.1 – QCM and infrared absorption responses to exposure porous ice film to ambient H <sub>2</sub>	190
Figure 6.2.2 – Changes in the infrared absorptions of solid H <sub>2</sub> and H <sub>2</sub> O <sub>2</sub> in an H <sub>2</sub> -laden ice film during 100 keV H <sup>+</sup> irradiation in the presence of ambient H <sub>2</sub>	193
Figure 6.2.3 – Suppression of H <sub>2</sub> O <sub>2</sub> production in radiolyzed H <sub>2</sub> -laden porous ice films exposed to varying pressures of ambient H <sub>2</sub> and ion fluxes, compared with an ice film irradiated in the absence of ambient H <sub>2</sub> .	194
Figure 6.2.4 – Decrease in normalized H <sub>2</sub> band area and simultaneous increase in normalized H <sub>2</sub> O <sub>2</sub> band area during irradiation of H <sub>2</sub> -laden porous ice films at varying ambient H <sub>2</sub> pressure	197

Table 3.2.1 – Ice film deposition techniques, experimental conditions, and crystallization parameters for previous ASW crystallization studies in the literature	103
Table 5.1 – Infrared absorption band positions of $^{13}\text{C}$ -containing molecules produced from 100 keV $\text{H}^+$ radiolysis of $^{13}\text{CH}_4$ -laden $\text{H}_2\text{O}$ ice film	143

## CHAPTER 1

### Introduction

The objective of this research is to provide quality laboratory data to understand the fundamental properties of ices abundant in astronomical environments and to aid interpretation of remote sensing observations of icy surfaces by telescopes and spacecraft. Most of our knowledge of water ice in space arises from studies of reflected solar or stellar light, which is influenced by properties such as the phase of the ice (amorphous or crystalline), the ice morphology (porosity), and the presence of other compounds mixed with the H<sub>2</sub>O. For instance, reflectance data gathered by *Galileo*'s Near Infrared Mapping Spectrometer (NIMS) at Europa, Ganymede, and Callisto (Carlson et al. 1996), and by *Cassini*'s Visual and Infrared Mapping Spectrometer (VIMS) around the moons and rings of Saturn (Brown et al. 2005), have exploited the diagnostic nature of characteristic molecular vibrations in H<sub>2</sub>O to constrain the composition and crystallinity of these icy Outer Solar System satellites (Hansen & McCord 2004, Brown et al. 2006, Cuzzi et al. 2009, Filacchione et al. 2012). On the lunar regolith, variations in the abundance and distribution of surficial OH/H<sub>2</sub>O have been deduced from changes in fundamental optical absorptions collected by space instruments such as the Moon Mineralogy Mapper (M<sup>3</sup>) onboard *Chandrayaan-1* (Pieters et al. 2009), VIMS on *Cassini* (Clark 2009), and the High-Resolution Instrument (HRI) infrared spectrometer on *Deep Impact* (DI) (Sunshine et al. 2009). In the interstellar medium (ISM), observations made at the Infrared Space Observatory (ISO) have significantly enhanced our knowledge of the gas-solid balance outside the Solar System (Whittet et al. 1996, Gibb et al. 2004, Tielens et al. 1983). And recently, telescopic observations of the trans-Neptunian objects (TNOs), including the Pluto-Charon system, have been vastly supplemented by reflectance data relayed by NASA's *New Horizons* mission, constraining the

chemical content of the atmospheres and icy surfaces of these remote satellites (Cruikshank et al. 2015, Grundy et al. 2016).

While data relayed by space missions provide a wealth of information based on snapshots of these remote bodies, the state of the ice is likely a result of ongoing processes that unfold over millions or billions of years, including thermal cycling, prolonged exposure to atmospheric gases, and interactions of the ice with energetic photons or particles from cosmic rays or solar/stellar wind. Controlled laboratory environments can simulate these environments under precise, known conditions and condense these processes into much shorter timescales, investigating how the optical, physical, and compositional properties of ice are affected by the deposition conditions, chemical environment, and radiation history. Together with observational data and models, we can thereby gain insight into how extraterrestrial ice has evolved over time, contributing to our understanding of the history of Solar System.

The projects described in this dissertation are particularly focused on vapor-deposited amorphous solid water (ASW), which is believed to be the most abundant form of water in the universe (Jenniskens et al. 1997, Roush 2001). Ices accreted from the vapor phase on surfaces colder than  $\sim 130$  K are amorphous, i.e. retaining local tetrahedral order but lacking long-range crystalline order (Sceats & Rice 1982). Condensation at higher temperatures, but below  $\sim 190$  K, leads to the cubic crystalline phase, while ices accreted above  $\sim 190$  K are hexagonal crystalline. ASW is metastable and converts to cubic crystalline ice at a temperature-dependent rate, and this transformation, as well as the transition from cubic to hexagonal crystalline ice, is thermally irreversible (Baragiola 2003). ASW has an intrinsic density of  $0.94 \text{ g cm}^{-3}$ , but a high-density form of amorphous ice ( $1.1 \text{ g cm}^{-3}$ ) has been observed below 10 K, transforming into ASW at  $\sim 114$  K (Handa et al. 1986, Jenniskens et al. 1995, Jenniskens & Blake 1994, 1996), although

this form may be confined to a very thin surface layer (Kolesnikov et al. 1997). Infrared studies have suggested that a continuum of polymorphs form (Schriver-Mazzuoli et al. 2000).

ASW is a major constituent of the surfaces of many satellites and rings in the Outer Solar System (Klinger et al. 1985, Schmitt et al. 1998), and OH groups, suggesting the existence of H<sub>2</sub>O, have been detected across the entire lunar regolith (Pieters et al. 2009). Water ice is also the principal constituent of the thin ice mantles that coat dust grains in the cold molecular clouds of the interstellar medium (ISM) (Whittet et al. 1996, Gibb et al. 2004, Tielens et al. 1983). The reflectance spectra of various bodies in space have also confirmed the presence of other, less abundant condensed species, including O<sub>2</sub>, O<sub>3</sub>, H<sub>2</sub>O<sub>2</sub>, CO<sub>2</sub>, CH<sub>4</sub>, NH<sub>3</sub>, and SO<sub>2</sub> in the Jovian and Saturnian systems (Dalton et al. 2010); CH<sub>4</sub>, N<sub>2</sub>, CH<sub>3</sub>OH, C<sub>2</sub>H<sub>6</sub>, CO, CO<sub>2</sub>, NH<sub>3</sub>, and HCN on the TNOs (Burgdorf et al. 2010, de Bergh et al. 2013, Cruikshank et al. 2015, Grundy et al. 2016); and CO, CO<sub>2</sub>, CH<sub>4</sub>, CH<sub>3</sub>OH, and NH<sub>3</sub> in the ISM (Gibb et al. 2004, Ehrenfreund & Schutte 2000, Allamandola et al. 1989, Wooden et al. 2004). Other species are expected to be important but are difficult to detect because of their weak infrared absorptions, such as solid H<sub>2</sub>.

This dissertation is a compilation of experiments that investigate the physical and chemical evolution of ice films in laboratory environments, simulating conditions on the lunar surface, giant planet satellites, TNOs and Centaurs, and interstellar dust grains. Water ice films condensed from the vapor phase onto cold substrates under ultrahigh vacuum (UHV) serve as laboratory-scale analogs of ice mantles on grains in most low-pressure astrophysical environments. We use techniques such as quartz crystal microgravimetry, infrared and ultraviolet-visible spectroscopy, and quadrupole mass spectroscopy in tandem with thermal desorption and vapor deposition to characterize (1) the evolution of amorphous ice to its



crystalline phase and (2) the photon- and ion-induced dynamics of gas removal versus retention in the ice.

We show that both of these phenomena are dramatically influenced by ice porosity, which is a salient feature of low-temperature, vapor-deposited ice (Baragiola 2003, Mayer & Pletzer 1986). Ices with pores  $<2$  nm are defined as microporous, whereas mesoporous ices are suspected of having pores from 2 nm up to 50 nm in diameter (Raut et al. 2007b, Rouquerol et al. 1999). In the laboratory, the extent of the ice porosity can be controlled by altering the incidence angle of the water vapor flux (Stevenson et al. 1999). Ballistic deposition simulations have attributed the variation of porosity with deposition angle to enhanced shadowing of incident molecules by protruding surface structures (Kimmel et al. 2001a, b). The type and extent of ice porosity is critical, as this influences physical parameters such as density, morphology, and index of refraction, as well as provides an internal surface area on the order of hundreds of  $\text{m}^2 \text{g}^{-1}$  that is effective at adsorbing local gases (Baragiola 2003, Stevenson et al. 1999). Thus, porosity is a highly influential factor throughout the experiments described in this dissertation.

Despite the ubiquity of ice pores in laboratory-generated ASW films (Raut et al. 2007b), the spectroscopic signature of porosity – the  $\sim 2.7\text{-}\mu\text{m}$  OH dangling bond absorption bands (Devlin & Buch 1995) – has not yet been observed in the reflectance spectra of interstellar (Keane et al. 2001) or Outer Solar System ices. Laboratory studies have shown that ice pores in ASW collapse when the ice is heated above its growth temperature (Johari et al. 1991, Tsekouras 1998, Giering & Haarer 1996, Bossa et al. 2012, Isokoski et al. 2014) or irradiated with keV ions (Raut et al. 2007a, 2008), both important processes on icy astronomical surfaces. We investigate both thermal- and radiation-induced changes in ASW films in the experiments described in this

dissertation, examining the role of pore compaction on the ice's phase-change kinetics and ambient gas adsorption dynamics.

In Chapter 3, we simulate the crystallization of ices in Outer Solar System environments to better understand the unexpected distribution of amorphous and crystalline ice observed on the surfaces of giant planet satellites and several TNOs (Grundy et al. 1999, Cruikshank et al. 2015, Grundy et al. 2016, Merlin et al. 2007, Jewitt & Lu 2014). Due to surface temperatures,  $\sim 100$  K or lower for most of the Jovian and Saturnian moons and less than  $\sim 50$  K for TNOs, we expect from laboratory measurements that ice accreted from vapor on these bodies would be amorphous. However, a surprising fraction of crystalline ice has been detected on most of the giant planet satellites (Dalton et al. 2010), on Pluto's moon Charon (Brown & Calvin 2000, Cruikshank et al. 2015, Grundy et al. 2016), and on some TNOs such as Quaoar (Jewitt & Lu 2004) and Haumea (Merlin et al. 2007), deduced from the near-infrared absorption band at  $1.65 \mu\text{m}$ , which is associated with crystalline ice (Schmitt et al. 1998). Previous estimates have suggested that transformation from amorphous to cubic crystalline ice would take more than  $\sim 10$  million years at 80 K (Baragiola 2003). However, the phase of ice depends not only on growth conditions and thermal history, but also on the local radiation environment, suggesting alternate timescales for crystallization on active planetary surfaces. Laboratory studies have shown that energetic irradiation can amorphize crystalline ice and reverse thermally-driven crystallization (Baratta et al. 1991, Moore & Hudson 1992, Kouchi & Kuroda 1990, Strazzulla et al. 1992, Leto & Baratta 2003, Famá et al. 2010).

Crystallization rates on surfaces in space can be estimated by extrapolation to low temperatures of laboratory data, and amorphous ice takes only a few hours to crystallize at typical laboratory crystallization temperatures of  $\sim 135$  K under UHV. However, there is

significant disagreement on both crystallization times and the phase change mechanism in the literature (Dowell & Rinfret 1960, Schmitt et al. 1989, Sack & Baragiola 1993, Kouchi et al. 1994, Hage et al. 1995, Jenniskens & Blake 1996, Dohnálek et al. 2000, Lofgren et al. 2003, Safarik et al. 2003, Backus et al. 2004, Smith et al. 2011), likely owing to large variation in experimental conditions and vacuum quality. We use transmission infrared spectroscopy, with well-defined crystalline/amorphous peak shapes for the O-H stretch absorption band at 3.1  $\mu\text{m}$ , to characterize the temperature dependence of isothermal crystallization kinetics at 130 to 141 K for amorphous ice deposited at 10 K under UHV. We extrapolate our measured crystallization times to lower, astronomically relevant temperatures.

We then expand our studies of isothermal crystallization to analyze the effects of ice porosity on crystallization rates. Varying ice porosity could be an explanation for the discrepancy in crystallization times in the literature, as well as a possible explanation for the high abundance of crystalline ice observed on low-temperature surfaces in the Outer Solar System. It has been shown in the laboratory that porosity exists in all ASW films deposited at low temperatures ( $<140$  K) (Raut et al. 2007b, Westley et al. 1998), but pores are known to collapse when ASW is warmed to a temperature higher than the deposition temperature but lower than the temperatures at which crystallization will rapidly progress in laboratory timescales (Johari 1991, Tsekouras 1998, Giering & Haarer 1996). However, we find that both microporous and mesoporous ASW films undergo only partial compaction during heating to laboratory crystallization temperatures, in agreement with a few other annealing studies (Raut et al. 2007b, Bossa et al. 2012, Isokoski 2014) and similar to irradiation-compacted ices (Raut et al. 2007a). Furthermore, we find that residual ice porosity at crystallization temperatures is a key factor in the phase transformation, with films of greater porosity crystallizing significantly faster than low-porosity

films, and suggest an empirical mechanism for the process. We extrapolate these faster crystallization times to temperatures relevant to icy satellites such as Europa, where multi-directional condensation of water vapor plumes (Roth et al. 2014a) may result in the accretion of porous ice.

In Chapter 4, we characterize the removal of monolayer-scale amounts of water from the surface of the Moon via photodesorption, using a 10-ns pulsed excimer laser at 193 nm. Infrared spectroscopic measurements of the lunar regolith have revealed the presence of H<sub>2</sub>O and/or OH groups within the upper-most layer of the entire surface (Pieters et al. 2009), with the greatest amount of water at the poles and higher latitudes. The abundance of water has also been shown to vary diurnally, suggesting that the regolith undergoes a cyclical water loss and replenishment process (Sunshine et al. 2009). While the replenishment mechanism has not yet been determined (Burke 2011, Schaible & Baragiola 2014), several water removal mechanisms have been put forward, including photodesorption and photodissociation, thermal desorption, meteorite impact, radiation damage, and sputtering. In this study, we simulate the lunar surface to examine the effects of photodesorption and sputtering of thin films of adsorbed water. We characterize the stability of water molecules under exposure to solar radiation and the solar wind, investigate causes for water migration to or from lunar cold traps at the poles, and determine possible mechanisms for the observed diurnal variation in surficial water abundances on the Moon.

Chapter 5 expands upon our studies of porous ices to investigate ion irradiation effects of ASW in a low-pressure methane environment, relevant to many of the TNOs, including Triton, Pluto and Charon, and Eris, as well as Centaurs. Shi et al. (2009) showed that when ASW is irradiated by ions in the presence of ambient oxygen, the adsorption of O<sub>2</sub> by the ice is enhanced multifold due to the creation of high-energy binding sites as the pores compact. The adsorbed gas

remained trapped in the ice even when the ambient gas was removed by pumping, implying that magnetospheric ions can be responsible for observed gas trapping on icy satellites of the Outer Solar System (Johnson 1981, Tokar 2006, Spencer 1995). Visible and near-infrared spectra of a number of the TNOs and Centaurs have shown that their surfaces are composed of ices containing  $\text{H}_2\text{O}$ ,  $\text{CH}_4$ ,  $\text{N}_2$ ,  $\text{CH}_3\text{OH}$ ,  $\text{C}_2\text{H}_6$ ,  $\text{CO}$ ,  $\text{CO}_2$ ,  $\text{NH}_3$ , and  $\text{HCN}$  (de Bergh et al. 2013, Burgdorf et al. 2010), with the relative amounts of the constituents varying among the TNOs. The Ralph visible and infrared spectrometer onboard the *New Horizons* spacecraft has recently constrained the surfaces of Pluto and its satellite Charon to spatially heterogeneous mixtures of  $\text{H}_2\text{O}$ ,  $\text{CH}_4$ ,  $\text{CO}$ ,  $\text{C}_2\text{H}_6$ ,  $\text{NH}_3$ , and  $\text{N}_2$  (Cruikshank et al. 2015, Grundy et al. 2016). The surfaces of TNOs are continually processed by energetic cosmic rays, solar wind, and photons, which changes the surface ice composition via radiolysis/photolysis and contributes to atmospheres via sputtering (impact desorption). Indeed, the *New Horizons* flyby revealed a layered atmospheric haze above Pluto, containing  $\text{N}_2$ ,  $\text{CH}_4$ ,  $\text{C}_2\text{H}_2$ ,  $\text{C}_2\text{H}_4$ , and  $\text{C}_2\text{H}_6$  (Gladstone et al. 2016). To understand the synergistic effects of ion irradiation and gas adsorption by the ice, we have irradiated porous  $\text{H}_2\text{O}$  ice films loaded with  $\text{CH}_4$ , two dominant species of the TNOs.

Finally, in Chapter 6, we examine irradiation effects of  $\text{H}_2$ -laden porous ASW films.  $\text{H}_2$  is the dominant gas in the dense clouds of the ISM, and ice-covered dust grains within the clouds become loaded with hydrogen over their lifetime as  $\text{H}_2$  diffuses into the pores of the ice and adsorbs at high-energy binding sites at low temperatures (Buch & Devlin 1991, Sandford et al. 1993). Due to impacts by galactic cosmic rays and stellar winds, the adsorbed  $\text{H}_2$  can be energetically released back into the gas phase via sputtering. In light of the observation of ion-enhanced adsorption for  $\text{O}_2$  (Shi et al. 2009) and related experiments for  $\text{CH}_4$  (Chapter 5, Mitchell et al. 2014), we investigate whether similar enhancement is observed for  $\text{H}_2$ , given its

smaller binding energy. We perform irradiations of porous amorphous  $\text{H}_2\text{O}$  films loaded with  $\text{H}_2$  to understand the effects of energetic particle bombardment on the stability of adsorbed  $\text{H}_2$  on ice-covered dust grains in interstellar molecular clouds. Such interplay between ion-induced ejection and adsorption of gas-phase molecules in the ice film can be important in determining the gas-solid balance in the ISM.

We then expand this study to analyze the synthesis of  $\text{H}_2\text{O}_2$ . The energy deposited by the charged particles leads to the dissociation of  $\text{H}_2\text{O}$  into species such as  $\text{H}$ ,  $\text{O}$ , and  $\text{OH}$  within the film, with the dominant dissociation channel producing  $\text{H}$  and  $\text{OH}$  (Slanger & Black 1982). Radiolytic  $\text{H}_2\text{O}_2$  is formed from the recombination of  $\text{OH}$  radicals. Despite the rich laboratory evidence for the synthesis of peroxide in ice films subjected to energetic processing (Gomis et al. 2004, Loeffler et al. 2006, Moore & Hudson 2000, Hand & Carlson 2011, Pan et al. 2004, Zheng et al. 2006, Gerakines et al. 2004, Laffon et al. 2006), only gas-phase  $\text{H}_2\text{O}_2$  has been detected toward the  $\rho$  Ophiuchus A cloud core at small abundances of  $10^{-10}$  relative to  $\text{H}_2$  (Bergman et al. 2011). The lack of detection of solid interstellar  $\text{H}_2\text{O}_2$  is puzzling, since interstellar ices are continually impacted by galactic cosmic rays and stellar winds. Although solid  $\text{H}_2$ , with its weak infrared absorption, has not yet been detected in the ISM, models suggest that it is present in appreciable amounts (Buch & Devlin 1994, Kristensen et al. 2011). H-enrichment in the ice may suppress the recombination between  $\text{OH}$  radicals due to the competing radiolytic pathway of regenerating  $\text{H}_2\text{O}$ , thus decreasing the production of  $\text{H}_2\text{O}_2$  as is known to occur in liquid water (Pastina & LaVerne 2001). This effect could be a contributing factor in the lack of detected solid-state peroxide in interstellar ice.

The results of this research will aid in interpretation of astronomical observations for water ice on the lunar surface, on icy satellites in the Outer Solar System, and in cold molecular clouds

in the ISM; the scope of this research can also be extended to ices on numerous extraterrestrial surfaces. The outcome of these experiments should be of interest to both astrophysics and astrochemical observational and modeling communities.

## References

- Allamandola, L.J., Tielens, A.G.G.M., Barker, J.R., *ApJS* **71**, 733 (1989).
- Backus, E.H.G., Grecea, M.L., Kleyn, A.W., Bonn, M., *Phys. Rev. Lett* **92**, 23 (2004).
- Baragiola, R.A., *Planet. Space Sci.* **51**, 953 (2003).
- Baratta, G.A., Leto, G., Spinella, F., Strazzulla, G., Foti, G., *A&A* **252**, 421 (1991).
- Bergman, P., Parise, B., Liseau, R., Larsson, B., Olofsson, H., Menten, K.M., Güsten, R., *A&A* **531**, L8 (2011).
- de Bergh, C. et al. In: Gudipati, M.S. and Castillo-Rogez, J., Editors, *The Science of Solar System Ices*, Springer, New York (2013).
- Bossa, J.-B., Isokoski, K., de Valois, M.S., Linnartz, H., *A&A* **545**, A82 (2012).
- Brown, M.E. and Calvin, W.M., *Science* **287**, 5450 (2000).
- Brown, R.H. et al., *Space Sci. Rev.* **115**, 111 (2005).
- Brown, R.H. et al., *Science* **311**, 1425 (2006).
- Buch, V. and Devlin, J.P., *J. Chem. Phys.* **94**, 4091 (1991).
- Buch, V., & Devlin, J. P., *Astrophys. J. Lett.*, 431, 135 (1994).
- Burgdorf, M., Cruikshank, D.P., Dalle Ore, C.M., Sekiguchi, T., Nakamura, R., Orton, G., Quirico, E., Schmitt, B., *Astrophys. J. Lett.* **718**, 2 (2010).
- Burke, D.J., Dukes, C.A., Kim, J.-H., Shi, J., Famá, M., Baragiola, R.A., *Icarus* **211**, 1082 (2011).

- Carlson, R.W. et al., *Science* **274**, 385 (1996).
- Clark, R.N., *Science* **326**, 562 (2009).
- Cruikshank, D.P., Grundy, W.M., DeMeo, F.E., Buie, M.W., Binzel, R.P., Jennings, D.E., Olkin, C.B., Parker, J.W., Reuter, D.C., Spencer, J.R., Stern, S.A., Young, L.A., Weaver, H.A. *Icarus* **246**, 82 (2015).
- Cuzzi, J.N. et al. Ring particle composition and size distribution, In: Dougherty, M.K., Esposito, L.W., Krimigis, S.M. (Eds.), *Saturn from Cassini-Huygens*, Springer, Berlin, 459 (2009).
- Dalton, J.B., Cruikshank, D.P., Stephan, K., McCord, T.B., Coustenis, A., Carlson, R.W., Caradini, A. *Space Sci. Rev.* **153**, 113 (2010).
- Devlin, J.P. and Buch, V., *J. Chem. Phys.* **99**, 16534 (1995).
- Dohnálek, Z., Ciolli, R.L., Kimmel, G.A., Stevenson, K.P., Smith, R.S., Kay, B.D., *J. Chem. Phys.* **110**, 5489 (2000).
- Dowell, L.G. and Rinfret, A.P., *Nature* **158**, 1144 (1960).
- Ehrenfreund, P. and Schutte, W.A., *ASR* **25**, 11 (2000).
- Famá, M., Loeffler, M.J., Raut, U., Baragiola, R.A., *Icarus* **207**, 314 (2010).
- Filacchione, G. et al., *Icarus* **220**, 1064 (2012).
- Gerakines, P.A., Moore, M.H., Hudson, R.L., *Icarus* **170**, 202 (2004).
- Gibb, E.L., Whittet, D.C.B., Boogert, A.C.A., Tielens, A.G.G.M., *ApJS* **151**, 1 (2004).
- Giering, T. and Haarer, D., *Chem. Phys. Lett.* **261**, 6, 677 (1996).
- Gladstone, G.R. et al, *Science* **351**, 6279 (2016).
- Gomis, O., Leto, G., Strazzulla, G., *Planet. Space Sci.* **52**, 371 (2004).
- Grundy, W.M., Buie, M.W., Stansberry, J.A., Spencer, J.R., *Icarus* **142**, 536 (1999).
- Grundy, W.M. et al., *Science* **351**, 6297 (2016).



- Hage, W., Hallbrucker, A., Mayer, E., Johari, G.P., J. Chem. Phys. **100**, 2743 (1994).
- Hand, K.P. and Carlson, R.W., Icarus **215**, 226 (2011).
- Handa, Y.P., Mishima, O., Whalley, E., J. Chem. Phys. **84**, 2766 (1986).
- Hansen, G.B. and McCord, T.B., J. Geophys. Res. **109**, E01012 (2004).
- Hansen, C.J., Esposito, L., Stewart, A.I.F., Colwell, J., Hendrix, A., Pryor, W., Shemansky, D., West, R. Science **311**, 1422 (2006).
- Isokoski, K., Bossa, J.-B., Triemstra, T., Linnartz, H., Phys. Chem. Chem. Phys. **16**, 3456 (2014).
- Jenniskens, P., and Blake, D.F., Science **265**, 753 (1994).
- Jenniskens, P., Wilson, D.F., Pohorille, A., Astrophys. J. **455**, 389 (1996).
- Jenniskens, P. and Blake, D.F., Astrophys. J. **473**, 1104-1113 (1996).
- Jenniskens, P., Barnhak, S.F., Blake, D.F., McCoustra, M.R.S., J. Chem. Phys. **107**, 1232 (1997).
- Jewitt, D.C. and Lu, J., Nature **432**, 731 (2004).
- Johari, G.P., Hallbrucker, A., Mayer, E., J. Chem. Phys. **95**, 2955 (1991).
- Johnson, R.E., Lanzerotti, L.J., Brown, W.L., Armstrong, T.P., Science **202**, 1027 (1981).
- Keane, J.V., Tielens, A.G.G.M., Boogert, A.C.A., Schutte, W.A., Whittet, D.C.B., A&A **376**, 254 (2001).
- Kimmel, G.A., Stevenson, K.P., Dohnálek, Z., Smith, R.S., Kay, B.D., J. Chem. Phys. **114**, 5284 (2001a).
- Kimmel, G.A., Dohnálek, Z., Stevenson, K.P., Smith, R.S., Kay, B.D., J. Chem. Phys. **114**, 5295 (2001b).
- Klinger, J., Benest, D., Dollfus, A., Smoluchowski, R. (Eds.), Ices in the Solar System, Reidel Publ., Norwell, MA (1985).

- Kolesnikov, A.I., Li, J.-C., Dong, S., Bailey, I.F., Eccleston, R.S., Hahn, W., Parker, S.F., Phys. Rev. Lett. **79**, 1869 (1997).
- Kouchi, A., Kuroda, T., Nature **344**, 134 (1990).
- Kouchi, T., Yamamoto, T., Kozasa, T., Kuroda, T., Greenberg, J.M. Astron. Astrophys. **290**, 1009 (1994).
- Kristensen, L. E., Amiaud, L., Fillion, J. H., Dulieu, F., & Lemaire, J. L. 2011, A&A, 527, 44 (2011).
- Laffon, C., Lacombe, S., Bournel, F., Ph, P., J. Chem. Phys. **125**, 204714 (2006).
- Leto, G. and Baratta, G.A., A&A **397**, 7 (2003)
- Loeffler, M.J., Raut, U., Vidal, R.A., Baragiola, R.A., Carlson, R.W., Icarus **180**, 265 (2006).
- Lofgren, P., Ahlstrom, P., Lausma, J., Kasemo, B., Chakarov, D., Langmuir **19**, 265 (2003).
- Mayer, E., and Pletzer, R., Nature **319**, 298 (1986).
- Merlin, F. et al., A&A **466**, 1185 (2007).
- Mitchell, E. H., Raut, U., & Baragiola, R. A., In: Lunar and Planetary Institute Science Conference Abstracts, Irradiation of Methane-Laden Water Ice Films: Relevance to TNOs and Centaurs, 1931 (2014).
- Moore, M.H. and Hudson, R.L., Astrophys. J. **401**, 353 (1992).
- Moore, M.H. and Hudson, R.J., Icarus **145**, 282 (2000).
- Pan, X., Bass, A.D., Jay-Gerin, J.-P., Sanche, L., Icarus **172**, 521 (2004).
- Pastina, B. and LaVerne, J.A., J. Phys. Chem. A. **105**, 9316 (2001).
- Pieters, C.M. et al., Science **326**, 568 (2009).
- Raut, U., Teolis, B.D., Loeffler, M.J., Vidal, R.A., Famá, M., Baragiola, R.A. J. Chem. Phys. **126**, 244511 (2007a).

- Raut, U., Famá, M., Teolis, B.D., Baragiola, R.A., J. Chem. Phys. **127**, 204713 (2007b).
- Raut, U., Famá, M., Loeffler, M.J., Baragiola, R.A., Astrophys. J. **687**, 1070 (2008).
- Roth, L., Saur, J., Retherford, K.D., Strobel, D.F., Feldman, P.D., McGrath, M.A., Nimmo, F. Science **343**, 171 (2014a).
- Rouquerol, F., Rouquerol, J., Sing, K., Adsorption by Powders & Porous Solids: Principles, Methodology and Applications, Academic, San Diego, 1999.
- Roush, T.L., J. Geophys. Res. **106E**, 33, 315 (2001).
- Sack, N.J. and Baragiola, R.A., Phys. Rev. B. **48**, 9973 (1993).
- Safarik, D.J., Meyer, R.J., Mullins, C.B., J. Chem. Phys. **118**, 4660 (2003).
- Sandford, S.A., Allamandola, L.J., Geballe, T.R., Science **262**, 400 (1993).
- Sceats, M.G., and Rice, S.A., In: Franks, F. (Ed.), Water, a Comprehensive Treatist, Vol. 7, Plenum, New York (1982).
- Schaible, M.J. and Baragiola, R.A., J. Geophys. Res. Planets, **119**, 2017 (2014).
- Schmitt, B., Espinasse, S., Grim, R.G.A., Greenberg, J.M., Klinger, J., Proc. of An International Workshop on Physics and Mechanics of Cometary Materials, Münster, FRG, 9-11 Oct. 1989.
- Schmitt, B., Quirico, E., Trotta, F., Grundy, W.M. In: Schmitt, B., De Bergh, C., Festou, M. (Eds.), Solar System Ices, Kluwer Academic, Norwell, MA (1998).
- Schriver-Mazzuoli, L., Schriver, A., Hallou, A., J. Mol. Struct. **554**, 289 (2000).
- Shi, J., Teolis, B.D., Baragiola, R.A., Phys. Rev. B. **79**, 235422 (2009).
- Slanger, T.G. and Black, G., J. Chem. Phys. **77**, 2432 (1982).
- Smith, R.S., Matthiesen, J., Knox, J., Kay, B.D., J. Phys. Chem. A. **115**, 5908 (2011).
- Spencer, J.R., Calvin, W.M., Person, M.J., J. Geophys. Res. **100**, 19049 (1995).

- Stevenson, K.P., Kimmel, G.A., Dohnálek, Z., Smith, R.S., Kelly, B.D., *Science* **283**, 1505 (1999).
- Strazzulla, G., Baratta, G.A., Leto, G., Foti, G. *Europhys. Lett.* **18**, 6 (1992).
- Sunshine, J.M., Farnham, T.L., Feaga, L.M., Groussin, O., Merlin, F., Milliken, R.E., Hearn, M.F., *Science* **326**, 565 (2009).
- Tielens, A.G.G.M., Hagen, W., Greenberg, J.M., *J. Phys. Chem.* **87**, 21 (1983).
- Tokar, R.L. et al., *Geophys. Res. Lett.* **32**, L14S04 (2006).
- Tsekouras, A.A., Iedema, M.J., Cowin, J.P., *Phys. Rev. Lett.* **80**, 5798 (1998).
- Waite, J.H., Combi, M.R., Ip, W-H, Cravens, T.E., McNutt, R.L. Jr., Kasprzak, W., Yelle, R., Luhmann, J., Niemann, H., Gell, D., Magee, B., Fletcher, G., Lunine, J., Tseng, W-L. *Science* **311**, 1419 (2006).
- Westley, M.S., Baratta, G.A., Baragiola, R.A., *J. Chem. Phys.* **108**, 3321 (1998).
- Whittet, D.C.B. et al., *A&A* **315**, 2 (1996).
- Wooden, D.H., Charnley, S.B., Ehrenfreund, P., In: Feston, M., Keller, H.U., Weaver, H.A. (Eds.), *Comets II*, University of Arizona Press (2004).
- Zheng, W., Jewitt, D., Kaiser, R.I., *ApJ* **639**, 534 (2006).

## CHAPTER 2

### Instrumentation and Methods

#### 2.1. Ultrahigh Vacuum Chamber

The experiments described in this dissertation were performed in an ultrahigh vacuum (UHV) stainless steel chamber, previously described in other dissertations (Loeffler 2007, Teolis 2007, Raut 2009). UHV base pressures of  $\sim 10^{-10}$  Torr, measured with a nude ionization gauge, are achieved with sequential use of scroll (Varian SH-110), turbomolecular (Oerlikon Leybold TW 250 S), and cryogenic (CTI Cryo-Torr 8) pumps. The chamber has 24 ports that house entry or exit windows for optical instruments, or that mount additional instruments, discussed later. A schematic of this chamber is shown in Figure 2.1.

Thin films of gases, condensed from the vapor phase, are deposited onto one of two possible substrates, a polished CsI optical transmission window or the optically flat gold electrode of a quartz crystal microbalance, described in Section 2.3. Depositions are made by an in-house-designed gas-vapor doser, described in Section 2.2. The substrates reside in a copper assembly block (Figure 2.2 and 2.3), which is attached to the second stage of a cryocooled coldfinger (Janis SHI-4-5-UHV coldfinger, CTI Cryogenics 8500 cryocooler). The ultimate minimum temperature for the substrates is 7 K, as measured with a silicon diode temperature sensor (Lake Shore DT-670B-CU) mounted on the copper block. The temperature of the substrates are stable to within  $\sim 0.01$  K by equilibrating heat withdrawn by the cryocooler (Sumitomo RDK-205E) with heat input from current passed through two 100- $\Omega$ , 100-W power resistors (Caddock Model MP9100) wired in parallel to yield 50- $\Omega$  resistance, also mounted on the copper assembly block. The copper block is surrounded by a cylindrical, highly-polished, oxygen-free, high thermal conductivity (OFHC) copper heat shield, mounted onto the first stage

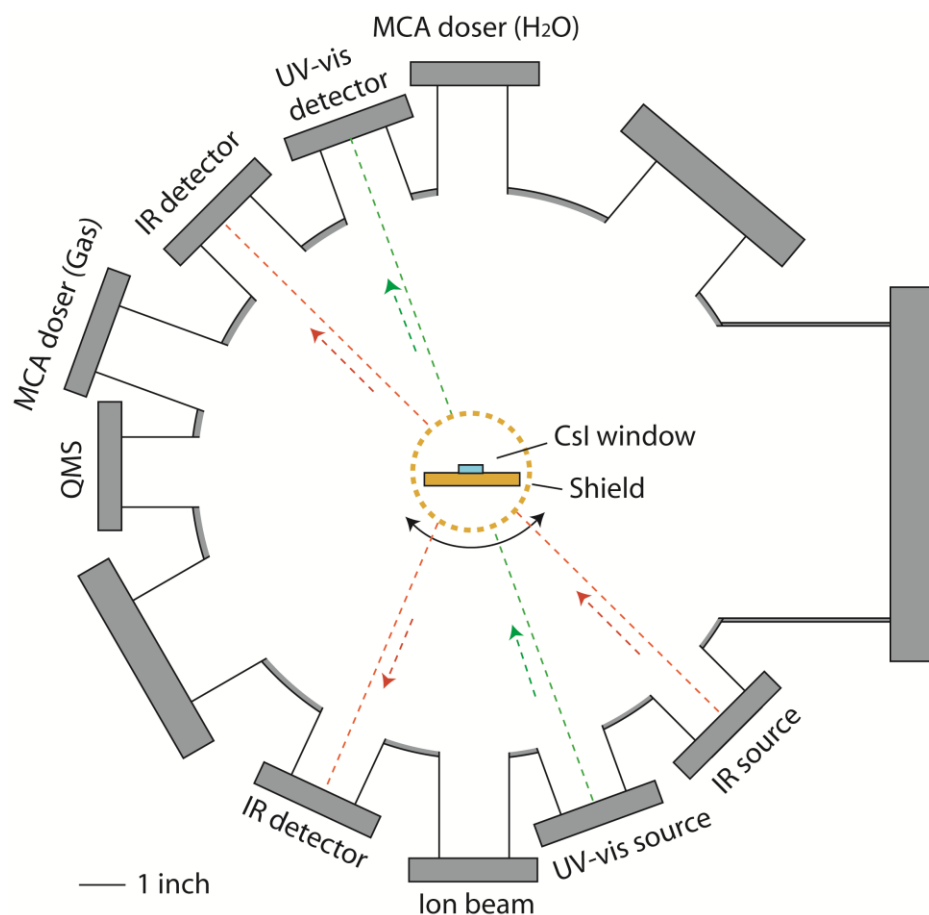


Figure 2.1 – Schematic illustration of the UHV chamber used in the experiments described in this dissertation. CsI substrate (shown in schematic) is used for transmission FTIR and ultraviolet (UV)-visible spectroscopy. The QCM substrate (not shown) is mounted 25.4 mm above the CsI substrate and is used for reflection FTIR spectroscopy and microgravimetry measurements. The second MCA doser was used in experiments in which H<sub>2</sub>O and H<sub>2</sub> were admitted into the chamber simultaneously, described in Chapter 6.2.

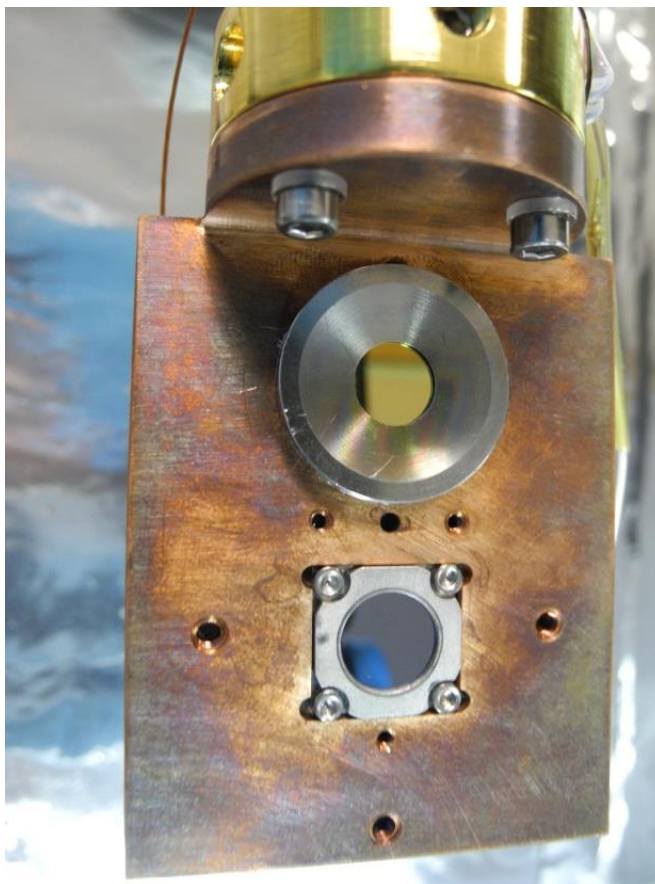


Figure 2.2 – Photograph of the front of the copper block target assembly, with the gold electrode of the QCM positioned 1 inch above the CsI transmission window. The copper target block is affixed vertically to an XYZ translation stage, which is electrically isolated by stainless steel screws and sapphire washers, with a thin sapphire disc seated between the copper target block and the coldfinger. Sapphire allows electrical isolation for current measurement and biasing while retaining good thermal contact.

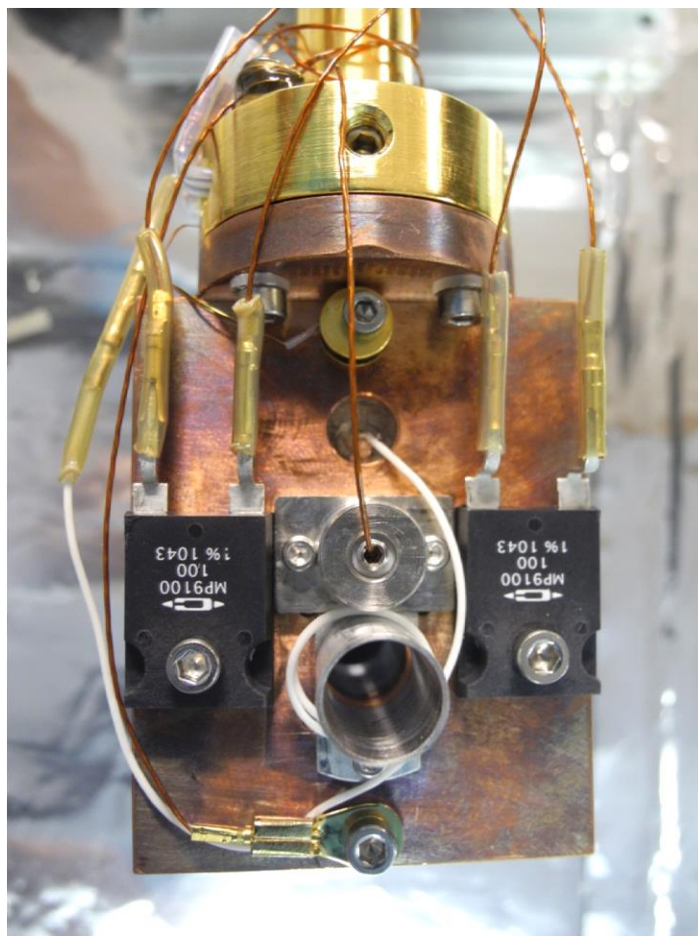


Figure 2.3 – Photograph of the back of the copper block sample holder assembly, showing the two 100- $\Omega$  resistive heaters on either side of the targets for uniform heating across the substrates (wired in parallel to provide 50- $\Omega$  resistance), the stainless steel shielding cylinder to minimize deposition on the non-dosing side of the CsI substrate, a Faraday cup (not used in the experiments described in this dissertation), the silicon diode (top of copper block), and a grounding cable (bottom of copper block).



of the cryocooler. The heat shield is sputter-coated with a thin layer of gold to reflect heat radiation emitted by the walls of the chamber. A second silicon-diode temperature sensor (Scientific Instruments Model Si-410C) is mounted on the heat shield, which can be cooled to 35 K in this configuration. The sample and shield temperatures are measured using a Lakeshore Model 331 temperature controller, which has a resolution of 0.01 K. We confirm the accuracy of the temperature measurements by dipping the target assembly in liquid nitrogen (77.2 K); see Section 2.10. Openings on both sides of the heat shield (Figure 2.4) allow access to the target substrates for gas dosing (Section 2.2), infrared spectroscopy (Section 2.5), ultraviolet-visible spectroscopy (Section 2.6), quadrupole mass spectroscopy (Section 2.7), as well as irradiation by photons (Section 2.8) or ions (Section 2.4). To prevent ice from accumulating on the back of the CsI substrate during vapor deposition, the rear of the copper block is fitted with a 2-cm-long stainless steel shielding cylinder around window (Figure 2.3).

The coldfinger and attached copper target assembly containing the substrates are vertically mounted and sit on an XYZ stage, enabling the substrate's position to be manipulated in three directions. The stage is mounted atop ball-bearings placed in a differentially-pumped groove between two Viton O-rings, allowing the unit to rotate about the central vertical axis of the chamber. The two substrates can thereby be turned to face any port on the chamber. The rotational stage (McAllister DPRF 600) is differentially pumped by an oil-free scroll pump (Varian SH-110) and an ion pump (HeatWave Labs 360518).

The analytical capabilities of the chamber are infrared spectroscopies (reflectance and transmission), mass spectroscopy, ultraviolet-visible spectroscopy, quartz crystal microgravimetry, irradiation by photon and ion sources, and temperature-programmed desorption. These techniques will be described in more detail in later sections.

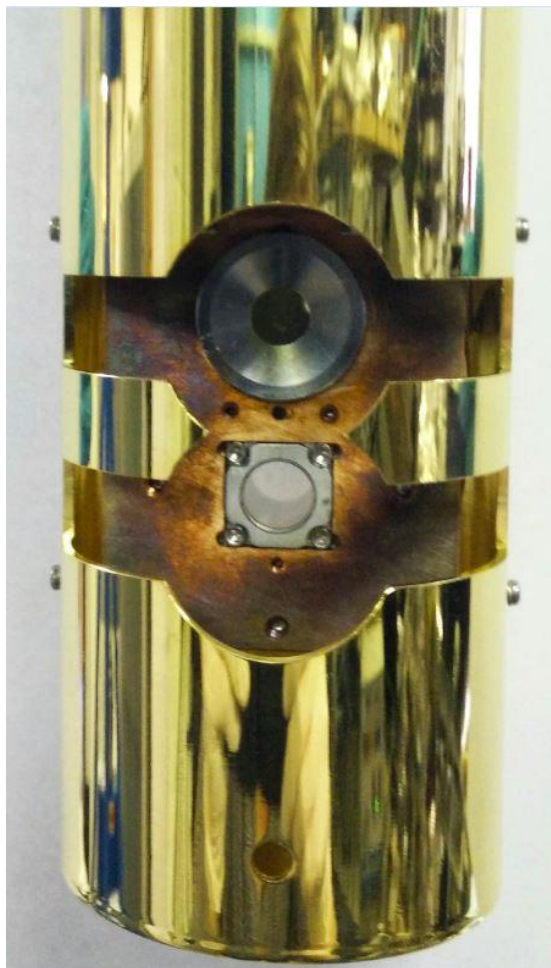


Figure 2.4 – Photograph of the gold-plated copper radiation shield surrounding the copper assembly block.

## 2.2. Microcapillary Array Doser

Collimated vapor deposition of gases such as  $\text{H}_2\text{O}$ ,  $\text{CH}_4$ , and  $\text{H}_2$  onto the gold or CsI substrate is achieved using a unique microcapillary array (MCA) doser. The main component of the MCA doser is a lead glass plate, 13 mm in diameter and 0.5 mm thick, etched with several thousand 10  $\mu\text{m}$ -diameter cylindrical capillaries to direct deposited gases. A  $\sim 10$  mm baffle sits in front of the MCA plate to allow multi-directional diffusion onto the target for uniform film growth. The glass plate is mounted on a retractable stainless steel tube with bellows, and a leak valve (Granville Phillips Series 203) connects the doser to a gas manifold. The manifold houses a glass ampoule containing high-performance liquid chromatography (HPLC)-grade water and lecture bottles pressurized with high-purity gases.

For film deposition, the gas manifold is evacuated to the lowest possible pressure using an oil-free scroll pump (5 to 15 mTorr). To grow an  $\text{H}_2\text{O}$  ice film, the liquid-water-containing ampoule is outgassed by exposing it to the manifold and pumping for about one minute. The ampoule is held or lightly shaken during pumping to prevent it from cooling down to the extent that the glass cracks. The valve is then closed and separated from the vacuum pump, and the film is deposited by opening the manifold leak valve to the UHV chamber. For  $\text{CH}_4$  and  $\text{H}_2$  deposition, the same pumping method is used to evacuate the manifold, then the valve to the scroll pump is closed and the regulator valve to the lecture bottle is slowly opened. Typical gas pressures in the manifold are 10 to 500 Torr, which provides a gas purity of  $10^{-3}$  to  $10^{-5}$ .

The background pressure in the chamber does not increase significantly during film deposition because most of the molecules from the doser stick to the cold target upon arrival; this prevents typical contaminants such as CO and residual hydrocarbons from desorbing from the chamber walls and becoming incorporated into the films during deposition.

For films in which H<sub>2</sub>O and H<sub>2</sub> were admitted into the UHV chamber simultaneously (Chapter 6.2), a second MCA doser on a separate chamber port was used (Figure 2.1).

### 2.3. Quartz Crystal Microbalance

The gold substrate – one of two possible substrates used in the experiments described in this dissertation – derives from the sputter-coating atop a piezoelectric quartz crystal, shown in Figures 2.2 and 2.3. An AC voltage, supplied by an oscillator circuit and an Inficon IC-5 controller, drives the quartz crystal microbalance (QCM) into 5.9 MHz electromechanical resonance. The QCM's resonant frequency decreases in response to film growth, which causes mass loading onto the gold electrode, and the change in resonant frequency can be converted to areal mass (g cm<sup>-2</sup>) according to  $\Delta f = \Delta m / \beta A$ , where  $A$  is the active area of the QCM ( $0.285 \pm 0.004$  cm<sup>2</sup>) and  $\beta$  is the crystal sensitivity factor with the value of  $1.227 \times 10^{-8}$  g s cm<sup>-2</sup> (Lu & Lewis 1984, Westley 1994). This can then be converted to column density  $\eta$  (molecules cm<sup>-2</sup>) when the film molecular mass is known.

The resonant frequency of the QCM drifts with temperature, and therefore blank experiments are performed in order to determine this temperature dependence. In experiments in which the temperature is varied while the deposited mass is changing, such as in temperature-programmed desorption, the mass-loading data is corrected for the temperature-related drift in resonant frequency. The QCM can detect mass loss of  $>4 \times 10^{13}$  H<sub>2</sub>O cm<sup>-2</sup> ( $\sim 0.04$  ML, where 1 ML is about a monolayer,  $1 \times 10^{15}$  H<sub>2</sub>O cm<sup>-2</sup>), corresponding to a frequency stability of 0.1 Hz.

## 2.4. Ion Accelerator

For experiments that simulate cosmic ray or stellar wind processing, ice films are irradiated with energetic ions produced by a 300-kV accelerator (Accelerator Inc. 300 MP). H<sub>2</sub>, Ar, or other gas is admitted via a leak valve into a quartz tube to pressures of 50 to 150 mTorr, and a plasma discharge is generated by applying a radio frequency (RF) power to a pair of oscillators around the quartz tube. Positive plasma ions from the plasma are electrostatically extracted by 0 to 5 kV, magnetically focused, and accelerated through a potential  $V$  of 20 to 300 kV to energies of  $qV$ , where  $q$  is the ion charge. The beam is shaped by a quadrupole before being  $m/q$ -selected and steered toward the UHV chamber via an analyzing electromagnet, with magnetic field  $B = r^{-1}(2mV/q)^{0.5}$ , where  $m$  is the ion mass,  $V$  is the potential gradient across which the ions are accelerated, and  $r$  is the deflection radius of curvature. The radius of curvature is constant in our system, and the accelerator is connected to the vacuum chamber through a differentially-pumped beamline with a 30° port. The electromagnet therefore allows ions of only the desired  $m/q$  ratio to reach the UHV chamber.

A retractable Faraday cup installed in the beamline measures the ion flux, shown in Figure 2.5. The ion beam is directed toward the Faraday cup using a voltage applied to electrostatic deflection plates in the beamline after  $m/q$  selection. The front plate of the Faraday cup, measuring 75 mm by 25 mm, has an aperture (1.2 mm) through which the ions enter an electrically insulated cylindrical cup (1.8 cm long). The cylindrical shape of the back tube helps to re-capture secondary electrons emitted by ions impacting the inner surface of the tube. The tube has a copper shield to prevent the entrance of stray ions or electrons from the ion pump installed below. Both the front plate and the Faraday cup are connected separately to an electrometer for current measurement; when current is measured on the cup, the front plate and

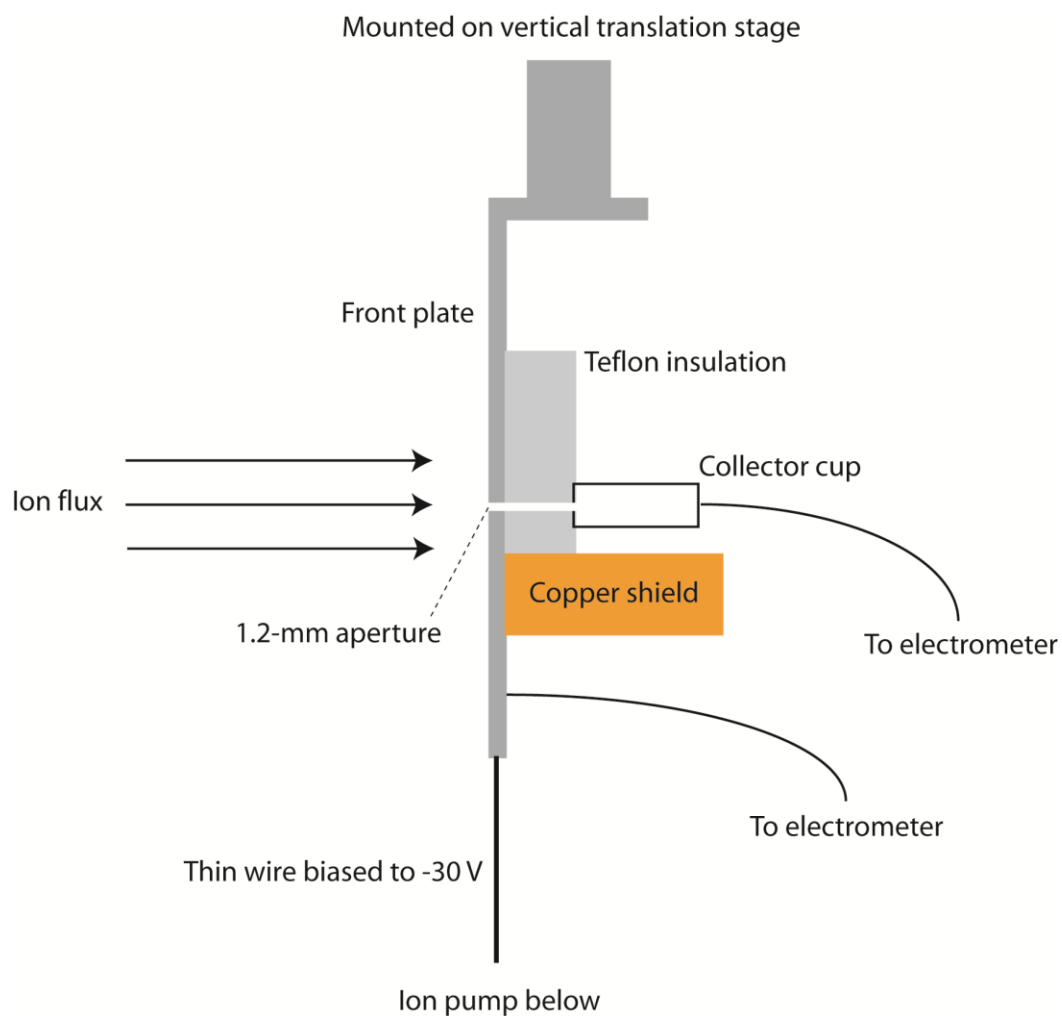


Figure 2.5 – Schematic of the beamline Faraday cup assembly used to measure ion beam current density and monitor beam stability, reproduced from (Raut 2009). Entire assembly is mounted vertically on linear translation stage.

the copper shield are grounded. Faraday cup measurements of ion flux are used to estimate target current density in the chamber. Typical fluxes used in our experiments are  $\sim 10^{10} - 10^{12}$  ions  $\text{cm}^{-2} \text{s}^{-1}$ .

Once the ion flux is determined, the Faraday cup is translated away from the path of the beam so that the ions are able to reach the target. The Faraday cup is mounted on a vertical stage, and a tungsten wire (0.123 mm in diameter) suspended from the front plate, is placed in the beam path so that the current can be monitored in real-time during irradiation of the sample. The current measured on the wire is related to the Faraday cup current by a constant factor. The wire is biased to  $-30$  V to repel electrons and negative ions from the ion pump. To ensure uniform irradiation across the sample, the beam is rastered using AC voltages ( $100 - 400$  V,  $100 - 400$  kHz) applied to horizontal and vertical deflection plates located just prior to the Faraday cup.

Before starting a set of experiments using the ion beam, the alignment of the ion beam on the target area is confirmed by irradiating a  $\sim 3$   $\mu\text{m}$ -thick film of condensed argon with  $\text{H}^+$  or  $\text{Ar}^+$ . The argon emits a green luminescence when irradiated (Grosjean et al. 1997), showing the size and position of the irradiation area on the sample. Using the chamber XYZ manipulator, the position of the target is adjusted relative to the ion beam, until the irradiation area is slightly larger than and concentric to the active area of the QCM. This ensures complete irradiation coverage across the QCM.

## **2.5. Infrared Spectrometer**

Infrared measurements of our condensed ice films were performed either in specular reflectance geometry mode ( $35^\circ$  reflectance relative to sample normal) from the gold QCM electrode, or in transmission mode through the CsI transmission window, using the external

beam from a Nicolet Nexus 670 Fourier-Transform Infrared (FTIR) Spectrometer. Reflectance mode and transmission mode require different port configurations of the UHV chamber for the detector system, so the two modes cannot both be used easily within the same experiment.

Incoherent light is emitted from a halogen source (white visible light,  $25000 - 5000 \text{ cm}^{-1}$ ) or an infrared ever-glo source (IR light,  $9000\text{-}50 \text{ cm}^{-1}$ ), and passed through a Michelson interferometer within the FTIR bench. The interferometer directs the light in two paths through a KBr beamsplitter – one part toward a stationary mirror, and the other toward a mirror moving a fixed distance back and forth at constant velocity, measured by a He-Ne laser. The two beams interfere at the beamsplitter, as the light reflected from the moving mirror has travelled some distance relative to the light reflected from the stationary mirror. The time-dependent interference of the two beams forms an interferogram. The light exits the spectrometer and is focused onto the sample using a flat mirror and a parabolic mirror (effective focal length [EFL] = 15.2 cm), into a beam spot  $\sim 5 \text{ mm}$  in diameter, slightly smaller than the CsI window and the active area of the QCM. For ion beam experiments, we ensure that the infrared beam spot is smaller than and concentric to the ion beam spot (determined using argon luminescence, Section 2.4), so that our measurements reflect only the changes induced by irradiation.

KBr windows ( $250 \text{ nm} - 26 \text{ }\mu\text{m}$ ) are used to transmit light into and out of the UHV chamber. The windows are placed between two O-rings to prevent thermal expansion-induced breakage during baking. Each window is housed in a conflat flange (McAllister DPW 275) and differentially pumped with an oil-free scroll pump (Varian SH-110). The light – whether reflected  $35^\circ$  from the sample on the gold substrate or transmitted directly ( $180^\circ$ ) through the sample and the CsI window – is collected by a parabolic mirror (EFL = 15.2 cm), sent to a second parabolic mirror (EFL = 5.84 cm), and focused on the active area of a Mercury-



Cadmium-Telluride (MCT-A) detector ( $12000 - 650 \text{ cm}^{-1}$ ). The detector converts photons into electrical signal, and a Fourier transform performed on the interferogram collected at the detector provides an infrared spectrum. More details about the types and optical ranges of light sources, beamsplitters, and detectors are documented in a previous dissertation from our laboratory (Loeffler 2007).

The spectrometer, detector, and infrared beam path are constantly purged with dry air to minimize the infrared-active atmospheric components, such as water vapor and gaseous  $\text{CO}_2$ , to very small and constant levels. Any remaining small absorptions are removed by taking the ratio of the measured spectra to a reference spectrum. The dry air also protects moisture-sensitive optical components in the spectrometer, such as the KBr beamsplitter. The dry air is supplied by a Parker Balston (75-60) air filtration system for “dry” compressed air from a Hitachi 5.5 oil-free scroll compressor.

A typical infrared reflectance spectrum collected using our setup is shown in Figure 2.6. A  $\sim 5000\text{-ML}$   $\text{H}_2\text{O}$  ice film was deposited on the QCM at 70 K, then cooled to 40 K and exposed to ambient  $^{13}\text{CH}_4$ , resulting in methane uptake by the ice pores. The spectrum was collected at a resolution of  $2 \text{ cm}^{-1}$  in specular reflectance mode. The spectrometer can collect spectra at a resolution as high as  $0.125 \text{ cm}^{-1}$ , although  $2 \text{ cm}^{-1}$  is what is typically used in our experiments. The resolution is determined by the distance travelled by the moving mirror in the interferometer, with longer distances resulting in higher resolution. Prior to depositing the ice film, the spectrum  $R_0$  of the bare gold substrate is collected, serving as the background spectrum. The spectra  $R$  collected during the experiments are divided by  $R_0$  and expressed in units of optical depth,  $-\ln(R/R_0)$ . For experiments performed using FTIR in transmission mode, optical depth is determined as  $-\ln(T/T_0)$ , where  $T_0$  is the infrared spectrum of the bare CsI substrate.

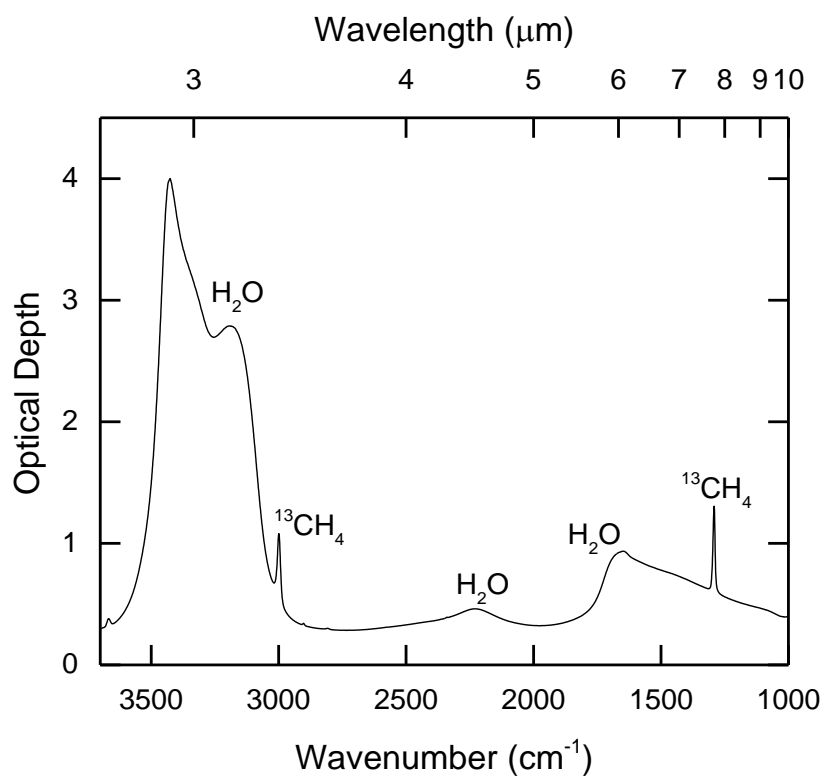


Figure 2.6 – Example infrared spectrum (reflectance mode) of water ice deposited at 70 K and exposed to ambient  $^{13}\text{CH}_4$  at 40 K, resulting in adsorption of methane within the water ice pores. The broad features peaking at 3.1  $\mu\text{m}$  (3500 – 3200  $\text{cm}^{-1}$ ), 4.6  $\mu\text{m}$  (2174  $\text{cm}^{-1}$ ), and 6.1  $\mu\text{m}$  (1639  $\text{cm}^{-1}$ ) are due to absorption from different vibrations and rotations of  $\text{H}_2\text{O}$  molecules in bulk ice. The sharp features at 3.3  $\mu\text{m}$  (2999  $\text{cm}^{-1}$ ) and 7.8  $\mu\text{m}$  (1291  $\text{cm}^{-1}$ ) are due to methane.

Molecules vibrate or rotate at characteristic frequencies, making infrared spectroscopy an ideal method for identifying chemical species within a condensed film. For example, the broad absorption feature at 3.1  $\mu\text{m}$  ( $3500 - 3200\text{ cm}^{-1}$ ) in Figure 2.6 is due to the absorption of light by the bending and stretching vibrations of the O-H bond in bulk water ice, known as the O-H stretch absorption band. The weaker band at 6.1  $\mu\text{m}$  ( $1639\text{ cm}^{-1}$ ) is the bending or scissoring absorption, while the band at 4.6  $\mu\text{m}$  ( $2174\text{ cm}^{-1}$ ) is a combination band. Comprehensive reviews of infrared spectra of water have been compiled by previous studies (Baragiola 2003, Devlin 1990, Hudgins et al. 1993, Sceats & Rice 1982). The sharp features at 3.3  $\mu\text{m}$  ( $2999\text{ cm}^{-1}$ ) and 7.8  $\mu\text{m}$  ( $1291\text{ cm}^{-1}$ ) are due to C-H stretching and bending modes in methane (Moore & Hudson 1998, Bennet & Kaiser 2007), respectively. We use FTIR throughout our experiments to determine the makeup of a film after deposition, as well as study physical or chemical changes induced by thermal or ion processing.

## 2.6. Ultraviolet-Visible Spectrometer

A FilmTek 2000 spectrophotometer is used to collect transmittance of ice films *in situ* for the 200 to 850 nm range, enabling the calculation of the density of ice films deposited on the CsI substrate. A deuterium discharge lamp provides the ultraviolet light, while visible light is discharged by a tungsten-halogen lamp. The light travels from the spectrophotometer through a silica fiber-optic cable and is focused onto the CsI substrate using a sapphire lens affixed to a custom-built conflat flange (MDC Vacuum Products) on the UHV chamber. The transmittance spectra are collected through a second window at the opposite end of the chamber via a second focusing lens and fiber optic cable. A linear charge-coupled device (CCD) array (2048-pixel)

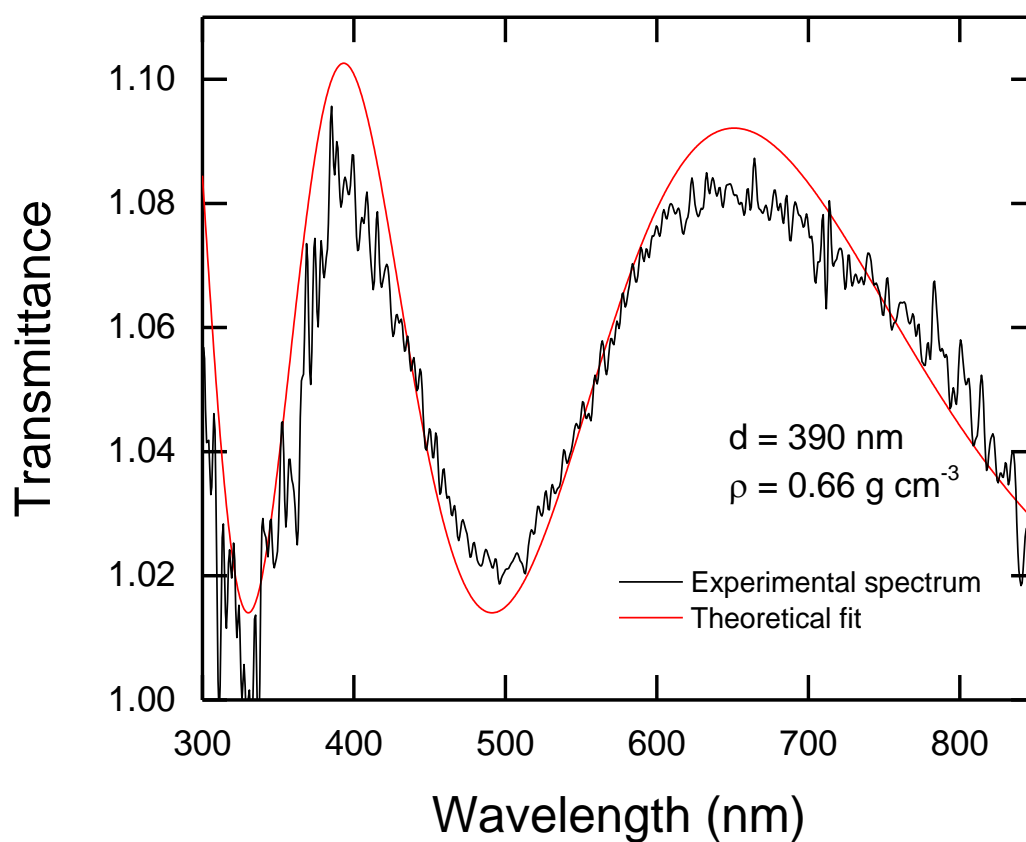


Figure 2.7 – Example UV-visible spectrum (black curve) of amorphous solid water film deposited on CsI substrate at 10 K. Red curve is a fit generated using Fresnel's equations, which gives a film thickness of 390 nm. A column density of  $8.78 \times 10^{17} \text{ H}_2\text{O cm}^{-2}$  is derived from QCM measurements, using a calibration technique described in Chapter 3.2. The fitted film thickness and measured column density give a film density of  $0.66 \text{ g cm}^{-3}$ .

measures light intensity at all wavelengths due to dispersion of the light as it travels through a 50- $\mu\text{m}$  pinhole and strikes a fixed grating.

A dark spectrum is collected before each experiment and subtracted from subsequent spectra, to account for any stray light measured on the detector. Figure 2.7 shows an example for the ultraviolet-visible transmission spectrum of a water ice film. A synthetic spectrum generated using Fresnel's equations is fit to the interference oscillations in the experimental spectrum, and a LabView program produces the best fit to the data by optimizing values of the refractive index, absorbance, and film thickness (Teolis 20007). The film density is calculated after estimating the column density of ice deposited on the CsI substrate. These column estimates are obtained by performing calibration experiments using the QCM; further details of this technique are in Chapter 3. The density  $\rho$  of the condensed ice films is used to determine the volumetric ice porosity,  $1 - \rho/\rho_c$ , where  $\rho_c = 0.94 \text{ g cm}^{-3}$ , the density of compact amorphous ice (Baragiola 2003).

## **2.7. Quadrupole Mass Spectrometer**

Molecules desorbing from the sample using temperature-programmed desorption (TPD) or via ion-induced sputtering are detected using an Amtek Dycor MA200 quadrupole mass spectrometer (QMS). The QMS is mounted on a flange with a cylindrical drift region differentially pumped with a Perkin Elmer ion pump ( $200 \text{ Liters s}^{-1}$ ). Neutral molecules are ionized by an electron-impact-based ionizer that produces electrons of energy around 70 eV, efficiently ionizing most molecules without causing excessive fragmentation. The energy of the electrons can be changed by adjusting the voltages applied to the filament and grid. The ionized molecules are passed into a quadrupole mass filter, where RF and DC voltages (2 to 3 MHz)

allow only ions of a certain  $m/q$  ratio (1 to 200) to travel along the length of the quadrupole rods (111.4 mm long, 6.35 mm diameter) to the particle detector. The ions are detected and counted by a single microchannel plate (MCP) multiplier, which is biased up to -1300 V. A proportionality factor is used to relate the current measured by the detector to the flux of molecules emanating from the sample. Mass spectra are collected as the quadrupole allows ions of only particular  $m/q$  to pass for a given time period through a selected mass range.

## **2.8. Excimer Laser**

The 193 nm pulses described in the photolysis experiments in Chapter 4 were generated by an Ex50 excimer laser (Gam Laser Inc.) using ArF. The laser produces 10 ns-wide pulses at 248, 193, or 157 nm, depending on whether KrF, ArF, or F<sub>2</sub> gas is used, respectively. We typically use pulse rates of 10 Hz or lower in our experiments, to avoid significant heating of the sample, although the laser can produce as many as 250 pulses per second. The maximum energy output is ~36 mJ per pulse for 193 nm photons. The laser beam is focused through a MgF<sub>2</sub> converging lens ( $f = 50$  cm) and expands to irradiate a rectangular spot (25 by 75 cm) at normal incidence at the target within the vacuum chamber, >120 cm from the laser. The energy profile is constant across the irradiation area, as measured by an Ophir Pe25 external detector at the target distance. The typical fluence used in the photolysis experiments is ~1 mJ cm<sup>-2</sup> per pulse. A rastering mirror is available, but was not used for these experiments.

## **2.9. Data Acquisition**

We use a LabView program to communicate with the QCM, QMS, and temperature controller during experiments, through a Serial RS-232 interface. The program is mainly

designed to collect and monitor data during experiments, and graphically displays temperatures of the target and shield, QCM frequency, chamber background pressure from an ionization gauge, and QMS partial pressures of up to 12 selected masses in real-time. The collected data are automatically saved at a selected time interval, typically every 5 seconds. The data acquisition program outputs a single data file containing synchronized signals from all of the interfaced instruments, facilitating instrumental comparative analysis.

## **2.10. Sources of Experimental Error**

The following are the main sources of experimental error in the experiments described in this dissertation:

- The silicon diode temperature sensor has a stated accuracy of  $\pm 1$  K within the range of 1.5 to 400 K. We immersed the unit in liquid nitrogen (77.2 K) to test the absolute accuracy of the silicon diode sensors mounted on the target assembly and the shield. The diodes measured 77.5 ( $\pm 0.3$ ) K.
- The accuracy of the QCM measurement of the areal mass of the condensed films is conditioned by the temperature stability, which is  $\pm 0.01$  K for our temperature controller. This corresponds to an error of 0.1 Hz in QCM frequency, introducing an error in column density of  $4 \times 10^{13}$  H<sub>2</sub>O cm<sup>-2</sup>, or 0.04 ML H<sub>2</sub>O.
- The determination of the ion beam fluence in our irradiation experiments are limited by measurements of the beam current. The current is measured using a Keithley 610 C electrometers with 2% full-scale accuracy in the mA to nA range. Instability of the beam current can lead to error, as well, with deviations in the current measured on the back of the Faraday cup introducing a total error of 5% in our determination of the ion fluence.

- The main source of error in porosity measurements for ice films (Chapter 3.2) originates from the estimates of the column density deposited on the CsI, which were determined using calibration experiments with the QCM, described in Chapter 3. This experimental technique introduces uncertainty in column density that corresponds to errors of  $\pm 0.03$  in porosity.
- The laser energy per pulse is 3% accurate at 193 nm, measured with the Ophir external detector. The pulse energy deviates by 3% between pulses during operation.

## References

- Baragiola, R.A., In: Water in Confining Geometries, Buch, V. & Devlin, J.P. (Eds.), Springer, New York (2003).
- Bennet, C.J. and Kaiser, R.I., *Astrophys. J.* **660**, 1289 (2007).
- Devlin, J.P., *Int. Rev. Phys. Chem.* **9**, 29 (1990).
- Grosjean, D.E., Vidal, R.A., Baragiola, R.A., Brown, W.L. *Phys. Rev. B.* **56**, 6975 (1997).
- Hudgins, D.M., Sandford, S.A., Allamandola, L.J., Tielens, A.G.G.M., *Astrophys. J. Supp.* **86**, 713 (1993).
- Loeffler, M.J., In: Space Weathering of Planetary Regoliths, Ph.D. Thesis, University of Virginia (2007).
- Lu, C. and Lewis, O., *J. Appl. Phys.* **56**, 608 (1984).
- Moore, M.H. and Hudson, R.L. *Icarus* **135**, 518 (1998).
- Raut, U., In: Laboratory Studies of Interstellar Ice Analogs, Ph.D. Thesis, University of Virginia (2009).
- Sack, N.J. and Baragiola, R.A., *Phys. Rev. B.*, **48**, 9973 (1993).



Sceats, , M.G. & Rice, S.A., In: Water, a Comprehensive Treatise, Franks, F. (Ed.), 7, Plenum, New York (1982).

Teolis, B.D., In: Radiation Processing of Water, Oxygen, and Ozone Ices, Ph.D. Thesis, University of Virginia (2007)

Westley, M.S., In: Vapor Deposited Water Ice: Structural Properties, Effects of Ultraviolet Light, and Astrophysical Implications, M.S. Thesis, University of Virginia (1994).

## CHAPTER 3

### Crystallization of Porous Ices in the Outer Solar System

---

#### 3.1. Isothermal Crystallization Kinetics of Amorphous Solid Water

##### Abstract

We present results on the isothermal transformation of vacuum-deposited amorphous water ice into cubic crystalline ice at temperatures between 130 and 141 K. The ice crystallized in two distinct stages at all temperatures, and crystallization rates increased with isothermal crystallization temperature. We measure crystallization activation energy of  $64 (\pm 3)$  kJ per mole. Temperature-dependent crystallization times are extrapolated to temperatures relevant to Jovian moons, with predicted crystallization time of  $\sim 1.2 \times 10^5$  years at 100 K, and can contribute to the understanding of the processes that have shaped the evolution of extraterrestrial bodies. In Chapter 3.2, we expand this study to examine the role of the ice pores in crystallization.

##### 3.1.1 Introduction

A strong motivation for this project is the puzzling distribution of amorphous and crystalline ice in the Outer Solar System. Some of the Galilean satellites contain amorphous ice at surprisingly high surface temperatures. On the other hand, an unexpected fraction of crystalline ice has been identified on the surface of most of the giant planet satellites (Dalton et al.), on Pluto's satellite Charon (Brown & Calvin 1999, Cruikshank et al. 2015, Grundy et al. 2016), and on some trans-Neptunian objects (TNOs) such as Quaoar (Jewitt & Lu 2004) and Haumea (Merlin et al. 2007). The crystalline content has been deduced from the near infrared

(NIR) absorption band at 1.65  $\mu\text{m}$ , which is associated with crystalline ice (Schmitt et al. 1998). However, the O-H stretch vibration at 3.1  $\mu\text{m}$  can also be used to diagnose the crystalline content of an ice film, if the band is not saturated. It dramatically narrows as the ice crystallizes due to decreased disorder in the ice from the oxygen positions and from decreasing microporosity (Baragiola 2003).

At the very low temperatures of giant planet satellites and TNOs, normal accretion should lead only to the amorphous phase. Even if the ice crystallizes, it would likely be progressively amorphized by exposure to space radiation: laboratory studies have shown that solar Lyman- $\alpha$ , cosmic rays, or energetic charged particles trapped by the planetary magnetic fields can amorphize crystalline ice (Baratta et al. 1991, Moore & Hudson 1992, 1995, Kouchi & Kuroda 1990, Leto & Baratta 2003). Several potential explanations have been invoked for the presence of crystalline ice, including cryo-volcanism (Jewitt & Lu 2004, Bauer et al. 2002), local heating by micrometeorite impacts (Porter et al. 2010), and porosity effects. This last possibility is the focus of Chapter 3.2.

When deposited from the vapor phase, water ice can be formed in crystalline phases, cubic or hexagonal, or amorphous phases (Baragiola 2003). The main condition that determines the phase of ice during growth is temperature; water deposited from the vapor phase onto substrates colder than  $\sim 130$  K is known to form amorphous solid water (ASW) (Sceats & Rice 1982). ASW is metastable and irreversibly converts to cubic crystalline ice at a temperature-dependent rate. In laboratory timescales, this transition occurs when ASW is warmed to temperatures above  $\sim 135$  K; this phase is stable and the transformation does not reverse at lower temperature. Upon heating to about  $\sim 200$  K, cubic crystalline ice transforms to the hexagonal crystalline phase. These transition temperatures are much lower over astronomical timescales.

Crystallization of amorphous solids occurs as a combination of nucleation and growth, and the evolution of the fraction of the crystalline phase  $\phi_c$  after time  $t$  can be described by (Avrami 1939):

$$\phi_c = 1 - \exp(-Kt^n) \quad (1)$$

where  $K$  is the rate constant and  $n$  is the Avrami exponent, which represents the crystal growth mechanism and is the sum of two terms,  $n = N + C$  (Rao & Rao 1978, Doremus 1985).  $N$  is usually called the nucleation term and takes the value of 0 or 1, corresponding to instantaneous (one-step) or continuous nucleation, respectively.  $C$  is the crystallization term and can take integer values of 1, 2, or 3, rod-like, disc-like, or spherical growth, respectively. Values of  $n$  that are greater than 4 or that are non-integers imply a more complicated nucleation process. The rate constant  $K$  has been found to depend on temperature in an Arrhenius relationship with activation energy  $\Delta H$  (Hage et al. 1994):

$$K^{1/n}(T) = K_0^{1/n} \exp(\Delta H/RT) \quad (2)$$

Reported values for the Avrami exponent  $n$  and for the activation energy  $\Delta H$  have varied throughout previous ASW crystallization studies; the exact mechanism of the phase transformation remains a matter of debate in the literature (Dowell & Rinfret 1960, Schmitt et al. 1989, Sack & Baragiola 2003, Hage et al. 1995, Jenniskens & Blake 1996, Dohnálek et al. 2000, Lofgren et al. 2003, Safarik et al. 2003, Backus et al. 2014, Kondo et al. 2007, Maté et al. 2012). It is necessary to resolve these contradictory values in order to extrapolate astronomical crystallization times from laboratory timescales. In this Chapter, we present results on isothermal crystallization kinetics of ices deposited at 130 – 141 K and use our laboratory measurements to predict crystallization times at astronomically relevant temperatures.

### 3.1.2 Experimental Methods

The experiments were performed in an ultrahigh vacuum chamber with a base pressure of  $\sim 10^{-10}$  Torr. Water ice films were vapor-deposited at normal incidence onto the CsI window at 10 K; these growth conditions are known to result in microporous ASW (Sceats & Rice 1982). The  $\text{H}_2\text{O}$  pressure was measured with a nude ionization gauge and corrected for gas-dependent sensitivity. The film thickness was determined using ultraviolet-visible interferometry and quartz crystal microgravimetry, in a technique described in detail in Chapter 3.2. The typical film thickness used in these experiments was  $\sim 1000$  ML  $\text{H}_2\text{O}$  ( $1 \text{ ML} = 1 \times 10^{15} \text{ H}_2\text{O cm}^{-2}$ , about a monolayer), or  $\sim 400$  nm.

The films were characterized using transmission Fourier transform infrared spectroscopy (FTIR) at  $2 \text{ cm}^{-1}$  resolution using a Thermo Nicolet Nexus 670 spectrometer thoroughly purged with dry air. The spectra  $T$  of the films were divided by the transmission spectrum  $T_0$  of the bare CsI window and then converted to optical depth,  $-\ln(T/T_0)$ . In particular, we focused on the changes on the O-H-stretch absorption band ( $3.1 \text{ }\mu\text{m}$ ) and the O-H dangling bond absorption features at  $\sim 2.7 \text{ }\mu\text{m}$ . Transmission infrared spectra were collected immediately after the deposition of the water films at 10 K. After deposition, the films were heated at  $1 \text{ K min}^{-1}$  to temperatures ranging from 130 to 141 K, with simultaneous collection of infrared spectra as the films were held at constant temperature. To deduce physical changes in the ice, straight-line baselines matching the absorption continuum were subtracted from the  $3.1\text{-}\mu\text{m}$  band.

### 3.1.3 Results and Discussion

Figure 3.1.1 shows changes in the normalized 3.1- $\mu\text{m}$  O-H-stretch absorption band due to  $1 \text{ K min}^{-1}$  heating from 10 to 141 K. These changes are due to the thermally-induced compaction of the micropores of the ice film, causing a decrease in film thickness (Johari 1991, Tsekouras 1998, Giering & Haarer 1996). This is supported by disappearance of the  $\sim 2.7\text{-}\mu\text{m}$  O-H dangling bond absorption features (inset), which are due to less-coordinated ( $<4$ ) water molecules on the internal surfaces of the pore walls and are thus diagnostic of microporosity (Devlin & Buch 1995). Above  $\sim 120 \text{ K}$ , the spectra do not change during steady heating to 141 K, suggesting that the pore compaction process is complete. However, previous studies of ices that were compacted via both thermal (Bossa et al. 2012, Isokoski et al. 2014) and ion processing (Raut et al. 2007a), have shown that the absence of dangling bond features does not necessarily imply lack of porosity in the ice. We characterize thermal-induced changes in ice porosity in Chapter 3.2.

In Figure 3.1.2, we show further changes in the 3.1- $\mu\text{m}$  absorption band when the ice film was held at 140 K, resulting in crystallization. The normalized bands narrow and shift from  $\sim 3252 \text{ cm}^{-1}$  to  $3223 \text{ cm}^{-1}$ ; non-normalized bands are also characterized by an increase in optical depth. The infrared spectra collected between 0 and 136 minutes at 140 K show the gradual transition from partially-compacted amorphous ice to cubic crystalline ice. Estimates of the amorphous and crystalline components of a partially crystallized ASW film were made using factor analysis: we assume that each spectrum  $S$  is the result of a weighted sum of the spectra corresponding to pure amorphous and crystalline ices, a method used previously in several studies (Malinowski 2002, Famá et al. 2010, Smith et al. 2011):

$$S = \phi_C T_C + \phi_A T_A \quad (3)$$

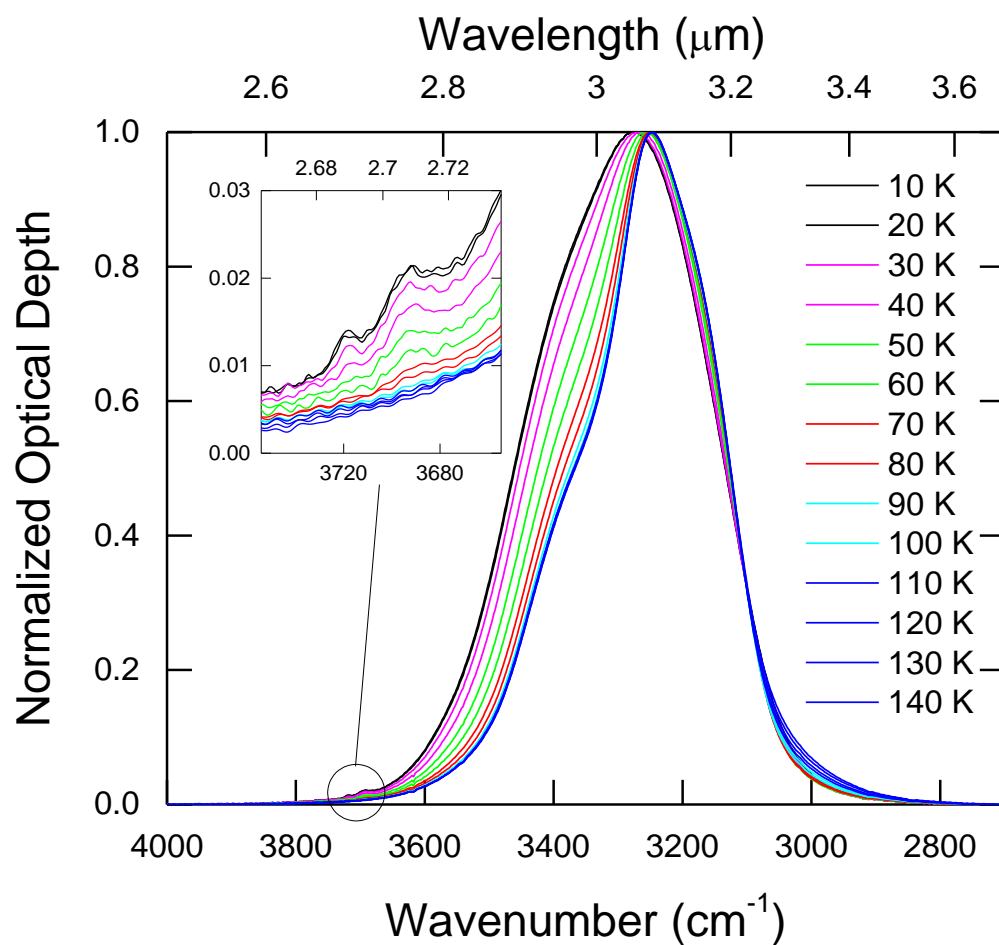


Figure 3.1.1 – Changes in normalized optical depth in the region of the 3.1- $\mu\text{m}$  O-H-stretch absorption band during heating of the  $\sim 1000$  ML-thick ice film from 10 to 140 K at  $1 \text{ K min}^{-1}$ . The film was deposited at 10 K at normal incidence. Inset shows decrease in  $\sim 2.7$ - $\mu\text{m}$  O-H dangling bond absorptions during heating.

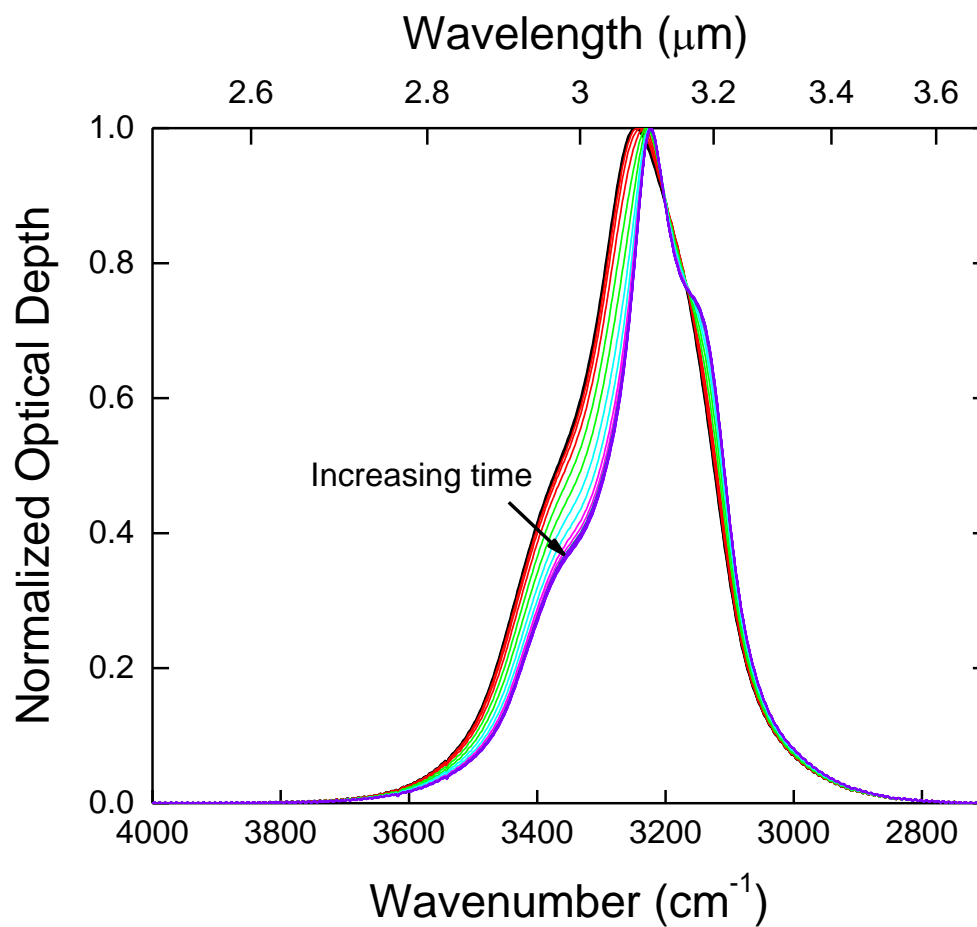


Figure 3.1.2 – Changes in normalized optical depth for 3.1-μm absorption band for ~1000-ML ice film deposited at 10 K, heated at 1 K min<sup>-1</sup>, and held at 140 K for 136 minutes. Spectra were collected 70 seconds apart.



where  $\phi_A$  and  $\phi_C$  are the fractions of amorphous and crystalline phases,  $\phi_A + \phi_C = 1$ , and  $T_A$  and  $T_C$  are the infrared spectra of the fully amorphous and crystalline ice. Each spectrum was deconvoluted to determine the  $\phi_A$  and  $\phi_C$  that yield a minimum in the root-mean-square. This calculation is shown illustratively in Chapter 3.2 (Figure 3.2.4). We perform this fit for sequential spectra throughout the crystallization process, allowing for the calculation of the crystalline fraction  $\phi_C$  (or, equivalently,  $\phi_A = 1 - \phi_C$ ) as a function of isothermal crystallization time.

Results of this calculation are shown in Figure 3.1.3 for ices crystallized between 136 and 140 K, with crystallization times significantly decreasing at higher isothermal crystallization temperatures. The crystallization time at the threshold  $\phi_A = 1/e$  ( $\phi_C = 0.63$ ), hereafter designated  $\tau_C$ , was  $\sim 13$  minutes at 140 K,  $\sim 7$  times faster than  $\tau_C$  for ice crystallized at 136 K. Ice held at 130 K, not shown in the Figure, took as long as  $\sim 19$  hours to reach  $\tau_C$ . There are several reports in the literature that suggest that ASW does not crystallize completely in the 130 to 150 K range (Dowell & Rinfret 1960, Hagen et al. 1983, Hallbrucker et al. 1989, Hessinger et al. 1996, Jenniskens & Blake 1996, Jenniskens et al. 1997). However, sublimation rates fall to the values of crystalline ice at  $\sim 140$  K (Sack & Baragiola 1993, La Spisa et al. 2001), suggesting that only a negligible fraction of ASW remains, since sublimation from cubic crystalline ice is about two orders of magnitude smaller than from ASW. We found that the spectra of films held between 130 and 139 K for long periods of time (several hours to several days, depending on the temperature) match the spectrum of ASW crystallized at 140 K for  $\sim 3$  hours, within  $< 1\%$ .

In order to better distinguish the crystallization process from Figure 3.1.3, we twice apply the natural logarithm to Eq. 1, resulting in a linear representation of the process:

$$\ln(-\ln[1 - \phi_C]) = \ln K + n \ln t \quad (4)$$

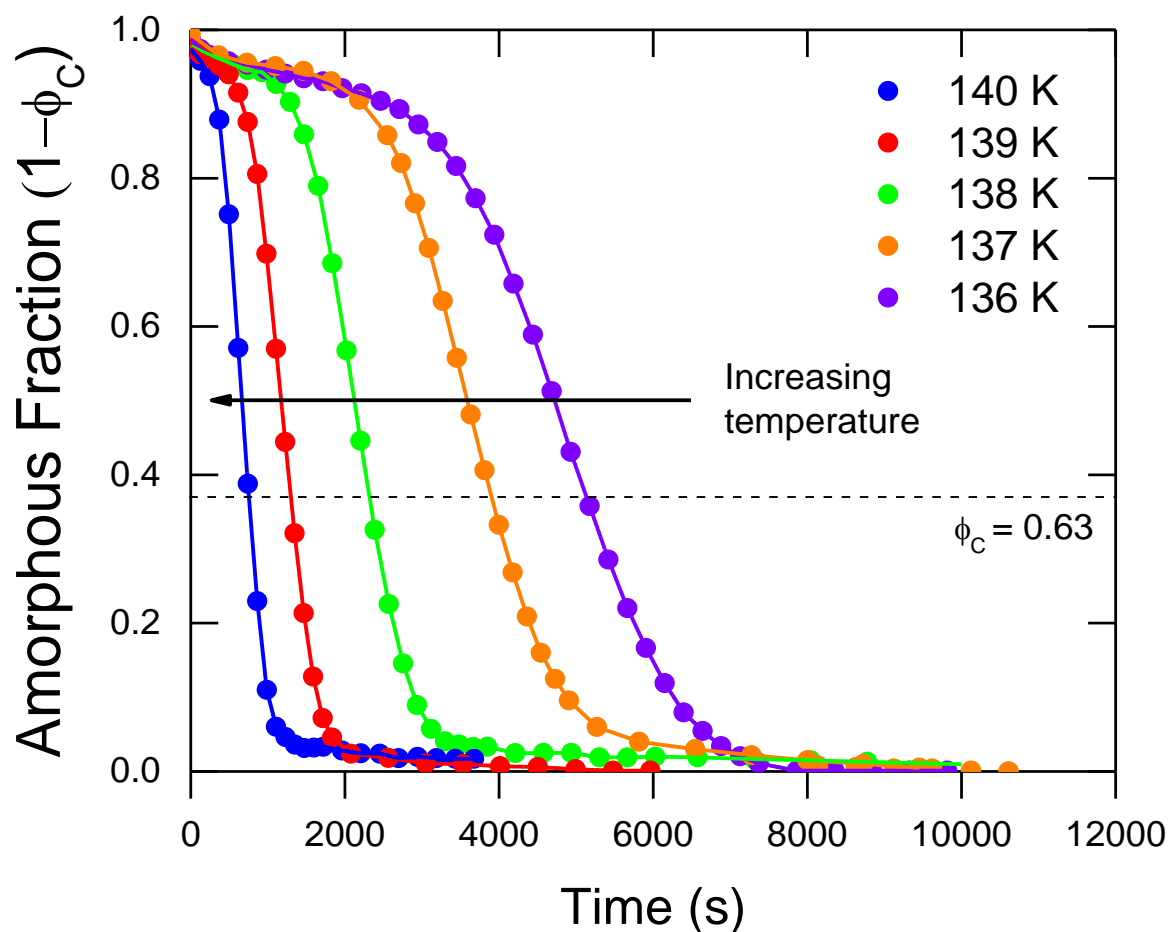


Figure 3.1.3 – Decrease in the amorphous fraction  $\phi_A = 1 - \phi_C$  during isothermal crystallization at 136 – 140 K. Ice films were deposited at normal incidence at 10 K and heated to crystallization temperatures at  $1 \text{ K min}^{-1}$ . The amorphous fractions were obtained from deconvolution of the  $3.1\text{-}\mu\text{m}$ , discussed in the text with an illustrative example shown in Figure 3.2.4. Lines are to guide the eye.

Figure 3.1.4 shows this representation of the data. Two distinct processes can be clearly distinguished. The first crystallization stage is characterized by Avrami exponent  $n_1 \sim 0.39$  ( $\pm 0.06$ ), independent of temperature, and crystallization rate  $K_1^{1/n_1} \sim (1 - 600) \times 10^{-8} \text{ s}^{-1}$ , increasing with temperature. This corresponds to rapid, one-step nucleation and inhibited one-dimensional growth geometry according to the typical interpretation of the Avrami exponent (Rao & Rao 1985, Doremus 1985). After reaching a crystalline phase concentration of  $\sim 9$  ( $\pm 2$ ) %, the second crystallization stage takes effect. During this second stage, nucleation and crystalline growth proceed according to  $n_2 \sim 4$  ( $\pm 0.7$ ), again independent of temperature, and  $K_2^{1/n_2} \sim (1 - 100) \times 10^{-5} \text{ s}^{-1}$ , with increasing isothermal crystallization temperature. The second crystallization stage occurs  $>100$  times faster than the first stage and is the dominant stage of nucleation and crystalline growth throughout the bulk of the ice. Our measurement of  $n_2 \sim 4$  implies continuous nucleation and unrestricted three-dimensional crystalline growth within the ice. We attribute and further discuss these two stages in Chapter 3.2.

A comparison of these results with previous studies is conditioned by widely varying ice generation techniques. Hage et al. (1994) and Maté et al. (2012), using FTIR, reported that crystallization proceeds according to a diffusion-controlled mechanism with  $n \sim 1$  to 2.5, as did Jenniskens & Blake (1996) using electron diffraction. Conversely, Dohnálek et al. (2000) measured  $n \sim 4$ , corresponding to constant nucleation and three-dimensional crystalline growth, using  $\text{N}_2$  desorption spectroscopy, as did Smith et al. (1996, 2011) via desorption rates and FTIR. A few studies (Hage et al. 1994, Jenniskens & Blake 1996) have reported an initial induction regime corresponding to  $n \sim 2$  to 2.5, followed by a dominant bulk crystallization regime that proceeds with  $n \sim 0.8$  to 0.9.

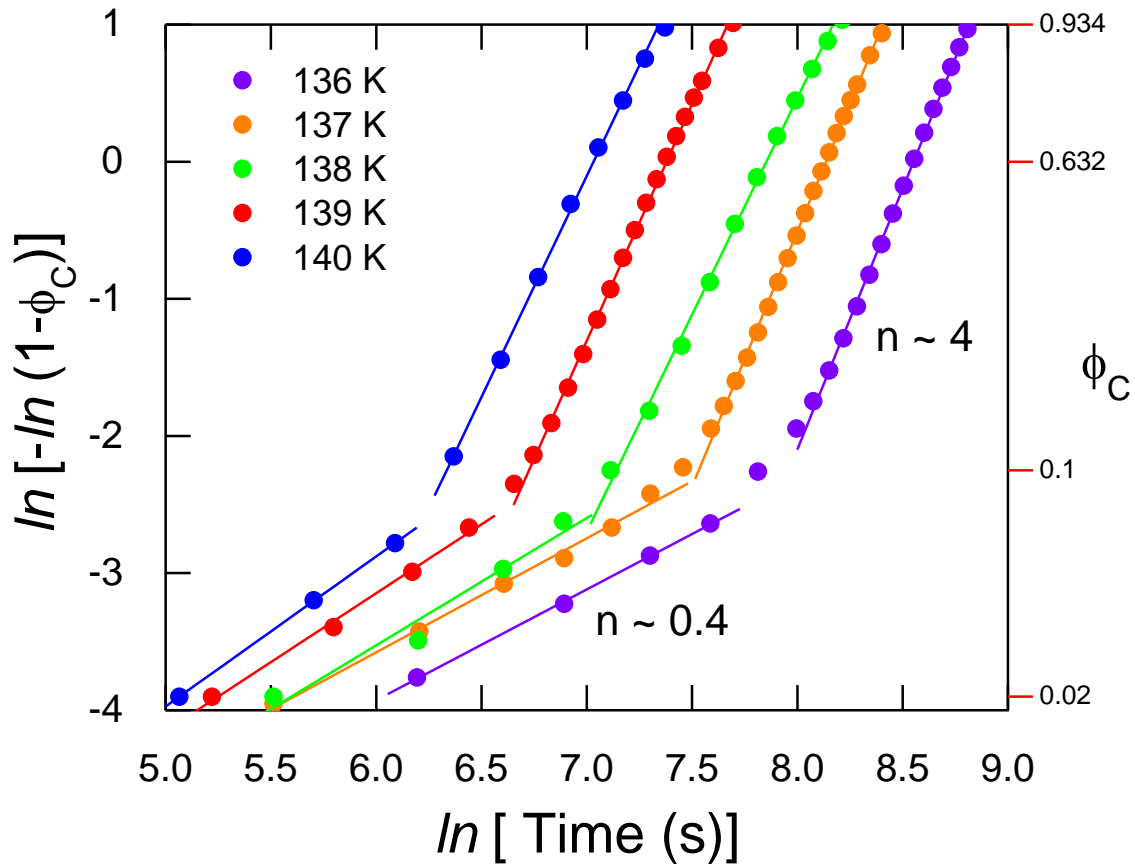


Figure 3.1.4 – Double natural logarithm representation of Fig. 3.1.3 shows that crystallization of amorphous ice films unfold in two distinct kinetic stages. The slopes and intercepts of the linear fits (solid lines as per Eq. 4) give Avrami parameters  $n$  and  $K$  for each crystallization stage, respectively. Only  $\sim 9\%$  of the ice is crystallized during the first stage. The second stage proceeds faster than the first stage, resulting in near-complete crystallization of the ice films.

In Figure 3.1.5, we show the temperature dependence of the second-stage rate constant  $K_2^{1/n_2}$  in an Arrhenius plot, from which the crystallization activation energy  $\Delta H$  can be extracted using a linear fit. We focus on the second stage because it is the dominant process behind the crystallization, driving the crystallization of ~91% of the film. We find  $\Delta H \sim 64 (\pm 3) \text{ kJ mol}^{-1}$ , similar to several measurements that have been reported previously (Dowell & Rinfret 1960, Jenniskens & Blake 1996, Dohnálek et al. 2000, Lofgren et al. 2003, Smith et al. 2011). Using Eq. 1 and 2, we can then use our measurement of  $\Delta H$  to extrapolate  $\tau_C$  to lower, astronomically relevant temperatures:

$$\tau_C = K_0^{-1/n_2} \exp(\Delta H/RT) \quad (5)$$

where  $K_0^{1/n_2}$  is the intercept of the Avrami fit in Figure 3.1.6. This extrapolation is shown in Figure 3.1.6, along with our laboratory measurements of  $\tau_C$  for isothermal crystallization in the 130 – 141 K range (black circles). We predict a crystallization time of  $\sim 1.2 \times 10^5$  years at 100 K, based on our experiments on ASW deposited at normal incidence. Results from previous experimental studies are drawn with solid lines (Dowell & Rinfret 1960, Schmitt et al. 1989, Sack & Baragiola 1993, Hage et al. 1995, Jenniskens & Blake 1996, Dohnálek et al. 2000, Lofgren et al. 2003, Smith et al. 2011). These data show a large spread in reported crystallization times, using widely varying ice deposition conditions and experimental techniques, summarized in Table 3.2.1 in the next section. We posit that differing ice porosities among previous studies can be at least partially responsible for the observed discrepancy in crystallization times, and we explore this topic in detail in Chapter 3.2.

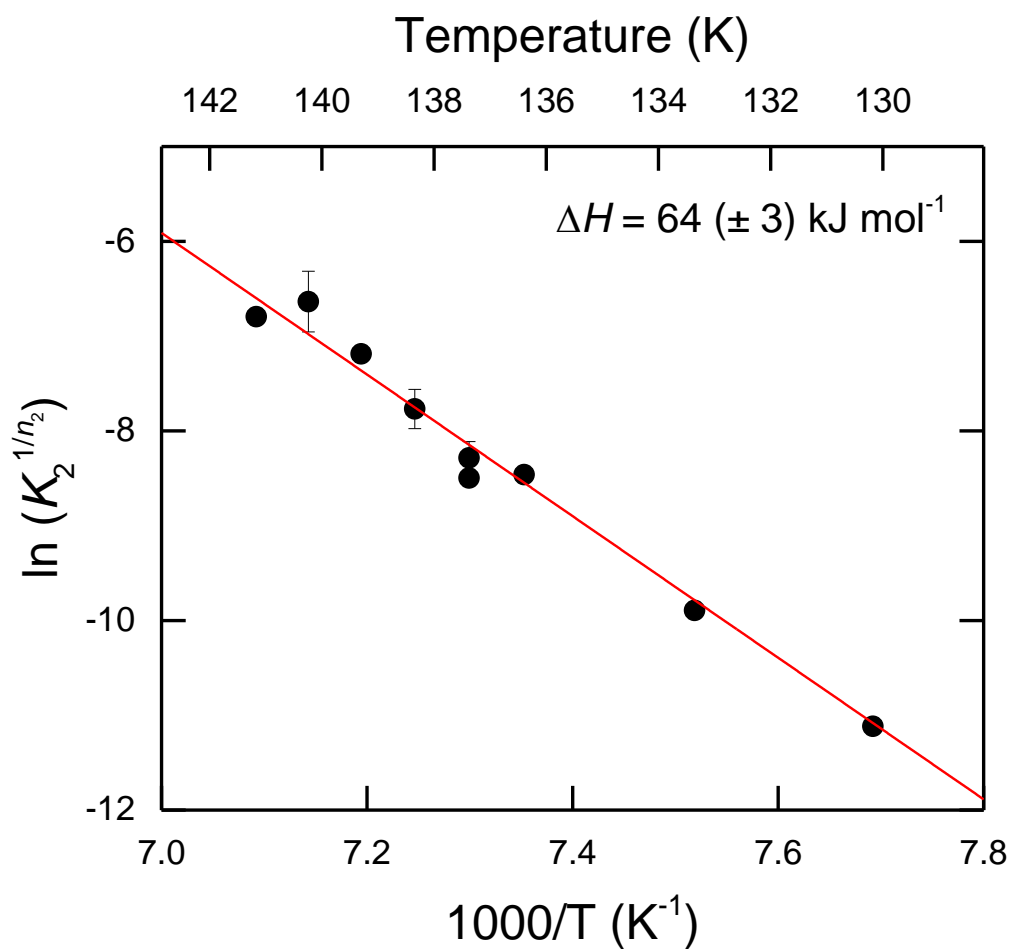


Figure 3.1.5 – Temperature dependence of second-stage crystallization rate  $K_2^{1/n_2}$  for ice films deposited at normal incidence at 10 K and isothermally crystallized at 130 – 141 K. Avrami fit (solid line) to the data gives a crystallization activation energy  $\Delta H \sim 64 \text{ kJ per mole}$ .

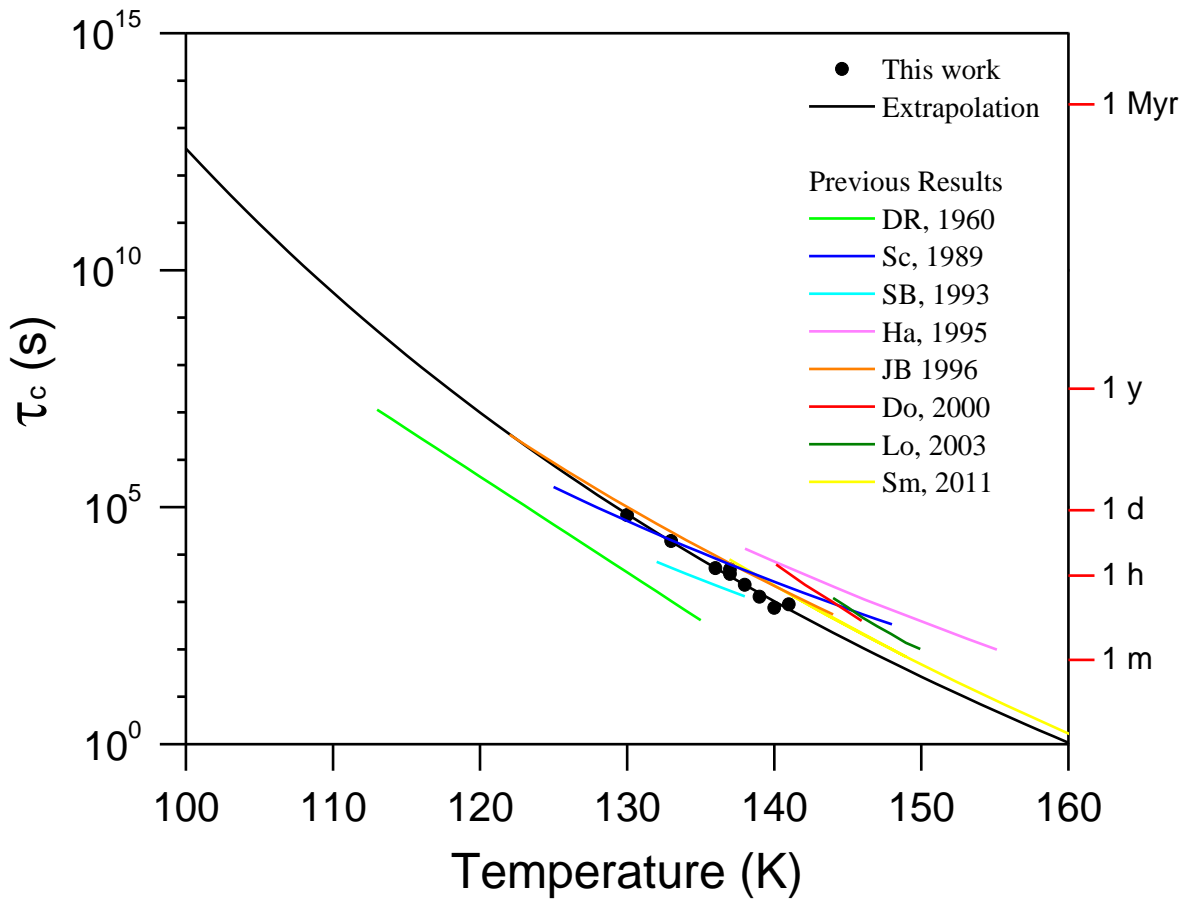


Figure 3.1.6 – Composite plot of experimental data for 63% isothermal crystallization times ( $\tau_c$ ) of vacuum-deposited amorphous ice available in the literature, partially reproduced from (Baragiola 2003): (DR, Dowell & Rinfret 1960; Sc, Schmitt et al. 1989; SB, Sack & Baragiola 1993; Ha, Hage et al. 1995; JB, Jenniskens & Blake 1996; Do, Dohnálek et al. 2000; Lo, Lofgren et al. 2003; Sm, Smith et al. 2011). We include our results of  $\tau_c$  vs. temperature for ice films deposited at 10 K at normal incidence. Solid line is an extrapolation of the fit of Eq. 6 to our data, which gives  $\tau_c$  for lower temperatures typical of Jovian moons.

### 3.1.1 Summary and Conclusions

We have investigated isothermal crystallization kinetics for amorphous solid water deposited at normal incidence, and used laboratory results in the 130 – 141 K range to estimate crystallization times on cold icy bodies in the Outer Solar System such as Jovian moons. Changes in the 3.1- $\mu\text{m}$  O-H-stretch absorption band reveal that the ice undergoes physical changes before the film begins to crystallize, due to thermal compaction of the micropores in a process that slows significantly above  $\sim 100$  K. The band changes dramatically during isothermal crystallization above 130 K, and the time-dependent evolution of the band was used to characterize the dynamics of the transition from amorphous to cubic crystalline ice. We find that crystallization time decreases with temperature in two distinct stages at all temperatures, and we measure crystallization activation energy of  $\sim 64$  kJ per mole using Avrami analysis, similar to previous measurements for the transformation of amorphous to cubic crystalline ice. The extrapolation of these results to 100 K leads to an estimated crystallization time of  $\sim 1.2 \times 10^5$  years. Additionally, we note a spread in reported isothermal crystallization times among previous studies, and examine a possible source for these differing results in Chapter 3.2.

### References

- Backus, E.H.G., Grecea, M.L., Kleyn, A.W., Bonn, M., *Phys. Rev. Lett* **92**, 23 (2004).
- Baratta, G.A., Leto, G., Spinella, F., Strazzulla, G., Foti, G., *A&A* **252**, 421 (1991).
- Baragiola, R.A., *Planet. Space Sci.* **51**, 953 (2003).
- Bauer, J.M., Roush, T.L., Geballe, T.R., Meech, K.J., Owen, T.C., Vacca, W.D., Rayner, J.T., Jim, K.T.C., *Icarus* **158**, 178 (2002).
- Bossa, J.-B., Isokoski, K., de Valois, M.S., Linnartz, H., *A&A* **545**, A82 (2012).



- Brown, M.E. and Calvin, W.M., *Science* **287**, 5450 (2000).
- Cruikshank, D.P., Grundy, W.M., DeMeo, F.E., Buie, M.W., Binzel, R.P., Jennings, D.E., Olkin, C.B., Parker, J.W., Reuter, D.C., Spencer, J.R., Stern, S.A., Young, L.A., Weaver, H.A., *Icarus* **246**, 82 (2015).
- Dalton, J.B., Cruikshank, D.P., Stephan, K., McCord, T.B., Coustenis, A., Carlson, R.W., Caradini, A. *Space Sci. Rev.* **153**, 113 (2010).
- Devlin, J.P. and Buch, V., *J. Chem. Phys.* **99**, 16534 (1995).
- Dohnálek, Z., Ciolli, R.L., Kimmel, G.A., Stevenson, K.P., Smith, R.S., Kay, B.D., *J. Chem. Phys.* **110**, 5489 (2000).
- Doremus, R.H., *Rates of Phase Transformations*, Academic, New York (1985).
- Dowell, L.G. and Rinfret, A.P., *Nature* **158**, 1144 (1960).
- Famá, M., Loeffler, M.J., Raut, U., Baragiola, R.A., *Icarus* **207**, 314 (2010).
- Giering, T. and Haarer, D., *Chem. Phys. Lett.* **261**, 6, 677 (1996).
- Grundy, W.M. et al. *Science* **351**, 6279 (2016).
- Hage, W., Hallbrucker, A., Mayer, E., Johari, G.P., *J. Chem. Phys.* **100**, 2743 (1994).
- Hagen, W., Tielens, A.G.G.M., Greenberg, J.M., *A&A* **51**, 389-416 (1983).
- Hallbrucker, A., Mayer, E., Johari, G.P., *J. Phys. Chem.* **93**, 4986 (1989).
- Hessinger, J., White Jr., B.E., Pohl, R.O., *Planet. Space Sci.* **44**, 937 (1996).
- Isokoski, K., Bossa, J.-B., Triemstra, T., Linnartz, H., *Phys. Chem. Chem. Phys.* **16**, 3456 (2014).
- Jenniskens, P. and Blake, D.F., *Astrophys. J.* **473**, 1104-1113 (1996).
- Jenniskens, P., Barnhak, S.F., Blake, D.F., McCoustra, M.R.S., *J. Chem. Phys.* **107**, 1232 (1997).
- Jewitt, D.C. & Luu, J., *Nature* **432**, 731 (2004).

- Johari, G.P., Hallbrucker, A., Mayer, E., J. Chem. Phys. **95**, 2955 (1991).
- Kondo, T., Kato, H.S., Bonn, M., Kawai, M., J. Chem. Phys. **127**, 094703 (2007).
- Kouchi, A., Kuroda, T., Nature **344**, 134 (1990).
- La Spisa, S., Waldheim, M., Lintemoot, J., Thomas, T., Naff, J., Robinson, M., J. Geophys. Res. **106**, 33351 (2001).
- Leto, G. & Baratta, G.A., A&A **397**, 7 (2003)
- Lofgren, P., Ahlstrom, P., Lausma, J., Kasemo, B., Chakarov, D., Langmuir **19**, 265 (2003).
- Malinowski, E.R. Factor Analysis in Chemistry, Third Edition. Wiley-Interscience, New York, 2002.
- Maté, B., Rodriguez-Lazcano, Y., Jerrero, V.J., Phys. Chem. Chem. Phys. **14**, 10595 (2012).
- Merlin, F. et al., A&A **466**, 1185 (2007).
- Moore, M.H. & Hudson, R.L., Astrophys. J. **401**, 353 (1992).
- Moore, M.H. & Hudson, R.L., Radiat. Phys. Chem. **45**, 5 (1995).
- Porter, S.B., Desch, S.J., Cook, J.C., Icarus **208**, 492 (2010).
- Rao, C.N.R. and Rao, K.J., Phase Transformations in Solids, McGraw-Hill (1985).
- Raut, U., Teolis, B.D., Loeffler, M.J., Vidal, R.A., Famá, M., Baragiola, R.A. J. Chem. Phys. **126**, 244511 (2007a).
- Sack, N.J. and Baragiola, R.A., Phys. Rev. B. **48**, 9973 (1993).
- Safarik, D.J., Meyer, R.J., Mullins, C.B., J. Chem. Phys. **118**, 4660 (2003).
- Sceats, M.G. & Rice, S.A. In: Franks, F. (Eds.), Water, a Comprehensive Treatise, Vol. 7. Plenum, New York (1982).
- Schmelzer, J., Moller, T.J., Slezov, V.V., J. Phys. Chem. Solids **56**, 1013 (1995).
- Schmitt. B., Espinasse, S., Grim, R.G.A., Greenberg, J.M., Klinger, J., Proc. of An International

Workshop on Physics and Mechanics of Cometary Materials, Münster, FRG, 9-11

Oct. 1989.

Schmitt, B., Quirico, E., Trotta, F., Grundy, W.M. In: Schmitt, B., De Bergh, C., Festou, M.

(Eds.), Solar System Ices, Kluwer Academic, Norwell, MA (1998).

Smith, R.S., Matthiesen, J., Knox, J., Kay, B.D., J. Phys. Chem. A. **115**, 5908 (2011).

Tsekouras, A.A., Iedema, M.J., Cowin, J.P., Phys. Rev. Lett. **80**, 5798 (1998).

### 3.2. Porosity-Driven Crystallization Kinetics of Amorphous Solid Water: Implications for Cold Icy Objects in the Outer Solar System

Submitted for publication: *Icarus* (2016).

#### Abstract

We have investigated the effects of porosity on the crystallization kinetics of amorphous solid water (ASW). Porosity in ASW films, condensed from the vapor phase at varying incidence angles at 10 K, was characterized using ultraviolet-visible interferometry and quartz crystal microgravimetry. The films were heated to crystallization temperatures between 130 and 141 K, resulting in partial pore compaction. The isothermal phase transformation was characterized using transmission infrared spectroscopy to monitor the time evolution of the 3.1- $\mu\text{m}$  O-H stretch absorption band. We find that ASW crystallization unfolds in two distinct stages. The first stage, responsible for  $\sim 10\%$  transformation, is initiated from nucleation at the external surface. The dominant second stage begins with nucleation at the internal pore surfaces and completes the transformation of the film at a faster rate compared to the first stage. A key finding is that porosity has major influence on crystallization kinetics; a film with five times higher porosity was observed to crystallize  $\sim 15$  times faster, compared to the less porous counterpart. We extrapolate our results to predict crystallization times for amorphous ices condensed on Europa's surface from plume sources, as recently observed by Hubble Space Telescope.

#### 3.2.1 Introduction

Crystalline ice is pervasive on many cold objects in the Outer Solar System. The near-infrared spectrum of Charon's surface from the 2015 *New Horizons* flyby shows the 1.65- $\mu\text{m}$

absorption band (Cruikshank et al. 2015, Grundy et al. 2016), diagnostic of crystalline ice (Schmitt et al. 1998). Other Kuiper Belt objects (KBOs) or trans-Neptunian objects (TNOs), like Haumea (Merlin et al. 2007) and Quaoar (Jewitt & Lu 2014), are also known to have crystalline ice, despite surface temperatures  $< 50$  K. Crystalline ice is also found on the surfaces of most Jovian and Saturnian satellites (Grundy et al. 1999), where temperatures are usually less than 130 K.

The presence of crystalline ice on these cold objects is puzzling, since laboratory studies show that ice films condensed from vapor at temperatures  $< 130$  K results only in the amorphous phase (Sceats & Rice 1982). Amorphous ice can form on the surfaces of cold astronomical objects from either condensation of sputtered molecules or vapor from plume sources, as observed on Enceladus (Hansen et al. 2006, Waite et al. 2006) and Europa (Roth et al. 2014a), returning in gravitationally-determined trajectories. Since amorphous ice is metastable, it will transform to the thermodynamically-stable cubic crystalline phase at a temperature-dependent rate. However, the transformation is extremely slow at colder temperatures, likely requiring  $\sim 10$  million years at 80 K (Baragiola 2003). Furthermore, the icy surfaces are continually bombarded by energetic particles and photon irradiation. Laboratory studies have shown that such energetic irradiation can amorphize crystalline ice, and more efficiently below 80 K, thereby reversing any thermally-driven crystallization on the cold surfaces of satellites and TNOs (Baratta et al. 1991, Moore & Hudson 1992, Kouchi & Kuroda 1990, Strazzulla et al. 1992, Leto & Baratta 2003, Famá et al. 2010).

A salient feature of vapor-deposited ASW films is its porosity, which increases with incidence of the vapor flux (Stevenson et al. 1999) and is known to affect other properties of amorphous ice such as gas retention capacity, mechanical strength, and thermal conductivity,

among others (Baragiola 2003). Irradiating ice films with energetic particles reduces the porosity, i.e. compaction (Raut et al. 2007a, 2008), as does thermal heating (Johari et al. 1991, Giering & Haarer 1996, Tsekouras et al. 1998, Bossa et al. 2012, Isokoski et al. 2014). Whether porosity can alter the crystallization kinetics of ASW films remains an open question, although such effects have been observed in other solids such as zeolites (Frances & O'Hare 1998) and titania (Kirsch et al. 2004).

Previous studies have shown that crystallization is initiated at the external surface of a thin non-porous film, where the nucleation barrier is reduced (Lofgren et al. 1996, Backus et al. 2004). This was attributed to the presence of surficial water molecules that can be easily rearranged into ordered, crystalline nuclei, compared to the tetrahedrally-bonded bulk molecules. Since porous ice films present large internal surface area,  $\sim$ hundreds of  $\text{m}^2 \text{g}^{-1}$ , they largely exceed non-porous films in the number of possible nucleation sites. Therefore, porosity is expected to enhance crystallization rates in ASW films. However, crystallization times in porous ASW and compact hyperquenched ice films showed no significant difference, despite seven-fold difference in surface area (Maté et al. 2012). Additionally, the onset site of crystallization in ASW films is still debated, with other studies reporting that formation of crystalline nuclei is more favored in the bulk rather than at the surfaces (Rowland et al. 1995, Buch et al. 1996, Kondo et al. 2007)

Here, we report on isothermal crystallization of vapor-deposited amorphous solid water with varying porosities over 130 – 141 K. The porosity of the ASW films is controlled at growth by changing the deposition incidence angle of the water vapor flux. We measure the dependence of crystallization rates and activation energy on porosity. We then extrapolate our results to

lower temperatures to predict porosity-dependent crystallization times on cold extraterrestrial surfaces.

### 3.2.2 Experimental Methods

The experiments were performed in an ultra-high vacuum (UHV) chamber cryopumped to a base pressure of  $\sim 10^{-10}$  Torr. Water ice films were vapor-deposited onto a CsI substrate cooled to 10 K by a two-stage Janis RDK-205E closed-cycle refrigerator; these growth conditions result in microporous ASW (Sceats & Rice 1982). An alkali halide substrate, as used in this work, makes optical analysis simpler since interference effects are minor in transmission compared to reflectance geometry (Teolis et al. 2007). Furthermore, an insulator substrate is an improved analog of icy satellite surfaces over metallic substrates previously used in several other studies (Dohnálek et al. 2000, Sack & Baragiola 1993, Lofgren et al. 2003, Safarik et al. 2003, Smith et al. 2011).

The deposition angle of the collimated vapor flux from a micro-capillary array (MCA) doser was varied from  $0^\circ$  to  $70^\circ$  with respect to the normal. In some instances, ice films were deposited from an omnidirectional vapor source. Films deposited from collimated fluxes will henceforth be referred to by their deposition angles (for instance, a  $45^\circ$  film) and the omnidirectionally-deposited films will be referred to as background-deposited ice (BDI). To prevent accumulation of ice on both sides of the CsI substrate, the side facing away from the doser was fitted with a cooled hollow shielding tube that blocks  $\sim 97\%$  of the water vapor flux from reaching the rear of the CsI substrate, while still allowing optical transmission.

The ice density  $\rho$  was calculated from the ratio of  $\eta$  to  $d$ , where  $\eta$  is the column density of the ice film deposited on the CsI substrate and  $d$  is the film thickness. To estimate  $\eta$  on the CsI

substrate, we performed a separate calibration experiment using a piezoelectric quartz crystal microbalance (QCM), mounted 25.4 mm above the CsI substrate in the cryogenically-cooled sample holder. The QCM is highly sensitive, able to detect accretion of  $\sim 0.1$  H<sub>2</sub>O ML (1 ML =  $10^{15}$  molecules cm<sup>-2</sup>, about a monolayer).

We began the calibration experiment by measuring the deposition rate  $R_{\text{QCM}}$  with the MCA doser and the QCM on the same vertical plane. The sample holder was then vertically translated with respect to the MCA doser, and we monitored the change in deposition rate measured by the QCM until the doser was facing the CsI substrate. The collimation of the water vapor flux effusing from the MCA doser has a forward cosine distribution (Winkler & Yates 1988), and the QCM thus intercepts a fraction of the vapor flux directed toward the CsI substrate,  $\sim 20\%$  in our setup. The deposition rate measured by the QCM when the doser is positioned to face the CsI substrate is denoted  $R_{\text{CsI}}$ , and it is related to  $R_{\text{QCM}}$  by  $\alpha = R_{\text{QCM}}/R_{\text{CsI}}$ .

We ensure that the H<sub>2</sub>O pressure, measured with a nude ionization gauge, is kept constant to within  $\sim 10\%$  during the vertical translation. We also assumed the sticking coefficient of water molecules impinging on the QCM and CsI substrates to be  $\sim 1$  at 10 K.

In subsequent experiments with the water vapor flux directed toward the CsI substrate for time  $t$ , we measure  $R_{\text{CsI}}$  in real-time and determine  $\eta$  using

$$\eta = R_{\text{CsI}} \times t \times \alpha . \quad (1)$$

The film thickness  $d$  was derived by fitting the Fresnel equations to the interference pattern in the optical transmission in the ultraviolet (UV)-visible range (Westley et al. 1998, Heavens 1991, Raut et al. 2008). Using  $0.94 \text{ g cm}^{-3}$  for the density of compact ice  $\rho_c$  (Narten et al. 1976), we obtained the porosity ( $\Phi = 1 - \rho/\rho_c$ ) of the ice films. Our method for estimating  $\eta$



from QCM calibration experiments yielded errors in  $\Phi$  of  $\pm 0.03$  for all  $\text{H}_2\text{O}$  incidence angles, larger than the  $\pm 0.01$  error inherent in the calculation of  $d$  from the fit of the interference pattern.

The films were also characterized by transmission Fourier transform infrared spectrometry (FTIR) at  $2\text{ cm}^{-1}$  resolution using a Thermo Nicolet Nexus 670 spectrometer thoroughly purged with dry air. The spectra  $T$  of the films were divided by the transmission spectrum  $T_0$  of the bare CsI window and then converted to optical depth,  $-\ln(T/T_0)$ . In particular, we focused on the changes of the O-H-stretch absorption band ( $3.1\text{ }\mu\text{m}$ ) and the O-H dangling bond (DB) absorption features at  $\sim 2.7\text{ }\mu\text{m}$ , due to heating and isothermal annealing at higher temperatures.

### 3.2.3 Results

#### *I. Porosity in ASW films*

Figure 3.2.1A shows infrared absorption spectra in the region of the dangling O-H bands ( $\sim 2.7\text{ }\mu\text{m}$ ) of ice films deposited at 10 K at different incidences. The absorption features, DB1 ( $3.06\text{ }\mu\text{m}$ ) and DB2 ( $2.71\text{ }\mu\text{m}$ ), are assigned to O-H vibrations of doubly- and triply-coordinated surface water molecules, respectively (Rowland & Devlin 1991), and are diagnostic of pore-related internal surface area (Devlin & Buch 1995, Raut et al. 2007b). Figure 3.2.1B shows transmittance spectra (black curves) of ice films deposited at 10 K at  $0^\circ$ ,  $45^\circ$ , and  $70^\circ$  incidences, together with fits (red curves) to the Fresnel equations (Heavens 1991). The oscillating pattern in the spectra is due to optical interference between directly transmitted light and light transmitted following multiple reflections at different interfaces. The ice layer serves as an anti-reflection coating, increasing the transmitted light intensity compared to that of the bare CsI substrate, i.e.  $T > 1$ . The film thickness  $d$  obtained from the fits, together with column density  $\eta$  determined

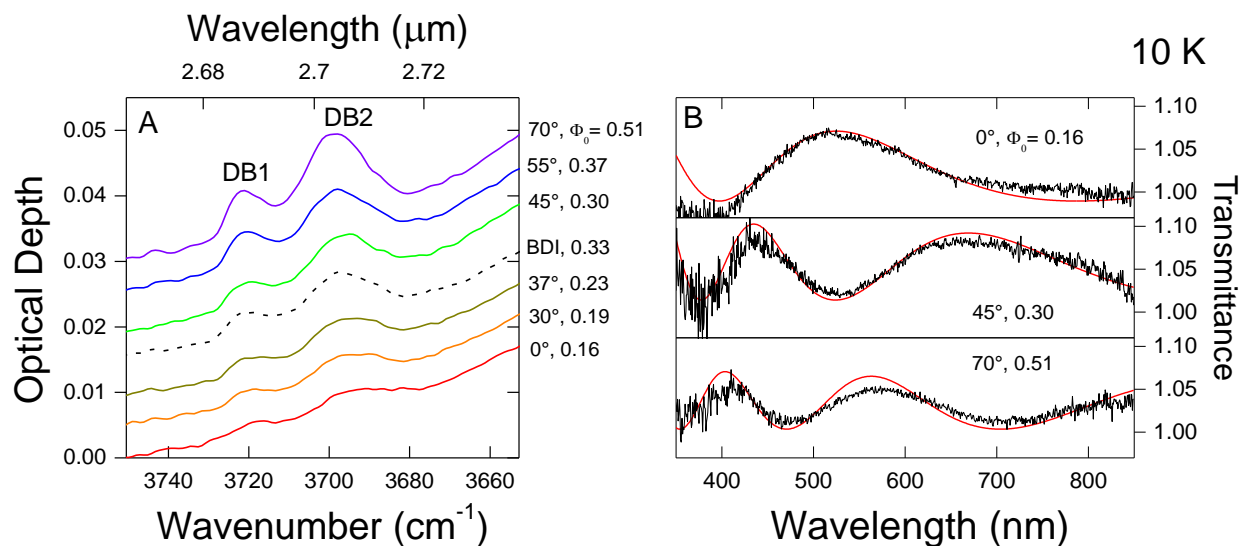


Figure 3.2.1 – (A) Infrared spectra showing dangling bond (DB1, DB2) absorptions in ~1000 ML-thick water ice films vapor-deposited onto CsI substrate at varying incidences at 10 K. The dangling bonds are diagnostic of porosity  $\Phi$ , which increases with incidence of the collimated water vapor flux. Spectra are labeled with deposition angle and the film porosities  $\Phi_0$  following deposition, and have been vertically shifted for clarity. The dashed spectrum labeled BDI is for a background-deposited film condensed from a diffuse, omnidirectional flux. (B) UV-visible transmittance spectra of the films deposited at 0, 45, and 70°. Red lines are synthetic spectra generated using Fresnel's equations to match the experimental spectra, to obtain the refractive index and the thickness of the films. Together with the ice column density ( $\sim 1000 \pm 30$  ML) constrained using a quartz crystal microbalance in close proximity of the CsI substrate, we obtain the initial porosities  $\Phi_0$ .

from the microbalance calibration experiment, gives the initial ice porosity  $\Phi_0$ . We have also included an infrared spectrum of a BDI film in Figure 3.2.1A. We find that BDI and  $45^\circ$  films have, within errors, similar integrated DB absorption band area ( $0.24 \pm 0.01 \text{ cm}^{-1}$ ) and porosity ( $0.30 \pm 0.03$ ). The dangling bond absorptions are larger in ice films with higher  $\Phi_0$ , resulting from deposition at higher incidences.

## II. *Thermal Compaction*

Figure 3.2.2A shows changes in the infrared absorption spectrum in the region of the  $3.1\text{-}\mu\text{m}$  O-H-stretch band of a  $45^\circ$  ice film during heating to 136 K at  $1 \text{ K min}^{-1}$  following deposition at 10 K. Heating the film results in narrowing and sharpening of the broad absorption and a  $\sim 35\text{-cm}^{-1}$  redshift in peak position. The inset shows disappearance of the DB absorption features with increasing temperature.

The film porosity and DB band areas have different dependences on temperature, as shown in Figure 3.2.2B, where the porosity and band areas have been normalized to their initial values. Heating the ice film to 136 K reduces the porosity by 40%, from 0.30 to 0.18, which is consistent with a previous report of  $\sim 12\%$  reduction in film thickness observed during heating of ice film to 120 K (Bossa et al. 2012). In contrast to the porosity, the DB2 band area is reduced to 90% of its initial value, while DB1 disappears by 75 K.

Figure 3.2.3 shows reduction in porosity during  $1 \text{ K min}^{-1}$  heating of ice films deposited at 0 to  $70^\circ$ . The average thermal compaction rate, defined as  $(d\Phi/dT) \times (dT/dt)$ , is  $1.6 (\pm 0.2) \times 10^{-5} \text{ s}^{-1}$ , independent of initial porosity. Above  $\sim 120 \text{ K}$ , the compaction rate decreases  $\sim$ three-fold despite continual heating. Films deposited at incidences  $\leq 45^\circ$  show larger reduction in porosity,

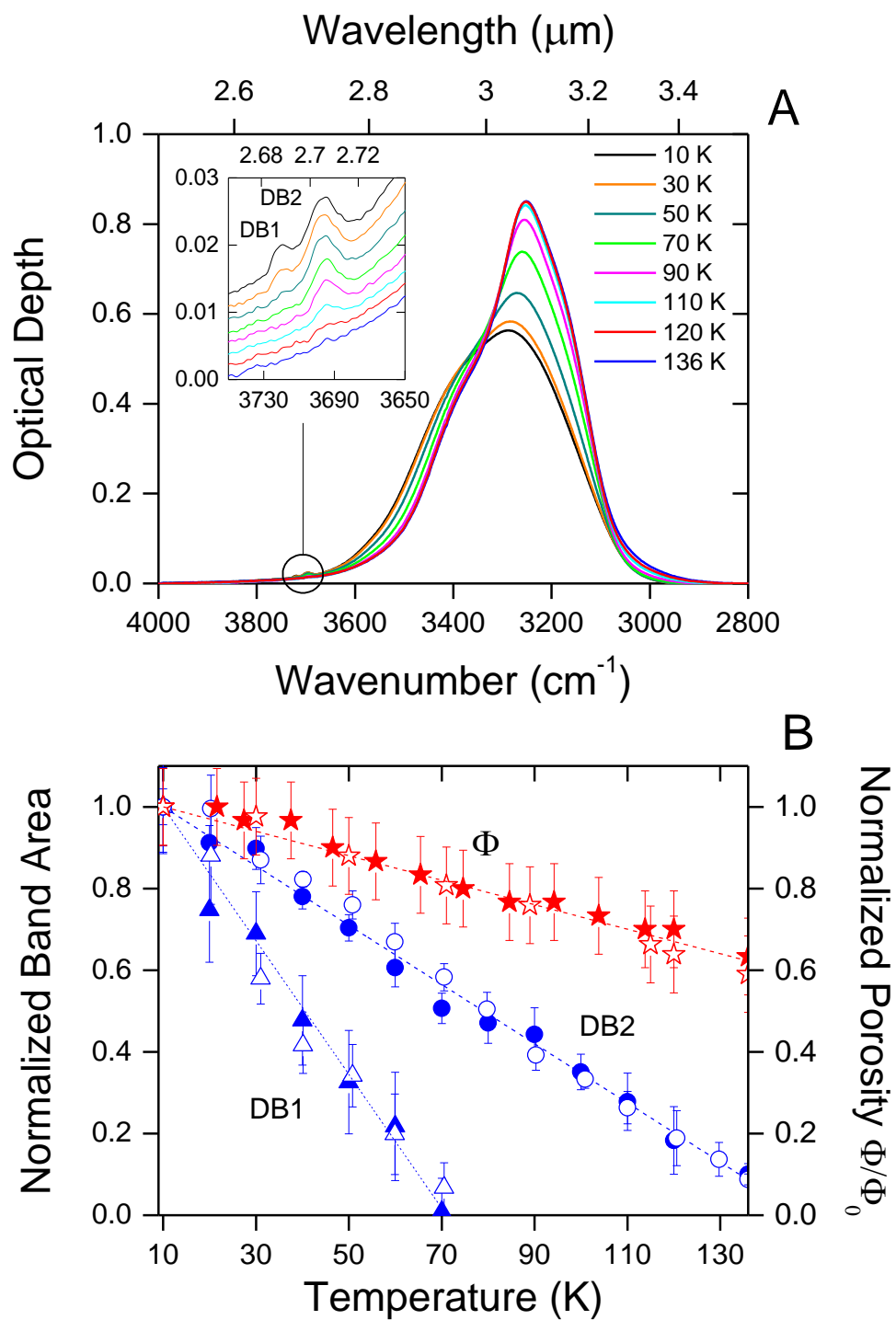


Figure 3.2.2 – A) Changes in optical depth in the region of the 3.1- $\mu\text{m}$  O-H-stretch absorption band during heating of the  $\sim 980$  ML-thick ice film from 10 to 136 K at  $1 \text{ K min}^{-1}$ . The film, deposited at 10 K at  $45^\circ$  incidence, developed an initial porosity  $\Phi_0$  of  $0.30 (\pm 0.03)$ . Inset shows decrease in dangling bond absorptions (DB1 and DB2) during heating. B) Decrease in ice porosities and DB1 and DB2 band areas of two  $45^\circ$  films (different symbols for different experiments), following subtraction of polynomial fitted to the continuum baseline. Both band areas and ice porosities have been normalized to their initial values at 10 K. We note only a  $\sim 40\%$  reduction in porosity by 136 K, compared to near-complete disappearance of DB2. The DB1 band area decreases at an even faster rate, disappearing by 75 K. Dotted lines are guides to the eye.

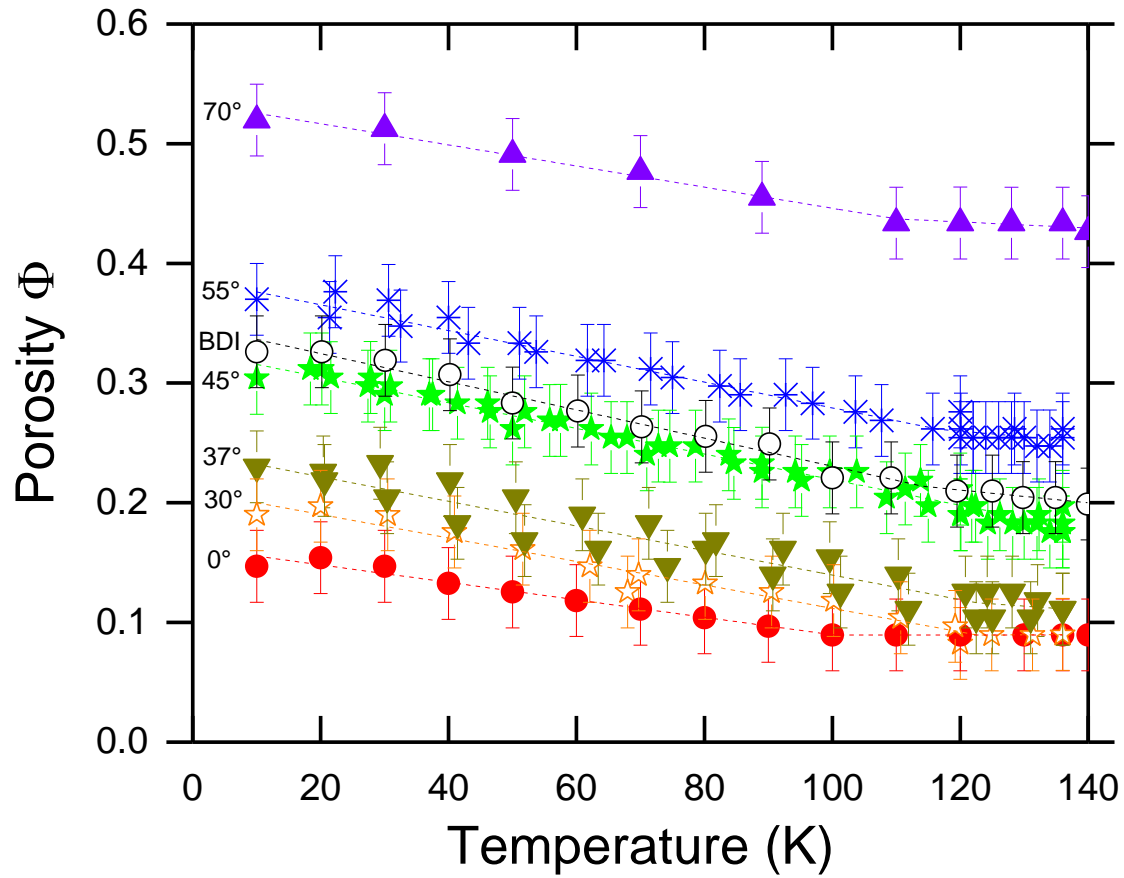


Figure 3.2.3 – Decrease in porosity  $\Phi$  during  $1 \text{ K min}^{-1}$  heating of ice films following deposition at various incidences (shown left of the data) at 10 K. We measure a thermal compaction rate of  $1.6 (\pm 0.2) \times 10^{-5} \text{ s}^{-1}$ , independent of initial porosity. The compaction rate decreases  $\sim$ three-fold above 120 K despite continual heating. Dashed lines are guides to the eye.

~30-50%, compared to films deposited at higher incidences that compact less, ~15%. At larger incidence angles the films develop larger mesopores, which resist thermal compaction (Raut et al. 2007b). We note that thermally-processed ice films can retain porosity while lacking dangling bonds, in agreement with previous studies (Raut et al. 2007b, Bossa et al. 2012, Isokoski et al. 2014) and similar to irradiation-processed ices (Raut et al. 2007a). Hence, absence of dangling bond features in infrared spectra of astronomical ices, processed thermally or irradiated, does not imply a fully compacted film.

### *III. Crystallization Kinetics*

Figure 3.2.4A shows the time-dependent evolution of the O-H stretch absorption band of a film with  $\Phi = 0.18$  ( $45^\circ$ ) during isothermal annealing at 136 K. In agreement with previous reports (Bertie et al. 1969, Hagen et al. 1981), we note further sharpening of the  $3.1\text{-}\mu\text{m}$  band with the appearance of a triplet structure and additional redshift in peak position as the ice gradually transitions from the pure amorphous phase (spectrum  $T_A$ , red) to the cubic crystalline phase ( $T_C$ , blue). Spectrum  $T_C$  was collected after 116 minutes elapsed at 136 K; subsequent spectra ceased to change, indicating completion of crystallization.

Estimates of the crystalline and amorphous components of a partially crystallized film  $T$  (green spectra, 20 minutes annealing time) is made using factor analysis technique (Malinowski 2002, Famá et al. 2010, Smith et al. 2011), which involves fitting experimental spectrum  $T$  with a synthetic spectrum  $S$  generated as

$$S = \phi_A T_A + \phi_C T_C \quad (2)$$

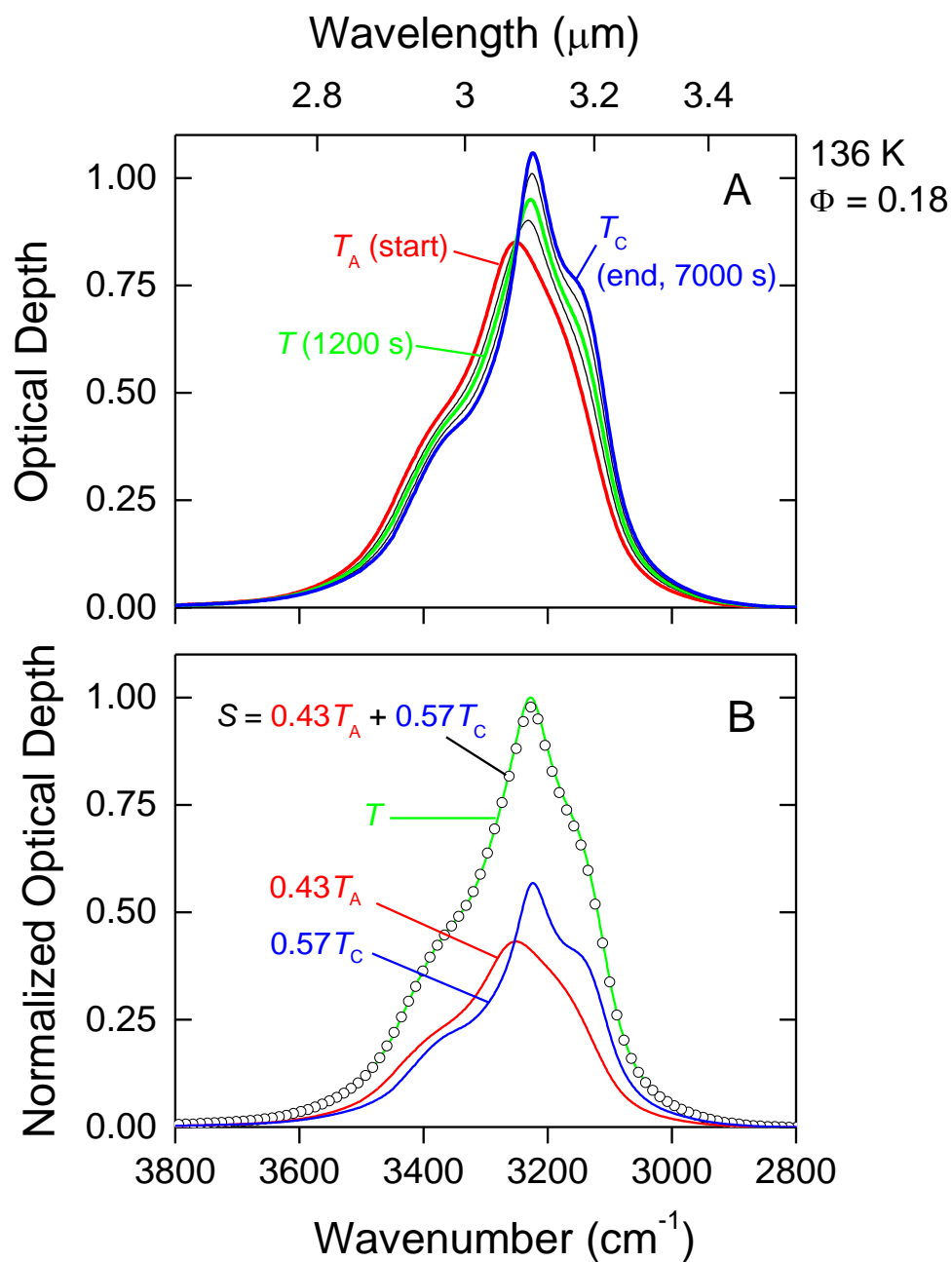


Figure 3.2.4 – A) Changes in O-H-stretch absorption band due to isothermal crystallization of a ~980 ML-thick  $\text{H}_2\text{O}$  ice film at 136 K. Film was deposited at  $45^\circ$  at 10 K, resulting in an initial



porosity of  $0.30 (\pm 0.03)$ , and heated to 136 K at  $1 \text{ K min}^{-1}$ . The ice was partially compacted during heating, retaining a porosity of  $0.18 (\pm 0.03)$  at 136 K. The transition from amorphous phase (transmittance spectrum  $T_A$ ) to crystalline phase (spectrum  $T_C$ ) is assumed complete at 7000 s or  $\sim 2$  h. The intermediate spectra labeled ( $T$ , 1200 s) has both amorphous and crystalline components, which are deconvoluted by fitting  $T$  with a synthetic spectra  $S$  generated by summing the estimated amorphous and crystalline contributions,  $\phi_A T_A = 0.43 T_A$  and  $\phi_C = 0.57 T_C$  (Eq. 2 in the text).

where  $\phi_A$  and  $\phi_C$  are the amorphous and crystalline fractions such that  $\phi_A + \phi_C = 1$ . Figure 3.2.4B shows that a synthetic spectrum (open circles) with 57% crystalline ice yields the best match to experimental spectrum  $T$ . This process is applied to all intermediate spectra to estimate the crystalline fraction as a function of isothermal annealing time. We note that porosity continues to decrease further by  $\sim 8\%$  while the ice crystallizes during annealing. The changes in the O-H stretch band (Figure 3.2.4A) are not due to this small reduction in porosity, but are driven by crystallization.

Figure 3.2.5A shows the time evolution of  $\phi_A$  for ices with different porosities  $\Phi$  retained after heating to 136 K. Films with higher porosities crystallize faster than less porous films. The time required for  $\phi_A$  to decrease to  $1/e$  of its initial value (indicated by the dashed line in 5A), hereafter designated  $\tau_c$ , is plotted against  $\Phi$  in Figure 3.2.5B. A five-fold increase in ice porosity reduces  $\tau_c$  by a factor of  $\sim 15$ . The BDI film crystallized at a rate nearly identical to the  $45^\circ$  film, since they have similar porosities.

Crystallization proceeds with the nucleation of microscopic crystallites and their subsequent growth in amorphous solids. The kinetics are described by the Avrami equation (Rao & Rao 1978, Doremus 1985), where the evolution of the crystalline fraction  $\phi_C$  after time  $t$  is given by

$$\phi_C = 1 - \exp(-Kt^n). \quad (3)$$

In Equation 3,  $K$  is a temperature-dependent crystallization rate constant and  $n$  is the Avrami exponent related to the nucleation and crystallization mechanism. For instance,  $n = 4$  corresponds to spatially random, continuous nucleation and growth of spherical crystallites, while values of 3 and 2 imply nucleation/growth of disc and rod-shaped nuclei, respectively.

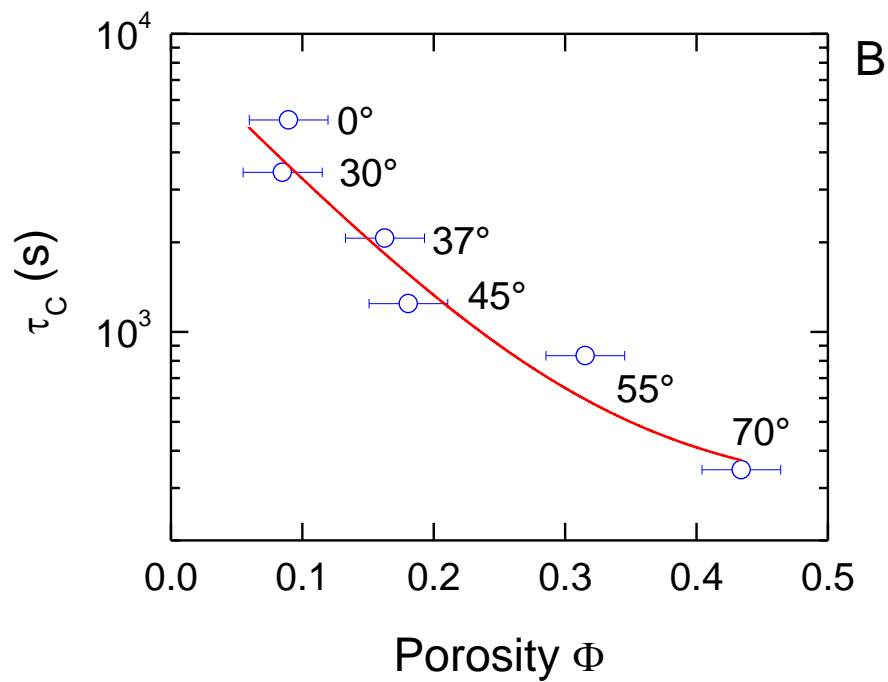
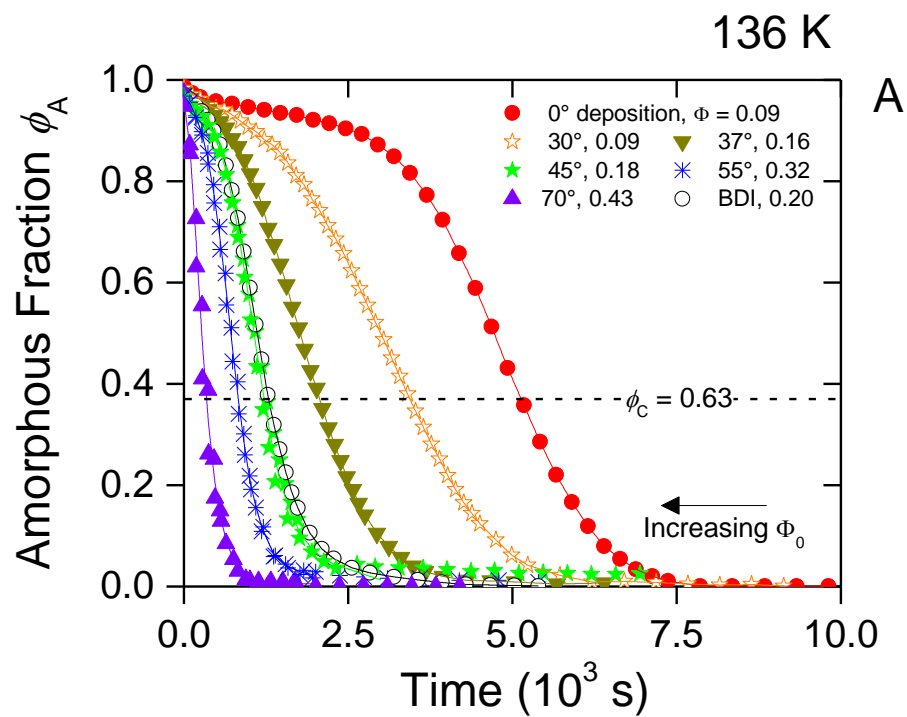


Figure 3.2.5 – A) Decrease in the amorphous fraction  $\phi_A$  during isothermal crystallization at 136 K. Ice films were deposited at 10 K at angles ranging from 0 to 70°, as well as background-deposited ice (BDI), and heated to 136 K at 1 K min<sup>-1</sup>. The amorphous fractions were obtained from deconvolution of the 3.1- $\mu$ m absorption band (Figure 3.2.3), discussed in the text. Lines are to guide the eye. B) Time required for 63% crystallization,  $\tau_c$ , as function of ice porosity  $\Phi$  at 136 K. Ice films with higher porosity have shorter  $\tau_c$ , crystallizing at higher rates. Lines are to guide the eye.

Values of  $n$  that are less than 1, exceed 4, or are non-integers imply a more complicated nucleation/crystallization process (Rao & Rao 1978, Doremus 1985).

The Avrami equation can be rearranged as

$$\ln(-\ln[1 - \phi_c]) = \ln K + n \ln t \quad (4)$$

such that the double logarithmic term has a linear dependence on  $\ln(t)$ . Figure 3.2.6 shows the fit of Equation 4 to the crystallization kinetics data shown in Figure 3.2.5A. The slope of the linear fit gives the value of the Avrami exponent, while the crystallization rate constant is extracted from the intercept of the fit.

We observe two linear regimes in Figure 3.2.6, implying that ASW crystallization unfolds in two distinct stages. About  $\sim 10\%$  of the ASW films is crystallized during the first stage, characterized by Avrami  $n_1 \sim 0.4 - 0.7$  and crystallization rates  $K_1^{1/n_1} \sim 0.5 - 100 \times 10^{-6} \text{ s}^{-1}$ , both increasing with  $\Phi$ . The transformation proceeds at higher rates  $K_2^{1/n_2} \sim 2 - 30 \times 10^{-4} \text{ s}^{-1}$  in the second stage, crystallizing the rest of the film. We find that  $K_2^{1/n_2}$  increases with porosity, while the second-stage Avrami exponent  $n_2 \sim 4 - 1.5$  decreases with increasing  $\Phi$ . For  $70^\circ$  ice, we only discern the second crystallization stage.

Additional measurements of isothermal crystallization were performed over 130-141 K for ice films of porosity  $\Phi = 0.09$  ( $0^\circ$  ice), 0.18 ( $45^\circ$ ), and 0.43 ( $70^\circ$ ). The kinetics data at different temperatures were fitted with Equation 4 to obtain  $n$  and  $K$  for the two crystallization stages. The rate constant is known to have an Arrhenius-type temperature dependence (Hage et al. 1994):

$$K^{1/n} = K_0^{1/n} \exp(-\Delta H/RT) \quad (5)$$

where  $K_0^{1/n}$  is a pre-exponential factor and  $\Delta H$  is the crystallization activation energy.

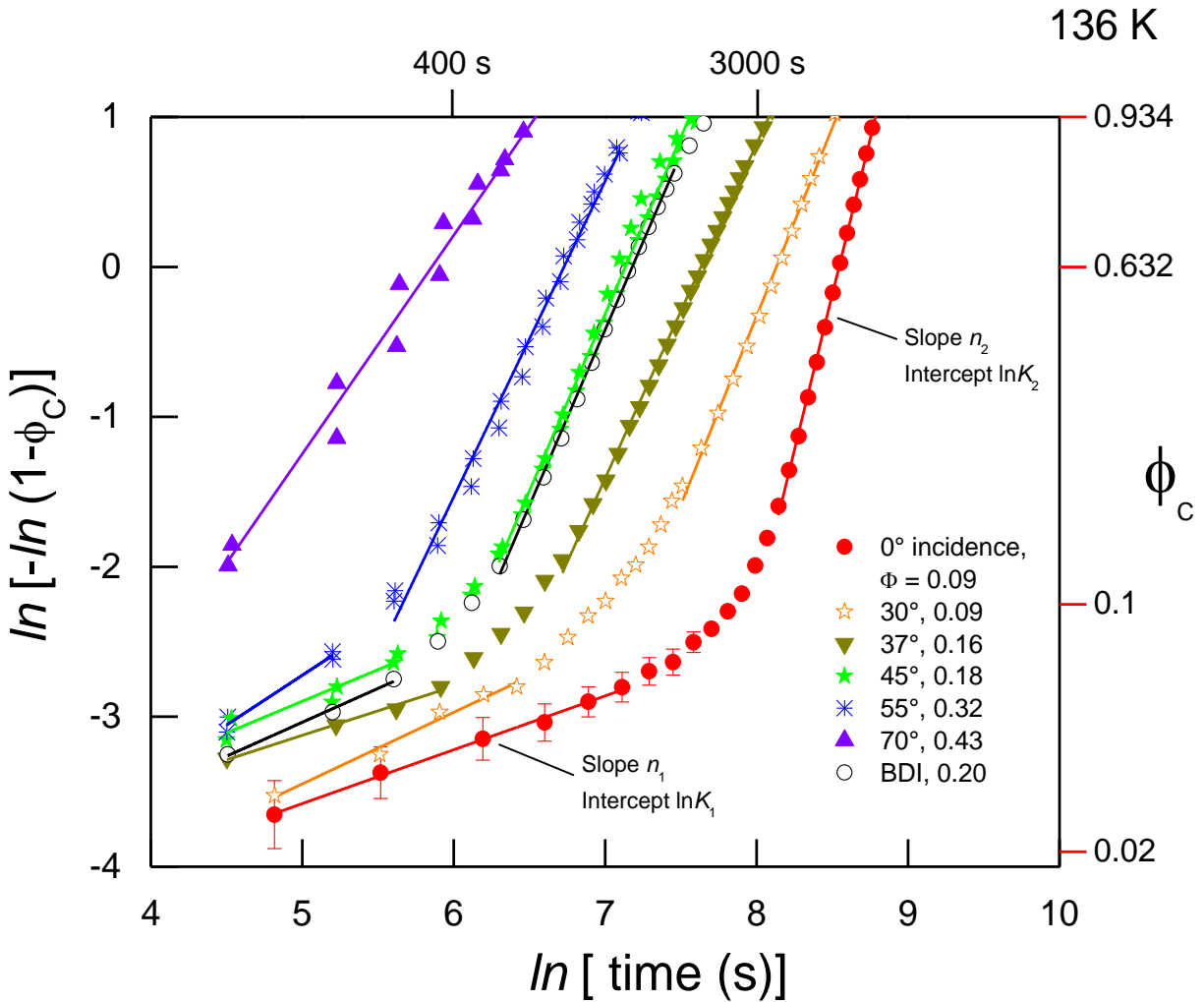


Figure 3.2.6 – Double natural logarithm representation of Fig. 3.2.5A shows that crystallization of amorphous ice films unfolds in two distinct kinetic stages. The slopes and intercepts of the linear fits (solid lines as per Eq. 4) give Avrami parameters  $n$  and  $K$ , respectively, for each crystallization stage. Only  $\sim 10\%$  of the ice is crystallized during the first stage. The second stage proceeds faster than the first stage, resulting in near-complete crystallization of the ice films.

In Figure 3.2.7, we plot  $\ln(K_2^{1/n2})$  against inverse temperature for ice films with different porosities. The porosities retained after heating to 130 K are within  $\sim 4\%$  of that for ice deposited at the same incidence angle and heated to 141 K. Here we focus on the second stage because it crystallizes  $\sim 90\%$  of the film and proceeds  $> 100$  times faster than the first stage, thus dominating the crystallization process. We observe that the second-stage crystallization rate constant increases with temperature for ices of all three porosities. Furthermore,  $K_2^{1/n2}$  increases with porosity over the temperature range studied. The crystallization activation energy  $\Delta H$  is deduced from the slope of the fits of Equation 5. We find  $\Delta H = 64 \pm 3 \text{ kJ mol}^{-1}$  for low-porosity ice, similar to several previous measurements (Dowell and Rinfret 1960, Hage et al. 1995, Jenniskens & Blake 1996, Dohnálek et al. 2000, Lofgren et al. 2003, Smith et al. 2011). Ice films with higher porosity have slightly smaller energy barrier to crystallization,  $\Delta H \sim 60 \pm 3 \text{ kJ mol}^{-1}$ .

### 3.2.4 Discussion

The strong inverse dependence of  $\tau_c$  on porosity (Figure 3.2.5B) implies that the internal surfaces of porous ices are key to the crystallization process. These findings are in agreement with reports of Backus et al. (2004), who performed experiments that selectively probed crystallization at three locations of the ASW films: the vacuum-ice interface, bulk, and substrate-ice interface. They showed that crystallization is initiated the external surface and progresses sequentially to the bulk and the substrate-ice interface in the case of nonporous, thin ice films (45 ML).

Crystallization occurs from the formation and growth of crystalline nuclei within the amorphous ice. The driver of nucleation is the negative net free energy resulting from the growth of the more thermodynamically-stable phase. Nucleation is countered, however, by the increase

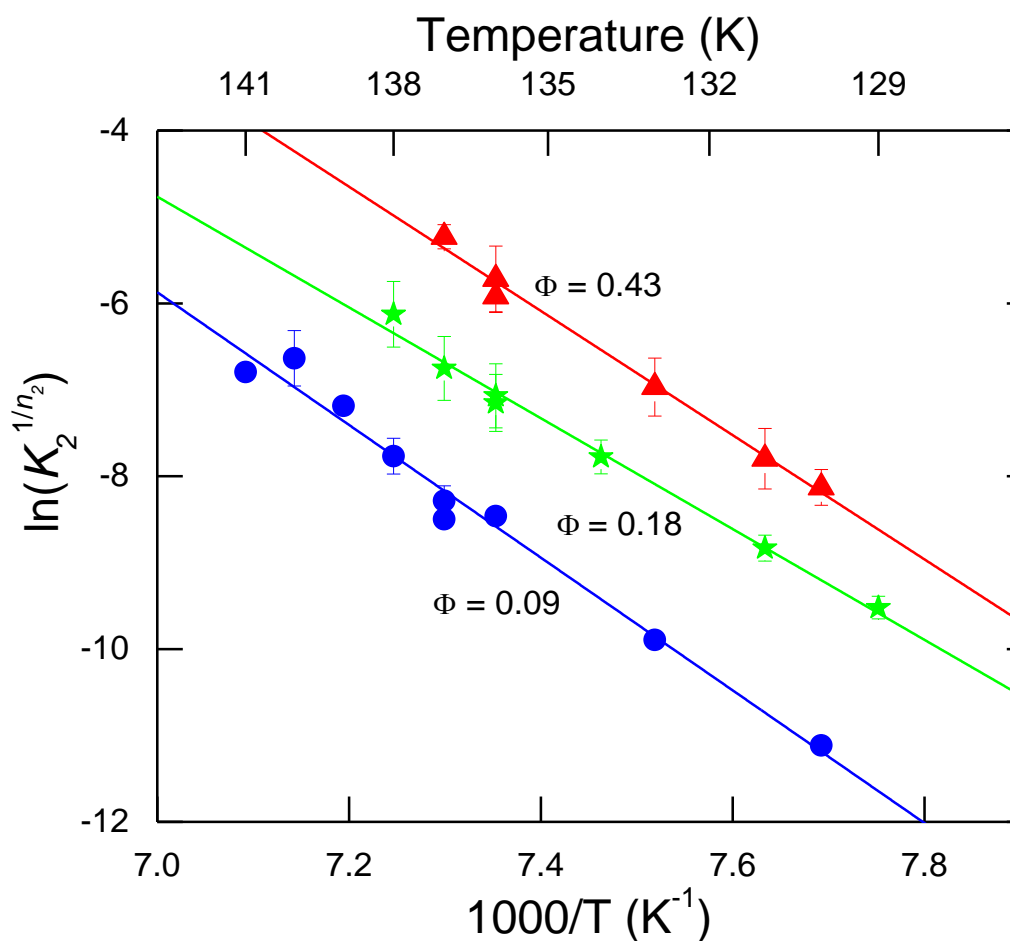


Figure 3.2.7 – Temperature dependence of second-stage crystallization rate  $K_2^{1/n_2}$  for ice films with different porosities,  $\Phi = 0.09$  ( $0^\circ$  ice, circles),  $0.18$  ( $45^\circ$ , stars) and  $0.43$  ( $70^\circ$ , triangles).

Avrami fits (solid lines) to the data give an average heat of crystallization  $\Delta H$  and  $K_{2_0}^{1/n_2}$  for each  $\Phi$  (Eq. 5). We measure  $\Delta H \sim 64 \pm 3 \text{ kJ mol}^{-1}$  for low-porosity ice ( $\Phi = 0.09$ ,  $0^\circ$ ), and  $\Delta H \sim 60 \pm 3 \text{ kJ mol}^{-1}$  for ices of higher porosity.



in interfacial energy due to the differing structure between the two phases (Gibbs 1928, Volmer & Weber 1926). A second opposing factor is the difference in local density between the two phases, although this is very slight for amorphous ( $\sim 0.94 \text{ g cm}^{-3}$ ) and cubic crystalline ice ( $\sim 0.93 \text{ g cm}^{-3}$ ) (Baragiola 2003, Ghormley & Hochanadel 1971, Narten et al. 1976, Berland et al. 1995).

Nucleation can be either heterogeneous, i.e. at an interface or impurity within the ice, or homogeneous, within structurally perfect regions of the ice bulk. The energy barrier for heterogeneous nucleation is significantly lower than that for homogeneous nucleation because the surfaces provide a portion of the interfacial energy required for nucleation to proceed (Gibbs 1928, Volmer & Weber 1926). Due to the large interfacial surface area of our ice films, both at the external surfaces and at the surfaces of the pores, we thus assume that the growth of the crystalline phase within the amorphous ice is driven entirely by heterogeneous nucleation.

Among the available interfaces at which crystalline nuclei can form, the external surfaces are the most energetically favorable because capillarity effects tend to raise the energy barrier for nucleation on curved surfaces, such as pore sites, relative to flatter surfaces (Hillert & Aaronson 1975). We therefore suggest that the first crystallization stage is due to heterogeneous nucleation and subsequent crystalline growth at these flatter external surfaces. We cannot differentiate between the ice-vacuum and the ice-substrate interfaces with our experiments, although Backus et al. (2004) have demonstrated that crystallization begins at the ice-vacuum interface. This initial crystallization stage could also include nucleation at side surfaces of the film. Our finding of  $n_1 < 1$  could imply instantaneous nucleation and restricted crystalline growth in one dimension (Rao & Rao 1978, Doremus 1985), consistent with crystallization along the external ice surfaces. We find that this stage of crystallization ends after the ice reaches  $\phi_C \sim 0.10$ , implying saturation of nucleation at the external surfaces.

We suggest that the second, more dominant crystallization stage is due to nucleation in the interior of the ice, at the surfaces of the pores. With micropore diameters  $< 2$  nm (Mayer & Pletzer 1986), the small radius of curvature of these interfaces raises the energy barrier for nucleation relative to the external surfaces (Hillert & Aaronson 1975), although nucleation at these sites is still significantly lower in energy than homogeneous nucleation. Crystallization at these high-curvature internal surfaces results in a second, distinctive crystallization regime, driving the crystallization of the rest of the ice film. Although ice porosity decreases after deposition during heating to crystallization temperatures of 130 – 141 K, we measure residual porosities of 0.09 – 0.43 ( $\pm 0.03$ ) at these temperatures, providing interfacial surface area that facilitates nucleation in the interior of the ice. We find decreasing  $\tau_c$  with increasing  $\Phi$ , consistent with more efficient nucleation in ices that are higher in internal interfacial area.

Ices with mesopores that resist thermal compaction (Raut et al. 2007b) may have a lower energy barrier to pore nucleation relative to microporous ices. Increasing pore size, and thus decreasing surficial curvature, could reduce the capillarity effects that counter nucleation at the surfaces of comparatively smaller pores, since the energy barrier for nucleation on a surface decreases with increasing radius of curvature (Hillert & Aaronson 1975). Although little is known about the shape and structure of ice pores, gas adsorption studies have suggested that mesopores can measure  $\sim 2 - 50$  nm in width (Raut et al. 2007b, Rouquerol et al. 1999) and ballistic deposition simulations have shown increased pore size at larger vapor deposition angles due to enhanced shadowing of incident molecules by protruding surface structures (Kimmel 2001a, b). For mesoporous ices deposited  $> 45^\circ$ , reduced pore curvature may decrease the energy barrier to nucleation, blurring the distinction between the first and second stages of

crystallization. This could explain why we distinguish only one crystallization stage for 70° ice (see Figure 3.2.6).

The Avrami exponent of the second crystallization stage is dependent on porosity, with  $n_2 \sim 4$  for an ice film with  $\Phi = 0.09$  (0°), decreasing with  $\Phi$  to  $n_2 \sim 1.5$  for a film with ~five-fold higher porosity (70°). Using the typical interpretation of the Avrami exponent, this corresponds to continuous nucleation with spherical crystalline growth for low-porosity ice, with more inhibited disc- or rod-like growth geometry for highly porous ices. A few other studies (Hage et al. 1994, Jenniskens & Blake 1996) have reported two-stage crystallization processes, with Avrami exponents  $n_1 \sim 2$  to 2.5 and  $n_2 \sim 0.8$  to 0.9 for what they attributed to be induction and steady-state crystallization regimes, respectively.

Previous studies of ASW crystallization have focused on nonporous ices (Hage et al. 1995, Dohnálek et al. 2000, Lofgren et al. 1996 & 2003, Safarik et al. 2003, Smith et al. 1996 & 2011), but as we show, even films deposited at normal incidence have residual porosity at laboratory crystallization temperatures, and these internal interfaces as well as impurities within the film can serve as nucleation sites that propagate growth of the crystalline phase. Our experiments on semi-compacted porous ices, which are likely more representative of astronomical ices, reveal the dramatic effect of surface-driven crystallization. Ices of higher porosity have significantly reduced crystallization times compared to low-porosity ices.

From Equations 3 and 5, the time required to achieve 63% crystallization time  $\tau_c$  is given by

$$\tau_c = K_{20}^{-1/n_2} \exp(\Delta H/RT) \quad (6)$$

Here, as a simplification, we assume the crystallization unfolds at rate  $K_2^{1/n_2}$ , ignoring the first-phase rate that governs the crystallization of only ~10% of the film. These  $\tau_c$  are plotted as a

function of isothermal crystallization temperature in Figure 3.2.8 for ices of porosity  $\Phi = 0.09$  ( $0^\circ$  ice, circles), 0.18 ( $45^\circ$ , stars), and 0.43 ( $70^\circ$ , triangles), with solid lines extrapolating  $\tau_c$  to lower temperatures, relevant to Jovian moons, using Equation 6 and measured values of  $\Delta H$  and  $K_{20}^{1/n_2}$  for each  $\Phi$  (Figure 3.2.7). Results from earlier experimental studies are shown with colored lines (Dowell & Rinfret 1960, Schmitt et al. 1989, Sack & Baragiola 1993, Hage et al. 1995, Jenniskens & Blake 1996, Dohnálek et al. 2000, Lofgren et al. 2003, Smith et al. 2011). These data show a large spread in reported crystallization times, possibly resulting from differing porosities due to variation in deposition temperature,  $H_2O$  incidence angle, vacuum quality, and substrate (Table 1). Our  $\tau_c$  for a film with  $\Phi = 0.09$  ( $0^\circ$  ice) fall within the wide range of the reported crystallization times for these earlier studies, which were either reported or are presumed to be nonporous, but it is possible that variations in porosity across these studies are responsible for the large spread in  $\tau_c$ , since we have shown that ices can retain porosity  $> 130$  K despite the disappearance of the dangling bond absorption features.

Reported values for the crystallization activation energy  $\Delta H$  have varied across previous ASW crystallization studies, with  $\Delta H$  generally ranging between  $\sim 40$  kJ mol $^{-1}$  (Sack & Baragiola 1993, Schmitt et al. 1989) to  $\sim 60$ -77 kJ mol $^{-1}$  (Hage et al. 1994, Jenniskens & Blake 1996, Dohnálek et al. 2000, Lofgren et al. 2003, Safarik et al. 2003, Smith et al. 2011).. Our average measurements of  $\Delta H \sim 64 \pm 3$  kJ mol $^{-1}$  for low-porosity ice and  $60 \pm 3$  kJ mol $^{-1}$  for ices of higher porosity fall within this higher range, about the energy required to break three hydrogen bonds in water ice (Buch 1992), but it is important to note that this measured activation energy likely has several different contributions resulting from both nucleation and crystalline growth processes.

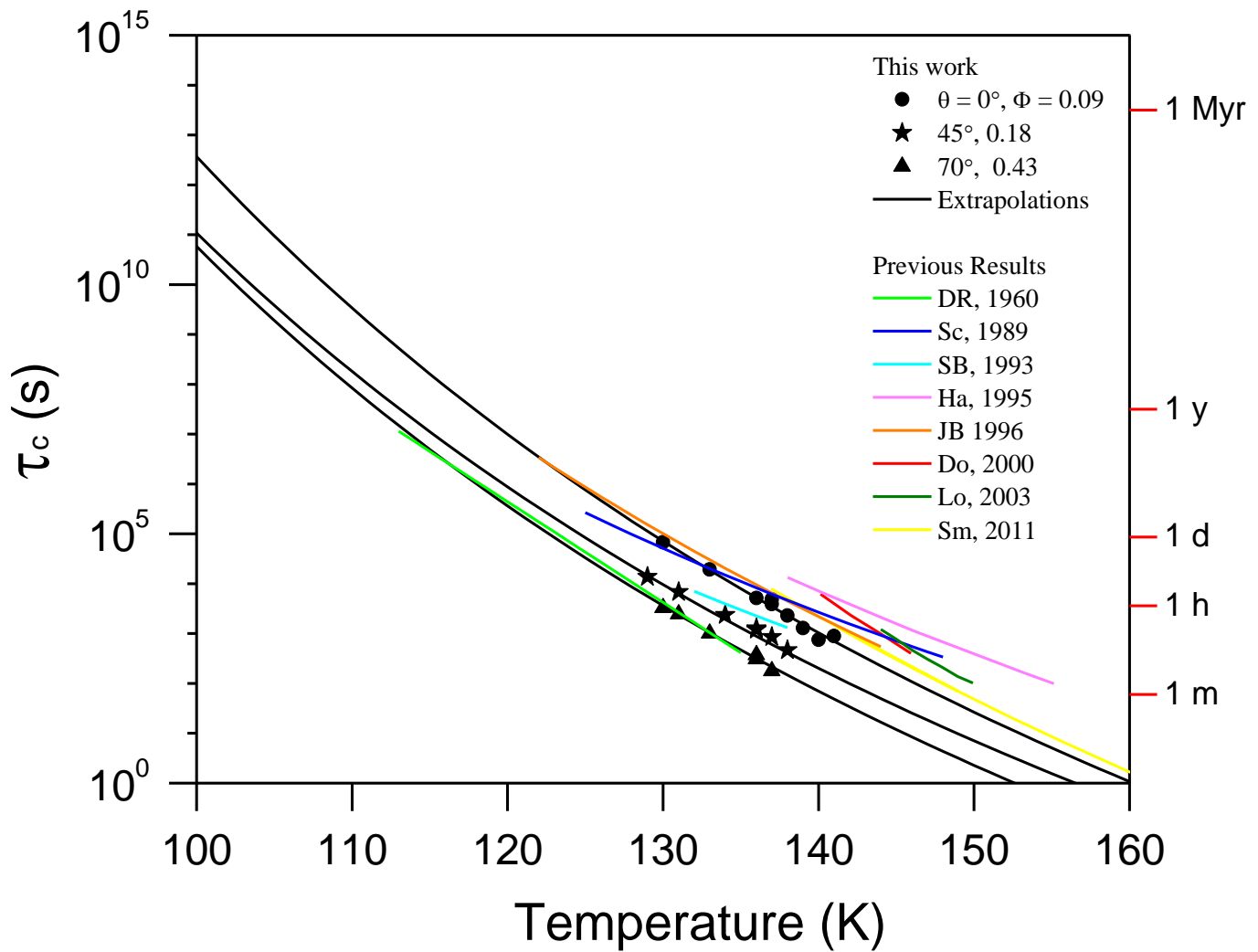


Figure 3.2.8 - Composite plot of experimental data for 63% isothermal crystallization times ( $\tau_c$ ) of vacuum-deposited amorphous ice available in the literature, partially reproduced from (Baragiola 2003): (DR, Dowell & Rinfret 1960; Sc, Schmitt et al. 1989; SB, Sack & Baragiola 1993; Ha, Hage et al. 1995; JB, Jenniskens & Blake 1996; Do, Dohnálek et al. 2000; Lo, Lofgren et al. 2003; Sm, Smith et al. 2011). We include our results of  $\tau_c$  vs. temperature for ices of porosity  $\Phi = 0.09$  ( $0^\circ$  ice),  $0.18$  ( $45^\circ$ ), and  $0.43$  ( $70^\circ$ ). Solid lines are extrapolations of the fits of Eq. 6 to our data, which gives  $\tau_c$  for lower temperatures typical of Jovian moons. Our systematic

study of  $\tau_c$  vs. temperature and its dependence on ice porosity can explain the spread in the available data. The differing crystallization times in these studies may result from differing porosities due to different deposition techniques and experimental conditions. See Table 3.2.1 for more details.

	Base $P$ (Torr)	Dep. $T$ (K)	Dep. method	Ice thick- ness (ML)	Crystallization characterization technique	$n$	$K_0^{1/n}$ (s <sup>-1</sup> )	$\Delta H$ (kJ mol <sup>-1</sup> )
Dowell & Rinfret (1960)	$5 \times 10^{-3}$	< 113	“Wet gas” deposition <sup>1</sup> from ~1 in. above sample	160,000 <sup>4</sup>	Electron diffraction	<i>Not reported</i>	<i>Not reported</i>	58
Schmitt et al. (1989)	<i>Not reported</i>	10	Vapor-deposited ASW	250 – 13,000 <sup>4</sup>	Transmission FTIR of 3.1, 6 $\mu$ m bands	<i>Not reported</i>	$1.0 \times 10^{13}$	45
Hage et al. (1995)	$\sim 10^{-7}$	78	Hyperquenched glassy water via rapid cooling of aerosol on BaF <sub>2</sub>	2,500 – 13,000 <sup>4</sup>	Transmission FTIR of 3.1- $\mu$ m band (138 – 146 K), DSC <sup>2</sup> (153 – 155 K)	1.01 – 1.74	$1.5 \times 10^{15}$	51
Sack & Baragiola (1993)	$\sim 10^{-10}$	30 – 120	Vapor-deposited ASW on Au QCM at 0°	3,000 <sup>4</sup>	Isothermal QCM sublimation rates	<i>Not reported</i>	$8.8 \times 10^{12}$	43
Jenniskens & Blake (1996)	$\sim 10^{-7}$	14	Vapor-deposited ASW on amorphous C	130 <sup>4</sup>	TEM with electron diffraction and bright- field imaging	2 stages: 2.0 $\pm$ 0.3, 0.8 $\pm$ 0.3	$\sim 5.3 \times 10^{11}$ , $\sim 2.0 \times 10^{18}$	39 $\pm$ 5, 58 $\pm$ 10
Dohnálek et al. (2000)	$\sim 10^{-10}$	22	Vapor-deposited ASW on Pt(111) at 0°	300	Mass spectrometry TPD <sup>3</sup> rates of physisorbed N <sub>2</sub> from ice surface	4.2 $\pm$ 0.4	$8.7 \times 10^{24}$	77
Lofgren et al. (2003)	$\sim 10^{-10}$	105	Vapor-deposited ASW on Pt(111) at 0°	80	Isothermal mass spectrometry desorption rates	<i>Not reported</i>	<i>Not reported</i>	75
Smith et al. (2011)	$\sim 10^{-10}$ Torr	20	Vapor-deposited ASW on Pt(111) at 0°	400	Mass spectrometry TPD rates (141 – 163 K),  Reflection FTIR of 3.1- $\mu$ m band (137 – 149 K)	3.5 – 5.5	$7.3 \pm 2.6 \times 10^{21}$ ,  $1.2 \pm 0.5 \times 10^{21}$	68.2 $\pm$ 0.5,  65.7 $\pm$ 0.5
This work	$\sim 10^{-10}$	10	Vapor-deposited ASW on CsI at varying angles	1000	Transmission FTIR of 3.1- $\mu$ m band	2 stages: 0.3 – 0.9, 1.5 – 4.8	$3.9 \times 10^{19}$ (Stage 2)	(60 – 64) $\pm$ 3 (Stage 2)

<sup>1</sup>N<sub>2</sub> gas passes through dH<sub>2</sub>O, effuses toward sample, and is pumped off

<sup>2</sup>Differential scanning calorimetry

<sup>3</sup>Temperature-programmed desorption

<sup>4</sup>Assuming ice density of 0.79 g cm<sup>-3</sup>, as measured for 0° vapor-deposited ASW at 10 K

Table 3.2.1 – Ice film deposition techniques, experimental conditions, and crystallization parameters for previous ASW crystallization studies in the literature. Crystallization times reported in these studies are shown in Figure 3.2.8.

### 3.2.5 Astrophysical Implications

Water vapor plumes have been detected on two icy satellites in the Outer Solar System, Europa (Roth et al. 2014a) and Enceladus (Hansen et al. 2006, Waite et al. 2006). The gas emanating from such plumes returns to the cold surface in gravitationally-bound trajectories, if the ejection velocity is less than the escape velocity. The trajectories can be altered by intermolecular collisions near the plume source, where mean-free-paths can be on the order of a few kilometers (Tian et al. 2007). The gravity capture is more pronounced on Europa compared to Enceladus, due to its larger size.

Hubble Space Telescope (HST) observations of Europa revealed one or more 200 km-high plumes with line-of-sight water vapor column density of  $\sim 10^{20} \text{ m}^{-2}$  (Roth et al. 2014a). A mass flux  $\sim 500 \text{ kg s}^{-1}$  per plume and ejection velocity of  $\sim 1 \text{ km s}^{-1}$  is required to match the reported abundance and its variation with altitude (Teolis et al. submitted 2016, Wyrick et al. LPSC 2016). Since the ejection velocity is less than the escape velocity, a significant fraction of the ejected water vapor will return to the surface, accreting at rates that vary with distance from the plume. A plume at the south pole, similar to that observed by the HST (Roth et. al 2014), will result in accretion rates  $\sim 6 \times 10^{13} \text{ H}_2\text{O cm}^2 \text{ s}^{-1}$  close to the eruption site, while decreasing to  $\sim 2 \times 10^{12} \text{ H}_2\text{O cm}^2 \text{ s}^{-1}$  toward the dayside equatorial region (Teolis et al. submitted 2016). The accretion rate largely exceeds the loss rate due to magnetospheric ion sputtering, estimated to be  $\sim 10^9 - 10^{10} \text{ H}_2\text{O cm}^{-2} \text{ s}^{-1}$  (Cassidy et al. 2013). On the dayside equatorial region, where the temperature can reach 132 K, loss from thermal desorption becomes significant,  $\sim 10^{11} \text{ H}_2\text{O cm}^{-2} \text{ s}^{-1}$  (Sack & Baragiola 1993). Plumes with higher mass-loading and lower velocity will increase the accretion rate.



The phase of the ice condensed from the plume vapor will be amorphous since the surface temperature on Europa ranges between 86 and 132 K, depending on latitude and solar illumination (Spencer et al. 1999). The ice film will also develop porosity, determined by the regolith temperature and the local,  $\mu\text{m}$ -scale morphology, which will constrain the incidences of the incoming vapor flux. In Figure 3.2.9, we show the latitudinal variation of average crystallization time on Europa's surface for amorphous ices with porosities 0.09 and 0.43. The diurnal variability of the surface temperature may cause the crystallization rate to slow/accelerate on the night/day hemispheres: for instance, the crystallization time drops to only a few hours at the maximum equatorial dayside temperature of 132 K. Accordingly, we estimated the mean crystallization times of Figure 3.2.9 by evaluating (by numerical integration, at each latitude) the time average of the crystallization rate (inverse of Equation 6) over one Europa day, taking into consideration Europa's diurnal temperature profile (Spencer et al. 1999, Teolis et al. submitted 2016). An amorphous ice layer with higher porosity ( $\Phi = 0.43$ ) will crystallize  $\sim 20$  times faster than a less porous film ( $\Phi = 0.09$ ) at the equatorial region.

The ice porosity is also altered by magnetospheric irradiation, but compaction timescales are much larger than crystallization timescales at equatorial latitudes. Magnetospheric ions require  $\sim 1$  year to deliver the compaction dose of  $1.5 \text{ eV mol}^{-1}$  (Raut et al. 2008) to the top surface ( $\sim 100\text{-}\mu\text{m}$  depth) of the European regolith (Paranicas et al. 2009). At the poles, ice can retain its amorphous nature indefinitely, since the thermally-driven crystallization time ( $\tau_c \sim 1$

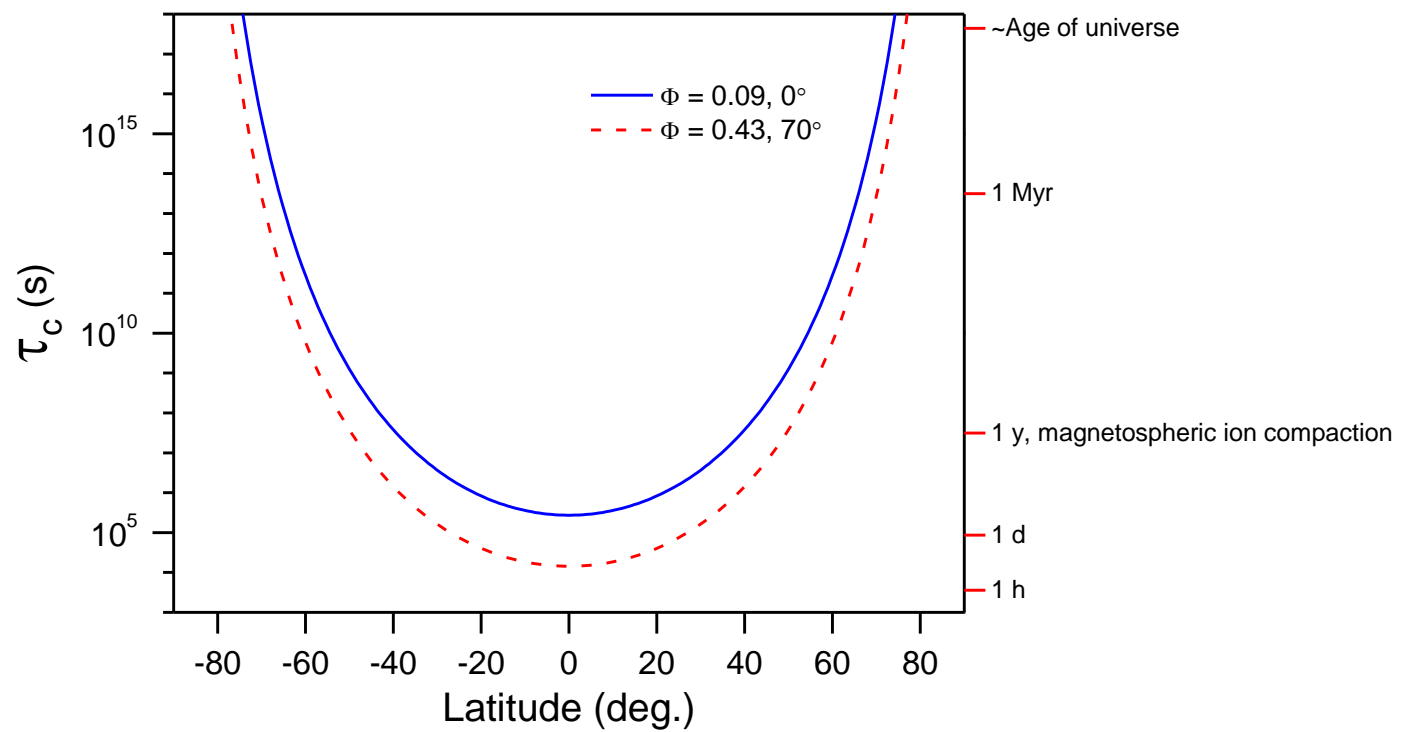


Figure 3.2.9 – Latitudinal dependence of the Europa's surface average 63% crystallization time  $\tau_c$  for ices with two different porosities, derived from Eq. 6 (discussed in text), by taking into account the diurnal time variation of the surface temperature, as estimated by (Teolis et al. submitted 2016, Spencer et al. 1999).

Myr) is much longer than the  $\sim 5$  years required for radiation-induced amorphization at the colder temperatures (Famá et al. 2010, Strazzulla et al. 1992).

Recent near-infrared data from the *New Horizons* flyby of the Pluto-Charon system show the 1.65- $\mu\text{m}$  feature on Charon's surface, diagnostic of crystalline ice (Grundy et al. 2016). Other processes must be responsible for the presence of crystalline ice on the much colder surfaces of Charon and other TNOs/KBOs ( $< 50$  K), since crystallization times exceed the age of the Solar System at these temperatures. Possible mechanisms could be local heating by micrometeorite impacts (Porter et al. 2010) or cryo-volcanism (Jewitt & Lu 2004, Bauer et al. 2002).

### 3.2.6 Conclusions

The large surface area presented by porous ice films provides preferred nucleation sites for the onset of crystallization, and ASW films with higher porosity therefore crystallize faster than less porous films. The crystallization times for astronomical ices will depend on surface temperature and porosity. On Europa, we predict that amorphous ice condensed from plume ejecta at mid-latitudes can crystallize in 3 months if the ice has substantial porosity, compared to 7 years for compact ice counterparts. Magnetospheric ion irradiation can compact porous ice in  $\sim 1$  year, potentially increasing the time required for crystallization. However, radiation-induced defects can also contribute to increased crystallization rates. Further experiments are needed to characterize the effects of ion irradiation on crystallization kinetics.

### Acknowledgements

We acknowledge support from NASA Outer Planetary Research Award NNX11AM42G. E.H. Mitchell acknowledges support from NASA Earth and Space Science Fellowship and

NASA Virginia Space Grant Consortium. We thank Gary J. Shiflet for useful discussion on nucleation theory.

Raúl A. Baragiola passed away on June 21, 2015. Co-authors Emily H. Mitchell, Ujjwal Raut, and Benjamin D. Teolis are grateful for his invaluable guidance and support – not only on the work presented herein, but over the many years that he advised their research.

## References

- Avrami, M., J. Chem. Phys. **7**, 1103 (1939).
- Backus, E.H.G., Grecea, M.L., Kleyn, A.W., Bonn, M., Phys. Rev. Lett **92**, 23 (2004).
- Baragiola, R.A., Planet. Space Sci. **51**, 953 (2003).
- Baratta, G.A., Leto, G., Spinella, F., Strazzulla, G., Foti, G., A&A **252**, 421 (1991).
- Bauer, J.M., Roush, T.L., Geballe, T.R., Meech, K.J., Owen, T.C., Vacca, W.D., Rayner, J.T., Jim, K.T.C., Icarus **158**, 178 (2002).
- Berland, B.S., Brown, D.E., Tolbert, M.A., George, S.M., Geophys. Res. Lett. **223**, 3473 (1995).
- Bertie, J.E., Labbé, H.J., Whalley, E. J. Chem. Phys. **50**, 4501 (1969).
- Bossa, J.-B., Isokoski, K., de Valois, M.S., Linnartz, H., A&A **545**, A82 (2012).
- Brown, M.E. and Calvin, W.M., Science **287**, 5450 (2000).
- Buch, V., J. Chem. Phys. **96**, 3814 (1992).
- Buch, V., Delzeit, L., Blackledge, C., Devlin, J.P. J. Chem. Phys. **100**, 3732 (1996).
- Cassidy, T.A., Paranicas, C.P., Shirley, J.H., Dalson, J.B. III, Teolis, B.D., Johnson, .R.E., Kamp, L., Hendrix, A.R. Planet. Space Sci. **77**, 64 (2013).
- Cruikshank, D.P., Grundy, W.M., DeMeo, F.E., Buie, M.W., Binzel, R.P., Jennings, D.E., Olkin, C.B., Parker, J.W., Reuter, D.C., Spencer, J.R., Stern, S.A., Young, L.A., Weaver, H.A.,

- Icarus **246**, 82 (2015).
- Devlin, J.P. and Buch, V., J. Chem. Phys. **99**, 16534 (1995).
- Dietrich, S. In: Domb. C., Lebowitz, J.L. (Eds.), Phase Transitions and Critical Phenomena, Vol. 12. Academic, London (1988).
- Dohnálek. Z., Ciolli, R.L., Kimmel, G.A., Stevenson, K.P., Smith, R.S., Kay, B.D., J. Chem. Phys. **110**, 5489 (2000).
- Doremus, R.H., Rates of Phase Transformations, Academic, New York (1985).
- Dowell, L.G. and Rinfret, A.P., Nature **158**, 1144 (1960).
- Famá, M., Loeffler, M.J., Raut, U., Baragiola, R.A., Icarus **207**, 314 (2010).
- Frances, R.J. & O'Hare, D., J. Chem. Soc., Dalton Trans., 3133 (1998).
- Gibbs, J.W., Collected Works, Longmans, Green and Co., New York (1928).
- Giering, T. and Haarer, D., Chem. Phys. Lett. **261**, 6, 677 (1996).
- Ghormley, J.A. and Hochanadel, C.J., Science **171**, 92 (1971).
- Grundy, W.M., Buie, M.W., Stansberry, J.A., Spencer, J.R., Icarus **142**, 536 (1999).
- Grundy, W.M. et al. Science **351**, 6279 (2016).
- Hage, W., Hallbrucker, A., Mayer, E., Johari, G.P., J. Chem. Phys. **100**, 2743 (1994).
- Hage, W., Hallbrucker, A., Mayer, E., J. Chem. Phys. **103**, 2 (1995).
- Hagen, W., Tielens, A.G.G.M., Greenberg, J.M., J. Chem. Phys. **56**, 367 (1981).
- Hansen, C.J., Esposito, L., Stewart, A.I.F., Colwell, J., Hendrix, A., Pryor, W., Shemansky, D., West, R. Science **311**, 1422 (2006).
- Heavens, O.S., Optical Properties of Thin Solid Films, Dover, New York (1991).
- Hillert, M. and Aaronson, H.I. Lectures on the Theory of Phase Transformations, Amer. Inst. Mining, Metallurgical and Petroleum Engrs, 1, (1975).

- Isokoski, K., Bossa, J.-B., Triemstra, T., Linnartz, H., *Phys. Chem. Chem. Phys.* **16**, 3456 (2014).
- Jenniskens, P. and Blake, D.F., *Astrophys. J.* **473**, 1104-1113 (1996).
- Jewitt, D.C. & Luu, J., *Nature* **432**, 731 (2004).
- Johari, G.P., Hallbrucker, A., Mayer, E., *J. Chem. Phys.* **95**, 2955 (1991).
- Jurac, S., Johnson, R.E., Richardson, J.D., Paranicas, C. *Planet. Space Sci.* **49**, 319 (2001).
- Kimmel, G.A., Stevenson, K.P., Dohnálek, Z., Smith, R.S., Kay, B.D., *J. Chem. Phys.* **114**, 5284, (2001a).
- Kimmel, G.A., Dohnálek, Z., Stevenson, K.P., Smith, R.S., Kay, B.D., *J. Chem. Phys.* **114**, 5295, (2001b).
- Kirsch, B.L., Richman, E.K., Riley, A.E., Tolbert, S.H., *J. Phys. Chem. B.* **108**, 12698 (2004).
- Kondo, T., Kato, H.S., Bonn, M., Kawai, M., *J. Chem. Phys.* **127**, 094703 (2007).
- Kouchi, A., Kuroda, T., *Nature* **344**, 134 (1990).
- Kouchi, T., Yamamoto, T., Kozasa, T., Kuroda, T., Greenberg, J.M. *Astron. Astrophys.* **290**, 1009 (1994).
- Leto, G. & Baratta, G.A., *A&A* **397**, 7 (2003)
- Lofgren, P., Ahlstrom, P., Chakarov, D.V., Lausma, J., Kasemo, B., *Surf. Sci.* **367**, L19 (1996).
- Lofgren, P., Ahlstrom, P., Lausma, J., Kasemo, B., Chakarov, D., *Langmuir* **19**, 265 (2003).
- Malinowski, E.R. *Factor Analysis in Chemistry*, Third Edition. Wiley-Interscience, New York, (2002).
- Maté, B., Rodriguez-Lazcano, Y., Jerrero, V.J., *Phys. Chem. Chem. Phys.* **14**, 10595 (2012).
- Mayer, E., and Pletzer, R., *Nature* **319**, 298 (1986).
- Merlin, F. et al., *A&A* **466**, 1185 (2007).

- Moore, M.H. & Hudson, R.L., *Astrophys. J.* **401**, 353 (1992).
- Narten, A.H., Venkatesh, C.G., Rice, S.A., *J. Chem. Phys.* **64**, 1106 (1976).
- Paranicas, C., Cooper, J.F., Garrett, H.B., Johnson, R.E., Sturmer, S.J. Europa, University of Arizona Press, Tucson, 529 (2009).
- Porter, S.B., Desch, S.J., Cook, J.C., *Icarus* **208**, 492 (2010).
- Rao, C.N.R. and Rao, K.J., *Phase Transformations in Solids*, McGraw-Hill (1978).
- Raut, U., Teolis, B.D., Loeffler, M.J., Vidal, R.A., Famá, M., Baragiola, R.A. *J. Chem. Phys.* **126**, 244511 (2007a).
- Raut, U., Famá, M., Teolis, B.D., Baragiola, R.A., *J. Chem. Phys.* **127**, 204713 (2007b).
- Raut, U., Famá, M., Loeffler, M.J., Baragiola, R.A., *Astrophys. J.* **687**, 1070 (2008).
- Roth, L., Saur, J., Retherford, K.D., Strobel, D.F., Feldman, P.D., McGrath, M.A., Nimmo, F. *Science* **343**, 171 (2014a).
- Rouquerol, F., Rouquerol, J., Sing, K., *Adsorption by Powders & Porous Solids: Principles, Methodology and Applications*, Academic, San Diego, (1999).
- Rowland, B. and Devlin, J.P. *J. Chem. Phys.* **94**, 812, (1991).
- Rowland, B., Kadagathur, N.S., Devlin, J.P. *J. Chem. Phys.* **102**, 13 (1995).
- Sack, N.J. and Baragiola, R.A., *Phys. Rev. B.* **48**, 9973 (1993).
- Safarik, D.J., Meyer, R.J., Mullins, C.B., *J. Chem. Phys.* **118**, 4660 (2003).
- Sceats, M.G. & Rice, S.A. In: Franks, F. (Eds.), *Water, a Comprehensive Treatise*, Vol. 7. Plenum, New York (1982).
- Schmitt. B., Espinasse, S., Grim, R.G.A., Greenberg, J.M., Klinger, J., *Proc. of An International Workshop on Physics and Mechanics of Cometary Materials*, Münster, FRG, 9-11 Oct. 1989.

- Schmitt, B., Quirico, E., Trotta, F., Grundy, W.M. In: Schmitt, B., De Bergh, C., Festou, M. (Eds.), *Solar System Ices*, Kluwer Academic, Norwell, MA (1998).
- Smith, R.S., Huang, C., Wong, E.K.L., Kay, B.D., *Surf. Sci.* **367**, L13 (1996).
- Smith, R.S., Dohnálek, Z., Kimmel, G.A., Teeter, G., Ayotte, P., Daschbach, J.L., Kay, B.D. In: Buch, V. & Devlin, J.P. (Eds.), *Water in Confining Geometries*, Springer, New York, NY (2003).
- Smith, R.S., Matthiesen, J., Knox, J., Kay, B.D., *J. Phys. Chem. A* **115**, 5908 (2011).
- Stevenson, K.P., Kimmel, G.A., Dohnálek, Z., Smith, R.S., Kelly, B.D., *Science* **283**, 1505 (1999).
- Spencer, J.R., Tamppari, L., Martin, T.Z., Travis, L.D. *Science* **284**, 5419 (1999).
- Strazzulla, G., Baratta, G.A., Leto, G., Foti, G. *Europhys. Lett.* **18**, 6 (1992).
- Teolis, B.D., Loeffler, M.J., Raut, U., Famá, M., Baragiola, R.A. *Icarus* **190**, 1, (2007).
- Teolis, B.D., Wyrick, D.Y., Bouquet, A., Magee, B.A., Waite, J.H., *Icarus*, submitted (2016).
- Tian, F., Stewart, A.I.F., Toon, O.B., Larsen, K.W., Esposito, L.W. *Icarus* **188**, 154 (2007).
- Tsekouras, A.A., Iedema, M.J., Cowin, J.P., *Phys. Rev. Lett.* **80**, 5798 (1998).
- Volmer, M. and Weber, A., *Z. Physik. Chem.* **119**, 277 (1926).
- Waite, J.H., Combi, M.R., Ip, W-H, Cravens, T.E., McNutt, R.L. Jr., Kasprzak, W., Yelle, R., Luhmann, J., Niemann, H., Gell, D., Magee, B., Fletcher, G., Lunine, J., Tseng, W-L. *Science* **311**, 1419 (2006).
- Westley, M.S., Baratta, G.A., Baragiola, R.A., *J. Chem. Phys.* **108**, 3321 (1998).
- Winkler, A. and Yates, J.T., Jr. *J. Vac. Sci. Technol. A* **6**, 5, (1988).
- Wyrick, D.Y., Teolis, B.D., Bouquet, A., Magee, B., Waite, J.H., Jr., J. Proc. Of 47<sup>th</sup> Lunar and Planetary Science Conference, The Woodlands, Texas, March



21-25, 2016.

## CHAPTER 4

### Ultraviolet Photodesorption as a Driver of Water Migration on the Lunar Surface

**Published:** *Planetary and Space Science* **89**, 42 – 46 (2013).

#### Abstract

We have studied the photodesorption of  $\sim$ monolayer coverage of water ice coating amorphous carbon by 193 nm photons. We found that the column density of water decreases exponentially with fluence during irradiation at 120 K and obtain a desorption cross-section of  $7.4 (\pm 0.5) \times 10^{-19} \text{ cm}^2$ . We estimate the lifetime for photodesorption to be  $\sim 12$  hours for average solar activity at the sub-solar point on the Moon. The photodesorbed molecules, based on other experiments, are expected to be slower than the escape velocity and to be re-adsorbed on the surface, contributing to water migration. For comparison, we determine the effect of 4 keV  $\text{He}^+$  on water-coated Apollo 16 soil (65901) under similar experimental conditions. We find a sputtering cross-section of  $1.2 (\pm 0.4) \times 10^{-16} \text{ cm}^2$ . Because of the much larger flux, we calculated that photodesorption by solar UV is four orders of magnitude more efficient than sputtering by the solar wind in causing the migration of adsorbed water on the lunar surface.

#### 4.1 Introduction

This work was motivated by recent reports of remote sensing of surficial OH/H<sub>2</sub>O on most of the lunar surface. Analysis of infrared spectroscopic measurements of the Moon obtained by three independent space instruments, the Moon Mineralogy Mapper (M<sup>3</sup>) on *Chandrayaan-1*, the Visual and Infrared Mapping Spectrometer (VIMS) on *Cassini* and the High-Resolution Instrument (HRI) infrared spectrometer onboard *Deep Impact* (DI), indicate the existence of H<sub>2</sub>O (and OH groups) within the uppermost layers of the lunar surface. Pieters et al. (2009) observed

that the infrared OH band depth varied with the mineralogy and location across the lunar surface. Sunshine et al. (2009) observed a diurnal dependence of the infrared absorption band, suggesting that the regolith undergoes a dynamic H<sub>2</sub>O loss (perhaps by photon-stimulated desorption, PSD) and rehydration cycle over the lunar day. A suggested alternative explanation has been that variations in band depth are due to surface topographic effects on reflectance (Clark 2009). The three reports agree in that H<sub>2</sub>O or OH is spatially distributed across the entire lunar landscape, with larger abundances observed at higher latitudes and the poles.

The presence of water on the lunar surface is surprising considering that many potential removal mechanisms exist, such as photodesorption (followed by photodissociation), thermal desorption, meteorite impact, radiation damage, and sputtering. The mechanism for water production or delivery to the lunar surface is unknown. However, some possible sources include: cometary or meteoritic delivery combined with surface diffusion, water/ice beneath the lunar surface diffusing from the interior, or chemical effects due to solar wind impact on the lunar regolith (Arnold 1979). An often-considered hypothesis is that OH and H<sub>2</sub>O are formed by the interaction of the solar wind with silicates and other oxygen-bearing minerals within the lunar basalt. Ion irradiation over a range of energies (0.5-3 keV) can lead to the breaking of chemical bonds within various minerals. Implanted or trapped protons from the solar wind may attach to those broken bonds and form OH and subsequently H<sub>2</sub>O. Such a mechanism is implied by Sunshine et al. (2009) to explain the apparent rehydration of the entire lunar surface, which requires a daily renewal source to propagate OH/H<sub>2</sub>O production.

We investigated this hypothesis in our laboratory (Burke et al. 2011) using Fourier Transform Infrared Spectroscopy (FTIR), X-ray Photoelectron Spectroscopy (XPS), and Secondary Ion Mass Spectroscopy (SIMS). The outcome was the absence of significant

formation of either OH or H<sub>2</sub>O, which was ascribed to the preferential depletion of oxygen by sputtering during proton irradiation. This depletion was confirmed by in situ post-irradiation surface analysis using XPS and SIMS. Our results provided no evidence to support the formation of significant amounts of H<sub>2</sub>O in the lunar regolith via implantation of solar wind protons as a mechanism responsible for the strength of OH absorption in recent spacecraft data. We determined an upper limit for the production of surficial OH on the lunar surface by solar wind irradiation to be 0.5% (absorption depth). Recent reports by Managadze et al. (2010) and Ichimura et al. (2012) show OH/OD formation from irradiating simulants or lunar soil with hydrogen (H, D) ions. Managadze et al. used SIMS to detect sputtered water ions from lunar simulants but did not correlate them to IR measurements. SIMS is orders of magnitude more sensitive than IR absorption and thus a small SIMS signal may not give an observable signal in IR. Ichimura et al. used high pressures (not ultrahigh vacuum) and multiple exposures to air. Furthermore, the possible contamination of the ion beam with OH<sup>+</sup> (OD<sup>+</sup>) ions in both studies make it difficult to assert that ion irradiation under lunar conditions can produce sufficient OH to account for the remote infrared observations of lunar soil.

Whatever the origin of lunar water, it is important to establish the stability of the water molecules, the migration from or to the polar cold traps, and the cause of the diurnal variations in infrared water signatures. In particular, it is of interest to determine the role of solar radiation and the solar wind in altering surficial water. Here we report measurements of photodesorption of adsorbed water on amorphous carbon and sputtering of adsorbed water from lunar highland soil (65901) at 120 K.

## 4.2 Experimental Methods

### *I. Photodesorption Experiments*

Experiments were performed in an ultrahigh vacuum chamber cryopumped to a base pressure of  $\sim 2 \times 10^{-9}$  Torr with a setup described in detail in Raut et al. (2012) and Fulvio et al. (2012). The chamber houses a quartz-crystal microbalance (QCM) cooled by a closed-cycle He-refrigerator. The QCM does not function when coated with lunar soil because the non-uniform soil with large grain size (more than a few microns) causes excessive mechanical damping. We coated the crystal with readily available amorphous carbon foil ( $\sim 50$ -nm thick), which was the substrate for water deposition. The advantage of carbon over the gold electrode of the QCM is that its electronic properties are closer to those of a non-metallic regolith. The carbon-coated QCM was irradiated with 100 keV  $\text{Ar}^+$  ions to fluences of  $\sim 10^{14}$  ions  $\text{cm}^{-2}$  to sputter-remove a few monolayers of impurities that coat the foil before transfer to the vacuum system. The surface was cooled and water was deposited from a microcapillary array doser at normal incidence to the substrate. The experiments were done at 120 K, the highest temperature at which adsorption of a monolayer becomes possible. The QCM measures the areal mass of the water film condensed on the carbon substrate, which is converted to column density. The column density of the deposited ice film was  $1.6 \times 10^{15}$   $\text{H}_2\text{O}$   $\text{cm}^{-2}$ , or about one monolayer, considering the roughness of the carbon foil.

The film was irradiated at normal incidence with 193 nm (6.41 eV) ultraviolet photons from an ArF excimer laser. Using a  $\text{MgF}_2$  lens (focal length = 50 cm), the beam was defocused to a rectangular spot ( $\sim 25$  mm  $\times$  75 mm) on the target, larger than the sensitive diameter of the QCM (6 mm). This ensured the absence of heating effects or multi-photon processes, in agreement with similar experiments by Wolf et al. (1991). The laser output was measured with

an Ophir power meter placed in the path of the beam. The 10-ns laser pulses had an average fluence of  $1.24 \pm 0.14 \text{ mJ cm}^{-2}$  at 1 Hz, or equivalently,  $\sim 1 \times 10^{15}$  photons  $\text{cm}^{-2}$  per pulse. The column density of water adsorbed on the carbon substrate was monitored via QCM during laser irradiation up to a fluence of  $\sim 4 \times 10^{18}$  photons  $\text{cm}^{-2}$ .

## *II. Sputtering Experiments*

Using XPS, we measured the sputtering cross-section for water vapor deposited on mature Apollo 16 highland soil (sample 65901) under 4 keV  $\text{He}^+$  irradiation. In these experiments, a small ( $\sim 0.1 \text{ g}$ ) sample of lunar soil was deposited in a 10 mm diameter x 1 mm deep copper cup and placed on a  $\text{LN}_2$ -cooled sample holder. The soil was neither compressed nor held with a bonding agent such as carbon tape. These ion irradiation experiments were conducted in an ultra-high vacuum (base pressure  $\sim 10^{-9}$  Torr) Physical Electronics 560 XPS/SAM system, equipped with an X-ray source mounted perpendicular to the double-pass, cylindrical-mirror electron energy analyzer (CMA). XPS is a quantitative surface analytical technique that uses mono-energetic X-rays that penetrate the sample surface, ejecting electrons of a characteristic binding energy (BE) with respect to the Fermi level. These photoelectrons have a kinetic energy in the spectrometer,  $E_x - BE - W$ , where  $W$  is the measured work function of the spectrometer. The signal is provided by those photoelectrons that leave the sample surface without energy loss, originating from a thin surface layer (2-4 nm on average, depending on the photoelectron energy). Quantitative information is obtained by incorporating the instrument sensitivity for each elemental transition, which has an accuracy of  $\sim 15\%$ . The CMA was operated at an energy resolution of 3.2 eV to provide high sensitivity, ensuring that all the surface constituents on each

mineral were identified to the <1% level. Data were taken using primarily Al ( $K\alpha_{1,2}$ ) X-rays to minimize the overlap of Auger and photoelectron spectra.

Before water growth, adventitious carbon and atmospheric water were removed from the surface by irradiating the sample using 1 keV  $\text{Xe}^+$  ions to a fluence of  $2 \times 10^{16}$  ions  $\text{cm}^{-2}$ . The removal of the atmospheric species was identified with XPS as a decrease in the atomic percentage of carbon present on the surface and in the oxygen to silicon ratio. The sample was then cooled to  $\sim 80$  K and dosed with water at normal incidence through a capillary array. The water deposit was thermally stable during the experiments at 120 K and desorbed completely at 180 K.

As mentioned above, we could not use a QCM for these experiment with non-uniform granular soil. Thus, the amount of water on the soil,  $\sim 2$  monolayers, was determined by the increase in atomic percentage of oxygen on the surface relative to Si. The soil was irradiated with 4 keV  $\text{He}^+$  ions rastered uniformly over an area larger than that sampled by XPS. The beam was positioned at an angle of  $25.3^\circ$  to the surface normal, but the roughness of the soil means that the local incidence angles varied. Irradiation was done at a flux of  $\sim 10^{14}$  ions  $\text{cm}^{-2} \text{ s}^{-1}$ , as measured with a Faraday cup. XPS measurements were taken after each irradiation period as a function of integrated fluence. This flux is seven orders of magnitude larger than at the Moon but, at  $0.064 \text{ W cm}^{-2}$ , the power density is insufficient to cause detectable heating.

### 4.3 Results

For photon irradiation, the  $\text{H}_2\text{O}$  column density decreased exponentially with fluence  $F$  during irradiation as expected from a single process that removes a monolayer or less of water in proportion to coverage (Figure 4.1). An exponential curve was fit to the data:

$$\eta = \eta(0) \exp(-\sigma_d F), \quad (1)$$

with  $\eta(0) = 1.6 \times 10^{15} \text{ H}_2\text{O cm}^{-2}$ .



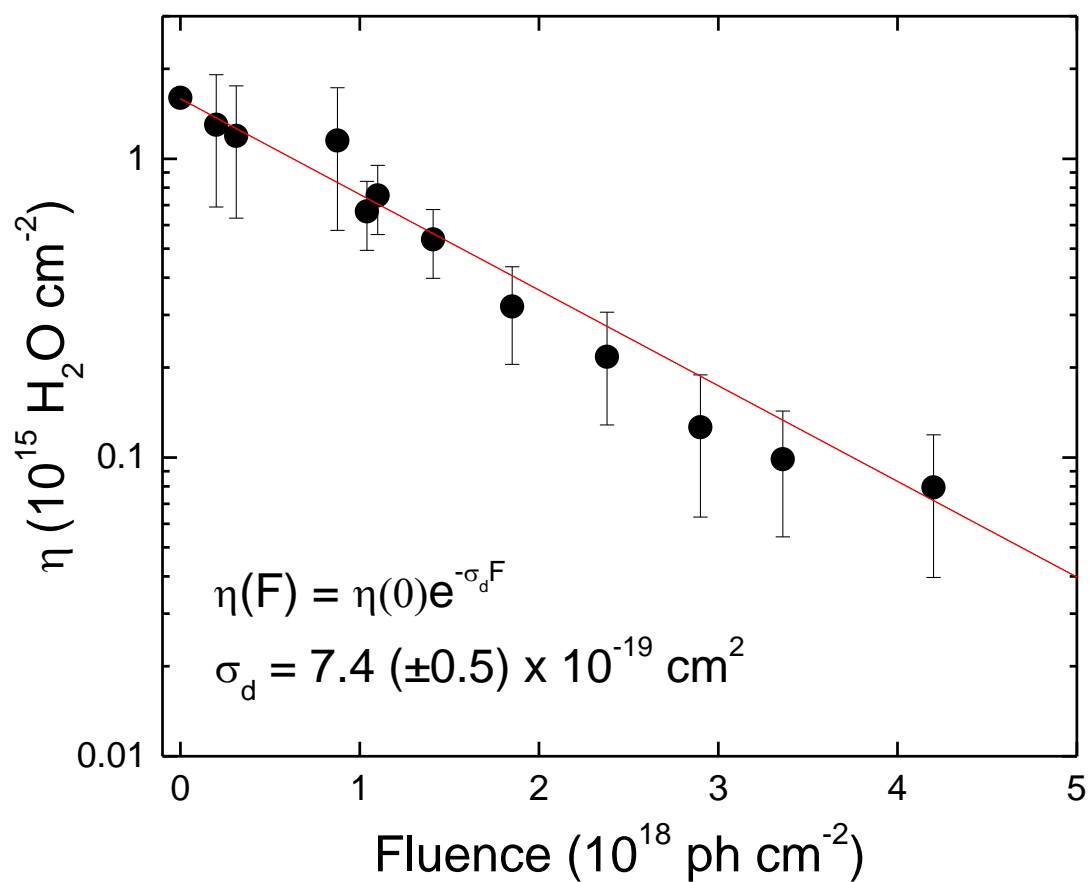


Figure 4.1 – Decrease in the column density  $\eta$  of water adsorbed on carbon vs. fluence  $F$  of 193 nm photons from a defocused ArF excimer laser. The data are fitted to an exponential decay that gives a photodesorption cross-section of  $7.4 (\pm 0.5) \times 10^{-19} \text{ cm}^2$ .

From this curve, we obtained a cross-section  $\sigma_d = 7.4 (\pm 0.5) \times 10^{-19} \text{ cm}^2$ , which describes the amount of water removed by 193 nm photons as a function of fluence. This value is about one-fifth of the temperature-independent value observed for photodesorption of water from ice by 121.6-nm photons (Westley et al. 1995).

In contrast to the PSD experiments, in the case of ion irradiation, the increase in the ratio of O to Si due to water adsorption, measured by XPS, as a function of fluence (Figure 4.2) shows a complex behavior. We fit two exponential decays with fluence, giving cross sections  $\sigma_1$  and  $\sigma_2$  for the initial and final decay. These are interpreted to correspond to the removal of about a monolayer of water in the form of ice and a residual monolayer of water adsorbed on the soil. The cross-section of  $\sigma_1 = 3 (\pm 1) \times 10^{-15} \text{ cm}^2$  and the column density of about one monolayer, or  $\eta \sim 1 \times 10^{15} \text{ H}_2\text{O cm}^{-2}$ , implies an initial sputtering yield  $Y = \sigma_1 \eta \sim 3$ , of the same order as the measured sputtering yield for ice (Famá et al. 2008). The second cross-section,  $\sigma_2 = 1.2 (\pm 0.4) \times 10^{-16} \text{ cm}^2$ , is interpreted as the desorption of a more tightly bound layer that remains adsorbed on the soil after the ice is removed. This type of behavior has been seen previously in the sputtering of Na from minerals (Dukes et al. 2011). As we will see, the uncertainties of this interpretation are not important in establishing that solar photons are much more efficient than the solar wind in removing adsorbed monolayers of water from surfaces.

## 4.4 Discussion

### *I. Photodesorption*

Our PSD experiments are similar to those of Wolf et al. (1991) for adsorbed water on transition metal surfaces under 6.4 eV laser irradiation, except for our use of the amorphous carbon substrate. Wolf et al. noted that, since water and ice are transparent to 6.4 eV photons, the desorption process must involve the absorption of the photon by the substrate, which they

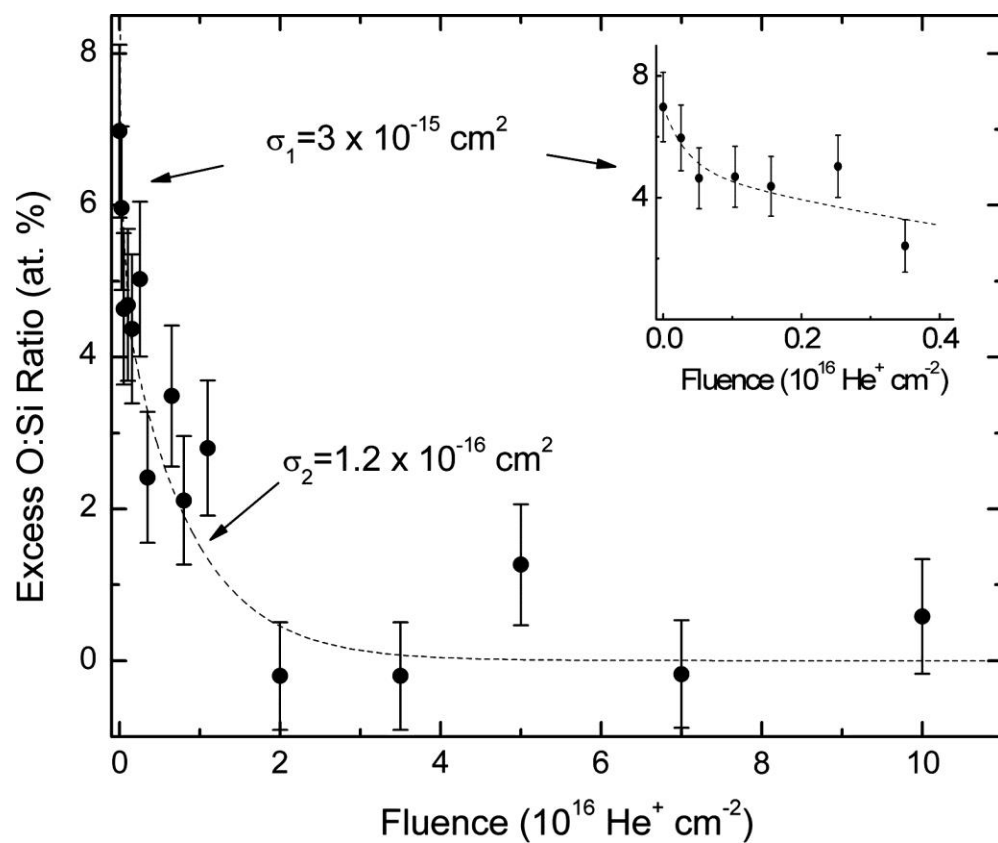


Figure 4.2 – Ratio of oxygen-1s to Si-2p XPS signals over the O:Si ratio of the soil vs. the fluence of 4 keV ions. The change in amount of water ice can be fitted with a double exponential, indicating sputtering of water molecules from two different binding sites.

estimate to have a probability of a few percent. The transient negative ion (TNI) mechanism, one of the most popular in PSD (Menzel 2012, Gadzuk 2012), is of rather general applicability, and has been applied not only to metals but also to iron oxide (Chiba et al. 2004). This is the mechanism proposed by Wolf et al. (1991); it starts with the ejection of a photoelectron from the substrate and its capture in a negative  $\text{H}_2\text{O}^-$  ion, which is attracted by its image charge to the surface. Upon neutralization, the former ion can then either dissociate into  $\text{OH} + \text{H}$  or form an  $\text{H}_2\text{O}$  molecule which, being closer to the surface than its value for adsorbed  $\text{H}_2\text{O}$  (due to the initial motion of the parent  $\text{H}_2\text{O}^-$  ion), is repelled from the surface and ejected into vacuum. In the experiments on metals by Wolf et al., both channels are important, and the dissociation channel also leads to desorption after the  $\text{OH}$  and  $\text{H}$  recombine into water in a subsequent event, leading to a complex dependence of desorption on fluence. The initial desorption cross-section for water on  $\text{Pt}(111)$  is  $3.2 \times 10^{-19} \text{ cm}^2$  (Zhu et al. 1991), about half the value that we measure for amorphous carbon. Our higher value may be due to differences in electronic structure of the substrate or to suppression of the dissociation channel, as suggested by the fact that the fluence decay shown in Fig. 1 is well described by a single exponential.

## *II. Estimation of Lifetime of Adsorbed Water*

We estimate the lifetime for desorption by normally incident solar photons near the equator at noon; data in other situations can be derived from local impact geometry. Although our discussion focuses on the lifetime of a water molecule particularly on the lunar surface, the measured desorption cross-sections may also be used in additional contexts pertinent to other airless planetary bodies.

To estimate the lifetime under photodesorption, we used the solar irradiance  $I$  as a function of wavelength (Woods et al. 1996). We assume a photodesorption threshold of 4.9 eV, following the rapid drop of the PSD cross-section with energy, observed by Wolf et al. (1991) and Zhu et al. (1991). We then assume that the cross-section grows linearly with energy above the threshold,  $\sigma_d = 4.9 \times 10^{-19} \text{ cm}^2 (E [\text{eV}] - 4.9 \text{ eV})$ , and that the cross-section is 0 at the threshold and our measured value  $7.4 \times 10^{-19} \text{ cm}^2$  at 6.4 eV. This model for the cross-section implies a value of  $2.6 \times 10^{-18} \text{ cm}^2$  at 10.2 eV, of the order of  $3.5 \times 10^{-18} \text{ cm}^2$ , the temperature-independent cross-section for removing water from the surface of the ice (Westley et al. 1995) by Ly- $\alpha$  radiation.

With this assumption, we obtain the desorption rate per second from

$$\xi = \int \frac{dI}{d\lambda} \sigma(\lambda) d\lambda = 6.84 \times 10^{-5} \text{ s}^{-1}, \quad (2)$$

as shown in Figure 4.3 using a flux  $I$  converted from the irradiance data of Woods et al. (1996) by dividing by the photon energy. Thus, the photodesorption lifetime is

$$\tau = \xi^{-1} = 1.47 \times 10^4 \text{ s} \quad (3)$$

or  $\sim 4$  hours for normal incidence at noon. We must take into account the effect of roughness of the soil, which allows re-condensation of adsorbed water. This leads to a reduction of the effective desorption by a factor of  $\sim 3$  in non-compacted, granular lunar soil (Loeffler et al. 2009), as predicted by models (Cassidy & Johnson 2005). This reduction in sputtering increases the lifetime of water to  $\sim 12$  hours at the sub-solar point. Considering the variation of the solar intensity across solar cycles, the lifetime can vary over the range of 5 to 40 hours. The lifetimes will increase in inclined surfaces by the secant of the incidence angle.

From other studies of photodesorption (Wolf et al. 1991, Zhu et al. 1991), the velocity of the desorbed molecule is expected to be smaller than the lunar escape velocity,  $2.38 \text{ km s}^{-1}$ . Thus,

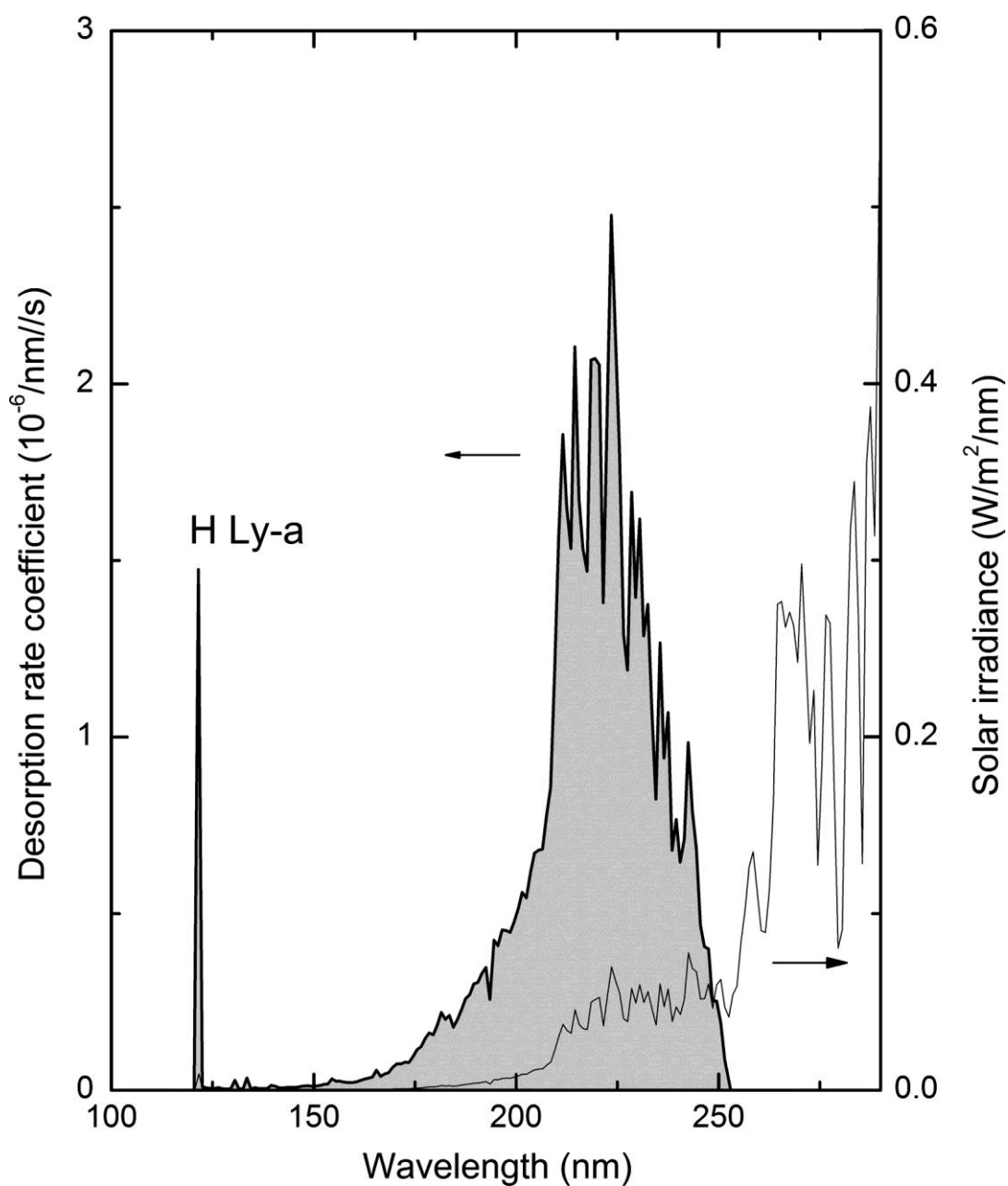


Figure 4.3 – Thin line: Solar irradiance on March 19, 1992, measured with UARS probe (Woods et al. 1996). Thick line: Desorption rate/nm at the sub-solar point. The area indicated by the shading gives the total desorption rate of  $7 \times 10^{-5} \text{ s}^{-1}$ .

most of the ejected water will be re-deposited, hopping on the surface with longer times between hops for decreased normal illumination, such as in slopes and at high latitudes. While hopping, the molecules may be removed from the exosphere by solar UV (Crider & Vondrak 2002). Using the photo-rates of Huebner et al. (1992), the water molecules diffusing above the lunar surface may be photoionized – at a rate of  $0.4 - 1 \times 10^{-6} \text{ s}^{-1}$  (quiet-active Sun) – and removed as solar wind pick-up ions. Alternatively, the water molecule may be photodissociated at a rate of  $1.2 - 2.1 \times 10^{-5} \text{ s}^{-1}$ . By momentum conservation in photodissociation, the lighter H carries most of the energy and may escape gravity, while the slower OH may remain on the soil.

The mechanism described can be responsible for redistributing water across the lunar surface, including transport of water from illuminated polar ice to warmer regions. For solar ion-derived desorption, we use a solar wind flux of  $\phi = 9.0 \times 10^6 \text{ He}^+ \text{ cm}^{-2} \text{ s}^{-1}$  (Johnson 1990) at 1 AU and measured sputtering cross section of  $1.2 \times 10^{-16} \text{ cm}^2$  to determine the lifetime of a water molecule adsorbed on the lunar surface. We find that water on lunar soil under helium ion bombardment is 29 years. Including the estimated contribution of sputtering by solar wind protons (96%), the lifetime decreases to ~12 years. These values are ~4 orders of magnitude larger than those for photodesorption; thus we conclude that water migration on the lunar surface by solar energetic radiation is dominated by ultraviolet photodesorption.

## Acknowledgements

This work was supported by NASA Cosmochemistry and an NESSF fellowship to MJS.

## References

Antoniewicz, P.R., Phys. Rev. B **21**, 3811 (1980).

- Arnold, J. R., J. Geophys. Res. **84**, 5659 (1979).
- Burke, D.J., Dukes, C.A., Kim, J.-H., Shi, J., Famá, M., Baragiola, R.A., Icarus **211**, 1082 (2011).
- Cassidy, T. A., Johnson, R.E., Icarus **176**, 499 (2005).
- Chiba, K., Tanaka, S., Yoneoka, T., J. Nucl. Mat. **335**, 493 (2004).
- Clark, R. N., Science **326**, 562 (2009).
- Crider, D.H. and Vondrak, R.R., Adv. Space Res. **30**, 1869 (2002).
- Famá, M., Shi, J., Baragiola, R.A., Surface Sci. **602**, 156-161 (2008).
- Fulvio, D., Raut, U., Baragiola, R.A., J. Astrophys. Lett. **752**, L33 (2012).
- Gadzuk, J.W., J. Chem. Phys. **137**, 091703 (2012).
- Huebner, W.F., Keady, J.J., Lyon, S.P., **195**, 1 (1992).
- Ichimura, A.S., Zent, A.P., Quinn, R.C., Sanchez, M.R., Taylor, L.A., Earth Planet. Sci. Lett. **345**, 90 (2012).
- Johnson, R.E., Energetic Charged-particle Interactions with Atmospheres and Surfaces, Springer-Verlag, Berlin (1990).
- Johnson, R.E., Baragiola, R.A., Geophys. Res. Lett. **18**, 2169 (1991).
- Loeffler, M.J., Dukes, C.A., Baragiola, R.A., J. Geophys. Res. **114**, E03003 (2009).
- Managadze, G.G., Cherepin, V.T., Shkuratov, Y.G., Kolesnik, V.N., Chumikov, A.E., Icarus **215**, 229 (2011).
- Menzel, D., J. Chem. Phys. **137**, 091702 (2012).
- Pieters, C. M. et al., Science **326**, 568 (1999).
- Raut, U., Fulvio, D., Loeffler, M. J., Baragiola, R. A., J. Astrophys. **752**, 159 (2012).



- Sunshine, J. M., Farnham, T. L., Feaga, L. M., Groussin, O., Merlin, F., Milliken, R. E., A'Hearn, M. F., *Science*. **326**, 565 (2009).
- Wolf, M., Nettensheim, S., White, J.M., Hasselbrink, E., Ertl, G., *J. Chem. Phys.* **94**, 4609 (1991).
- Woods, T.N. et al., *J. Geophys. Res.* **101**, 9541 (1996).
- Woods, T.N., Rottman, G., *Geophys. Monograph Ser.* **230**, 221 (2002).
- Zhu, X.-Y., White, J.M., Wolf, M., Hasselbrink, E., Ertl, G., *J. Phys. Chem.* **95**, 8393 (1991).

## CHAPTER 5

### Irradiation Effects of Methane-Laden Porous Amorphous Solid Water Films in the Outer Solar System

---

#### Abstract

We report that irradiation, in the presence of ambient methane, by 100-keV protons of microporous amorphous water (ASW) ice increases gas adsorption within the ice pores by as much as ~35% at 50 K. A previous study has shown that irradiation-induced adsorption enhancement can be caused by increased binding energy within the radiation-modified pores, before the pores collapse due to sustained ion impact (Shi et al. 2009). We find that the effect is greatest for lower ion fluxes due to increased time between pore-collapse events to allow for maximum methane adsorption. The gas uptake equilibrates above ion doses of  $\sim 5 \times 10^{14} \text{ H}^+ \text{ cm}^{-2} \text{ s}^{-1}$ . The impinging protons also cause dissociation of water and adsorbed methane molecules within the ice pores, and recombination into other C-, H-, and O-containing species such as  $\text{CO}_2$ , CO,  $\text{CH}_3\text{OH}$ , and  $\text{H}_2$ , which become trapped in the radiolyzed ice and contribute to increased adsorption. These experiments suggest a dual mechanism for enhanced gas trapping on the surfaces of icy Outer Solar System satellites with tenuous atmospheres that are subject to radiation processing, such as trans-Neptunian objects (TNOs) and Centaurs, including the Pluto-Charon system observed by NASA's *New Horizons* mission.

#### 5.1 Introduction

Visible and near-infrared spectra of a number of the TNOs and Centaurs have shown that their surfaces are composed of ices containing primarily  $\text{H}_2\text{O}$ ,  $\text{CH}_4$ ,  $\text{N}_2$ ,  $\text{CH}_3\text{OH}$ ,  $\text{C}_2\text{H}_6$ , CO,  $\text{CO}_2$ ,  $\text{NH}_3$ , and HCN, with relative amounts of different constituents varying among the TNOs,

including Triton, Pluto and Charon, and Eris, as well as Centaurs (de Bergh et al. 2013). Recently, the Ralph visible and infrared spectrometer onboard *New Horizons* constrained the surface compositions of Pluto and Charon to spatially heterogeneous mixtures of H<sub>2</sub>O, CH<sub>4</sub>, CO, C<sub>2</sub>H<sub>6</sub>, NH<sub>3</sub>, and N<sub>2</sub> (Cruikshank et al. 2015, Grundy et al. 2016).

The surfaces of TNOs are continually processed by energetic cosmic rays, solar wind ions, electrons, and ultraviolet photons. Radiation processing of planetary surfaces is known to result in the production of atmospheres/exospheres via sputtering, as well as changes in surface composition due to radiolysis, photolysis, and radio/photosynthesis. Indeed, laboratory experiments have demonstrated that ion irradiation reduces the porosity of microporous ices (Palumbo et al. 2006, Raut et al. 2007a, 2008, Famá et al. 2010). However, the exact nature of the pore collapse is not well understood, and may result from a process of pore coalescence, preferential depletion of smaller pores, or pore wall smoothing, as the pore internal surface area has been observed to decrease at a faster rate than the pore volume (Raut et al. 2007a). Although ASW films deposited at low temperatures develop porosity upon accretion regardless of growth conditions (Raut et al. 2007b), the spectroscopic signature of porosity – the ~2.7- $\mu$ m O-H dangling bond absorption bands – has not yet been detected on the Outer Solar System satellites. One possibility is that continual exposure to radiation by cosmic rays and solar wind has compacted the surficial ice over time, diminishing the O-H signal, although the absence of dangling bonds does not necessarily imply non-porous ices (Raut et al. 2007a), also demonstrated in Chapter 3.2 for thermally-compacted ice.

In Outer Solar System environments, an additional factor is the exposure of the irradiated ice to ambient gases, allowing possible synergistic effects between radiation-induced pore collapse and gas adsorption by the ice. Observations made during the *New Horizons* flyby

revealed a layered atmospheric haze above Pluto, dominated by molecular nitrogen but also containing  $\text{CH}_4$ ,  $\text{C}_2\text{H}_2$ ,  $\text{C}_2\text{H}_4$ , and  $\text{C}_2\text{H}_6$  (Gladstone et al. 2016), similar in composition to other TNOs such as Triton. Interaction between the ice, ambient gas, and radiation has been investigated previously by Shi et al. (2009), who found that ASW, irradiated by ions in the presence of ambient oxygen, has enhanced adsorption of  $\text{O}_2$  as high as five-fold compared with  $\text{O}_2$  adsorption by unirradiated ice. The adsorbed  $\text{O}_2$  remained trapped in the ice even when the ambient gas was removed by pumping, suggesting that magnetospheric ion interaction with icy surfaces may be responsible for trapped gases observed on Outer Solar System satellites (Johnson 1981, Tokar 2006, Spencer 1995, Cruikshank et al. 2015, Grundy et al. 2016).

Previous studies have shown that ion irradiation affects the ice pores in two ways. First, it increases the binding energy of an empty adsorption site, thereby making it available for gas adsorption under the same pressure (Shi et al. 2009). Increased binding energy with the adsorbate can result, for example, from ion-induced reduction in pore size (Raut et al. 2007a, Shi et al. 2009) for pores that had dimensions of a few molecular diameters prior to irradiation (Mayer & Pletzer 1986). Binding energy with the adsorbate increases with the proximity of the pore walls, which increases the extent of overlapping between interaction potentials of opposite walls and thus deepens the potential well for adsorption (Rouquerol et al. 1999). The second way in which ion impacts influence the ice pores is by causing them to collapse over time, decreasing the number of sites available for adsorption (Palumbo 2006, Raut et al. 2007a). The net effect of competition between these two processes – increased binding energy and pore collapse – results in increased gas adsorption when the ice is exposed to ambient  $\text{O}_2$  under ion irradiation (Shi et al. 2009), and, as we show in Chapter 6.1, a net adsorption *decrease* with ambient  $\text{H}_2$  (Raut et al. 2015).

To better understand the process for gas adsorption on icy bodies in the Outer Solar System, we performed 100 keV  $H^+$  irradiation of porous  $H_2O$  ice films loaded with  $CH_4$ , two abundant molecular species on TNOs. Previous high-energy proton irradiation studies of co-deposited  $H_2O$ - $CH_4$  mixtures at low temperatures have shown the production of radiolytic molecules such as  $C_2H_6$ ,  $C_2H_4$ ,  $CH_3OH$ ,  $C_2H_5OH$ ,  $CO$ ,  $CO_2$ ,  $H_2CO$ ,  $CH_3COH$ ,  $CH_4$ , and  $C_3H_8$ , whose relative abundances depended on the initial  $H_2O$ - $CH_4$  ratio (Moore & Hudson 1998). We look for similar radiolytic synthesis during the 100 keV  $H^+$  irradiation of pure  $H_2O$  ice exposed to ambient  $CH_4$ , analyzing the chemical changes and gas adsorption kinetics to understand the effects of ion bombardment on the interaction between the ice and exospheric gases.

## 5.2 Experimental Methods

The experiments were performed in an ultrahigh vacuum (UHV) chamber cryopumped to a base pressure of  $\sim 10^{-10}$  Torr. Water ice films were vapor-deposited at an angular incidence of  $45^\circ$  onto the optically flat gold electrode of a quartz crystal microbalance (QCM) through a collimating micro-capillary array (MCA) doser at 70 K. Target temperatures were maintained by a closed-cycle refrigerator with controlled resistive heating, and measured with a silicon diode mounted next to the QCM. The porosity of the films was  $\sim 21\%$  according to measurements by Shi et al. (2009), using UV-visible spectroscopic interferometry for ice deposited at the same deposition temperature and incidence angle. The column density  $\eta$  (molecules  $cm^{-2}$ ) of the water ice films was determined from the change in resonant frequency of the QCM by dividing by the molecular mass (Sack & Baragiola 1993). All films were deposited to a column density of 5000 ML  $H_2O$ , where  $1 \text{ ML} = 10^{15} \text{ H}_2\text{O cm}^{-2}$ , in order to compare with previous experiments using  $O_2$  and Ar (Shi et al. 2009). Films were deposited at a rate of  $1.2 (\pm 0.5) \text{ ML s}^{-1}$ .

Following the growth of the water ice films at 70 K, the films were cooled to temperatures between 40 K and 50 K and subsequently exposed to background  $^{13}\text{CH}_4$  at a constant pressure of  $7 (\pm 1) \times 10^{-7}$  Torr, using the MCA doser. Isotopic methane was chosen because the infrared absorption bands of  $^{13}\text{C}$ -containing substances are shifted to lower wavenumbers than their  $^{12}\text{C}$ -containing counterparts, allowing experimental differentiation from adventitious  $^{12}\text{C}$  that can accumulate in the film from spurious sources. The column density of  $^{13}\text{CH}_4$  absorbed by the porous water ice films was obtained from the measured decrease in QCM frequency.

While maintaining the ice temperature and ambient methane pressure, the films were irradiated at  $9^\circ$  incidence from surface normal, with 100-keV protons from a 300-kV ion accelerator with a magnetic mass/charge filter. The beam was rastered by electrostatic deflection plates to ensure uniform irradiation of the films. The ion irradiation fluxes were varied from 2.2 to  $196 \times 10^{10} \text{ H}^+ \text{ cm}^{-2} \text{ s}^{-1}$ , monitored by a thin wire placed in the path of the beam, calibrated against a Faraday cup in the same position. The integrated fluences reached up to  $1.5 \times 10^{15} \text{ H}^+ \text{ cm}^{-2}$ .

The chemical changes in the films induced by ion irradiation were studied using infrared spectroscopy. Specular reflectance spectra of the films were collected at  $35^\circ$  incidence using a Thermo Nicolet 670 Fourier transform infrared (FTIR) spectrometer, thoroughly purged with dry air, at  $2 \text{ cm}^{-1}$  resolution. The ion beam was aligned by exploiting the ion-induced luminescence of a deposited Ar film in a separate experiment (Grosjean et al. 1997), in a technique described in Chapter 2.4. Single-beam infrared spectra  $R$  were divided by the reflectance spectrum  $R_0$  of the bare gold QCM substrate, which was collected prior to ice deposition. The ratios were then converted to optical depth,  $-\ln(R/R_0)$ . The areas of infrared absorption bands were calculated

from the optical depth spectra by subtracting polynomial baselines that matched the absorption continuum, then integrating the absorption region.

### 5.3 Results and Discussion

#### *I. Temperature Dependence of Methane Adsorption in Ice Pores*

Figure 5.1 shows the increase in column density  $\eta$  of methane adsorbed in 5000-ML porous ASW films during exposure of the unirradiated ice to an ambient  $^{13}\text{CH}_4$  background of  $7 (\pm 1) \times 10^{-7}$  Torr. During methane exposure at 40 to 50 K, above the temperature ( $\sim 35$  K) at which multilayer condensation occurs (Raut et al. 2007a), the column density of  $^{13}\text{CH}_4$ -equivalent molecules, as measured by the QCM, increased steadily due to the net effect between adsorption due to the constant methane flux and thermal desorption. After methane was admitted into the chamber, the uptake by the film increased linearly with time and asymptotically approached an equilibrium level at which the adsorption and desorption rates equilibrate. At higher ice temperatures, the equilibrium uptake of methane at constant pressure decreased and was reached more quickly, since desorption rates increase with temperature. The equilibrium amounts of methane uptake by the ice films were 384 ML at 40 K, 238 ML at 45 K, and 78 ML at 50 K. The adsorbed gas was not permanently trapped in water ice at these temperatures; all adsorbed gas left the ice film when the ambient pressure was removed by pumping. Previous work on  $\text{O}_2$  has shown that gas uptake by ASW films does not increase linearly with increasing film thickness, implying that the adsorption mainly occurs within the micropores near the ice surface (Shi et al. 2009).

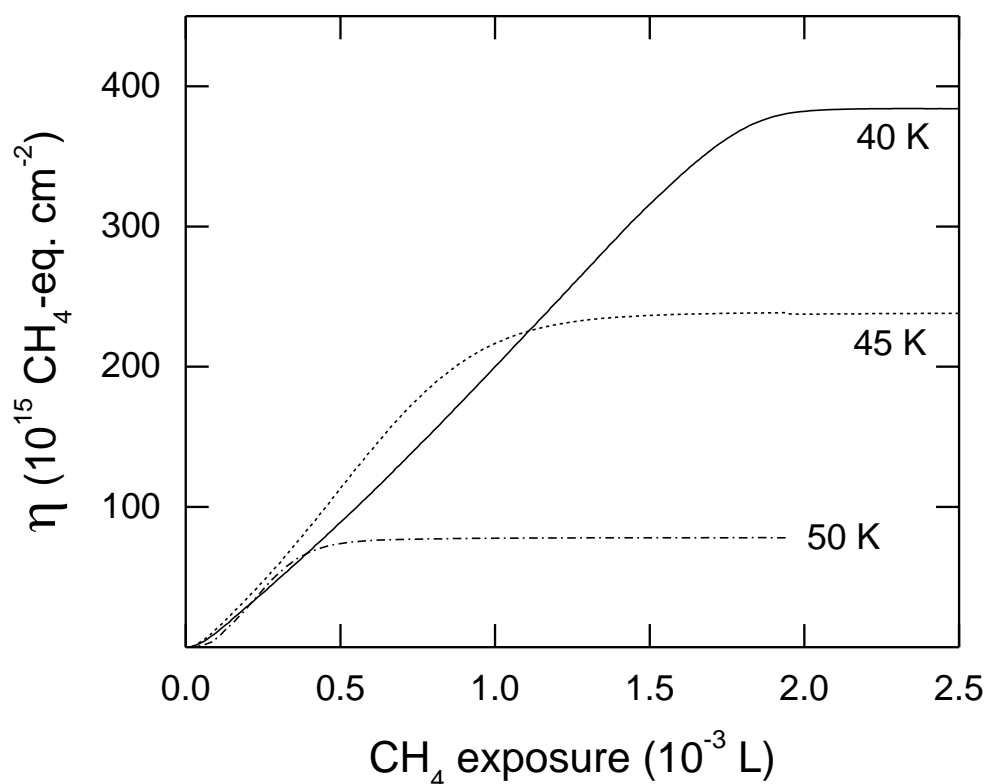


Figure 5.1 – Kinetics of  $^{13}\text{CH}_4$  uptake during methane exposure of unirradiated porous ice films to  $7 (\pm 1) \times 10^{-7}$  Torr of  $^{13}\text{CH}_4$  at 40 K, 45 K, and 50 K. Ice films, 5000 ML thick, were deposited at  $45^\circ$  incidence at 70 K. The amount of  $^{13}\text{CH}_4$  uptake as measured by the microbalance increases with time until a temperature-dependent saturation point is reached. The equilibrium amounts of methane uptake by the ice films were 384 ML at 40 K, 238 ML at 45 K, and 78 ML at 50 K. 1 Langmuir (L) =  $10^{-6}$  Torr-second.



A previous study has shown that gas uptake in porous ASW will reach an equilibrium level for methane pressures  $P_{\text{max}} < 2 \times 10^{-5}$  Torr at 40 K (Raut et al. 2007a, b). Above  $P_{\text{max}}$ , methane continuously condenses on the ice and forms layers. For low pressures  $P$  where the relative pressure  $p = P/P_{\text{max}} < 0.1$ , the equilibrium adsorption has been shown to occur at high-energy binding sites, such as in small pores. For increasing  $p$ , adsorption sites of successively lower binding energy, i.e. sites with less proximal pore walls (Rouquerol et al. 1999), are filled until equilibrium is reached. In our experiments,  $p \sim 0.04$ , placing us well within the low- $p$  regime in which adsorption occurs in high-energy binding sites. Since adsorption binding energy is related to temperature as well as the close proximity of pore walls (Rouquerol et al. 1999), there is a smaller distribution of high-energy binding sites at increasing temperatures with constant pressure. Coupled with the increase in thermal desorption with increasing temperature, this can explain the observed temperature dependence of methane adsorption isotherms at constant pressure.

## II. *Ion-Enhanced Gas Adsorption*

Figure 5.2A shows increased adsorption  $\Delta\eta$  at 50 K – above the equilibrium uptake of 78 ML – during 100 keV  $\text{H}^+$  irradiation of the ASW film in presence of constant  $^{13}\text{CH}_4$  pressure. The increase in gas adsorption with irradiation is consistent with previous measurements with oxygen and argon (Shi et al. 2009). The films were irradiated at constant flux and temperature, and under constant methane pressure, until a second, higher equilibrium in adsorption was reached by ion fluences of  $\sim 5 \times 10^{14} \text{ H}^+ \text{ cm}^{-2} \text{ s}^{-1}$ . The maximum uptake varied with irradiation flux, from 13 to  $200 \times 10^{10} \text{ H}^+ \text{ cm}^{-2} \text{ s}^{-1}$ . As we will show in Section III, the increase in column density can be attributed to the entrapment of multiple molecular species in the ice, rather than

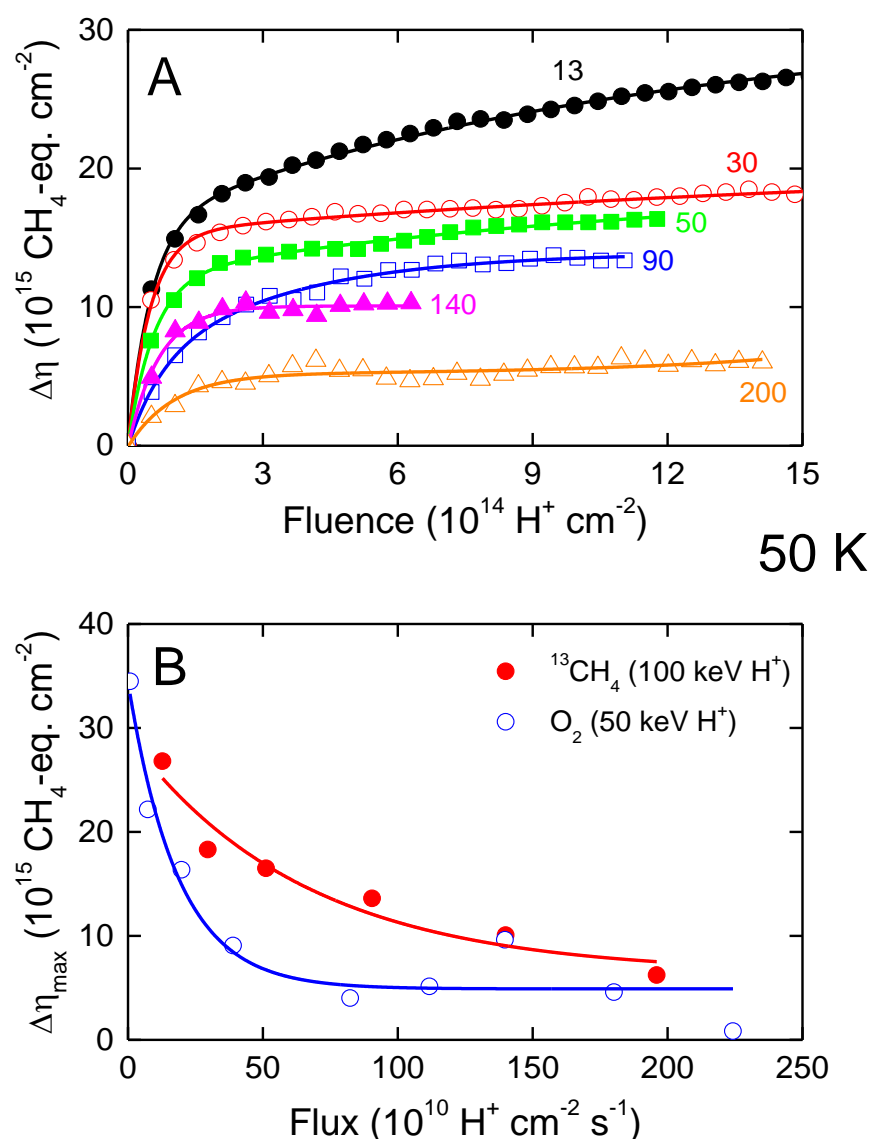


Figure 5.2 – Panel A: Net ion-induced equivalent  $\text{CH}_4$  uptake ( $\Delta\eta$ ) in 5000-ML porous  $\text{H}_2\text{O}$  ice films vs. fluence during 100 keV  $\text{H}^+$  irradiation at 50 K, following a pre-irradiation uptake of 78 ML from  $\sim 7 \times 10^{-7}$  Torr  $\text{CH}_4$  exposure for different ion fluxes. This pressure was maintained during irradiation. The curves are labelled with the flux, in  $10^{10} \text{ H}^+ \text{ cm}^{-2} \text{ s}^{-1}$ . Panel B: Flux dependence of the maximum ion-induced uptake. The methane uptake is compared to that of similar experiments with  $\text{O}_2$  (Shi et al. 2009). Lines are to guide the eye.

solely  $^{13}\text{CH}_4$ , and thus the increase in column density is expressed in units of  $^{13}\text{CH}_4$ -equivalent per unit area. For the low-flux irradiation at  $13 \times 10^{10} \text{ H}^+ \text{ cm}^{-2} \text{ s}^{-1}$ , the amount of adsorbed gas in the ice film did not reach saturation after 3.5 hours of irradiation, at which point the experiment was stopped.

Figure 5.2B shows the flux dependence of the ion-induced methane uptake enhancement in the radiolyzed ice film. Each data point (closed red circles) represents the maximum  $^{13}\text{CH}_4$ -equivalent column density reached during irradiation at a given flux in Figure 5.2A. The adsorption enhancement is largest at low fluxes, with  $\eta$  increasing by as much as 34% before the lowest-flux experiment was stopped, and decreases with increasing flux. This data is compared with the adsorption enhancement of  $\text{O}_2$  in radiolyzed porous water ice films, deposited using similar conditions and irradiated with 50 keV  $\text{H}^+$  irradiation at 50 K (Shi 2009). The fit to the  $\text{O}_2$  trapping data is discussed by Shi et al. (2009).

We find that, similar to the case of  $\text{O}_2$ , competition between pore collapse and the conversion of low- into high-energy binding sites has the net effect of increasing gas adsorption in porous ice films irradiated in the presence of ambient methane. This is supported by the observed dependence on irradiation flux: The increased time duration between successive proton impacts allows for more gas adsorption at sites that are increasing in binding energy within the gradually compacting pores. The differing behavior in flux dependence between the  $\text{CH}_4$  and  $\text{O}_2$  experiments are likely not due to the different ion energies used between the experiments, since TRIM calculations show that the electronic stopping power for 100-keV  $\text{H}^+$  in ice is only  $\sim 2\%$  larger than that for 50-keV  $\text{H}^+$  (Ziegler & Biersack 2013). The different flux dependences are more likely caused by additional factors behind adsorption enhancement in  $\text{CH}_4$  that were not observed for  $\text{O}_2$ , such as the synthesis of radiolytic molecules.

### III. *Radiolytic Conversion of Methane and Water Ice into New Species*

Figure 5.3 shows the infrared absorption features, as a function of ion fluence, in the 4350 to 960  $\text{cm}^{-1}$  range at 40 K during 100 keV  $\text{H}^+$  irradiation of ice in the presence of a constant pressure of  $^{13}\text{CH}_4$ . The spectra, collected prior to irradiation and after ion doses of 0.90 and  $10.2 \times 10^{15} \text{ H}^+ \text{ cm}^{-2}$ , reveal that the adsorbed methane present in the pores reacts with the ice matrix during ion irradiation to form new molecular species. These spectral changes include the decrease in  $^{13}\text{CH}_4$  adsorption bands (4291, 4192, 2998, 2902, 1294  $\text{cm}^{-1}$ ) and the increase in adsorption bands of  $^{13}\text{C}$ -containing molecules such as  $\text{CO}_2$  (2275  $\text{cm}^{-1}$ ),  $\text{CO}$  (2088  $\text{cm}^{-1}$ ),  $\text{H}_2\text{CO}_3$  (2826, 2596, 1458  $\text{cm}^{-1}$ ),  $\text{CH}_3\text{OH}$  (1120, 997  $\text{cm}^{-1}$ ),  $\text{HCO}$  (1815  $\text{cm}^{-1}$ ),  $\text{CH}_3\text{CHO}$  (1333  $\text{cm}^{-1}$ ), and  $\text{C}_2\text{H}_5\text{OH}$  (1065  $\text{cm}^{-1}$ ), as well as  $\text{H}_2$  (4140  $\text{cm}^{-1}$ ). Besides these molecules, additional  $^{13}\text{C}$ -containing radiolytic products, whose features are not visible in Figure 5.3, were observed in the spectra, including  $\text{C}_3\text{H}_8$  (2908, 1331  $\text{cm}^{-1}$ ),  $\text{C}_2\text{H}_6$  (2932, 2908, 2859, 1445  $\text{cm}^{-1}$ ),  $\text{C}_3\text{O}_2$  (2258  $\text{cm}^{-1}$ ),  $\text{H}_2\text{CO}$  (1477, 1220  $\text{cm}^{-1}$ ), and additional  $\text{H}_2\text{CO}_3$  features (1675, 1268  $\text{cm}^{-1}$ ). Infrared positions of  $^{13}\text{C}$ -containing species, as well as the positions of their  $^{12}\text{C}$ -containing counterparts from the literature, are listed in Table 5.1. We note that the optical depth of  $^{13}\text{CO}_2$  at the maximum fluence of  $10.2 \times 10^{15} \text{ H}^+ \text{ cm}^{-2}$  is  $\sim 80$  times that of  $^{12}\text{CO}_2$  (2343  $\text{cm}^{-1}$ ), implying a negligible amount of adventitious  $^{12}\text{C}$  adsorbed in the  $\text{H}_2\text{O}$  film.

The ion-induced dissociation of methane in  $\text{H}_2\text{O}$  ice and the production of C-containing radiolytic species occur simultaneously. As they move through the solid, protons displace atoms and electrons, breaking molecular bonds of the  $\text{CH}_4$  into constituent species: C, CH,  $\text{CH}_2$ ,  $\text{CH}_3$ , and H as inferred by the infrared spectra. Gas-phase studies have shown that  $\text{H}_2\text{O}$  ice is radiolyzed predominantly through the  $\text{H}_2\text{O} \rightarrow \text{OH} + \text{H}$  dissociation channel (Slanger & Black 1982), rather than  $\text{H}_2\text{O} \rightarrow \text{O} + \text{H}_2$ , and this pathway may be even more likely in the solid phase

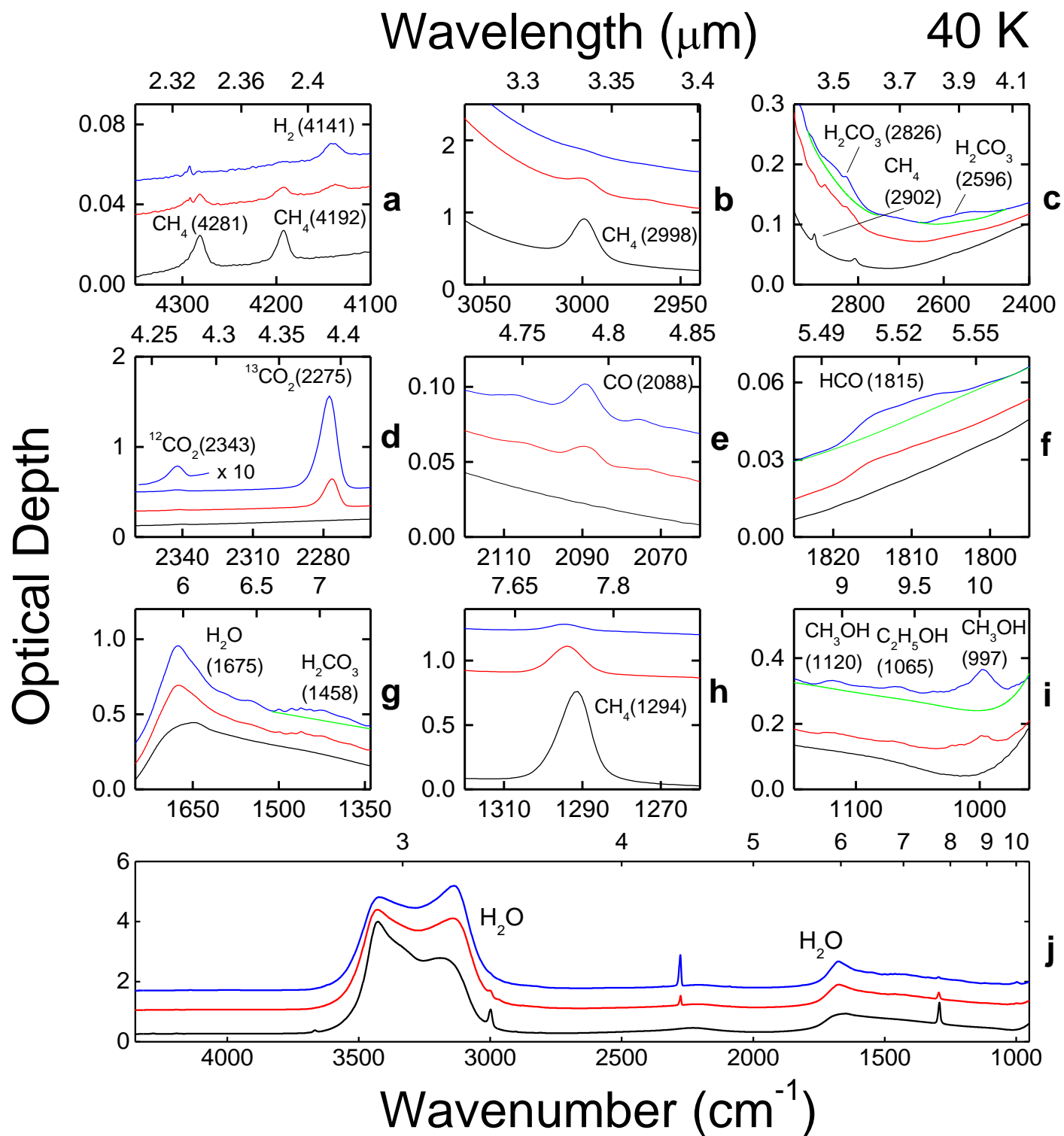


Figure 5.3 – Changes in absorption features in the infrared spectra of a 5000-ML porous H<sub>2</sub>O ice film irradiated with 100 keV H<sup>+</sup> in the presence of ambient <sup>13</sup>CH<sub>4</sub> at 40 K. The equilibrium uptake of methane within the ice pores was 384 ML prior to the onset of irradiation. Irradiation flux was  $2 \times 10^{12} \text{ H}^+ \text{ cm}^{-2} \text{ s}^{-1}$ . Black line in each panel shows the unirradiated sample, while the red and blue lines correspond to fluences of 0.90 and  $10.2 \times 10^{15} \text{ H}^+ \text{ cm}^{-2}$ , respectively. The green lines are polynomial fits to the baselines. Irradiation causes destruction of CH<sub>4</sub> (panel a, b and h) and production of many species, some of which are listed (with peak positions in cm<sup>-1</sup>) adjacent to the absorption bands. The full spectrum is shown in panel j. All spectra are vertically shifted for clarity. Table 5.1 lists additional <sup>13</sup>C-containing molecules produced from radiolysis of methane-water ice.

Species	<sup>13</sup> C absorption (cm <sup>-1</sup> )	<sup>12</sup> C absorption (cm <sup>-1</sup> )
CH <sub>4</sub>	4281	4300 <sup>1</sup>
	4192	4201 <sup>1</sup>
	2998	3007 <sup>2</sup>
	2902	2904 <sup>2</sup>
	1294	1302 <sup>3</sup>
CO <sub>2</sub>	2275	2342 <sup>3</sup>
CO	2088	2137 <sup>3</sup>
H <sub>2</sub> CO <sub>3</sub>	2826	2850 <sup>4</sup>
	2596	2620 <sup>4</sup>
	1675	1705 <sup>5</sup>
	1458	1483 <sup>4</sup>
	1268	1292 <sup>4</sup>
CH <sub>3</sub> OH	1120	1128 <sup>3</sup>
	997	1017 <sup>3</sup>
HCO	1815	1844 <sup>6</sup>
CH <sub>3</sub> COH	1333	1350 <sup>3</sup>
C <sub>2</sub> H <sub>5</sub> OH	1065	1091 <sup>3</sup>
C <sub>3</sub> H <sub>8</sub>	2908	2962 <sup>3</sup>
	1331	1373 <sup>3</sup>
C <sub>2</sub> H <sub>6</sub>	2932	2975 <sup>3</sup>
	2908	2940 <sup>3</sup>
	2859	2881 <sup>3</sup>
	1445	1464 <sup>3</sup>
C <sub>3</sub> O <sub>2</sub>	2258	2237 <sup>3</sup>
H <sub>2</sub> CO	1477	1499 <sup>7</sup>
	1220	1248 <sup>7</sup>

<sup>1</sup>Brunetto et al. 2005

<sup>2</sup>Bennett & Kaiser 2007

<sup>3</sup>Moore & Hudson 1998

<sup>4</sup>Zheng & Kaiser 2007

<sup>5</sup>Moore & Khanna 1991

<sup>6</sup>Moore et al. 1995

<sup>7</sup>Hudson & Moore 2000

Table 5.1 – Absorption band positions in the infrared spectra of <sup>13</sup>C-containing molecules produced from 100 keV H<sup>+</sup> irradiation of 5000-ML porous H<sub>2</sub>O film in the presence of ambient <sup>13</sup>CH<sub>4</sub> at 40 K. Infrared absorption positions for <sup>13</sup>C-containing species are compared their <sup>12</sup>C-containing counterparts available in the literature.

due to the cage effect (Loeffler et al. 2006). This allows for numerable routes by which new molecular species can be formed via recombination of radicals. For example, a possible route for the solid-state formation of methanol is the transfer of energy from the incident proton, resulting in dissociation of methane into methyl and H radicals (Moore & Hudson 1998),



followed by the reaction of the methyl radical with radiolytic hydroxyl, from dissociated  $\text{H}_2\text{O}$  (Moore & Hudson 1998):



However, the methyl radical could also react with another  $\text{CH}_3$  to form ethane (Moore & Hudson 1998):



We detect both  $\text{CH}_3\text{OH}$  and  $\text{C}_2\text{H}_6$  in our radiolyzed ice, indicating competition between multiple dissociation and recombination pathways.

The observation of trapped radiolytic  $\text{H}_2$  is surprising because it would typically be expected to easily diffuse out of the ice. We show another instance of  $\text{H}_2$  trapping in radiolyzed porous ice in Chapter 6.1. Additionally, as a homonuclear molecule that undergoes no net change in its dipole moment from infrared absorption,  $\text{H}_2$  is typically infrared-inactive. However, interactions of  $\text{H}_2$  with neighboring water molecules can perturb the vibrational mode (Warren et al. 1980), allowing some absorption of infrared radiation. A weak feature for  $\text{H}_2$  at  $4140 \text{ cm}^{-1}$ , noted previously (Sandford & Allamandola 1993, Loeffler et al. 2010), is observed to increase with fluence (panel a).

Figure 5.4 shows the exponential decrease in the  $^{13}\text{C}$ -H-bending absorption band at  $1294 \text{ cm}^{-1}$  for  $^{13}\text{CH}_4$ , with increasing fluence at 40 K, to a maximum ion dose of  $1 \times 10^{16} \text{ H}^+ \text{ cm}^{-2}$ .



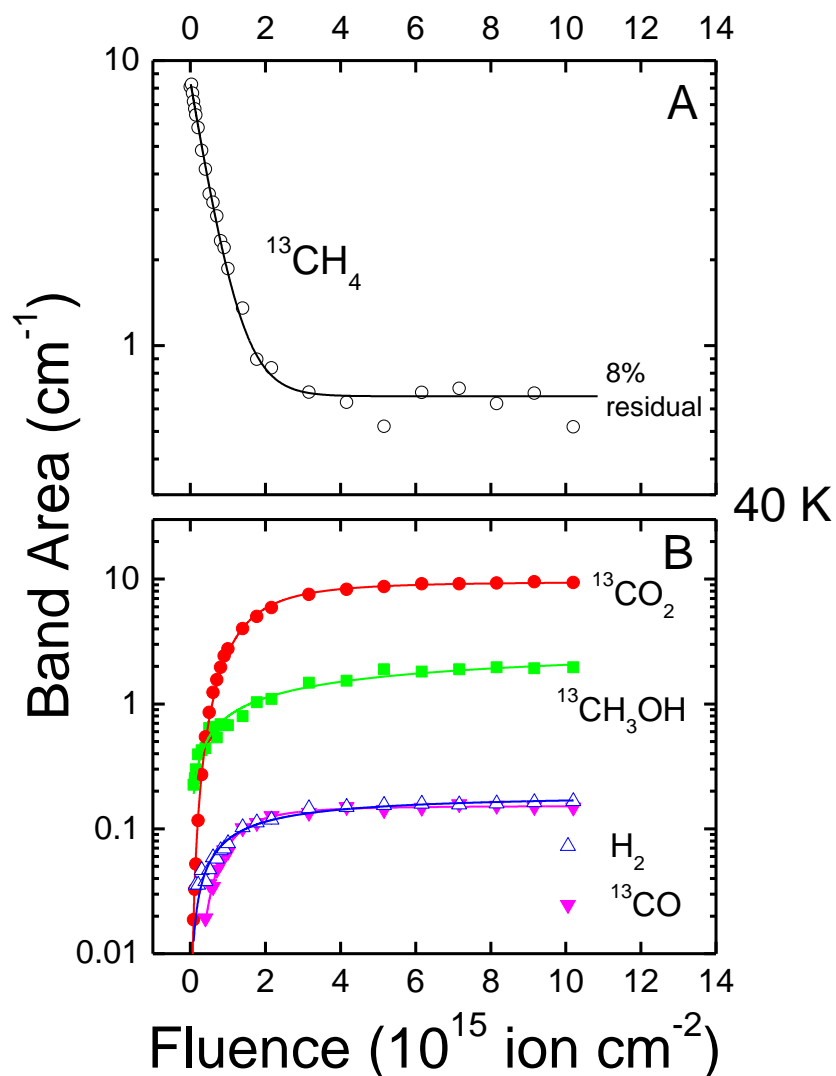


Figure 5.4. – Fluence dependence of band areas of  $^{13}\text{CH}_4$  ( $1294 \text{ cm}^{-1}$ ),  $^{13}\text{CO}_2$  ( $2275 \text{ cm}^{-1}$ ),  $^{13}\text{CO}$  ( $2088 \text{ cm}^{-1}$ ),  $\text{H}_2$  ( $4140 \text{ cm}^{-1}$ ), and  $^{13}\text{CH}_3\text{OH}$  ( $997 \text{ cm}^{-1}$ ) during 100 keV  $\text{H}^+$  irradiation of a 5000-ML  $\text{H}_2\text{O}$  porous ice film initially containing 384 ML of  $^{13}\text{CH}_4$  at 40 K. Irradiation flux was  $2 \times 10^{12} \text{ H}^+ \text{ cm}^{-2} \text{ s}^{-1}$ . The solid black line through  $^{13}\text{CH}_4$  data points is an exponential fit (Eq. 4) with extracted destruction cross-section  $\sigma_d = 1.89 (\pm 0.05) \times 10^{-15} \text{ cm}^2$ . Other lines are guides to the eye.

Prior to the onset of irradiation, 384 ML methane was adsorbed in the pores of the 5000-ML ice film, corresponding to a band area of  $\sim 8 \text{ cm}^{-1}$ . The total amount of adsorbed methane decreased during irradiation, radiolytically decomposing to reach an equilibrium level at ion fluences greater than  $\sim 3.5 \times 10^{15} \text{ H}^+ \text{ cm}^{-2}$ . The  $\text{CH}_4$  abundance equilibrium occurs at 8% of the original adsorbed methane and is due to (1) residual gas trapped at high-energy binding sites within the collapsed pores and (2) regenerated  $\text{CH}_4$  by synthesis of disassociation products. The decrease in methane as a function of fluence for  $\text{CH}_4$ -loaded  $\text{H}_2\text{O}$  at 40 K was fitted to an exponential function of the form:

$$B(F) = B_0 e^{-\sigma_d F} + B_\infty, \quad (4)$$

where  $B_0$  is the pre-irradiation band area of  $^{13}\text{CH}_4$  adsorbed in the ice pores,  $B_\infty$  is the saturation band area, and the methane destruction cross-section  $\sigma_d$  is  $1.89 (\pm 0.05) \times 10^{-15} \text{ cm}^2$ .

Simultaneous with the decrease of methane in the ice film is the increase in infrared absorption band areas of radiolytic species  $^{13}\text{CO}_2$ ,  $^{13}\text{CO}$ ,  $\text{H}_2$ , and  $^{13}\text{CH}_3\text{OH}$  with fluence, shown in Figure 5.4B. The production of these species saturates above  $\sim 5 \times 10^{14} \text{ H}^+ \text{ cm}^{-2}$ , coinciding with the saturation of the decrease in  $\text{CH}_4$ . As noted previously, the 8% retention of methane at high fluence may partially arise from recombination of radiolyzed  $\text{CH}_4$  and  $\text{H}_2\text{O}$  radicals to reform  $\text{CH}_4$ .

We hypothesize that radiation chemistry can be partially responsible for the observed increase in gas uptake by the film, if the synthesized species are less volatile than methane. Similar effects have been noted previously: photodissociation by 193-nm photons was found solely responsible for enhanced mass uptake of  $\text{O}_2$  in  $\text{H}_2\text{O}$  ice at 40 – 80 K, due to photolytic production of  $\text{H}_2\text{O}_2$  and  $\text{O}_3$  (Shi et al. 2011). Pore compaction was ruled out as a contributing factor to the increase in adsorption because the impinging photons decreased the dangling bond

absorption bands by only a small amount. However, the reverse was true for 50-keV proton-irradiated ice in the presence of O<sub>2</sub> at 50 K (Shi et al. 2009); radiolysis was not observed in this instance, implying that only the net effect between pore collapse and increasing binding energy was responsible for the increase in O<sub>2</sub> adsorption. Similar adsorption enhancement and trapping was observed for ambient argon in ASW, implying that gas trapping can indeed result without contribution from radiation chemistry (Shi et al. 2009). According to our infrared results, however, most of the CH<sub>4</sub> adsorbed in the pores of the ice film is radiolytically decomposed into new species, contributing to the observed adsorption uptake. To further understand the extent to which radiolytic species such as CO<sub>2</sub>, CO, and CH<sub>3</sub>OH are trapped in the ice, we performed temperature-programmed desorption of the radiolyzed film, described in the next section.

#### IV. *Thermal Desorption of Irradiated Films*

In one experiment, following the growth of a 5000-ML porous ice film at 70 K and methane adsorption saturation of 375 ML at 40 K, the film was cooled to 20 K, and the ambient <sup>13</sup>CH<sub>4</sub> was gradually removed by pumping. The temperature decrease leads to increased adsorption of methane within the ice pores, which we equilibrated by simultaneously reducing the ambient CH<sub>4</sub> pressure. The cooling rate and methane pressure were controlled such the resonant frequency measured by the QCM, which decreases during cooling with species adsorption and increases with mass loss, was held constant. The methane adsorbed in the pores is condensed onto the pore surfaces by 20 K, where thermal desorption is negligible (Raut et al. 2007a). Controlled cooling during ambient gas reduction monitoring via QCM ensured that *multilayers* of methane did not condense overtop the <sup>13</sup>CH<sub>4</sub>-saturated H<sub>2</sub>O pores. The condensed <sup>13</sup>CH<sub>4</sub>-H<sub>2</sub>O film was then irradiated at 20 K with 100 keV H<sup>+</sup> ( $2 \times 10^{12}$  H<sup>+</sup> cm<sup>-2</sup> s<sup>-1</sup>) to a fluence

of  $1.0 \times 10^{16} \text{ H}^+ \text{ cm}^{-2}$ , and then heated to 250 K at  $1 \text{ K min}^{-1}$ . The thermal desorption of the species trapped in the film due to irradiation were monitored via QCM, IR, and quadrupole mass spectrometry (QMS, 0 to 200 amu).

Figure 5.5A shows the mass loss rate of the column density  $\eta$  of  $\text{H}_2\text{O}$ -equivalent molecules, as measured by the QCM, begin to increase above  $\sim 150 \text{ K}$  and maximizes  $180 \text{ K}$ , the thermal desorption temperature for an  $\text{H}_2\text{O}$  ice film under UHV. Figure 5.5A shows that most of the mass loss by the film occurs at the temperature at which  $\text{H}_2\text{O}$  sublimates. Figure 5.5B shows mass profiles of  $^{13}\text{CH}_4$ ,  $^{13}\text{CH}_3$ ,  $^{13}\text{CH}_2$ ,  $^{13}\text{C}$ , and  $\text{H}_2$  desorbing at lower temperatures. In particular, residual trapped  $^{13}\text{CH}_4$  desorbs by  $\sim 80 \text{ K}$ . The partial pressures of  $\text{H}_2\text{O}$  and  $\text{OH}$  maximize at  $\sim 170 \text{ K}$ , corresponding well with the QCM measurements (Figure 5.5A).

Additional experiments are needed with the QMS mass-selected for other radiolytic species, including  $^{13}\text{CO}_2$ ,  $^{13}\text{CO}$ , and  $^{13}\text{CH}_3\text{OH}$ . However, infrared spectra reveal that these molecules remain trapped in the ice at surprisingly high temperatures (Figure 5.5C). The desorption trend of  $^{13}\text{CO}_2$  ( $2275 \text{ cm}^{-1}$ ) mirrors that of the ice matrix, suggesting that it is intimately correlated to the ice and remains trapped in pores, without diffusing, until the ice film is desorbed. On the other hand,  $^{13}\text{CO}$  ( $2088 \text{ cm}^{-1}$ ) is completely removed at lower temperatures, more gradually than  $^{13}\text{CO}_2$ , beginning at  $\sim 80 \text{ K}$  and disappearing by  $165 \text{ K}$ , consistent with the lower binding energy of  $\text{CO}$  with the ice, relative to  $\text{CO}_2$  (Sandford & Allamandola 1990). Methanol ( $997 \text{ cm}^{-1}$ ) begins to desorb above  $\sim 100 \text{ K}$  and decreases sharply at  $\sim 140 \text{ K}$ , consistent with previous  $\text{CH}_3\text{OH}$  studies (Notesco & Bar-Nun 1997, Burke & Brown 2010). Surprisingly,  $\text{H}_2$  ( $4140 \text{ cm}^{-1}$ ) remains trapped in the pores and does not disappear from the ice until it reaches  $\sim 150 \text{ K}$ , although thermal desorption begins to proceed gradually above  $\sim 40 \text{ K}$ , as is also evident from its mass spectrometry signal (Figure 5.5B). Although  $^{13}\text{CO}$ ,  $^{13}\text{CH}_3\text{OH}$ , and  $\text{H}_2$  desorb

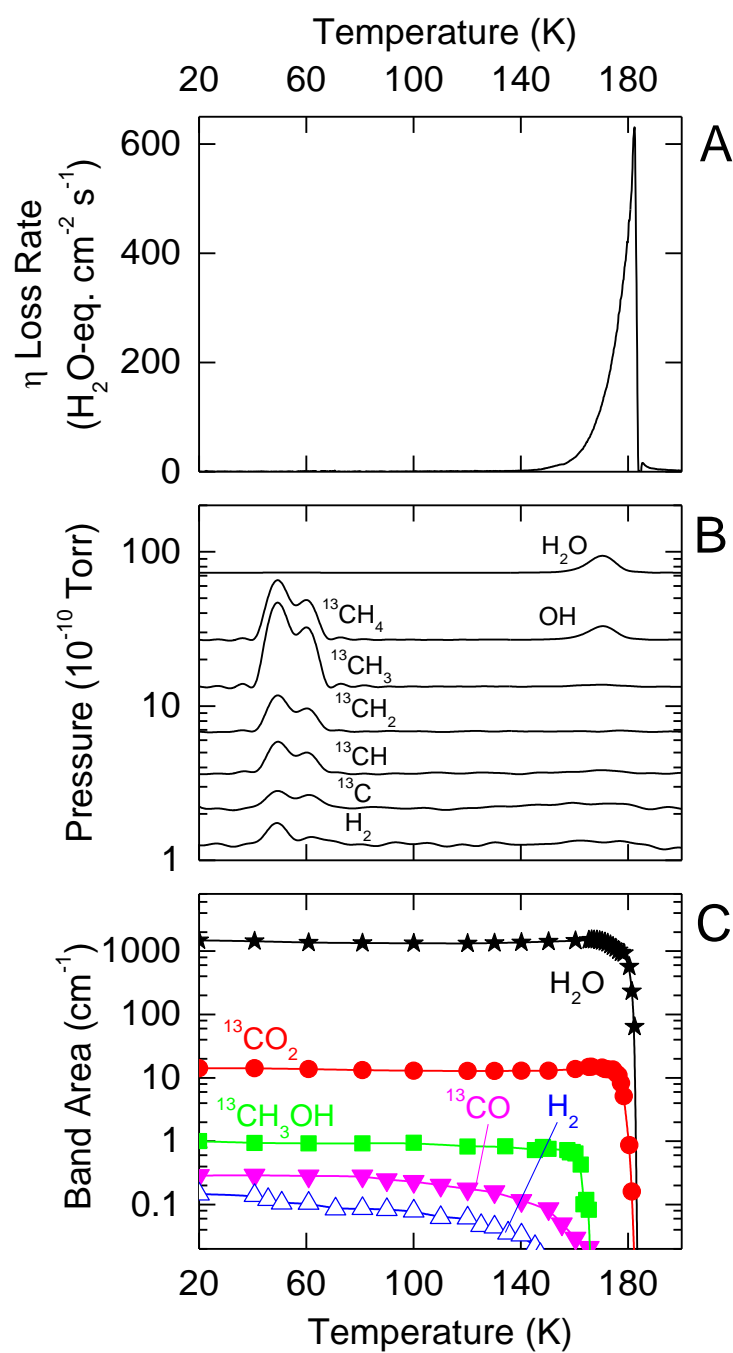


Figure 5.5 – Panel A: Rate of loss of column density  $\eta$  of  $\text{H}_2\text{O}$ -equivalent molecules in irradiated sample during warm-up from 20 K, following 100 keV  $\text{H}^+$  irradiation ( $2 \times 10^{12} \text{ H}^+ \text{ cm}^{-2} \text{ s}^{-1}$ ) of 5000-ML  $\text{H}_2\text{O}$  ice film loaded with 375 ML  $^{13}\text{CH}_4$  at 40 K, then cooled to 20 K while the

ambient methane was pumped. The condensed  $^{13}\text{CH}_4\text{-H}_2\text{O}$  film was irradiated at 20 K to a fluence of  $1 \times 10^{16} \text{ H}^+ \text{ cm}^{-2}$  and then heated at  $1 \text{ K min}^{-1}$ . The majority of mass is lost as the ice film sublimates at  $\sim 180 \text{ K}$ . Panel B: Mass spectrometer readings of multiple species desorbed at different temperatures, contributing to mass loss. Panel C: Band areas of  $\text{H}_2\text{O}$  ( $3300 \text{ cm}^{-1}$ ) and radiolytic products  $^{13}\text{CO}_2$  ( $2275 \text{ cm}^{-1}$ ),  $^{13}\text{CH}_3\text{OH}$  ( $997 \text{ cm}^{-1}$ ),  $^{13}\text{CO}$  ( $2088 \text{ cm}^{-1}$ ), and  $\text{H}_2$  ( $4140 \text{ cm}^{-1}$ ), and as a function of temperature. Lines are guides to the eye.

before the H<sub>2</sub>O sublimes, their retention until relatively high temperatures implies that these radiolytic molecules are trapped within the collapsed pores until they are able to diffuse out at higher temperatures. For <sup>13</sup>CO and H<sub>2</sub>, this is a gradual, temperature-dependent diffusional escape process, whereas it occurs more suddenly for <sup>13</sup>CH<sub>3</sub>OH. For other trapped molecules, such as residual <sup>13</sup>CH<sub>4</sub> and H<sub>2</sub>CO<sub>3</sub>, the areas of the absorption bands could not be calculated due to a changing continuum baseline during heating, although Figure 5.5B shows <sup>13</sup>CH<sub>4</sub> desorption by ~80 K.

Infrared spectra shown in Figure 5.6 reveal that, even above the temperature at which the H<sub>2</sub>O thermally desorbs (~180 K) and up to 250 K, absorption peaks continue to exist in the film residue at 2826, 2596, 1675, 1458, and 1268 cm<sup>-1</sup>, attributed to <sup>13</sup>C-containing H<sub>2</sub>CO<sub>3</sub> (Zheng & Kaiser 2007, Moore & Khanna 1991), as well as unidentified bands at 1563 and 1105 cm<sup>-1</sup>. Comparing the areal mass on the QCM before and after each experiment, we estimate that this small residue, the mass of which corresponds to about 18 Hz, remained on the gold QCM substrate even after the sample reached room temperature. If the residue is taken to be H<sub>2</sub>CO<sub>3</sub>, the 18 Hz remaining on the QCM at room temperature is equivalent to  $\sim 4.5 \times 10^{15}$  H<sub>2</sub>CO<sub>3</sub> cm<sup>-2</sup>. Carbonic acid has also been identified as a dominant reaction product for H<sub>2</sub>O-CO<sub>2</sub> ice mixtures (Zheng & Kaiser 2007) and bears potential astrobiological significance. The residue may also help explain surface reddening observed on TNOs (Cruikshank et al. 2016).

## 5.4 Summary and Conclusions

We have reported enhanced adsorption of methane and trapping of radiolytic species within gradually collapsing pores of ice films exposed to atmospheric methane, subject to energetic ion bombardment. These findings support a physical mechanism for observed gas

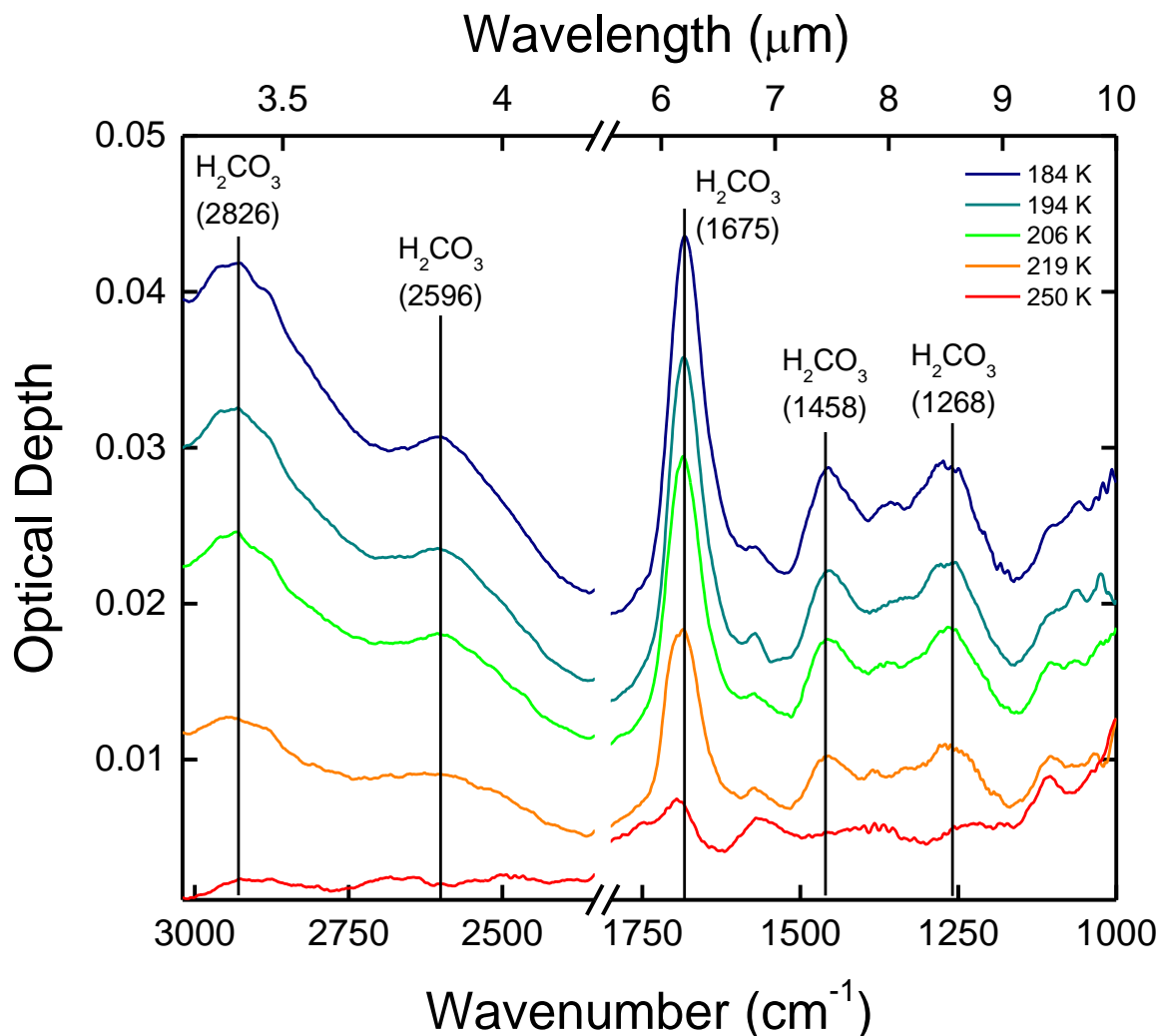


Figure 5.6 – Absorption spectra of irradiated sample during warm-up from 20 K reveals that a trace amount of radiolytic product remains after the thermal desorption of H<sub>2</sub>O at ~180 K, and even above 250 K. Black lines indicate locations of absorption peaks for temperatures between 184 K and 250 K. Peak positions are given in units of cm<sup>-1</sup>. Spectra are vertically shifted for clarity.



retention on satellite surfaces in the Outer Solar System, such as the TNOs and Centaurs. Similar effects have been reported for ices in oxygen atmospheres (Shi et al. 2009), and can also be extended to porous ice surfaces containing ambient gases, typical in astronomical environments.

We find that porous, micron-scale ASW films in a thin ( $P \sim 7 \times 10^{-7}$  Torr) methane atmosphere under ion impingement undergoes enhancement in gas adsorption, due to the net effect of competition between pore collapse and the conversion of low- into high-energy binding sites.  $\text{CH}_4$  uptake reaches the highest levels,  $> 35\%$  of pre-irradiation adsorption, at low fluxes because additional gas can adsorb in new high-binding sites within the pores with additional time between each ion impact, before the pores collapse. Ion irradiation of ice in the presence of ambient methane causes an exponential decrease in methane concentration as a function of ion fluence, with destruction cross-section  $\sigma_d = 1.89 (\pm 0.05) \times 10^{-15} \text{ cm}^2$ , and the simultaneous production of radiolytic molecules, formed by the reaction between the dissociated radicals from the constituents of  $\text{CH}_4$  and  $\text{H}_2\text{O}$ . Identified radiolytic molecules include  $\text{CO}_2$ ,  $\text{CO}$ ,  $\text{CH}_3\text{OH}$ ,  $\text{H}_2$ ,  $\text{H}_2\text{CO}_3$ ,  $\text{HCO}$ ,  $\text{CH}_3\text{CHO}$ ,  $\text{C}_2\text{H}_5\text{OH}$ ,  $\text{C}_3\text{H}_8$ ,  $\text{C}_2\text{H}_6$ , and  $\text{C}_3\text{O}_2$ . A residual amount (8%) of the initial  $\text{CH}_4$  remains trapped in the pores at high fluence and is accompanied by saturation in radiolytic production.

Radiolytic  $\text{CO}_2$  remains trapped in the film until the ice is thermally desorbed at  $\sim 180 \text{ K}$ .  $\text{CO}$ ,  $\text{CH}_3\text{OH}$ , and  $\text{H}_2$  are retained in the ice until  $\sim 140 - 165 \text{ K}$ , when they diffuse out of the ice at higher temperatures. Residual  $\text{CH}_4$  desorbs earlier, by  $\sim 80 \text{ K}$ , suggesting that radiolytic species have overall effect of binding to the ice more effectively than  $\text{CH}_4$ , contributing to the observed increase in mass uptake by the ice film during irradiation. Trace amounts of radiolytic product – perhaps attributable to  $\text{H}_2\text{CO}_3$  – remain adsorbed on the substrate after the thermal

desorption of the ice, and up to room temperature. This residue could be relevant to surface reddening by tholins on surfaces of TNOs and Centaurs.

## References

- Bennet, C.J. and Kaiser, R.I., *Astrophys. J.* **660**, 1289 (2007).
- de Bergh, C. et al. In: Gudipati, M.S. and Castillo-Rogez, J., Editors, *The Science of Solar System Ices*, Springer, New York (2013).
- Brunetto, R., Baratta, G.A., Domingo, M., Strazzulla, G., *Icarus* **175**, 226 (2005).
- Burgdorf, M., Cruikshank, D.P., Dalle Ore, C.M., Sekiguchi, T., Nakamura, R., Orton, G., Quirico, E., Schmitt, B., *Astrophys. J. Lett.* **718**, 2 (2010).
- Burke, D.J., & Brown, W.A., *Phys. Chem. Chem. Phys.* **12**, 5947 (2010).
- Cruikshank, D.P., Grundy, W.M., DeMeo, F.E., Buie, M.W., Binzel, R.P., Jennings, D.E., Olkin, C.B., Parker, J.W., Reuter, D.C., Spencer, J.R., Stern, S.A., Young, L.A., Weaver, H.A. *Icarus* **246**, 82 (2015).
- Famá, M., Loeffler, M.J., Raut, U., Baragiola, R.A., *Icarus* **207**, 314 (2010).
- Gladstone, G.R. et al, *Science* **351**, 6279 (2016).
- Grosjean, D.E., Vidal, R.A., Baragiola, R.A., Brown, W.L. *Phys. Rev. B.* **56**, 6975 (1997).
- Grundy, W.M. et al., *Science* **351**, 6297 (2016).
- Hudson, R.L. and Moore, M.H., *Icarus* **145**, 661 (2000).
- Johnson, R.E., Lanzerotti, L.J., Brown, W.L., Armstrong, T.P., *Science* **202**, 1027 (1981).
- Loeffler, M. J., Raut, U., Vidal, R. A., Baragiola, R. A., Carlson, R. W., *Icarus* **180**, 265 (2006).
- Loeffler, M. J., Raut, U., Baragiola, R. A., *J. Chem. Phys.* **132** (2010).
- Mayer, E., and Pletzer, R., *Nature* **319**, 298 (1986).

- Moore, M.H. and Hudson, R.L. *Icarus* **135**, 518 (1998).
- Moore, M.H. and Khanna, R.K., *Spectrochimica Acta* **47A**, 2 (1991).
- Notesco, G. & Bar-Nun, A., *Icarus* **126**, 336 (1997).
- Palumbo, M.E., *A&A*. **453**, 903 (2006).
- Raut, U., Teolis, B.D., Loeffler, M.J., Vidal, R.A., Famá, M., Baragiola, R.A., *J. Chem. Phys.* **126**, 244511 (2007a).
- Raut, U., Famá, M., Loeffler, M.J., Baragiola, R.A., *Astrophys. J.* **687**, 1070 (2008).
- Raut, U., Mitchell, E.H., Baragiola, R.A., *J. Astrophys.* **811**, 2 (2015).
- Rouquerol, F., Rouquerol, J., Sing, K., *Adsorption by Powders & Porous Solids: Principles, Methodology and Applications*, Academic, San Diego, (1999).
- Sack, N.J. and Baragiola, R.A., *Phys. Rev. B.* **48**, 9973 (1993).
- Sandford, S.A. & Allamandola, L.J., *Astrophys. J.* **355**, 357 (1990).
- Sandford, S. A., & Allamandola, L. J., *Astrophys. J. Lett.*, 409, L65 (1993).
- Shi, J., Teolis, B.D., Baragiola, R.A. *Phys. Rev. B.* **79**, 235422 (2009).
- Shi, J., Raut, U., Kim, J.-H., Loeffler, M., Baragiola, R.A. *Astrophys. J. Lett.* **738**, 1 (2011).
- Slinger, T.G. and Black, G., *J. Chem. Phys.* **77**, 2432 (1982).
- Spencer, J.R., Calvin, W.M., Person, M.J., *J. Geophys. Res.* **100**, 19049 (1995).
- Tokar, R.L. et al., *Geophys. Res. Lett.* **32**, L14S04 (2006).
- Warren, J. A., Smith, G. R., & Guillory, W. A. *J. Chem. Phys.* **72**, 4901, (1980).
- Zheng, W. and Kaiser, R.I. *Chem. Phys. Lett.* **450**, 55 (2007).
- Ziegler, J.F. & Biersack, J.P., *Stopping and Range of Ions in Matter* (2013).

## CHAPTER 6

### Irradiation Effects of H<sub>2</sub>-Laden Porous Water Ice Films: Implications for Interstellar Ices

---

#### 6.1. Ion Irradiation of H<sub>2</sub>-Laden Porous Water Ice Films

**Published:** *The Astrophysical Journal* **811**, 2 (2015).

#### Abstract

To understand the effects of cosmic ray impacts on interstellar icy grains immersed in H<sub>2</sub> gas, we have irradiated porous water ice films loaded with H<sub>2</sub> with 100 keV H<sup>+</sup>. The ice films were exposed to H<sub>2</sub> gas at different pressures following deposition and during irradiation. A net H<sub>2</sub> loss is observed during irradiation due to competition between ion-induced sputtering and gas adsorption. The initial H<sub>2</sub> loss cross-section,  $4 (\pm 1) \times 10^{-14} \text{ cm}^2$ , was independent of film thickness, H<sub>2</sub> and proton fluxes. In addition to sputtering, irradiation also closes nanopores, trapping H<sub>2</sub> in the film with binding that exceeds physical absorption energies. As a result, 2 to 7% H<sub>2</sub> is retained in the ice following irradiation to high fluences. We find that the trapped H<sub>2</sub> concentration increases with decreasing  $\zeta$ , the ratio of ion to H<sub>2</sub> fluxes, suggesting that as high as 8% solid H<sub>2</sub> can be trapped in interstellar ice by cosmic ray or stellar wind impacts.

##### 6.1.1 Introduction

Hydrogen is the dominant gas in the interstellar medium (ISM). In a cold molecular cloud with dust and  $10^5 \text{ H}_2 \text{ cm}^{-3}$ , an H<sub>2</sub> molecule arrives at the surface of a 0.1- $\mu\text{m}$ -sized, ice-covered dust grain once every few seconds (Tielens 2005). At 10 K, H<sub>2</sub> can diffuse into the pores

of the ice mantle and adsorb at high-energy binding sites, loading the ice with hydrogen over the lifetime of the cloud (Buch & Devlin 1994, Sandford et al. 1993). These icy grains are also impacted by galactic cosmic rays and by stellar winds in clouds with embedded protostars. Based on the available cosmic proton flux spectrum (Webber & Yushak 1983), we estimate a small impact rate of  $\sim 1 \text{ H}^+$  hit per year on a  $0.1\text{-}\mu\text{m}$ -sized grain, or  $10^{-7}$  times the impact frequency of the thermal  $\text{H}_2$ . Similar calculations have been detailed elsewhere for Fe cosmic rays (Bringa et al. 2007). The energy deposited by such impacts can release the adsorbed  $\text{H}_2$  back into the gas phase, i.e. impact desorption or sputtering. On the other hand, such impacts could also generate  $\text{H}_2$  from radiation processing of H-bearing precursor molecules in the ice, such as  $\text{NH}_3$  (Loeffler et al. 2010),  $\text{CH}_4$  (Mitchell et al. 2014, Chapter 5), and  $\text{CH}_3\text{OH}$ . Ammonia and methanol are known constituents of interstellar ice, at abundances ranging from 5 to 10% relative to water (Gibb et al. 2004).

Recently, we reported on a new process of ion-induced enhanced adsorption, in which ambient gas molecules are incorporated into the ice film during irradiation. This ion-enhanced adsorption was observed for  $\text{O}_2$ , Ar (Shi et al. 2009) and  $\text{CH}_4$  (Mitchell et al. 2014, Chapter 5). The enhancement in Ar adsorption was small compared to that of  $\text{O}_2$  and attributed to its smaller binding energy to  $\text{H}_2\text{O}$  ice (Shi et al. 2009). We pose the question: Would similar adsorption enhancement be observed in the case of  $\text{H}_2$ , given its even smaller binding energy to ice than Ar (Bar-Nun et al. 1985)? If so, it could result in increased trapping of hydrogen in the icy mantles of interstellar grains immersed in  $\text{H}_2$  gas when impacted by cosmic rays or stellar winds.

These processes of ion-induced adsorption of interstellar gas and ejection of adsorbed ices are important in determining the gas-solid balance in the ISM. Therefore, to understand the effects of cosmic ray/stellar wind impacts on interstellar ice immersed in  $\text{H}_2$  gas, we have

irradiated porous amorphous ice films loaded with  $\text{H}_2$  following ice growth. The irradiations were performed with 100 keV  $\text{H}^+$  using fluxes of  $10^{10}$  to  $10^{12} \text{ H}^+ \text{ cm}^{-2} \text{ s}^{-1}$  at 7 K, in the presence of ambient  $\text{H}_2$  at pressures ranging from  $10^{-5}$  to  $10^{-7}$  Torr. Here, we report a net loss in adsorbed  $\text{H}_2$  during irradiation, as a result of ion-induced ejection and re-adsorption. We discuss the dependence of  $\text{H}_2$  net loss on important parameters such as ice film thickness ( $d$ ), ion flux ( $f$ ) and the ambient  $\text{H}_2$  pressure that determines the  $\text{H}_2$  flux ( $F_H$ ) arriving at the surface of the ice film.

We note that  $f$  and  $F_H$  in our experiments are higher than interstellar values by many orders of magnitude. However, the parameter critical to synergistic trapping of hydrogen in ices when irradiation is performed in presence of ambient  $\text{H}_2$  is the flux ratio,  $\zeta = f / F_H$ . This ratio determines the probability that an  $\text{H}_2$  molecule, following its arrival on the ice surface and its subsequent incorporation into the pores, can be trapped via compaction events induced by the ions. The smallest value of  $\zeta$  in our experiments is only 5 times larger than the estimated interstellar value. We use our results to predict trapped  $\text{H}_2$  concentration in interstellar ices, where  $\zeta \sim 10^{-7}$ .

### 6.1.2 Experimental Methods

The experiments were conducted in a cryopumped ultrahigh vacuum chamber with a base pressure of  $\sim 10^{-10}$  Torr. Water ice films were grown by the deposition of vapor passing through a micro-capillary array to impact, at  $45^\circ$  incidence, a gold-coated quartz crystal microbalance (QCM) cooled to 7 K by a two-stage Janis RDK-205E closed-cycle refrigerator. A radiation shield cooled to 40 K by the same refrigerator encloses the copper sample holder where the microbalance is mounted. Openings in the radiation shield allow for film deposition and optical measurements. The microbalance measures the areal mass of the deposit, which is converted to

column density by dividing the areal mass by the mass of the molecule (Sack & Baragiola 1993). The deposition angle was chosen to ensure growth of a porous film (Raut et al. 2007a, Stevenson et al. 1999). The ice films were varied in thickness, ranging from 200 to 5000 ML (1 ML =  $10^{15}$  molecules  $\text{cm}^{-2}$ , about a monolayer). Following ice deposition,  $\text{H}_2$  gas (99.9% purity) was leaked into the chamber at pressures ranging from  $10^{-5}$  to  $10^{-7}$  Torr. The  $\text{H}_2$  pressure  $P$  is measured outside the radiation shield with a nude ionization gauge and corrected for gas-dependent sensitivity; the pressure readings are accurate to 20%.

The mass uptake by the ice films in response to  $\text{H}_2$  exposure was measured with the QCM, with a sensitivity of 0.63 ML for  $\text{H}_2$ . At a constant  $\text{H}_2$  pressure, the column density  $\eta(\text{H}_2)$  increased linearly with time and asymptotically approached an equilibrium value  $\eta_0$ , where adsorption and desorption rates are equal. The ice films loaded with a pre-irradiation value of  $\eta_0$  were then irradiated at  $9^\circ$  incidence with a mass-analyzed, 100 keV  $\text{H}^+$  beam from an ion accelerator, in the presence of ambient  $\text{H}_2$ . The ion flux, measured with a calibrated thin wire placed in the path of the beam, was varied from  $\sim 10^{10}$  to  $10^{12}$   $\text{H}^+ \text{cm}^{-2} \text{s}^{-1}$ . The beams were scanned uniformly over the ice using electrostatic deflection plates. The energy deposited by the ions per unit path length in the film, the stopping power  $dE/dx$ , remained constant to within 15% up to 3000 ML, the maximum thickness of films irradiated in these experiments (Ziegler & Biersack 2013). Films thicker than 3000 ML cracked at the onset of irradiation. The QCM gives the net change in  $\eta(\text{H}_2)$  due to irradiation, which first caused mass loss due to expulsion of volatile  $\text{H}_2$  from the “hot” track created in the film by the energetic protons. This sputtering is followed by mass uptake as the  $\text{H}_2$  at  $P$  refills the pores that were emptied and modified by radiation.

We also used infrared spectroscopy to monitor changes induced by radiation. Specular reflectance of the films was obtained at an incident angle of  $35^\circ$  using a Thermo Nicolet Nexus 670 spectrometer at  $2\text{ cm}^{-1}$  resolution. The spectra  $R$  of the films, collected following ice film deposition,  $\text{H}_2$  uptake, and after irradiation steps of incremental fluences, were divided by the reflectance spectrum of the gold substrate  $R_o$ , and then converted to optical depth,  $-\ln(R/R_o)$ . In particular, we focus on the changes of the  $\text{H}_2$  absorption band that peaks at  $2.42\text{ }\mu\text{m}$  ( $4131\text{ cm}^{-1}$ ) and the OH dangling bond absorption features at  $\sim 2.7\text{ }\mu\text{m}$  induced by the presence of  $\text{H}_2$  in the ice and subsequent irradiation. We note that all  $\text{H}_2$  column densities were calculated using the QCM rather than infrared spectroscopy, due to complications inherent in the reflectance geometry (Teolis et al. 2007).

### 6.1.3 Results and Discussion

#### *I. Kinetics: $\text{H}_2$ Sputtering and Adsorption*

Figure 6.1.1 shows the QCM measurements of the kinetics of  $\text{H}_2$  adsorption at 7 K, following removal of adsorbed  $\text{H}_2$  by sputtering in response to irradiation pulses labeled *IB*. The porous water ice film (1060 ML) was exposed to  $\text{H}_2$  gas at  $\sim 2 \times 10^{-7}$  Torr, which resulted in  $\eta_0 = 80$  ML of  $\text{H}_2$ . The film was then irradiated with 100 keV  $\text{H}^+$ , using a flux of  $\sim 10^{12}\text{ H}^+\text{ cm}^{-2}\text{ s}^{-1}$ , while maintaining the gas pressure. The first three irradiations in Figure 6.1.1 were short,  $\sim 3$  seconds in duration, each delivering a fluence of  $\sim 3 \times 10^{12}\text{ H}^+\text{ cm}^{-2}$ . The QCM registers downward spikes at the start of the irradiation that ceases when the beam is blocked; these events are traced by the vertical dotted blue lines. Such spikes result from stresses that develop in the ice film and quartz crystal from ion impact (Allodi et al. 2013). The decrease in  $\eta(\text{H}_2)$ , shown as  $D$ , is due to ion-induced sputtering of the adsorbed  $\text{H}_2$ . Following each irradiation step,  $\eta$  initially



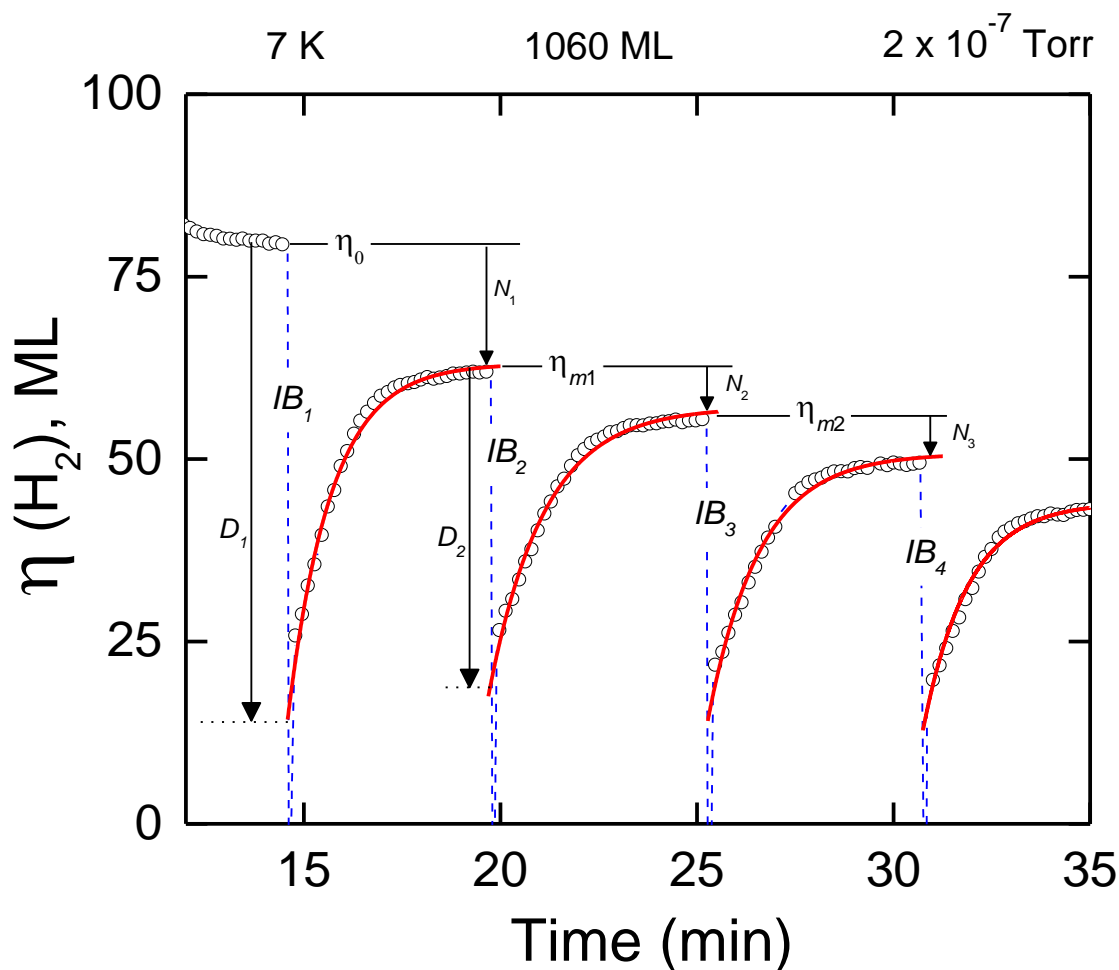


Figure 6.1.1 – The kinetics of adsorption of  $\text{H}_2$  following sputtering, measured by the quartz crystal microbalance, due to irradiation of a  $\sim 1060$  ML-thick porous ice film with  $100 \text{ keV H}^+$  at  $7 \text{ K}$ , at a constant  $\text{H}_2$  pressure of  $\sim 2 \times 10^{-7} \text{ Torr}$ . The irradiations  $IB_i$  (traced by the vertical dotted blue lines) decrease the column density,  $D_i$ , due to sputtering of adsorbed  $\text{H}_2$ . Following each  $IB$ , the column density  $\eta$  shows an initial linear increase and then approaches a constant value  $\eta_m$ , due to  $\text{H}_2$  uptake in radiation-modified pores; this absorption is traced by the red solid curves, which are fits to Eq. 1 discussed in the text.  $N_i$  indicates the net loss in  $\text{H}_2$ .

increases linearly due to uptake of hydrogen by the radiation-modified pores, shown by the circles in Figure 6.1.1. The gas uptake rate  $\dot{R}$  slows down with time as the number of sites available for adsorption decreases;  $\eta$  asymptotically approaches a saturation value  $\eta_m$  at which adsorption and desorption rates become equal. We observe a net decrease in  $H_2$  column density, indicated by  $N$ , following each irradiation step.

The main effect of irradiation on this  $H_2$ -laden ice film is the ejection of the adsorbed hydrogen. The  $H_2$  loss in response to the first irradiation is 66 ML,  $\sim 82\%$  of the pre-irradiation uptake at  $2 \times 10^{-7}$  Torr. A 100-keV proton will deposit most of its energy in the ice by generating excitations and ionizations of the molecules in its track. Ionizations can initiate molecular motion via Coulomb repulsion between closely-spaced charged species in the track. Additionally, excited species can de-excite to repulsive states, which leads to dissociation into energetic fragments that can further displace other atoms/molecules, creating a collision cascade. Such a cascade can be roughly viewed as a transient thermal spike around the ion track, where the temperature can reach as high as  $\sim 10^4$  K and decay at rates of  $\sim 10^{14}$  Ks $^{-1}$  (Bringa & Johnson 2004, Szenes 2002). The volatile  $H_2$  can diffuse along the “hot” track across the entire thickness of the film and escape from the ice, causing the observed substantial mass loss. For the initial irradiations we measure the sputtering yield in the range of 1 to  $2 \times 10^4$   $H_2/H^+$ , decreasing with increasing proton fluence. The yields are larger than sputtering yields of 4 to  $8 \times 10^2$   $H_2/H^+$  for pure solid  $H_2$  films irradiated with 5 to 10 keV  $H^+$  at 2 K (Schou 2002; Stenum et al. 1991). This is due to the 8-fold larger stopping power in our experiments than in the studies at 5 keV (Ziegler & Biersack 2013).

This mass loss is followed by hydrogen uptake by the radiation-modified pores, partially emptied by sputtering. Previous studies have shown that ion irradiation changes the pores in the

ice film in two ways: (1) it collapses the pores, decreasing the number of sites available for gas adsorption, (Palumbo 2006, Raut et al. 2007b) and (2) it increases the binding energy of an empty adsorption site by altering its size, thereby making it available for adsorption under the same pressure. The second process is responsible for ion-enhanced adsorption when irradiation is performed in the presence of ambient gas (Shi et al. 2009). Our results shows that the radiation enhancement of adsorption is absent for the case of H<sub>2</sub>; the ion-induced transformation of the pores does not increase the H<sub>2</sub> uptake. Instead, ice compaction dominates, reducing the H<sub>2</sub> adsorption capacity by  $N$ , as shown in Figure 6.1.1.

At  $2 \times 10^{-7}$  Torr, the  $\sim 3$ -s duration of the irradiations, shown in Figure 6.1.1, is small compared to the few minutes required for H<sub>2</sub> adsorption to reach the saturation value  $\eta_m$ . The H<sub>2</sub> uptake rate  $\dot{R} = d\eta/dt$  is also sufficiently slow such that re-adsorption is well-separated in time from sputtering. This is not the case at higher pressures.

The kinetics of H<sub>2</sub> uptake following irradiation is given by

$$\eta(t) = \eta_m [1 - \exp(-aPt)], \quad (1)$$

which reduces to

$$\eta(t) = \eta_m aPt = sF_H t \quad (2)$$

in the limit of  $\eta \ll \eta_m$ , where  $s$  is the sticking coefficient (Shi et al. 2009) and  $a$  is a constant.

The solid red curves in Figure 6.6.1 are fits of Equation 1 to the adsorption data at  $2 \times 10^{-7}$  Torr following the irradiation pulses, which yields  $a = 4 (\pm 1) \times 10^6 \text{ Torr}^{-1} \text{ min}^{-1}$ . The time required for  $\eta$  to increase to  $0.63 \eta_m$ ,  $\tau_{ad} = 1/aP = 75 \text{ s}$ . The slopes from the initial linear dependence gives an H<sub>2</sub> uptake rate  $\dot{R} = 0.2 \text{ to } 0.3 \text{ ML s}^{-1}$ , or a sticking coefficient  $\dot{R}/F_H = 0.7$  to 1, in agreement with published data (Matar et al. 2010). At  $2 \times 10^{-7}$  Torr, we estimate  $F_H \sim 0.3 \times$

$10^{15} \text{ H}_2 \text{ cm}^{-2} \text{ s}^{-1}$ , taking into consideration the effects of the radiation shield openings on  $\text{H}_2$  flux and thermal transpiration (Takaishi & Sensui 1963).

## II. *Effects of Film Thickness*

Porous ice films of different thicknesses (200-3000 ML) were exposed to  $\text{H}_2$  at  $2 \times 10^{-5}$  Torr and irradiated with 100 keV  $\text{H}^+$  while maintaining this pressure at 7 K. Figure 6.1.2A shows a decrease in  $\eta(\text{H}_2)$  with increasing fluence  $F$  for the thicknesses studied. A linear fit to the low-fluence regime of the  $\eta/\eta_0$  vs.  $F$  data, as per Equation 6 (discussed in Section IV), gives an effective  $\text{H}_2$  net loss cross-section of  $\sigma^* = 4 (\pm 1) \times 10^{-14} \text{ cm}^2$ , independent of the ice film thickness (Figure 6.1.2B).

Without irradiation,  $\eta_0$  scales linearly with ice column density up to 1100 ML (Figure 6.1.2C). The slope of this linear region gives an average initial  $\text{H}_2$  concentration in the films of 12%. Above this thickness,  $\eta_0$  approaches a constant value as indicated by the dotted curve. We measured initial uptakes for films with  $\eta_{\text{ice}} > 3000$  ML. However, these films cracked at the onset of irradiation, due to uneven stress build-up, which causes instabilities in QCM readings. Therefore we could not obtain the fluence dependence of  $\eta(\text{H}_2)$  for the thicker ice films.

This result has important astrophysical significance; the  $\text{H}_2$  retention capacity of interstellar ices does not scale with ice thickness above a critical value, despite constant porosity. This thickness could be interpreted as the penetration range of thermal  $\text{H}_2$  in ice of this porosity. The limit on penetration range can result from the topology of the pore network, with fewer pores connected to the surface at greater depths. We rule out obstruction in porous channels by pre-adsorbed  $\text{H}_2$ , since  $\text{H}_2$  is known not to hinder penetration of other molecules (Bar-Nun et al.

## Effect of Ice Thickness

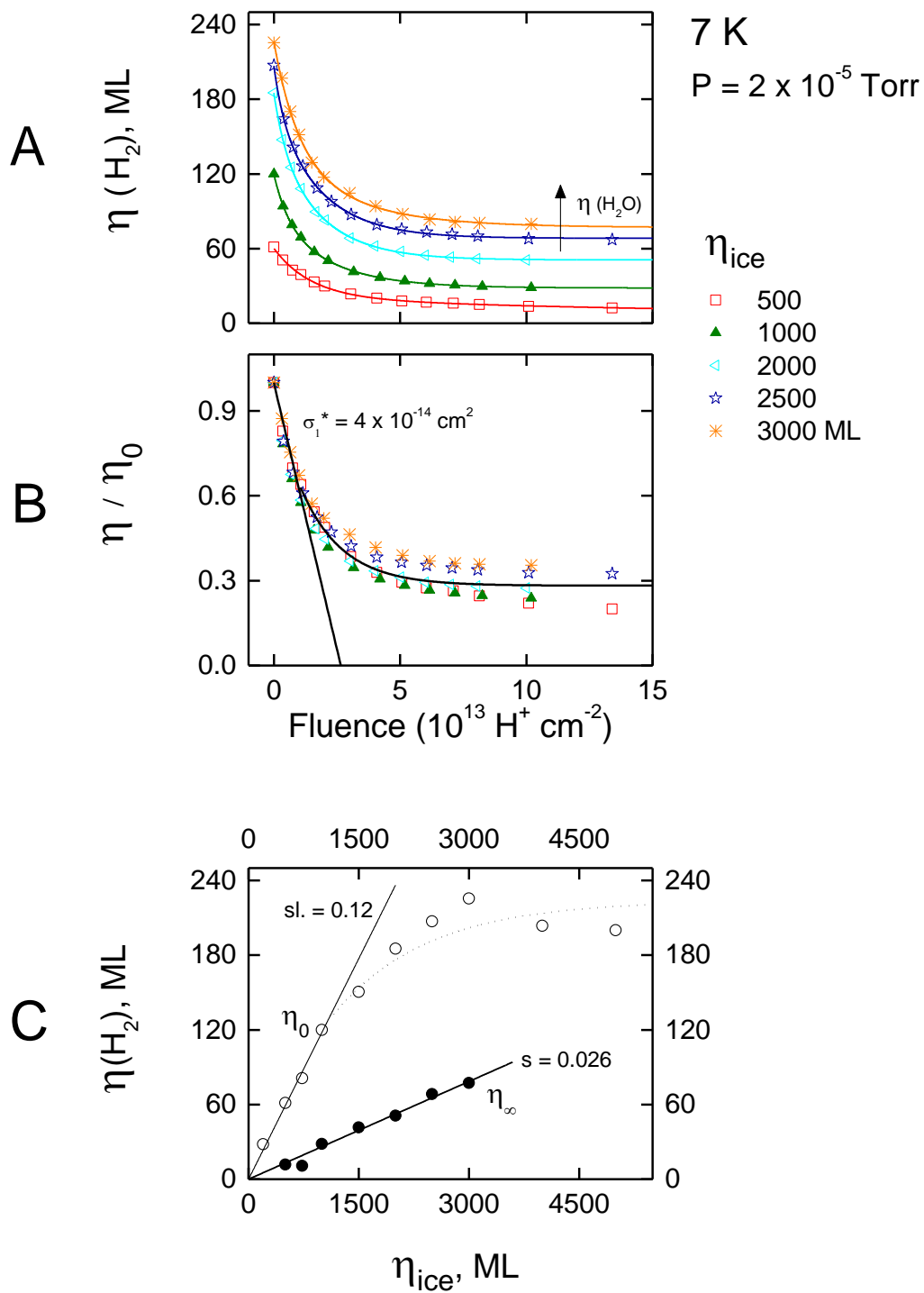


Figure 6.1.2 – Panel A shows the decrease in H<sub>2</sub> column density  $\eta$  with ion fluence  $F$  in ice films of varying thickness when irradiated with 100 keV H<sup>+</sup>. The curves are to guide the eye. Irradiation to high  $F$  traps H<sub>2</sub> in the ice films, which remains even upon removal of ambient H<sub>2</sub>. This residual hydrogen,  $\eta_{\infty}$ , is ~25-30% of the initial amounts,  $\eta_0$ , as shown in panel B. The fit of Eq. 6 to the data at low  $F$  gives an initial net loss cross-section,  $\sigma^* = 4 \times 10^{-14} \text{ cm}^2$ . Panel C shows that  $\eta_0$  increases linearly with ice thickness, but plateaus as  $\eta_{\text{ice}}$  exceeds 1100 ML (dotted curve). The slope from the linear fit of  $\eta_0$  vs.  $\eta_{\text{ice}}$  gives the average initial H<sub>2</sub> concentration, ~12%.  $\eta_{\infty}$  also increases linearly with ice thickness up to 3000 ML. For all films,  $\eta_{\infty} = 0.026 \eta_{\text{ice}}$ .

1985). A possible explanation is the appearance of easy desorption paths when thick films develop cracks.

Prolonged irradiation leads to trapping of hydrogen, which is stable even upon removal of ambient H<sub>2</sub> and up to temperatures of 170 K, where the ice desorption begins. This residual H<sub>2</sub>, ~ 25 to 30% of  $\eta_0$  (Figure 6.1.2B), corresponds to an average concentration of 2.6%, as indicated by the slope of  $\eta_\infty$  vs.  $\eta_{ice}$  (Figure 6.1.2C). Throughout this Chapter, concentrations are the ratio of number of molecules.

### *III. Effects of H<sub>2</sub> Pressure*

Figure 6.1.3 shows the dependence of the normalized H<sub>2</sub> uptake,  $\eta(F)/\eta_0$ , on irradiation fluence in several ice films (~1060 ML thick) during 100 keV H<sup>+</sup> irradiation in presence of ambient H<sub>2</sub> at different pressures. The inset shows the dependence of the pre-irradiation uptake  $\eta_0$  on pressure. The initial H<sub>2</sub> concentration ( $\eta_0/\eta_{ice}$ ) increased from 3.5 to 12% in response to the ~10<sup>3</sup>-fold increase in pressure, following a power-law dependence typical of microporous solids (Raut et al. 2007a, Tóth 2002). Irradiation leads to a decrease in  $\eta(H_2)$  at all pressures. As observed in the thickness dependence study, ~25 to 35% of the initial  $\eta_0$  remains trapped at high  $F$ , independent of H<sub>2</sub> pressure. The residual H<sub>2</sub> concentration is 2% at  $2 \times 10^{-7}$  Torr, doubling to 4% at  $2 \times 10^{-5}$  Torr. The fit of Equation 6 (discussed in Section 3.4) to the low-fluence data gives an effective H<sub>2</sub> net loss cross-section,  $\sigma^* = 4(1) \times 10^{-14}$  cm<sup>2</sup> (Figure 6.1.3). The data from two different experiments at  $2 \times 10^{-7}$  Torr show reproducibility within 25%.

## Effect of H<sub>2</sub> Pressure

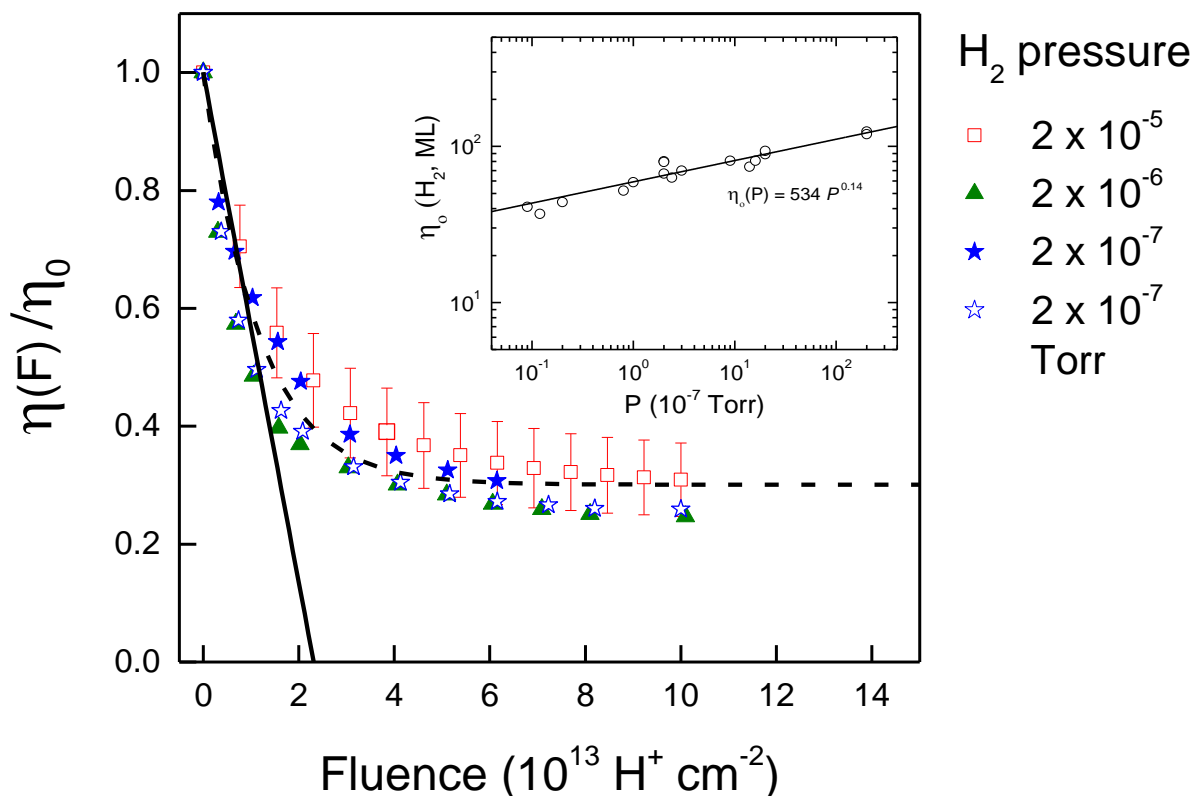


Figure 6.1.3 – The decrease in  $\eta(\text{H}_2)$  with fluence  $F$  during 100 keV  $\text{H}^+$  irradiation of  $\sim 1060$  ML porous ice films loaded with  $\text{H}_2$  at different pressures at 7 K, with  $\eta$  normalized to the pre-irradiation uptake  $\eta_0$ . At high  $F$ ,  $\eta$  approaches a constant value;  $\sim 25\text{--}35\%$  of  $\eta_0$ . The residual  $\text{H}_2$  is 2–4% relative to water ice, increasing with  $\text{H}_2$  pressure. The effective  $\text{H}_2$  net loss cross-section of  $4 (\pm 1) \times 10^{-14} \text{ cm}^2$  is obtained from the linear fit of Eq. 6 applied to low  $F$ . The dashed curve is to guide the eye. The inset shows the power-law dependence of  $\eta_0$  on  $\text{H}_2$  pressure.



#### IV. Rate Equations

We assume that the ice has three types of pores: *I*, *II* and *III*. The pores that are connected to the surface are *Type I* or *Type II* depending on whether they are pristine or have been irradiated. Therefore, initially the ice is entirely *Type I*. Isolated pores, with no gas path to the surface, are labeled *Type III*. The evolution of H<sub>2</sub> in the ice films in response to irradiation is determined by the mass loss and gain rates, which is given by

$$d\eta_1/dF = -\sigma_{L1}\eta_1 - \sigma_{L12}\eta_1 + \sigma_G R \tau_{ad} \phi_0 \exp(-\sigma F) \quad (3)$$

where the first loss term accounts for sputtering. Prior to irradiation, we assume that all hydrogen is trapped in *Type I* pores with a column density  $\eta_1$ , and lost with a sputtering cross-section  $\sigma_{L1}$ . Irradiation affects *Type I* pores by decreasing the total pore volume, modifying the previously unoccupied sites to have higher binding energies, and restricting pore access to the external surface. In the second term in Equation 3, the cross-section to transfer gas from *Type I* to *II* pores is  $\sigma_{L12}$ . The third term, which depends on pressure, describes the mass gain due to gas uptake in the radiation-modified pores, where  $\sigma_G$  is the mass gain cross-section and  $\phi_0 \exp(-\sigma F)$  is the fluence-dependent porosity of the ice film (Raut et al. 2008), *Type I* and *II* inclusive. For small fluences, the H<sub>2</sub> uptake rate  $R$  and the time constant for H<sub>2</sub> adsorption,  $\tau_{ad}$ , are independent of  $F$  at a given pressure. From our kinetics analysis, we obtained  $R = 0.2$  to  $0.3$  ML s<sup>-1</sup> and  $\tau_{ad} = 1.25$  min at  $2 \times 10^{-7}$  Torr (Figure 6.1.1).

Further irradiation leads to H<sub>2</sub> loss from *Type II* pores, in addition to loss from *Type I* pores. The dependence of H<sub>2</sub> in *Type II* pores ( $\eta_2$ ) on fluence is described by

$$d\eta_2/dF = -\sigma_{L2}\eta_2 - \sigma_{L23}\eta_2 + \sigma_{L12}\eta_1 + \sigma_G R \tau_{ad} \phi_0 \exp(-\sigma F) \quad (4)$$

The first term accounts for sputtering loss from *Type II* pores. The cross-section  $\sigma_{L2}$  would likely be smaller than  $\sigma_{L1}$  due to reduced access to the external surface, which would imply that  $H_2$  molecules exiting *Type II* pores collide more frequently with the pore walls where they may re-adsorb. Further irradiation isolates *Type II* pores from the external surface, trapping  $H_2$  in the ice film. The cross-section for the formation of isolated *Type III* pores is  $\sigma_{L23}$ . The second term accounts for loss in  $\eta_2$  due to  $H_2$  transfer to *Type III* pores. The third term describes the  $H_2$  gain from *Type I* pores.  $H_2$  uptake in available pores is described by the fourth term. At large  $F$ , only *Type III* pores exist in the film, enclosing the trapped  $H_2$ . There is no net  $H_2$  loss from the *Type III* pores, i.e.  $d\eta_3/dF = 0$ , since such pores are isolated from the external surface.

We make several simplifications about these processes at low fluences. First, all the adsorbed  $H_2$  are in *Type I* pores prior to irradiation i.e.  $\eta_1 = \eta$ . This is supported by previous observations of other gases like  $O_2$ . All of the adsorbed  $O_2$  (within the QCM sensitivity of 0.04 ML) desorbed from the ice when ambient pressure was removed (Shi et al. 2009). Then, at low  $F$ ,  $\eta_2 \ll \eta$ . Since the change in ice porosity is small, less than 10% for fluences below  $10^{13} H^+ cm^{-2}$  (Raut et al. 2008),  $\phi_0 \exp(-\sigma F)$  can be treated as a constant  $\phi_0$ , the initial ice porosity. Therefore, at low fluences Equation 3 simplifies to

$$d\eta/dF = -\sigma'_L \eta + \sigma_G \alpha, \quad (5)$$

where  $\sigma'_L$  is the effective  $H_2$  loss cross-section, which describes loss due to sputtering and  $H_2$  transfer to *Type II* pores, and  $\alpha = R\tau_{ad}\phi_0$ .

Equation 5 integrates to

$$\eta(F)/\eta_0 = 1 - (\sigma'_L - \alpha\sigma_G/\eta_0)F = 1 - \sigma^*F \quad (6)$$

which defines an effective  $\text{H}_2$  net loss cross-section,  $\sigma^* = (\sigma'_L - \alpha\sigma_G/\eta_0)$ .

The fit of Equation 6 to the low-fluence data ( $F < 10^{13} \text{ H}^+ \text{ cm}^{-2}$ ) in Figure 6.1.2B and 6.1.3 gives an effective net loss cross-section of  $\sigma^* = 4(1) \times 10^{-14} \text{ cm}^2$ .

## V. *Infrared Results*

$\text{H}_2$  is a homonuclear molecule and the stretch vibration of the H-H bond induced by absorption of infrared light does not produce a net change in its dipole moment, thus making a free  $\text{H}_2$  molecule infrared-inactive. However, the vibrational mode of  $\text{H}_2$  embedded in a solid matrix, such as water ice, is perturbed by the interactions with the neighboring water molecules, making the embedded  $\text{H}_2$  infrared-active. This weak feature is observed at  $2.42 \mu\text{m}$  ( $4132 \text{ cm}^{-1}$ ) and is shown in the top panel of Figure 6.1.4, together with the dangling bond absorptions at  $\sim 2.7 \mu\text{m}$  ( $\sim 3700 \text{ cm}^{-1}$ ) in the infrared spectrum of a 3000 ML-thick ice film loaded with 225 ML of  $\text{H}_2$ . The DB absorptions are due to water molecules in the internal surface of the porous film that lack the tetrahedral coordination (Buch & Devlin 1991, Raut et al. 2007a, Rowland et al. 1995). The peak position of the  $\text{H}_2$  band is affected by the host matrix (Warren et al. 1980): We measure  $4132 \text{ cm}^{-1}$ ,  $\sim 10 \text{ cm}^{-1}$  larger than previous reports for  $\text{H}_2\text{O}$ -rich ice containing smaller quantities of  $\text{CH}_3\text{OH}$ ,  $\text{NH}_3$ , and  $\text{CO}$  (Sandford & Allamandola 1993) and  $7 \text{ cm}^{-1}$  larger than in films containing  $\text{NH}_3$  and  $\text{N}_2$  (Loeffler, et al. 2010).

The  $\text{H}_2$  uptake also produces changes in the dangling bond absorptions; the shift in the vibrational frequencies,  $\sim 2 \text{ cm}^{-1}$ , is small compared to the  $30\text{-cm}^{-1}$  blue shifts due to adsorption of heavier molecules like methane (Raut et al. 2007a). The shift in a 3000-ML film is smaller than previously reported (Rowland et al. 1991, Sadlej et al. 1995). A fraction of the pores in films >

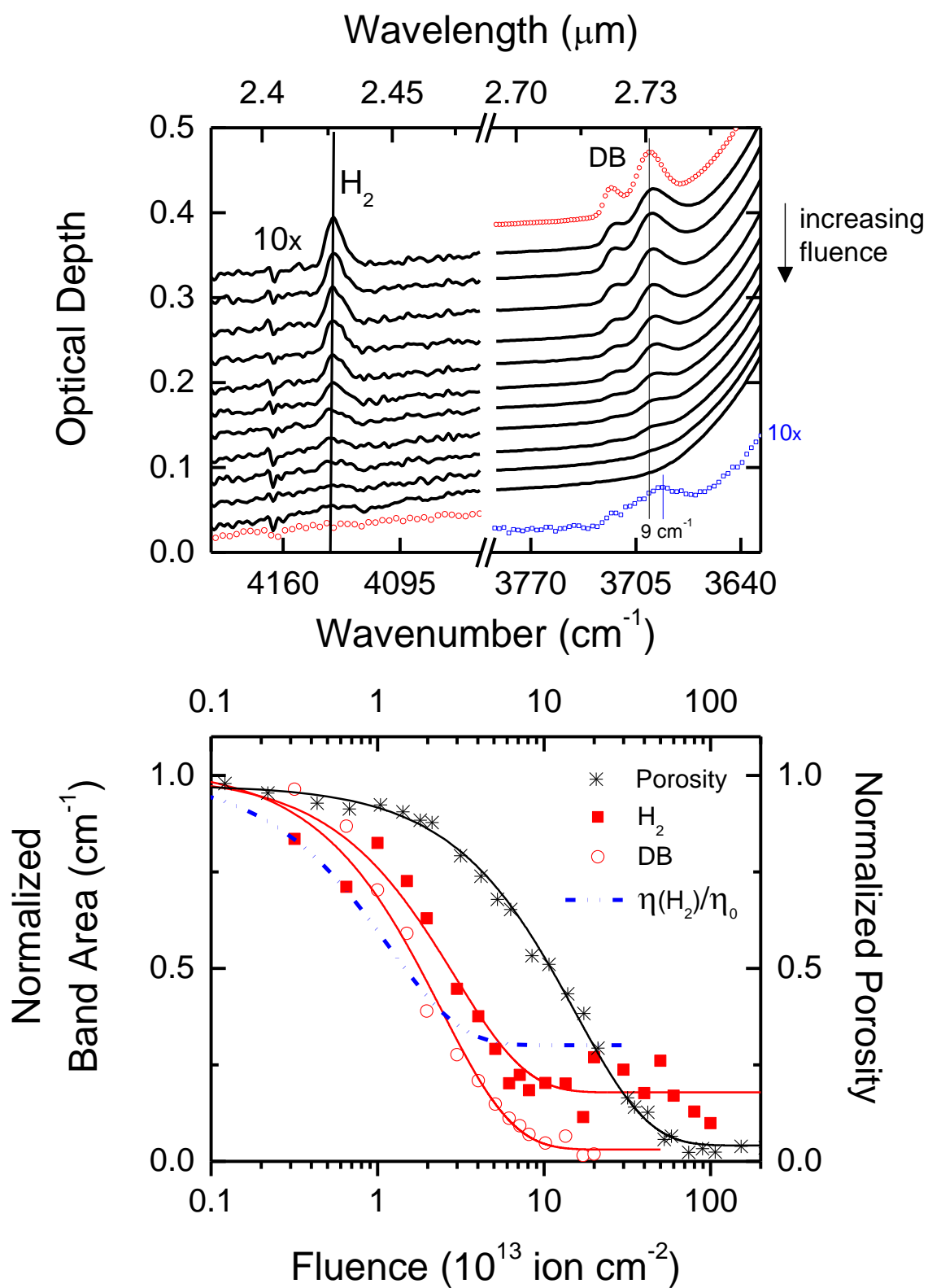


Figure 6.1.4 – Top panel shows the decrease in the intensities of the weak  $\text{H}_2$  ( $4132\text{ cm}^{-1}$ ) and the dangling O-H ( $\sim 3700\text{ cm}^{-1}$ ) absorptions during  $100\text{ keV H}^+$  irradiation of a  $3000\text{ ML}$ -thick ice film at  $7\text{ K}$  loaded with  $\text{H}_2$  at  $2 \times 10^{-7}\text{ Torr}$ . The spectrum indicated by red open circles is that of a pure water ice film, without  $\text{H}_2$ . For comparison, we show the spectrum of a  $500\text{-ML}$  film loaded with  $12\%$  molar  $\text{H}_2$  (blue open squares), multiplied 10-fold. Larger blueshifts in DB peak positions occur in thinner films due to complete pore filling. Spectra have been vertically shifted for clarity. The bottom panel shows the dependence of normalized band areas ( $\text{H}_2$  and DB) on ion fluence. The blue curve (dot-dash) is the  $\eta(\text{H}_2)/\eta_0$  vs.  $F$  obtained from Figure 3 (QCM measurement). Also shown for comparison is the porosity vs.  $F$  data for a  $1000\text{-ML}$  pure water ice film irradiated with  $80\text{ keV H}^+$  (Raut et al. 2008).

1100 ML are inaccessible to hydrogen, as inferred from Figure 6.1.2 and discussed in Section 3.2. In films  $< 1100$  ML, a shift of  $\sim 9 \text{ cm}^{-1}$  is observed, resulting from near-complete pore filling by the adsorbed  $\text{H}_2$ . We include a spectrum of a 500-ML film loaded with 12%  $\text{H}_2$  molar (blue open squares), showing the larger shift in agreement with previous studies. We also note that the DB absorptions become less discernible as the bands merge with  $\text{H}_2$  uptake.

Irradiation decreases the intensities of the  $\text{H}_2$  and DB absorptions. The bottom panel of Figure 6.1.4 compares the fluence dependence of these absorptions and that of porosity for ice irradiated with 80 keV protons. The stopping powers of 80 and 100 keV protons in ice are the same, within errors (Bauer et al. 1994). The fluence dependences are normalized to their respective values at  $F = 0$ . The fit to the  $\eta/\eta_0$  vs.  $F$  data obtained using the microbalance (Figure 6.1.3) is also included in the bottom panel of Figure 6.1.4 (dash-dotted curve).

The DB destruction cross-section is  $4.2 (0.3) \times 10^{-14} \text{ cm}^{-2}$ , the same as reported for 200 keV  $\text{H}^+$  (Palumbo 2006). The stopping powers of protons in water ice at the two energies differ by only 20% (Bauer et al. 1994). The similar decrease in DB and  $\text{H}_2$  signals (from IR and QCM measurements) implies that the internal surface area available for adsorption rather than the cumulative pore volume determines gas retention. The DB and  $\text{H}_2$  loss curves diverge at larger fluence; at  $10^{14} \text{ H}^+ \text{ cm}^{-2}$ , the  $\text{H}_2$  absorbance is  $\sim 20\%$  of its initial value, in reasonable agreement with QCM estimates of trapped  $\text{H}_2$ , while the DB absorbance is  $< 5\%$  of its initial value. The divergence supports the idea that the absence of DB features do not imply a fully compact ice (Raut et al. 2007b). Pores without dangling water molecules can still trap gas. The transient local heating around the ion track could rearrange the dangling water molecules into the tetrahedral bonding configuration, as observed in thermal compaction (Isokoski et al. 2014, Noble et al. 2014). Such difference in fluence dependences of gas retention and DB absorbance has been

noted previously for CO (Palumbo 2006). The different fluence dependence of the porosity and the dangling bond absorbance has been previously noted (Raut et al. 2007b) and is attributed to faster reduction in the internal surface area than the pore volume by irradiation.

The  $H_2$  that is stable even upon removal of the ambient pressure and retained in the ice to sublimation temperatures is trapped in *Type III* voids, disconnected from the external surface. The *Type III* porosity at  $\sim 0.13$  at  $10^{14} \text{ H}^+ \text{ cm}^{-2}$  is nearly half the value at  $F = 0$ . Continued irradiation to higher fluence ( $\sim 10^{15} \text{ H}^+ \text{ cm}^{-2}$ ) further reduces the porosity to  $< 5\%$  of the initial value. The  $H_2$  is most likely dispersed in the compacted ice, occupying either interstitial sites or radiation-induced bubbles (Johnson & Jesser 1997, Loeffler et al. 2010).

## VI. *Effects of Irradiation Flux*

Figure 6.1.5 shows the decrease in  $\eta(H_2)$  with increasing fluence for ice films, 1060 ML thick, irradiated with 100 keV  $H^+$  at different fluxes under  $H_2$  pressure of  $2 \times 10^{-5}$  Torr. The pre-irradiation uptake  $\eta_0$  at  $F = 0$  is 120 ML at this pressure. The slope of the linear fit to  $H_2$  loss data at low  $F$ , divided by  $\eta_0$ , gives the effective  $H_2$  net loss cross-section of  $\sigma^* = 3 \times 10^{-14} \text{ cm}^2$ , in agreement with values from thickness and pressure dependence studies. At large  $F$ , we observe that the amount of residual  $H_2$  in the ice film increases with decreasing ion flux, to concentrations as high as 7%. The increased trapping is likely due to more time available for  $H_2$ , between ion-induced pore collapse events (conversion from *Type I* to *III*), to find irradiation-modified sites with increased binding at lower fluxes (Shi et al. 2009).

## Effect of Ion Flux

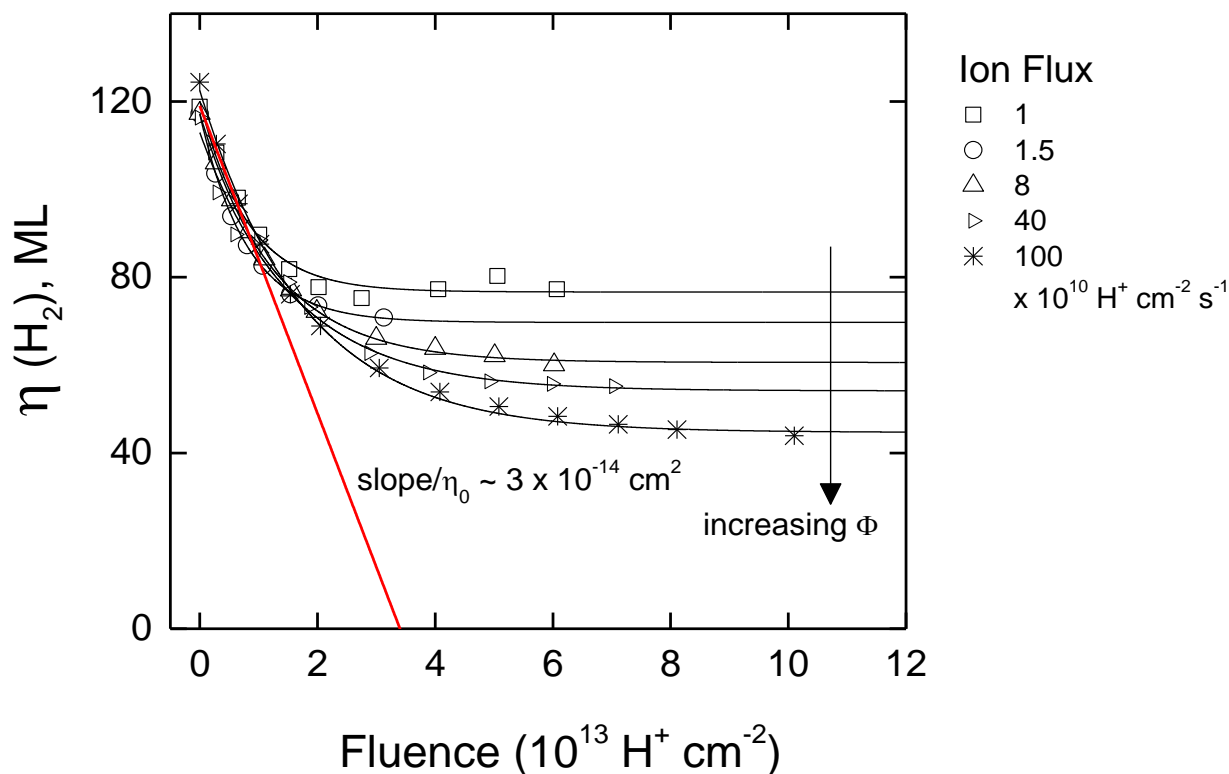


Figure 6.1.5 – Adsorbed  $\text{H}_2$  vs.  $F$  in  $\sim 1060 \text{ ML}$  porous ice films irradiated with  $100 \text{ keV H}^+$  using different fluxes. The residual  $\text{H}_2$  ( $\eta_\infty$ ) increased with decreasing ion flux, when irradiations were performed with ambient  $\text{H}_2$  at  $2 \times 10^{-5} \text{ Torr}$ . The slope at low  $F$ , normalized to the pre-irradiation uptake  $\eta_0$ , gives an  $\text{H}_2$  net loss cross-section  $3 \times 10^{-14} \text{ cm}^2$ , consistent with thickness and pressure studies (Figures 6.1.2B and 6.1.3).



## VII. $\zeta$ -dependent $H_2$ trapping

Synergistic trapping of  $H_2$  in ice films exposed simultaneously to gas and energetic ion fluxes depends on the time it takes for an  $H_2$  molecule to find adsorption sites in pores of the film between ion-driven compaction events that isolate the pores from the external surface. We previously noted that both the  $H_2$  and the ion fluxes are many orders of magnitude larger than interstellar values. However, despite the use of high fluxes in our experiments, we are able to predict the level of residual  $H_2$  in interstellar ices compacted by cosmic rays since our data were taken not far from the interstellar ratio  $\zeta = f/F_H$ . In Figure 6.1.6, we show that the amount of  $H_2$  trapped in irradiated ices increases with decreasing  $\zeta$ . We compiled variation in  $\zeta$  from the two sources: (1) changing  $H_2$  flux under constant ion flux and (2) altering the ion flux under a constant  $H_2$  flux at a pressure of  $2 \times 10^{-5}$  Torr. At the lowest  $\zeta$  obtained in our experiment, which is only 5 times larger than the interstellar value (as indicated by the red marker labeled IS), the trapped  $H_2$  concentration is 7%. This residual hydrogen, at a concentration of 2 to 7%, likely occupies either interstitial sites or is trapped in radiation-induced bubbles (Johnson & Jesser 1997, Loeffler et al. 2010) within the compacted film, in contrast to  $H_2$  occupying pores before the onset of irradiation.

### 6.1.4 Astrophysical Implications

Several important astrophysical implications emerge from this work.

- We constrain the amount of  $H_2$  in interstellar ice. This is important because the  $H_2$  concentration directly affects the chemistry occurring on the icy mantles by, for instance, determining water ice formation via the  $H_2 + OH$  channel (Tielens & Hagen 1982).

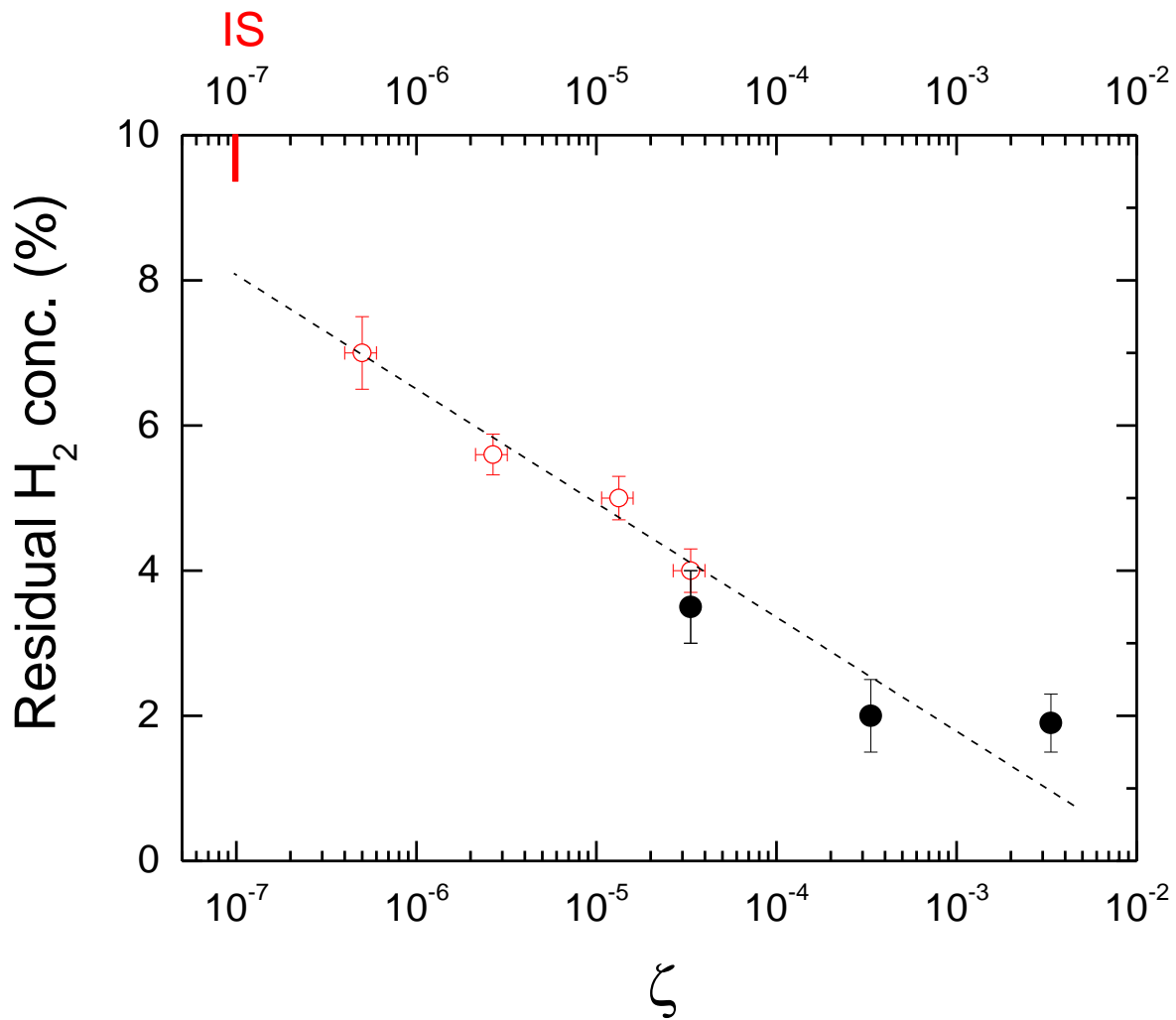


Figure 6.1.6 – The residual H<sub>2</sub> concentration,  $\eta_{\infty}(\text{H}_2) / \eta_{\text{ice}}$ , increases with decreasing  $\zeta$ , the ratio of ion to H<sub>2</sub> fluxes.  $\zeta$  was varied by adjusting the H<sub>2</sub> flux under constant ion flux (•) and by changing the proton flux under constant H<sub>2</sub> flux (o). The H<sub>2</sub> trapped in compacted interstellar ice, where  $\zeta \sim 10^{-7}$  (red marker labeled IS), could be as high as 8% molar. The estimate of interstellar  $\zeta$  is explained in the text. The dotted line is to guide the eye.

Several models have predicted  $\text{H}_2$  abundances between 5 to 30% relative to water ice (Buch & Devlin 1994, Kristensen et al. 2011). We measured concentrations of 3.5 to 12%, but higher pressures ( $10^{-8}$  to  $10^{-5}$  Torr) are required to maintain the equilibrated uptakes. The  $\text{H}_2$  uptake exhibits a power-law dependence,  $\eta_0(P) = 534 P^{0.14}$  over these pressures. Under interstellar conditions, we expect  $\text{H}_2$  concentrations to be  $< 3.5\%$ , smaller than the model predictions. However, higher  $\text{H}_2$  concentrations are possible if the interstellar ice is formed via chemical routes (rather than by accretion of water vapor as presented by our experiments) and presents adsorption sites with increased binding. The  $\text{H}_2$  concentration could also be higher due to additional sources of  $\text{H}_2$ , resulting from processing of H-bearing precursor molecules including  $\text{CH}_4$ ,  $\text{NH}_3$ , and  $\text{CH}_3\text{OH}$  (Sandford et al. 1993).

- The  $\text{H}_2$  adsorption capacity of interstellar ice mantles remains constant above a critical thickness, despite a thickness-independent porosity. At 7 K, we estimate this critical thickness to be  $\sim 1100$  ML (Figure 6.1.2C). Therefore, thicker ice mantles do not necessarily hold more  $\text{H}_2$  than thin ones.
- Cosmic ray (CR) impacts on  $\text{H}_2$ -laden interstellar mantles will decrease the amount of adsorbed  $\text{H}_2$ . At 100 keV, the sputtering yield of  $\text{H}_2$  is  $\sim 10^4$  times that of  $\text{H}_2\text{O}$  ice. Using the quadratic dependence of sputtering on electronic stopping (Brown et al. 1982), recently demonstrated to be valid at GeV energies (Dartois et al. 2015), and assuming the yield ratio of  $10^4$  at all energies, we find that heavier nuclei such as Fe are  $\sim 15$  times more efficient than protons at removing  $\text{H}_2$  adsorbed in interstellar ices. This is despite the  $10^4$ -fold smaller total Fe flux compared to H (Webber & Yushak 1983). We estimate a CR-driven  $\text{H}_2$  loss rate of  $6 \times 10^{12} \text{ H}_2 \text{ cm}^{-2} \text{ y}^{-1}$ , much smaller than the accretion rate of 3

$\times 10^{16} \text{ H}_2 \text{ cm}^{-2} \text{ y}^{-1}$  in a dense cloud with  $10^5 \text{ H}_2 \text{ cm}^{-3}$  at 10 K. Additional experiments are required to examine the validity of a constant  $\text{H}_2\text{O}:\text{H}_2$  yield ratio at different energies.

- Cosmic rays fully compact porous interstellar ices over 2-30 million years (Dartois et al. 2013, Palumbo 2006, Raut et al. 2008). Since the  $\text{H}_2$  accretion rate exceeds the CR-driven loss rate, we can expect pores to be refilled with decreasing amounts of  $\text{H}_2$  over the compaction timescale. The residual  $\text{H}_2$  concentration in irradiated compact ice mantles can be as high as 8% if the initial  $\text{H}_2$  concentration exceeds the values observed in our experiments, due to burial by other accreting gases (Teolis et al. 2006).

### 6.1.5 Conclusions

$\text{H}_2$ -laden ice films held at 7 K were irradiated with 100 keV protons in the presence of ambient hydrogen gas. The amount of  $\text{H}_2$  in the pores of the ice films was ~3.5 to 12% prior to irradiation. Proton impact led to expulsion of  $\text{H}_2$  from the ice film and reduced its porosity. The pores in the compacting film were refilled with decreasing amounts of  $\text{H}_2$  in presence of ambient  $\text{H}_2$ . The initial effective  $\text{H}_2$  net loss cross-section is  $4 (\pm 1) \times 10^{-14} \text{ cm}^2$  at low fluence, independent of  $\text{H}_2$  pressure, film thickness and ion flux. Irradiation to high fluence led to trapping of  $\text{H}_2$  in interstitial sites or radiation-induced bubbles of the compacted film. Reducing  $\zeta$  resulted in an increase of the residual  $\text{H}_2$  concentration; we predict ~8% trapped hydrogen in interstellar ices immersed in ambient  $\text{H}_2$  and compacted by cosmic rays.

## Acknowledgements

We acknowledge support from NASA Origins of the Solar Systems program. E. H. Mitchell acknowledges support from NASA Earth and Space Science Fellowship and Virginia Space Grant Consortium fellowship.

## References

- Allodi, M., et al., Space Sci. Rev. **180**, 101 (2013).
- Bar-Nun, A., Herman, G., Laufer, D., Rappaport, M. L., Icarus **63**, 317 (1985).
- Bauer, P., Käferböck, W., Necas, V., Nuclear Instruments and Methods in Physics Research Section B: Beam Interactions with Materials and Atoms **93**, 132 (1994).
- Bringa, E. M., & Johnson, R. E., Astrophys. J. **603**, 159 (2004).
- Bringa, E. M. et al., Astrophys. J. **662**, 372 (2007).
- Brown, W.L., Augustyniak, W.M., Simmons, E., Marcantonio, K.J., Lanzerotti, L.J., Johnson, R.E., Boring, J.W., Reimann, C.T., Nucl. Inst. Phys. Res. **198**, 1 (1982).
- Buch, V., & Devlin, J. P. J. Chem. Phys. **94**, 4091 (1991).
- Buch, V., & Devlin, J. P., Astrophys. J. Lett. **431**, L135 (1994).
- Dartois, E. et al., A&A **576**, A125 (2015).
- Dartois, E., et al., A&A **557**, A97 (2013).
- Gibb, E. L., Whittet, D. C. B., Boogert, A. C. A., Tielens, A. G. G. M., Astrophys. J. Suppl. **151**, 35 (2004).
- Isokoski, K., Bossa, J. B., Triemstra, T., Linnartz, H., Phys. Chem. Chem. Phys. **16**, 3456 (2014).
- Johnson, R. E., & Jesser, W. A., Astrophys. J. Lett. **480**, L79 (1997).
- Kristensen, L. E., Amiaud, L., Fillion, J. H., Dulieu, F., Lemaire, J. L., A&A **527**, 44 (2011).

- Loeffler, M. J., Raut, U., Baragiola, R. A., J. Chem. Phys. **132** (2010).
- Matar, E., Bergeron, H., Dulieu, F., Chaabouni, H., Accolla, M., Lemaire, J. L., J. Chem. Phys. **133**, 104507 (2010).
- Mitchell, E. H., Raut, U., & Baragiola, R. A., In: Lunar and Planetary Institute Science Conference Abstracts, Irradiation of Methane-Laden Water Ice Films: Relevance to TNOs and Centaurs, 1931 (2014).
- Noble, J. A., Martin, C., Fraser, H. J., Roubin, P., Coussan, S., J. Phys. Chem. Lett. **5**, 826 (2014).
- Palumbo, M. E., A&A **453**, 903 (2006).
- Raut, U., Fama, M., Loeffler, M. J., Baragiola, R. A., Astrophys. J. **687**, 1070 (2008).
- Raut, U., Fama, M., Teolis, B. D., & Baragiola, R. A., J. Chem. Phys. **127**, 204713 (2007a).
- Raut, U., Teolis, B. D., Loeffler, M. J., Vidal, R. A., Fama, M., Baragiola, R. A., J. Chem. Phys. **126**, 244511 (2007b).
- Rowland, B., Fisher, M., & Devlin, J. P., J. Chem. Phys. **95**, 1378 (1991).
- Rowland, B., Kadagathur, N. S., Devlin, J. P., Buch, V., Feldman, T., & Wojcik, M. J., J. Chem. Phys. **102**, 8328 (1995).
- Sack, N. J., & Baragiola, R. A., Phys. Rev. B. **48**, 9973 (1993).
- Sadlej, J., Rowland, B., Devlin, J. P., Buch, V., J. Chem. Phys. **102**, 4804 (1995).
- Sandford, S. A., & Allamandola, L. J., Astrophys. J. Lett. **409**, L65 (1993).
- Sandford, S. A., Allamandola, L. J., Geballe, T. R., Science **262**, 400 (1993).
- Schou, J., J. Nucl. Sci. Tech. **39**, 354 (2002).
- Shi, J., Teolis, B. D., Baragiola, R. A., Phys. Rev. B **79**, 235422 (2009).
- Stenum, B., Schou, J. r., Ellegaard, O., Sorensen, H., Pedrys, R., Phys. Rev. B **67**, 2842 (1991).

- Stevenson, K. P., Kimmel, G. A., Dohnalek, Z., Smith, R. S., Kay, B. D., Science **283**, 1505 (1999).
- Szenes, G., Nuclear Inst. and Methods in Physics Research B **191**, 54 (2002).
- Takaishi, T., & Sensui, Y., Trans Faraday Soc. **59**, 2503 (1963).
- Teolis, B. D., Loeffler, M. J., Raut, U., Fama, M., Baragiola, R. A., Astrophys. J. Lett. **644**, L141 (2006).
- Teolis, B. D., Loeffler, M. J., Raut, U., Famá, M., Baragiola, R. A., Icarus **190**, 274 (2007).
- Tielens, A. G. G. M., The Physics and Chemistry of the Interstellar Medium, Cambridge University Press (2005).
- Tielens, A. G. G. M., & Hagen, W., A&A **114**, 245 (1982).
- Tóth, J., Adsorption: Theory, Modeling, and Analysis, Marcel Dekker, New York (2002).
- Warren, J. A., Smith, G. R., Guillory, W. A., J. Chem. Phys. **72**, 4901 (1980).
- Webber, W. R., & Yushak, S. M., Astrophys. J. **275**, 391 (1983).
- Ziegler, J. F., & Biersack, J. P., Stopping and Range of Ions in Matter (2013).

## 6.2. Suppression of $\text{H}_2\text{O}_2$ in Radiolyzed $\text{H}_2$ -Laden Ice Films

### Abstract

We report the suppression of  $\text{H}_2\text{O}_2$  synthesis in initially porous water ice films when irradiated with 100 keV  $\text{H}^+$  in the presence of ambient  $\text{H}_2$  at 7 K. Compared to irradiated pure water ice, the amount of  $\text{H}_2\text{O}_2$  produced in ice films with adsorbed  $\text{H}_2$  is reduced by  $\sim 16\%$ , estimated from the strength of the  $3.5\text{-}\mu\text{m}$   $\text{H}_2\text{O}_2$  absorption feature, due to  $\text{H}_2$  adsorbed in the pores of the ice film. We find that the suppression does not change with the irradiation flux or for ambient  $\text{H}_2$  pressures between  $10^{-5}$  and  $10^{-7}$  Torr. However, we find that  $\text{H}_2\text{O}_2$  production is reduced by up to  $\sim 50\%$  when  $\text{H}_2\text{O}$  is deposited in the presence of ambient  $\text{H}_2$ , rather than exposing the  $\text{H}_2\text{O}$  film to  $\text{H}_2$  only after deposition. Peroxide production decreases with H-enrichment, which reduces the concentration of radiolytic OH in the films and limits the OH-OH recombination into  $\text{H}_2\text{O}_2$ . This effect could help explain the absence of solid  $\text{H}_2\text{O}_2$  trapped in icy grains immersed in neutral  $\text{H}_2$  in the dark clouds of the interstellar medium, potentially reducing  $\text{H}_2\text{O}_2$  production below observable levels.

### 6.2.1 Introduction

Water ice has been identified as the dominant constituent,  $\sim 60$  to  $70\%$ , of the thin mantles that coat dust grains in interstellar molecular clouds (Gibb et al. 2004, Tielens et al. 1983, van Dishoeck et al. 1996). The grains are impacted by energetic cosmic rays and stellar winds from embedded protostars that may produce chemical changes in the ice at cold temperatures ( $\sim 10$  K), including the production of  $\text{H}_2\text{O}_2$  in water ice films.



Laboratory experiments show the formation of hydrogen peroxide in water ice by energetic ions (Gomis et al. 2004; Loeffler et al. 2006; Moore & Hudson 2000), electrons (Hand & Carlson 2011; Pan et al. 2004; Zheng et al. 2006), and photons (Gerakines et al. 2004; Laffon et al. 2006). The energy deposited by charged particles or photons leads to the formation of species such as H, O, and OH within the ice film, following the excitation and subsequent dissociation of H<sub>2</sub>O. Previous studies have shown that the  $\text{H}_2\text{O} \rightarrow \text{OH} + \text{H}$  channel accounts for 10% of the dissociations in the gas phase (Slanger & Black 1982), compared to  $\text{H}_2\text{O} \rightarrow \text{H}_2 + \text{O}$ , and the former dissociation channel is likely to be even more dominant in the solid phase (Loeffler et al. 2006). Upon radiolytic dissociation, the lighter H received most of the incident ion's kinetic energy, making it much more likely than the slower OH to escape the surrounding molecular cage formed from neighboring H<sub>2</sub>O. The cage effect tends to confine the OH radicals close to the ion track where they were formed, allowing them to react with other OH to form hydrogen peroxide. The production of H<sub>2</sub>O<sub>2</sub> decreases with increasing temperature, which is attributed to the increased escape rate of hydrogen and the diffusion of OH away from the ion track, making H<sub>2</sub>O<sub>2</sub> production less efficient (Loeffler et al. 2006).

The aforementioned laboratory studies have confirmed that H loss (OH enrichment) from water ice during irradiation enhances the production of H<sub>2</sub>O<sub>2</sub>. Here we investigate the reverse effect: How is the radiation synthesis of peroxide affected in ices containing significant quantities of adsorbed hydrogen? The composition of gases surrounding ice-coated grains in the interstellar medium (ISM) is overwhelmingly H<sub>2</sub>, accounting for 90% of the total number density (Tielens 2005, 2013). H<sub>2</sub> can diffuse into the pores of the ice mantle at 10 K, adsorbing at high-energy binding sites and loading the ice with hydrogen over the lifetime of the cloud (Buch & Devlin 1994, Sandford et al. 1993). H<sub>2</sub> can also be incorporated into the ice mantle as it forms

via condensation of ambient water vapor onto the grains. Several models estimate the interstellar abundance of adsorbed  $\text{H}_2$  between 5 and 30% relative to water ice (Buch & Devlin 1994, Dissly et al. 1994, Kristensen et al. 2011, Solomon & Wickramasinghe 1969). Furthermore, interstellar mantles are known to contain molecules such as  $\text{CH}_4$ ,  $\text{NH}_3$ , and  $\text{CH}_3\text{OH}$ , though in smaller quantities relative to  $\text{H}_2\text{O}$  ice (Gibb et al. 2004). Radiation processing of these H-bearing precursors can result in additional  $\text{H}_2$  buildup in the ice, as observed for  $\text{NH}_3$ - $\text{H}_2\text{O}$  mixtures in the laboratory (Loeffler et al. 2010; Sandford et al. 1993). Laboratory studies have assigned the weak absorption feature at  $4141\text{ cm}^{-1}$  ( $2.42\text{ }\mu\text{m}$ ) to solid  $\text{H}_2$  perturbed by the host matrix (Warren et al. 1980, Sandford & Allamandola 1993, Loeffler et al. 2010). To date, solid  $\text{H}_2$  has not been positively identified in interstellar spectra, but this does not preclude its presence in the mantles as it is difficult to detect spectroscopically.

How could this “excess” hydrogen in ice affect the peroxide synthesis that results from particle or photon irradiation? To date, only gas-phase  $\text{H}_2\text{O}_2$  has been detected toward the  $\rho$  Ophiuchus A cloud core at a small abundance of  $10^{-10}$  relative to  $\text{H}_2$  (Bergman et al. 2011). The lack of detection of solid interstellar  $\text{H}_2\text{O}_2$  is puzzling, since laboratory studies show that peroxide readily synthesizes at  $\sim 0.1\%$  concentrations in ice films subjected to energetic processing, and interstellar ices are continually impacted by cosmic rays and stellar winds. Solid  $\text{H}_2$ , if indeed present in appreciable amounts as suggested by models, could suppress the recombination between OH radicals produced in the tracks of the impinging ions and decrease the production of  $\text{H}_2\text{O}_2$ , as is known to occur in liquid water (Pastina & LaVerne 2001). This effect could partially explain the absence of peroxide in the  $\text{H}_2$ -laden interstellar ice. Here, we report on experiments investigating the effects of hydrogen enrichment on  $\text{H}_2\text{O}_2$  production in porous ice films deposited at 7 K and irradiated with 100 keV  $\text{H}^+$  in the presence of ambient  $\text{H}_2$ .

### 6.2.2 Experimental Methods

The experiments were conducted in a cryopumped ultrahigh vacuum (UHV) chamber with a base pressure of  $\sim 10^{-10}$  Torr. Water ice films were vapor-deposited onto a gold-coated quartz crystal microbalance (QCM) cooled to 7 K, through a collimating micro-capillary array (MCA) doser at  $45^\circ$  incidence. The microbalance measures the areal mass of the film, which is converted to column density by dividing by the mass of the molecule. For these experiments, the ice films were grown to column density  $\sim 1060$  ML ( $1 \text{ ML} = 10^{15} \text{ H}_2\text{O cm}^{-2}$ , about a monolayer). The deposition angle was chosen to ensure growth of a porous film (Raut et al. 2007b, Stevenson et al. 1999).

Following ice deposition,  $\text{H}_2$  gas (99.9% purity) was admitted into the chamber at pressures ranging from  $2 \times 10^{-4}$  to  $10^{-7}$  Torr. The  $\text{H}_2$  pressure  $P$ , measured with a nude ionization gauge, has been corrected for gas-dependent sensitivity and is accurate within 20%. At a pressure of  $2 \times 10^{-7}$  Torr, mass spectrometer readings showed  $\sim 100$  times more  $\text{H}_2$  than adventitious background  $\text{H}_2$  at a base pressure of  $10^{-10}$  Torr in the UHV chamber.

The uptake  $\eta$  by the ice films in response to  $\text{H}_2$  exposure was measured with the QCM, which has a sensitivity of 0.63 ML for  $\text{H}_2$ . The ice films were initially exposed to  $\text{H}_2$  at  $2 \times 10^{-4}$  Torr, which resulted in a near-instantaneous uptake of  $\text{H}_2$  as measured by the decreased frequency of the QCM. At a constant  $\text{H}_2$  pressure,  $\eta$  increased linearly with time and asymptotically approached an equilibrium value  $\eta_0$ , where adsorption and desorption rates are equal. The pressure was either maintained at  $2 \times 10^{-4}$  or lowered to between  $2 \times 10^{-5}$  and  $2 \times 10^{-7}$  Torr, resulting in a loss of  $\text{H}_2$  from the film.  $\text{H}_2$  uptake equilibrates at different  $P$ -dependent values of  $\eta_0$ .

In a separate set of experiments,  $\text{H}_2\text{O}$  and  $\text{H}_2$  were co-deposited at 7 K in a scenario similar to the ISM environment. This was achieved by first admitting  $\text{H}_2$  into the vacuum chamber through an MCA doser to pressures of  $2 \times 10^{-4}$  to  $10^{-6}$  Torr; no  $\text{H}_2$  adsorption on the bare QCM substrate was observed at 10 K.  $\text{H}_2\text{O}$  was then slowly admitted into the chamber via a different MCA doser in the presence of a constant pressure of ambient  $\text{H}_2$ , and a 1060 ML-thick  $\text{H}_2\text{-H}_2\text{O}$  film was deposited on the QCM. We are unable to discern  $\eta(\text{H}_2)$  for co-deposited  $\text{H}_2\text{-H}_2\text{O}$  films from a single mass-loading rate measured by the QCM. However,  $\text{H}_2$  trapped in the ice matrix is detected using infrared spectroscopy.

The  $\text{H}_2\text{O}$  (or  $\text{H}_2\text{-H}_2\text{O}$ ) films were then irradiated at  $9^\circ$  from normal incidence with  $m/q$ -selected, 100 keV  $\text{H}^+$  from an ion accelerator, in the presence of ambient  $\text{H}_2$ . The ion flux, measured with a Faraday cup in the sample position and monitored by a thin wire placed in the path of the beam, was varied from  $\sim 10^{10}$  to  $10^{12} \text{ H}^+ \text{ cm}^{-2} \text{ s}^{-1}$ . Electrostatic deflection plates were used to raster the beam for uniform irradiation of the films.

A Thermo Nicolet Nexus 670 infrared spectrometer was used to collect specular reflectance spectra at  $35^\circ$  incidence with  $2 \text{ cm}^{-1}$  resolution. Spectra were collected following ice film deposition,  $\text{H}_2$  exposure, and after irradiation steps of incremental fluence. To obtain the reflectance  $R$ , the spectra of the ice films were divided by the reflectance spectrum  $R_0$  of the gold substrate and then converted to optical depth,  $-\ln(R/R_0)$ . In particular, we focus on the changes in the  $2.42\text{-}\mu\text{m}$  and  $3.5\text{-}\mu\text{m}$  absorption bands for  $\text{H}_2$  and  $\text{H}_2\text{O}_2$ , respectively. The  $\text{H}_2\text{O}_2$  band area was obtained by integrating over the  $3.5\text{-}\mu\text{m}$  absorption region after subtraction of polynomial baseline fitted to the curved continuum, while straight lines were subtracted to calculate the  $\text{H}_2$  band areas.

### 6.2.3 Results

Figure 6.2.1A shows the sharp hydrogen uptake within the pores of a 1057 ML-thick porous H<sub>2</sub>O ice film when exposed to H<sub>2</sub> at  $2 \times 10^{-4}$  Torr. The H<sub>2</sub> uptake, measured by the microbalance, amounted to 126 ML of H<sub>2</sub>. Following the initial saturation of adsorption, the H<sub>2</sub> pressure was reduced to  $2 \times 10^{-6}$  Torr, allowing 33 ML of H<sub>2</sub> to desorb from the ice. The equilibrium  $\eta_0(\text{H}_2)$  at  $2 \times 10^{-6}$  Torr relative to  $\eta(\text{H}_2\text{O})$  is ~9 molecular-%.

The H<sub>2</sub> adsorbed in the pores of ice film shows a weak absorption with maxima at 4133 cm<sup>-1</sup> (2.419  $\mu\text{m}$ ) (Figure 6.2.1B). This homonuclear H<sub>2</sub> vib-rotational transition, forbidden in gas-phase, becomes weakly infrared-active in solid matrices due to symmetry-breaking perturbations at the walls of the pores. The band strength, position, and width of this H<sub>2</sub> absorption is known to be affected by both the matrix composition and H<sub>2</sub> concentration (Remigis & Welsh 1970; Warren et al. 1980). Sandford et al. (1993) reported a peak position of 4137-4140 cm<sup>-1</sup> for photosynthesized H<sub>2</sub>, different from our measurements. However, their experiments investigated H<sub>2</sub>O-rich films containing small quantities of CH<sub>3</sub>OH, NH<sub>3</sub>, and CO, rather than H<sub>2</sub> adsorbed in high-purity H<sub>2</sub>O (Sandford & Allamandola 1993; Sandford et al. 1993). The matrix effect might explain the discrepancy in the peak positions between the two experiments. The absorption position also depends on the spin state of the H<sub>2</sub> molecule; the Q<sub>1</sub>(0) transition in para-H<sub>2</sub> results in absorption between 4138-4145 cm<sup>-1</sup>, while the Q<sub>1</sub>(1) transition in ortho-H<sub>2</sub> lies in between 4127-4132 cm<sup>-1</sup> (Buch & Devlin 1994). As per this assignment, most of the H<sub>2</sub> trapped in the pores of our films are in the triplet or ortho state.

The adsorption of H<sub>2</sub> within the ice pores also affects the OH dangling bond (DB) absorption features at ~2.7  $\mu\text{m}$  (Figure 6.2.1B). H<sub>2</sub> uptake of 126 ML (spectrum *b*) causes ~4- to 5-cm<sup>-1</sup> blueshifts in the positions of the dangling bond (DB1 and DB2) absorptions. The shifts

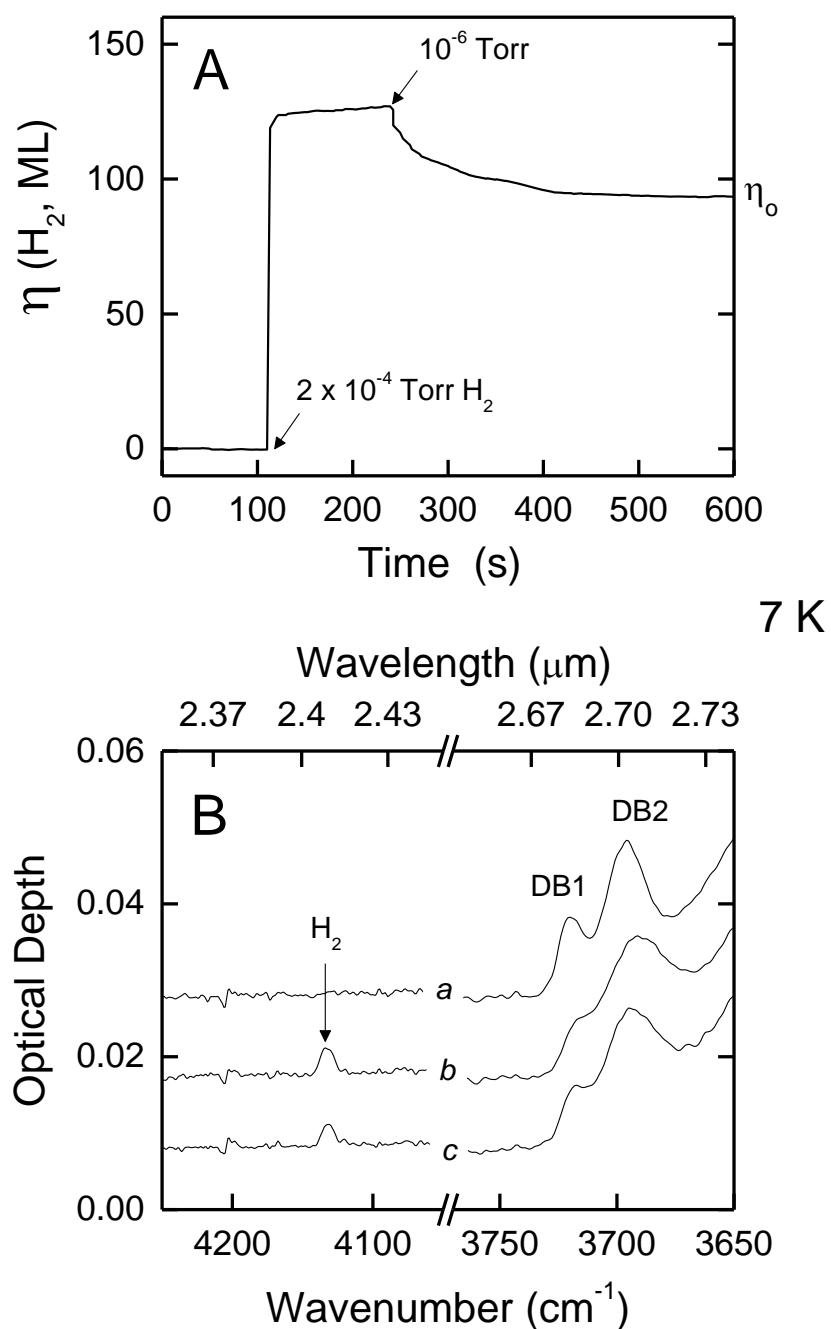


Figure 6.2.1 – Top panel: Uptake of 126 ML of  $\text{H}_2$  by a 1057-ML  $\text{H}_2\text{O}$  ice film at 7 K from exposure of  $\text{H}_2$  gas at  $2 \times 10^{-4}$  Torr. The pressure was then reduced to  $2 \times 10^{-6}$  Torr, causing  $\eta(\text{H}_2)$  to reduce to 93 ML,  $\sim 9\%$  of  $\eta(\text{ice})$ . Bottom panel: Effects of  $\text{H}_2$  uptake on dangling bond

(DB) absorptions. Spectrum *a* shows ice film without H<sub>2</sub>. Spectra *b* and *c* show infrared absorptions at 4133 cm<sup>-1</sup> due to 126 and 93 ML of H<sub>2</sub> respectively. The H<sub>2</sub> uptake causes small blueshifts (2-5 cm<sup>-1</sup>) in the DB positions, in addition to band broadening that results in the merging of DB 1 and 2. All spectra have been vertically shifted for clarity.

are small compared to  $\sim 30\text{-cm}^{-1}$ -shifts caused by the presence of heavier molecules such as methane in  $\text{H}_2\text{O}$  (Raut et al. 2007b). The DB features also broaden and merge with increased  $\text{H}_2$  adsorption, making the well-resolved peaks nearly indistinguishable. Spectrum *c* shows the ice film with 93 ML of  $\text{H}_2$  after ambient pressure was reduced. The blueshifts are even smaller, 1 to  $2\text{ cm}^{-1}$ , with smaller amounts of  $\text{H}_2$ .

Figure 6.2.2 shows changes in the infrared spectra for the  $2.42\text{-}\mu\text{m}$   $\text{H}_2$  (Panel A) and  $3.5\text{-}\mu\text{m}$   $\text{H}_2\text{O}_2$  (Panel B) absorptions as a function of 100 keV proton fluence using a flux of  $\sim 1 \times 10^{12}\text{ H}^+\text{ cm}^{-2}\text{ s}^{-1}$ . The  $\text{H}_2\text{O}_2$  absorption band from the spectrum irradiated to high fluence,  $1.02 \times 10^{15}\text{ H}^+\text{ cm}^{-2}$ , is shown in the shaded blue region, following subtraction of the polynomial baseline indicated by the blue dotted curve. The peak position of the  $\text{H}_2\text{O}_2$  feature ( $2852\text{ cm}^{-1}$ ) at 7 K is identical to that measured previously at 20 K (Loeffler et al. 2006). However, the band at 7 K is broader, with a full-width half-maximum (FWHM) of  $120\text{ cm}^{-1}$ , compared to  $98\text{ cm}^{-1}$  at 20 K and  $70\text{ cm}^{-1}$  at 80 K (Loeffler et al. 2006). We note that the  $\text{H}_2$  band diminishes, while the  $\text{H}_2\text{O}_2$  band increases in intensity, with increasing ion fluence.

Figure 6.2.3, column A, top panel, shows the  $\text{H}_2\text{O}_2$  absorption feature for an  $\text{H}_2\text{O}$  film irradiated in the presence of  $\sim 10^{-10}$  Torr background  $\text{H}_2$  (open symbols), as well as  $\text{H}_2\text{O}$  films irradiated in the presence of  $\text{H}_2$  gas (closed symbols), after an ion fluence  $F$  of  $\sim 1 \times 10^{14}\text{ H}^+\text{ cm}^{-2}$  using a flux of  $10^{12}\text{ H}^+\text{ cm}^{-2}\text{ s}^{-1}$ . Polynomials fitted to the curved baseline have been subtracted from the absorption bands. Exposure to  $\text{H}_2$  gas at pressures of 2 (red), 20 (green), and  $200 \times 10^{-7}$  Torr (dark blue) resulted in the pre-irradiation uptake of 81, 93, and 120 ML  $\text{H}_2$ , respectively, in the pores of the  $\text{H}_2\text{O}$  film; these spectra are labelled “P” in the figure. No  $\text{H}_2$  uptake by the ice was detected due to background  $\text{H}_2$  at base pressure  $\sim 10^{-10}$  Torr. The peroxide absorption band areas are reduced by  $\sim 16\%$  in the irradiated P-type  $\text{H}_2\text{O}$  films with respect to ice irradiated in the



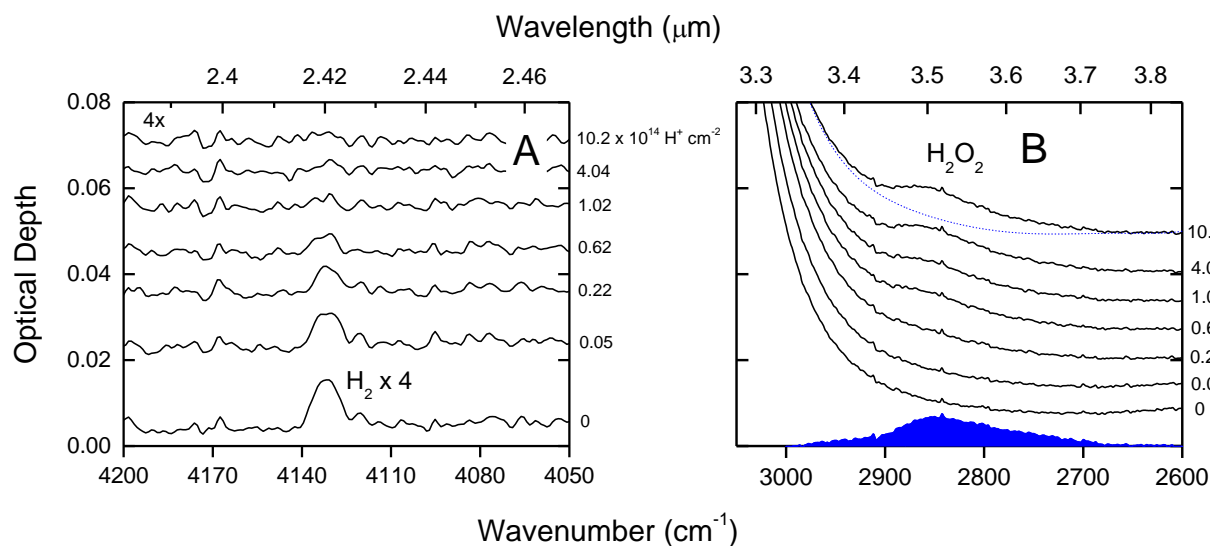


Figure 6.2.2 – Changes in the infrared absorptions of solid  $H_2$  (left) and  $H_2O_2$  (right) in a 1057-ML  $H_2O$  ice film during 100 keV  $H^+$  irradiation in presence of  $H_2$  at  $2 \times 10^{-6}$  Torr. The pre-irradiation  $H_2$  uptake by the ice film at 7 K was 93 ML. The  $H_2$  spectra are multiplied by 4. The blue shaded region is the  $H_2O_2$  band following subtraction of the polynomial baseline (blue dotted curve) from the spectra of the film irradiated to  $1.02 \times 10^{15} H^+ cm^{-2}$ . The numbers adjacent to the spectra are fluence in units of  $10^{14} H^+ cm^{-2}$ . All spectra are vertically shifted for clarity.

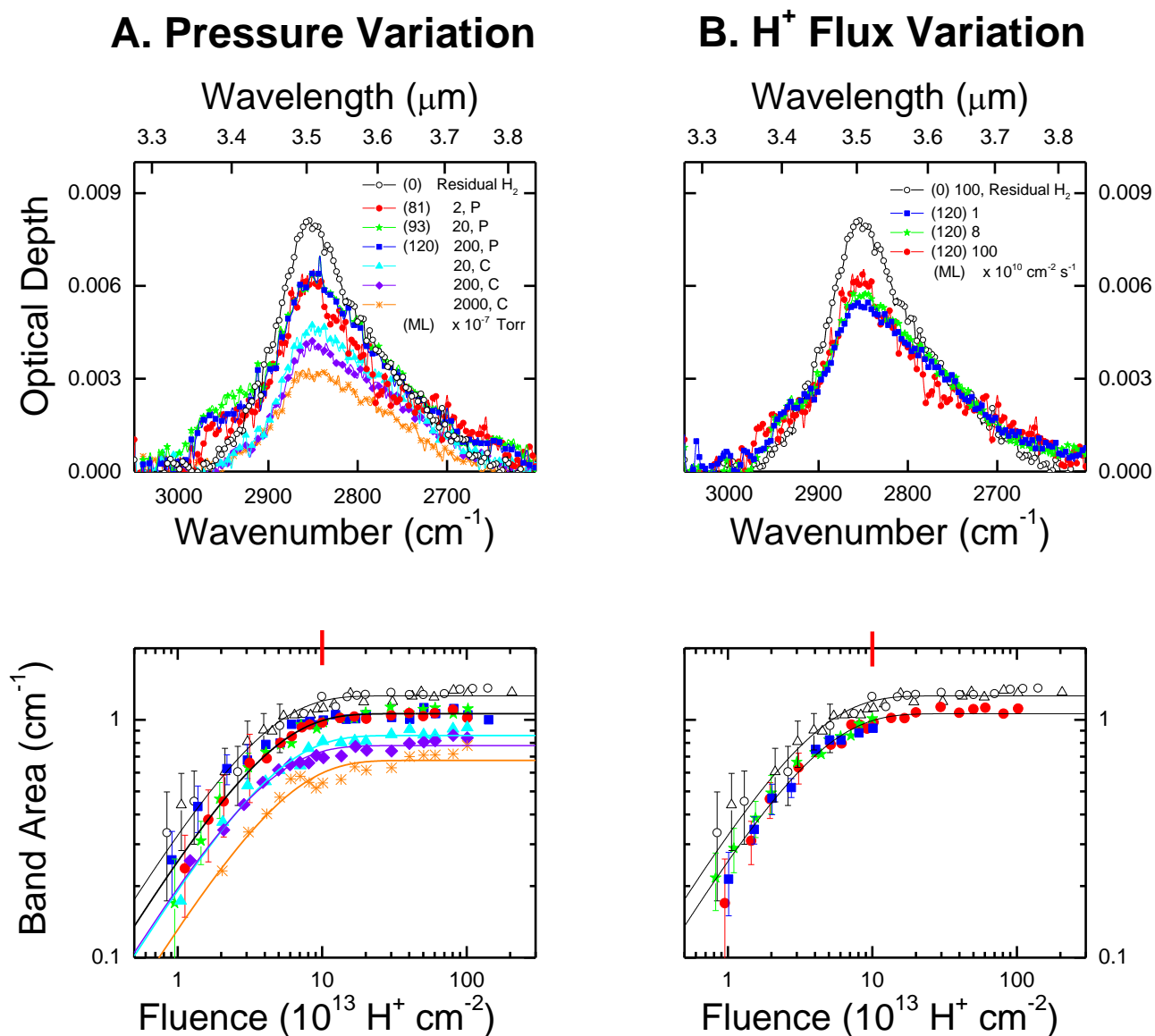


Figure 6.2.3 – Top panel in column *A* shows background-subtracted H<sub>2</sub>O<sub>2</sub> absorptions in spectra of ice films with adsorbed H<sub>2</sub> (filled symbols) vs. a film without deliberate exposure to H<sub>2</sub> (unfilled circles). The ~1060-ML films are irradiated with 100 keV H<sup>+</sup> to a fluence of  $1 \times 10^{14} \text{ cm}^{-2}$ , using a flux of  $10^{12} \text{ H}^+ \text{ cm}^{-2} \text{ s}^{-1}$ . The spectra are labeled with pre-irradiation H<sub>2</sub> uptake

(ML) corresponding to different  $P$  ( $10^{-7}$  Torr). The fluence dependence of the band areas (bottom panel *A*) shows a systematic ( $16 \pm 0.7$ ) % suppression in  $\text{H}_2\text{O}_2$  production in films with  $\text{H}_2$  (filled symbols), compared to those without  $\text{H}_2$  (unfilled symbols). Lines are guides to the eye. Red marker on top axis indicates the fluence of the spectra in top panel. In column *B*, we compare  $\text{H}_2\text{O}_2$  bands for films exposed to  $200 \times 10^{-7}$  Torr  $\text{H}_2$  and irradiated to  $1 \times 10^{14}$   $\text{H}^+$   $\text{cm}^{-2}$  using various  $\text{H}^+$  fluxes, against the  $\text{H}_2\text{O}_2$  bands in film irradiated in the presence of adventitious background  $\text{H}_2$  using  $10^{12}$   $\text{H}^+$   $\text{cm}^{-2}$   $\text{s}^{-1}$ . The films exposed to  $\text{H}_2$  adsorb 120 ML prior to irradiation. No detectable  $\text{H}_2$  adsorbs in the ice at background  $\text{H}_2$  pressure (UHV base pressure  $\sim 10^{-10}$  Torr).

presence of background  $\text{H}_2$ , independent of ambient  $\text{H}_2$  pressure. Based on the profile of the 3.5- $\mu\text{m}$  absorption, the  $\text{H}_2\text{O}_2$  produced from ion irradiation at 7 K exists as  $\text{H}_2\text{O}_2\cdot 2\text{H}_2\text{O}$  trimers mixed in water (Loeffler & Baragiola 2005).

We also show the  $\text{H}_2\text{O}_2$  absorption bands for co-deposited  $\text{H}_2$ - $\text{H}_2\text{O}$  films (labelled “C” in Figure 6.2.3A) irradiated in the presence of ambient  $\text{H}_2$  at pressures of 20 (light blue), 200 (purple), and  $2000 \times 10^{-7}$  Torr (orange). We observe greater suppression in  $\text{H}_2\text{O}_2$  production for these C-type ices, compared with the  $\sim 16\%$  decrease for P-type ice. With respect to films irradiated with background  $\text{H}_2$ , the peroxide absorption band is reduced by  $\sim 32$ , 38, and 47%, with increasing  $\text{H}_2$  pressure.

In the bottom panel of Figure 6.2.3, column A, we show the increase in  $\text{H}_2\text{O}_2$  production with ion fluence. The amount of  $\text{H}_2\text{O}_2$  produced is suppressed at all fluences by  $(16 \pm 0.7)\%$  in hydrogen-containing  $\text{H}_2\text{O}$  (P-type ice) when compared with  $\text{H}_2\text{O}$  with only background  $\text{H}_2$  exposure, independent of ambient  $\text{H}_2$  for  $P \geq 2 \times 10^{-7}$  Torr. For co-deposited  $\text{H}_2$ - $\text{H}_2\text{O}$  films irradiated in the presence of ambient  $\text{H}_2$  (C-type ice), the peroxide production is reduced by  $(32 \pm 1)$ ,  $(38 \pm 0.2)$ , and  $(47 \pm 0.2)\%$  at all fluences, for  $\text{H}_2$  pressures of 20, 200, and  $2000 \times 10^{-7}$  Torr, respectively.

Column B shows similar  $\text{H}_2\text{O}_2$  suppression effects for  $\text{H}_2\text{O}$  films exposed to  $200 \times 10^{-7}$  Torr ambient  $\text{H}_2$  (P-type), resulting in an uptake of 120 ML  $\text{H}_2$  in the pores of the ice, and irradiated to  $1 \times 10^{14} \text{ H}^+ \text{ cm}^{-2}$  at fluxes of 1, 8, and  $100 \times 10^{10} \text{ H}^+ \text{ cm}^{-2} \text{ s}^{-1}$ . We again observe a  $(16 \pm 0.7)\%$  decrease in the  $\text{H}_2\text{O}_2$  band area at all fluences, independent of irradiation flux, compared to ice films irradiated at  $100 \times 10^{10} \text{ H}^+ \text{ cm}^{-2} \text{ s}^{-1}$  in the presence of background  $\text{H}_2$ .

In Figure 6.2.4, we show the increase in normalized  $\text{H}_2\text{O}_2$  absorption band area (closed symbols) for  $\text{H}_2\text{O}$  ice exposed to varying pressures of ambient  $\text{H}_2$  (P-type ice) and irradiated at a

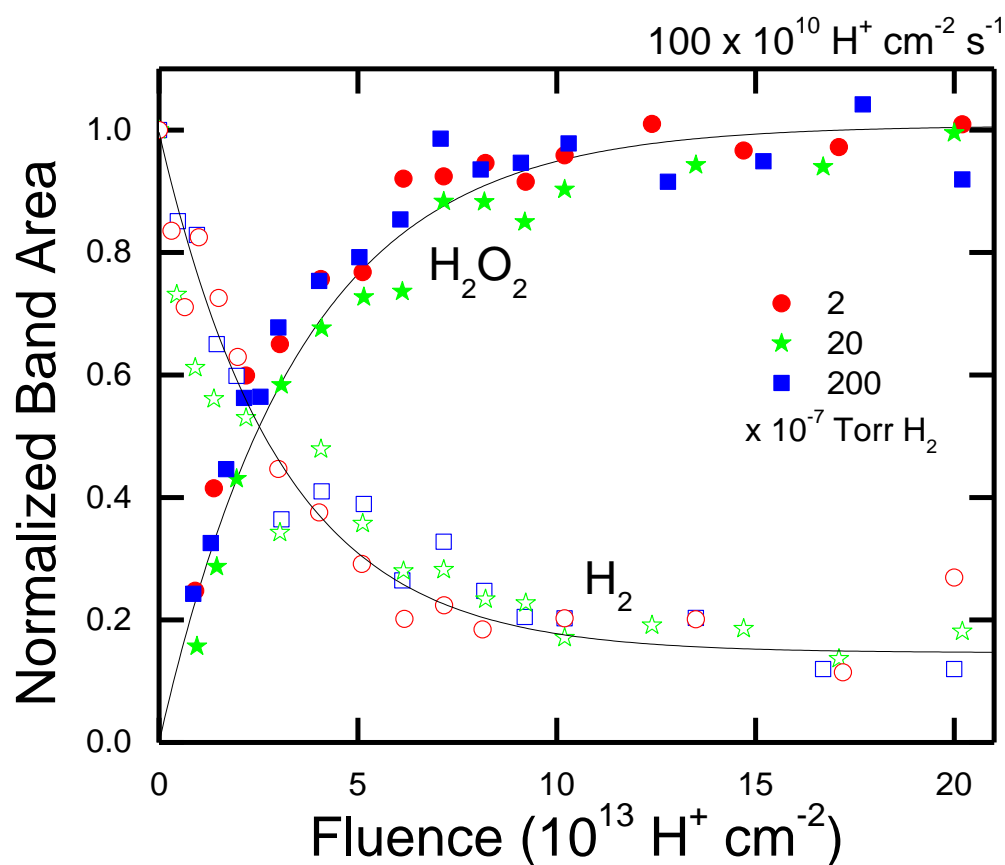


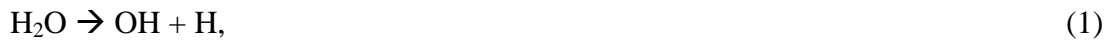
Figure 6.2.4 – Decrease in normalized  $\text{H}_2$  absorption band area ( $2.42 \mu\text{m}$ ) and simultaneous increase in normalized  $\text{H}_2\text{O}_2$  absorption band area ( $3.5 \mu\text{m}$ ) during  $100 \text{ keV H}^+$  irradiation of  $1060\text{-ML H}_2$ -laden porous ice films, exposed to  $\text{H}_2$  at pressures of 2, 20, and  $200 \times 10^{-7} \text{ Torr H}_2$  (P-type). Ion flux was  $1 \times 10^{12} \text{ H}^+ \text{ cm}^{-2} \text{ s}^{-1}$ . Lines are guides to the eye.

constant flux of  $1 \times 10^{12} \text{ H}^+ \text{ cm}^{-2} \text{ s}^{-1}$ , with simultaneous decrease in the normalized  $\text{H}_2$  absorption band area ( $4133 \text{ cm}^{-1}$ ). The production of  $\text{H}_2\text{O}_2$  and sputtering of adsorbed  $\text{H}_2$  saturate at high fluences. Previous studies done in our laboratory have shown that loss of adsorbed  $\text{H}_2$  is due to sputtering, and that the amount of  $\text{H}_2$  in the ice approaches a pressure-independent level,  $\sim 25$  to  $35\% \eta_0$  (Raut et al. 2015, Chapter 6.1).

#### 6.2.4 Discussion and Astrophysical Implications

The results of the experiments show that  $\text{H}_2\text{O}_2$  production in ice films with adsorbed  $\text{H}_2$  is suppressed compared to ice films exposed to only residual amounts of  $\text{H}_2$ , when irradiated with 100 keV protons. Previous experiments done in our laboratory (Raut et al. 2015, Chapter 6.1) have shown that proton impacts cause adsorbed  $\text{H}_2$  to be sputtered from the ice film, simultaneous with ion-induced pore collapse, trapping  $\text{H}_2$  at concentrations of 2 to 7% in interstitial sites or radiation-induced bubbles (Johnson & Jesser 1997, Loeffler et al. 2010). This  $\text{H}_2$  remains trapped in the ice even upon removal of ambient  $\text{H}_2$  and up to temperatures of 170 K, where  $\text{H}_2\text{O}$  desorption begins. Although the amount of adsorbed  $\text{H}_2$  decreases during irradiation, H-enrichment in the film evidently reduces the production of radiolytic  $\text{H}_2\text{O}_2$ .

The most likely channel for  $\text{H}_2\text{O}_2$  synthesis results from the dissociation of the ice (Slanger & Black 1982):



followed by the recombination of OH radicals (Loeffler et al. 2006):



This pathway causes the film to become O-enriched as the lighter H receives most of the kinetic energy upon ion impact and more easily escapes the molecular cage. This O-enrichment,

favoring  $\text{H}_2\text{O}_2$  production, decreases for films with adsorbed  $\text{H}_2$ . The presence of  $\text{H}_2$  also introduces competing radiolytic channels such as:



thus suppressing the production of  $\text{H}_2\text{O}_2$ , as has been observed in liquid water (Pastina & LaVerne 2001).

We find  $\sim 16\%$  suppression in  $\text{H}_2\text{O}_2$  production for  $\text{H}_2\text{O}$  ice films immersed in ambient  $\text{H}_2$ , irrespective of both  $\text{H}_2$  pressure (for pressures  $\geq 2 \times 10^{-7}$  Torr) and proton flux. This is somewhat unexpected, given that the  $\text{H}_2$  concentration with respect to the ice – ostensibly the key factor in suppressing  $\text{H}_2\text{O}_2$  formation – varies with both  $\text{H}_2$  pressure and proton flux (Raut et al. 2015, Chapter 6.1). It is possible, however, that with the  $\text{H}_2$  limited to adsorption sites within the pores of the ice, the difference in  $\text{H}_2$  concentration for varying ambient  $\text{H}_2$  pressures is not significant enough to produce a dependence on ambient pressure above  $2 \times 10^{-7}$  Torr. Indeed, we do see such  $\text{H}_2$  pressure dependence on the suppression of  $\text{H}_2\text{O}_2$  synthesis, up to  $\sim 50\%$  reduction, when the  $\text{H}_2$  is dispersed uniformly throughout the entire ice film for co-deposited films (C-type), compared to P-type films, where  $\text{H}_2$  is confined to the pores. The uniform distribution of  $\text{H}_2$  could result in increased interaction with OH radicals formed in the ion track, which also forms uniformly over the irradiated volume.

Both P- and C-type  $\text{H}_2$  integration are likely to be important in understanding the dynamics of peroxide synthesis in interstellar environments, as  $\text{H}_2$  can diffuse into the pores of an existing ice mantle or become incorporated into the ice as it forms via condensation. In the ISM,  $\sim 99\%$  of the ordinary mass is attributed to gas-phase matter, three-quarters of which is due to  $\text{H}/\text{H}_2$ . We have shown in previous studies that adsorption of local  $\text{H}_2$  within the ice pores, gradually collapsing due to prolonged exposure to cosmic rays and stellar wind, can lead to

residual concentrations as high as  $\sim 8\%$  in interstellar ice (Raut et al. 2015, Chapter 6.1). According to our results, this adsorbed hydrogen would inhibit the radiolytic production of  $\text{H}_2\text{O}_2$  as compared to its synthesis in pure radiolyzed ice grains, possibly reducing  $\text{H}_2\text{O}_2$  abundance below observable levels and explaining the lack of detected peroxide in the ISM.

## References

- Bergman, P., Parise, B., Liseau, R., Larsson, B., Olofsson, H., Menten, K. M., Güsten, R.,  
A&A **531**, L8 (2011).
- Buch, V., & Devlin, J. P., J. Astrophys. Lett. **431**, L135 (1994).
- Dissly, R. W., Allen, M., Anicich, V. G., J. Astrophys. **435**, 685 (1994).
- van Dishoeck, E.F. et al., A&A **315**, L349 (1996).
- Gerakines, P. A., Moore, M. H., Hudson, R. L., Icarus **170**, 202 (2004).
- Gibb, E. L., Whittet, D. C. B., Boogert, A. C. A., Tielens, A. 2004, J. Astrophys. Suppl. **151**,  
35 (2004).
- Gomis, O., Satorre, M. A., Strazzulla, G., Leto, G., Planet. Spa. Sci. **52**, 371 (2004).
- Hand, K. P., & Carlson, R. W. Icarus **215**, 226 (2011).
- Johnson, R. E., & Jesser, W. A., J. Astrophys. Lett. **480**, L79 (1997).
- Kristensen, L. E., Amiaud, L., Fillion, J. H., Dulieu, F., Lemaire, J. L. A&A **527**, 44 (2011).
- Laffon, C., Lacombe, S., Bournel, F., Ph, P. J. Chem. Phys. **125**, 204714 (2006).
- Loeffler, M. J., & Baragiola, R. A., Geophys. Res. Lett. **32**, L17202 (2005).
- Loeffler, M. J., Raut, U., Baragiola, R. A., J. Chem. Phys. **132** (2010).
- Loeffler, M. J., Raut, U., Vidal, R. A., Baragiola, R. A., Carlson, R. W., Icarus **180**, 265  
(2006).



- Moore, M. H., & Hudson, R. L., *Icarus* **145**, 282 (2000).
- Pan, X., Bass, A. D., Jay-Gerin, J.-P., Sanche, L., *Icarus* **172**, 521 (2004).
- Pastina, B., & LaVerne, J. A., *J. Phys. Chem. A*. **105**, 9316 (2001).
- Raut, U., Fama, M., Teolis, B. D., Baragiola, R. A., *J. Chem. Phys.* **127**, 204713 (2007b).
- Raut, U., Mitchell, E.H., Baragiola, R.A., *J. Astrophys.* **811**, 2 (2015).
- Remigis, J. D., & Welsh, H. L., *Can. J. Phys.* **48**, 1622 (1970).
- Sandford, S. A., & Allamandola, L. J., *J. Astrophys. Lett.* **409**, L65 (1993).
- Sandford, S. A., Allamandola, L. J., Geballe, T. R., *Science* **262**, 400 (1993).
- Slanger, T. G., & Black, G., *J. Chem. Phys.* **77**, 2432 (1982).
- Solomon, P. M., & Wickramasinghe, N. C., *J. Astrophys.* **158**, 449 (1969).
- Stevenson, K. P., Kimmel, G. A., Dohnalek, Z., Smith, R. S., Kay, B. D., *Science* **283**, 1505 (1999).
- Tielens, A., Hagen, W., Greenberg, J.M., *J. Phys. Chem.* **87**, 21 (1983).
- Tielens, A. G. G. M., *The Physics and Chemistry of the Interstellar Medium*, Cambridge University Press (2005).
- Tielens, A.G.G.M., *Rev. Mod. Phys.* **85**, 1021 (2013).
- Warren, J. A., Smith, G. R., Guillory, W. A., *J. Chem. Phys.* **72**, 4901 (1980).
- Zheng, W., Jewitt, D., Kaiser, R. I., *J. Astrophys.* **639**, 534 (2006).

## CHAPTER 7

### Conclusions

The research presented in this dissertation is centered on porous water ice in astronomical environments, and we have created laboratory simulations of H<sub>2</sub>O that has been detected on the lunar surface, giant planet satellites, trans-Neptunian objects, and dust grains in interstellar molecular clouds. We have investigated how environmental conditions such as temperature, accretion source, and atmospheric content affect ice porosity and phase. The ices were thermally processed and exposed to energetic particle bombardment to examine the role of pervasive space phenomena on the state of the ices, to contribute to the understanding of the history and evolution of extraterrestrial ice. Analogs of extraterrestrial ice were created by depositing H<sub>2</sub>O films under various environmental conditions on cold substrates from the vapor phase under ultrahigh vacuum. We have used several experimental techniques in tandem to probe the physical and chemical changes induced in these astronomical analogs, including quartz crystal microgravimetry, infrared spectroscopy, ultraviolet-visible spectroscopy, and mass spectrometry. The following is a synopsis of the key findings and conclusions of the research presented in this dissertation.

First, we characterized the temperature dependence of isothermal crystallization kinetics of amorphous ice between 130 and 141 K, finding that crystallization time decreases with temperature with a crystallization activation energy of ~64 kJ per mole for low-porosity ice. We found decreased crystallization times with increasing isothermal crystallization temperature, and observed that crystallization unfolds in two distinct stages at all temperatures. The first stage is due to nucleation at the external surfaces of the ice, and the second stage is attributed to nucleation at the surfaces of semi-compacted pores within the bulk of the ice. We found that the

second stage drives the crystallization of ~90% of the ice film. We used our laboratory measurements to estimate crystallization times at lower temperatures relevant to Jovian moons.

We then characterized potential porosity effects by depositing amorphous ice of varying porosity at 10 K, measured the extent of their compaction during heating, and isothermally crystallized the films between 130 and 141 K. We found that the ices thermally compact at a rate that is independent of initial porosity, but that this rate slows significantly above ~120 K, causing the retention of porosity in the films despite the disappearance of the dangling bond absorption features. The retained porosity in the ice films caused a significant decrease in crystallization times, a ~15-fold reduction in time for a film of five-fold greater porosity, as well as smaller crystallization activation energy (~60 kJ per mole) for ices of high porosity compared to low-porosity ice (~64 kJ per mole).

We suggested that the spread in crystallization time reported in the literature for ostensibly nonporous films could be attributed to porosity effects, due to widely varying ice deposition conditions in previous studies and considering our finding that even low-porosity ice resists complete thermal compaction up to laboratory crystallization temperatures. The strong dependence of crystallization time on ice porosity implies a surface-driven crystallization process, which we again found to proceed in two distinct stages. However, these two stages were less distinguishable for mesoporous films, suggesting that capillarity effects opposing nucleation are reduced at the surfaces of the mesopores, decreasing the relative energy barrier between the internal and external ice surfaces. Using our laboratory measurements, we predict that amorphous ice condensed from water vapor plume ejecta on Europa at mid-latitudes can crystallize in 3 months if the ice is substantially porous, compared to 7 years for compact ice.

The crystallization time could be further reduced by exposure to magnetospheric ions; further experiments are needed to examine these effects.

We have also simulated the radiation environment surrounding the ~monolayer coverage of water on the lunar regolith, to investigate the mechanism behind the observed diurnal and latitudinal variation of H<sub>2</sub>O. Two different laboratory analogs were created. For the first simulation, we deposited a single monolayer of H<sub>2</sub>O from the vapor phase onto a carbon substrate on the microbalance, and irradiated with 193 nm photons. We found that the column density of water decreased exponentially with ion dose, and measured a photodesorption cross-section of  $7.4 (\pm 0.5) \times 10^{-19} \text{ cm}^2$ . This leads to an estimated lifetime for photodesorption of ~12 hours on the lunar surface for average solar activity at the sub-solar point, or 5 to 40 hours considering the variation of the solar intensity across solar cycles. In the second simulation, we irradiated water-coated Apollo 16 lunar soil with 4-keV He<sup>+</sup> and found a sputtering cross-section of  $1.2 (\pm 0.4) \times 10^{-16} \text{ cm}^2$ . We estimate a ~12-year lifetime for water on the lunar surface due to solar wind protons. Comparing the two simulations, we found that photodesorption by solar UV is four orders of magnitude more efficient than sputtering by the solar wind. We proposed a mechanism for the redistribution of water across the lunar surface, whereby most of the ejected water is re-adsorbed on the surface due to estimates of the molecular escape velocity, hopping across the surface with longer time between hops for decreased normal illumination in slopes and at high latitudes.

We then studied the synergistic effects of ices undergoing ion irradiation in the presence of ambient methane, to explain observations of gas retention by ices on satellite surfaces in the Outer Solar System, such as the TNOs and Centaurs. These experiments were performed by exposing microporous water ice to ambient methane at 40 to 50 K, resulting in the adsorption of

methane within the pores of the ice, but not multilayer condensation atop the ice film. The ambient methane pressure was maintained during irradiation of 100-keV  $\text{H}^+$ . We found that the ion impingement causes enhanced gas adsorption by the ice film. One mechanism for this increase in methane uptake is the conversion of low- into high-energy binding sites, due to the ice pores changing size and/or shape as irradiation proceeds. Methane uptake enhancement was largest at low fluxes, because the increased time duration between proton impacts allows for more gas adsorption within the compacting pores at sites that are increasing in binding energy.

The second mechanism for the observed increase in methane adsorption is radiation chemistry. Infrared studies revealed an exponential decrease in the amount of adsorbed methane, with a destruction cross-section of  $1.89 (\pm 0.05) \times 10^{-15} \text{ cm}^2$ , and a simultaneous increase in C-, H-, and O-containing species, including  $\text{CO}_2$ ,  $\text{CO}$ ,  $\text{CH}_3\text{OH}$ ,  $\text{H}_2$ ,  $\text{H}_2\text{CO}_3$ ,  $\text{HCO}$ ,  $\text{CH}_3\text{CHO}$ ,  $\text{C}_2\text{H}_5\text{OH}$ ,  $\text{C}_3\text{H}_8$ ,  $\text{C}_2\text{H}_6$ ,  $\text{H}_2\text{CO}$ , and  $\text{C}_3\text{O}_2$ . These radiolytic molecules are formed from the energetic dissociation of  $\text{CH}_4$  and  $\text{H}_2\text{O}$ , and the recombination of radicals into molecules that can bind to the ice film more effectively than methane, contributing to the observed increase in mass uptake by the film during irradiation. We found that ~8% of the initial amount of observed methane remained trapped at high-energy binding sites within the collapsed pores at high fluence. Another likely cause for the residual methane is that  $\text{CH}_4$  is itself a radiolytic molecule, re-formed by dissociated radicals. The radiolytic molecules remained trapped in the ice after irradiation was stopped and ambient methane was removed by pumping.  $\text{CO}$ , methanol, and  $\text{H}_2$  were retained by the ice during heating up to ~140 to 165 K, whereas  $\text{CO}_2$  did not escape until the ice film thermally desorbed at ~180 K. Even at room temperature, trace amounts of radiolytic product remained on the microbalance substrate, which will require further analysis.

We expanded our studies of the synergistic effects of ion bombardment and ambient gas exposure to examine the irradiation effects of H<sub>2</sub>-laden porous water ice films. The goal of these experiments was to understand the effects of cosmic ray impacts on ice-covered dust grains in the interstellar medium, immersed in H<sub>2</sub> gas. These experiments were accomplished by exposing porous ice films to ambient H<sub>2</sub> gas at varying pressure, and maintaining the ambient pressure during irradiation by 100-keV H<sup>+</sup>. Unlike our experiments with irradiated methane-laden films, in which we observed an ion-induced increase in trapped gas, irradiation led to a decrease in H<sub>2</sub> adsorption. This H<sub>2</sub> loss was due to a net effect between ion-induced sputtering and gas adsorption. We measured an initial H<sub>2</sub> loss cross-section of  $4 (\pm 1) \times 10^{-14} \text{ cm}^2$ , independent of film thickness, H<sub>2</sub> flux, and proton flux. Irradiation also causes the ice pores to collapse, trapping H<sub>2</sub> in interstitial sites or radiation-induced bubbles, resulting in retained H<sub>2</sub> concentration of 2 to 7% at high fluence. At estimated interstellar values of the cosmic ray flux and H<sub>2</sub> accretion rate, we predict residual H<sub>2</sub> concentration as high as 8%.

Finally, we observed suppression in H<sub>2</sub>O<sub>2</sub> synthesis by the radiolyzed H<sub>2</sub>-laden water ice films, compared to the amount of H<sub>2</sub>O<sub>2</sub> produced from 100-keV H<sup>+</sup> irradiation of pure H<sub>2</sub>O films. These films were prepared identically to those of the H<sub>2</sub> experiments described above. The presence of ambient H<sub>2</sub> during irradiation suppresses H<sub>2</sub>O<sub>2</sub> synthesis by ~16%, deduced from the strength of the 3.5- $\mu\text{m}$  H<sub>2</sub>O<sub>2</sub> absorption feature. The suppression did not change with ambient H<sub>2</sub> pressure for  $P \geq 2 \times 10^{-7} \text{ Torr}$ , or with proton flux for  $10^{10}$  to  $10^{12} \text{ H}^+ \text{ cm}^{-2} \text{ s}^{-1}$ . However, we find that the suppression effect increases with ambient pressure when the ice was co-deposited with H<sub>2</sub> before exposing the film to ambient H<sub>2</sub>, up to ~50% suppression. The presence of ambient H<sub>2</sub> decreases H<sub>2</sub>O<sub>2</sub> production due to H-enrichment, which limits the concentration of radiolytic OH in the films. The recombination of H<sub>2</sub> and OH to form H<sub>2</sub>O competes with the OH-OH

recombination channel for  $\text{H}_2\text{O}_2$  formation. This effect could be a possible contributing mechanism for the lack of detected solid-state  $\text{H}_2\text{O}_2$  on ice-covered grains immersed in  $\text{H}_2$  gas in the dark clouds of the interstellar medium.